Investigating Microstructural Effects on Short Crack Growth and Fatigue Life Behavior of WE43 Magnesium

by

Jacob F. Adams

A dissertation submitted in partial fulfillment
of the requirements for the degree of
Doctor of Philosophy
(Materials Science and Engineering)
in the University of Michigan
2018

Doctoral Committee:

Professor John E. Allison, Co-Chair
Professor Emeritus J. Wayne Jones, Co-Chair
Professor Amit Misra
Associate Professor Veera Sundararaghavan

Jacob F. Adams

jfadams@umich.edu

ORCID iD: 0000-0001-9076-1361

For my family

ACKNOWLEDGEMENTS

There are many friends, family, and colleagues who have supported and advised me through my academic journey. I would like to extend my thanks to all who have contributed their time and effort to help me achieve my goals.

First, I would like to thank my academic advisors, Dr. John Allison and Dr. J. Wayne Jones, for their guidance and support, without which this body of research would not have been possible. I appreciate their patience, insight, and advice, and I owe them a great deal for the time that they contributed to both my academic and personal development throughout the past few years I have spent at the University of Michigan. I would also like to thank the other members of my thesis committee, Dr. Amit Misra and Dr. Veera Sundararaghavan, for their assistance and careful consideration in developing this dissertation.

I would also like to recognize Chris Torbet of the University of California Santa Barbara, who assisted in the design and building of the UFSEM system utilized in this research, and who provided vital insight and advice on ultrasonic fatigue testing. I also feel indebted to John Lasecki, for his assistance with experimental equipment throughout the research lab, and who aided and simplified much of the work performed in this dissertation. I must also thank my many fellow students and colleagues, who provided assistance and friendship through these past few years: Dr. Jiashi Miao, Dr. Xianfeng Ma, Dr. Qianying Shi, Dr. Alfred Okello, Dr. Michael Kimiecik, Dr. Tracy Berman, Dr. Jason Geathers, Dr. Vir Nirankari, Dr. Erin Deda, Dr. Anna Trump, Dr. Kevin Fisher, Dr. Ellen Solomon, Dr. Aaron Lamoureux, Dr. Evan Anderson, Sinsar

Hsie, Alan Githens, Aeriel Murphy, Zhihua Huang, Jacob Garves, Zhenjie Yao, and Duncan Greeley. I would also like to thank Dr. Shardul Panwar for collaborating with me on the modeling of very high cycle fatigue behavior and crack propagation.

During the course of my research, I had the good fortune to collaborate with Dr. Ashley Spear of the University of Utah, who provided invaluable insight and guidance in the development of this work. I would also like to thank Dr. Shiu Fai Li, Dr. Jonathan Lind, Dr. Peter Kenesei, and Jayden Plumb for providing valuable discussions and for their critical assistance in the collection and analysis of experimental data gathered at the Advanced Photon Source, a U.S. Department of Energy (DOE) Office of Science User Facility operated for the DOE Office of Science by Argonne National Laboratory under Contract No. DE-AC02-06CH11357.

I would like to extend special thanks to my parents, Stephen and Michele Adams, whose love, support, and sacrifice have provided me many opportunities throughout my life, and whose encouragement led me to pursue a graduate degree.

Most importantly, I extend my deepest gratitude to my wife, Brenna, and my daughters Natalie and Arbor, who have encouraged me and given me unconditional support through many busy days and late nights of research. Without their love and encouragement, all of this would not have been possible.

Lastly, I gratefully acknowledge the U.S. Department of Energy, Office of Basic Energy Sciences, Division of Materials Sciences and Engineering for providing the funding for this research, under award #DE-SC0008637, as part of the Center for Predictive Integrated Structural Materials Science (PRISMS Center) at the University of Michigan. I would also like to acknowledge the Rackham Merit Fellowship Program at the University of Michigan for

providing initial funding for my graduate career. I would also like to extend a special thanks to Bruce Davis of Magnesium Elektron for providing the alloy used in this dissertation. I am also grateful to the researchers at the University of Michigan Center for Materials Characterization for their assistance with facilities use that was necessary for this research.

TABLE OF CONTENTS

LIST OF TABLES

LIST OF FIGURES

LIST OF APPENDICES

ABSTRACT

Magnesium alloys are increasingly being used in structural applications due to their excellent strength-to-weight ratio, particularly in applications where reductions in weight can result in significant improvements to fuel efficiency. Extending the service lives of these components into the very high cycle fatigue (VHCF) regime ($>10^7$ cycles) requires an understanding of the complex role local microstructure plays in determining fatigue behavior. In this thesis, ultrasonic fatigue has been used to characterize the effects of microstructure on VHCF behavior in the hot-rolled magnesium alloy WE43.

Crack initiation, short crack growth, and VHCF life behavior have been investigated for three microstructural conditions of WE43 magnesium. As-received (T5) WE43 with a relatively fine grain size was solution treated and aged to produce precipitation strengthened coarse-grained microstructures in the underaged and peak-aged (T6) conditions. Ultrasonic axial fatigue tests with a cyclic frequency of 20kHz were conducted using cylindrical specimens. Crack growth behavior and fatigue crack-grain boundary interactions were investigated in high resolution using a unique combination of ultrasonic fatigue instrumentation and scanning electron microscopy (UFSEM). The UFSEM system was also used to investigate fatigue crack propagation in vacuum, *in situ*. Fatigue crack-grain boundary interactions were more closely studied using thin (150 μm) foil specimens under positive mean axial stress in ultrasonic fatigue. Post-mortem measurements of a microstructurally small fatigue crack were made using X-ray computed tomography to provide high-resolution reconstructions of the 3-D crack surface morphology, and near-field high-energy X-ray diffraction microscopy to provide 3-D grain geometries and orientations adjacent to fatigue-crack surfaces.

A number of findings have resulted from these experiments and analyses, providing new insight into the role of local microstructure on fatigue behavior. Heat treatment was shown to have a strong effect on fatigue strength, with the fine-grained, strain-hardened T5 condition exhibiting much higher values than the coarse-grained underaged and T6 conditions of WE43. Differences in precipitation strengthening between the underaged and T6 conditions resulted in no significant difference in fatigue strength. It was found that average short crack growth rates for the three conditions were similar and had no clear dependence on microstructural condition, despite the significant differences in grain size. Crack initiation lifetime was shown to be particularly sensitive to grain size and occurred through cyclic slip deformation in particularly large and favorably oriented grains in each condition. Environment was shown to have a significant effect on crack growth rate, with rates in vacuum nearly two orders of magnitude lower than in laboratory air. Investigations of fatigue in in situ and foil specimens revealed that current models of the fatigue crack-grain boundary interaction based on boundary and microstructural parameters are inadequate to describe the complex interaction between the fatigue crack and local microstructure. Results indicate that more comprehensive modeling of three-dimensional microstructures using crystal-plasticity finite-element analyses is necessary to accurately predict fatigue behavior. The combined use of X-ray tomography and near-field HEDM allows for the high-resolution characterization of three-dimensional fatigue behavior, specifically fracture surface morphology and crystallography, a first step to three-dimensional modeling of fatigue and microstructure interactions.

CHAPTER 1

INTRODUCTION

Understanding of fatigue behavior is critical, as a large portion of all mechanical failures have been attributed to fatigue. Concurrently, there is a growing need to extend the service life of components beyond the traditional design limits of the high cycle fatigue (HCF) regime (10^7 cycles) to the gigacycle (10^9 cycles) or very high cycle fatigue (VHCF) regime. Increasing the service lives of components requires an understanding of how variations in material properties, such as microstructure, affect fatigue behavior in this under-characterized regime.

Magnesium alloys are increasingly being utilized in structural applications due to their excellent properties, such as low density and high specific strength. These lightweight alloys are particularly attractive in applications where reductions in weight can result in significant improvements to fuel efficiency. Automotive experts have suggested that the weight of a passenger car could be reduced by as much as 15% if suitable magnesium alloys were made available [1]. However, the fatigue behavior in magnesium alloys has not been investigated as fully as in other structural alloy systems, and the roles of microstructure on fatigue mechanisms are not yet well understood, especially in the VHCF regime, where local microstructure can have a significant effect on fatigue behavior.

The fatigue response of an alloy is comprised of different behavioral regimes, including crack initiation, short crack growth, and long crack growth behaviors, which together determine the total fatigue life of a structure. Fatigue life in the VHCF regime is dominated by crack initiation and microstructurally small crack growth, and variation in these behaviors can have a significant effect on total component lifetime [2]. Even at nominally elastic strain levels, cyclic damage can accumulate and lead to crack initiation and failure beyond the HCF regime, which is often considered a fatigue limit for many non-ferrous materials [3–5].

Interrogation of fatigue behavior in the VHCF regime presents additional challenges when considering the significant effect microstructural variability can have on fatigue behavior. Before the advent of ultrasonic fatigue, fatigue predictions were normally based on data limited to between 10^6 and 10^7 cycles, due to the limits on testing speed of conventional fatigue testing equipment [6]. Extrapolation of fatigue data from these lower lifetime regimes to the BHCF regime can lead to non-conservative fatigue life estimates in some materials, due to the occurrence of fatigue failures well below the mean life behavior. Ultrasonic testing methods allow for the investigation of fatigue behavior in the VHCF regime much more rapidly than is possible with conventional servo-hydraulic testing methods. Recent progress has further improved the capability of ultrasonic testing methods to characterize fatigue, and the effects of microstructural variability on crack initiation, crack growth, and fatigue life behaviors [6–8]. Despite these advances and the many other studies of fatigue that have been conducted, the interaction between fatigue cracks and local microstructural features is not yet fully understood. In evaluating fatigue behavior in the VHCF regime, the following questions remain:

1. How do variations in heat treatment, microstructure, and mechanical properties affect fatigue behavior (crack initiation, short crack growth, and very high cycle fatigue lifetimes)?
2. What role do local microstructural features (crystallographic orientations, boundary misorientation, grain size, etc.) play in crack initiation and short crack propagation?

3. Considering the three-dimensional nature of fatigue crack growth, how can fatigue behavior be sufficiently characterized and modeled?

The present work is focused on addressing these questions regarding the role of microstructure on crack growth and very high cycle fatigue behavior of WE43 magnesium using a direct experimental approach. Experimental methodologies utilized in this work combine ultrasonic fatigue with scanning electron microscopy and post-mortem characterization using high energy X-rays to enable two- and three-dimensional characterization of fatigue behavior.

Characterization of fatigue behavior using ultrasonic fatigue has largely been limited to the determination of total fatigue life, crack growth rates, and deformation processes that are inferred from post-failure surface microscopy or fractography. Generally, observations on crack initiation and failure have been linked to microstructural features using a “before-and-after” methodology, although recent advances have combined ultrasonic fatigue with more advanced characterization techniques to interrogate fatigue behavior in an ex-situ manner and to investigate fatigue beyond surface measurements [5,9]. Geathers et al. and Adams et al. have used a unique combination of scanning electron microscopy and ultrasonic fatigue, which will be discussed in this work, to investigate cyclic damage accumulation and crack propagation *in situ*, as well as the effect of environment of fatigue crack propagation in titanium and magnesium [10,11]. The majority of fatigue characterization techniques involve two-dimensional measurements, but complex crack path morphologies, crystallography, and local crack growth rates cannot be described sufficiently by free-surface measurements. In order to investigate the three-dimensional evolution of fatigue cracks, there is a need for quantitative characterization methods beyond conventional free-surface observations. Until recent advances in high-energy X-ray characterization methods, non-destructive investigation of three-dimensional fatigue behavior has been mostly limited to laborious characterization of the fracture surface using scanning electron microscopy and electron backscatter diffraction microscopy [12]. By combining high-resolution X-ray tomography with 3-D X-ray diffraction microscopy, new methods have been developed that allow for the non-destructive characterization of three-dimensional crack morphology, grain morphology, and crack path crystallography [12–14].

The overall aim of this dissertation research was to develop a fundamental understanding of microstructural influences on fatigue damage mechanisms in WE43 magnesium in the VHCF regime, in order to further the understanding of critical microstructural features in fatigue behavior, leading to improved fatigue properties in magnesium alloys.

The specific objectives of this thesis work were to:

1. Determine the effects of three different heat treatments (and the associated microstructural differences) on the fatigue life response, microstructurally short crack growth, and fatigue crack initiation behavior of a commercial hot-rolled WE43 magnesium alloy;
2. Identify the microstructural features leading to crack initiation, and add to our understanding of the mechanisms of fatigue crack initiation and growth in the VHCF of magnesium;
3. Characterize the interaction between microstructurally short fatigue cracks and grain boundaries, and identify critical crack, microstructural, and boundary parameters governing crack retardation and arrest at these boundaries;
4. Characterize the three-dimensional fatigue behavior of microstructurally short cracks in WE43 magnesium using a combination of post-mortem observations

including quantitative fractography, X-ray tomography, and near-field high energy X-ray diffraction microscopy.

Chapter 2 provides a review of literature that is relevant to the present work, including studies of fatigue behavior in a variety of magnesium alloys, as well as a discussion of advanced characterization techniques. In Chapter 3, the experimental methods for VHCF studies are described, along with details of instrumentation developed for *in situ* SEM studies and procedures for three-dimensional characterization of crack growth. Chapters 4, 5, and 6 represent three studies prepared for publication, resulting in some repetition of background information provided in each chapter. Chapter 4 presents a detailed description of the effect of variation in heat treatment and microstructure on fatigue behavior in three conditions of WE43 magnesium. The results of a study of the interaction between short fatigue cracks and grain boundaries are presented in Chapter 5, using ultrasonic fatigue of *in situ* and thin foil specimens. A detailed study of the three-dimensional fatigue behavior of a WE43 specimen is discussed in Chapter 6. Finally, conclusions and recommendations for future work are detailed in Chapter 7.

CHAPTER 2

LITERATURE REVIEW

In this chapter, a review of the literature relevant to understanding the objectives, the approach, and the results of this dissertation is presented. Section 2.1 describes the physical and mechanical metallurgy of rare-earth magnesium alloys, as well as a discussion of deformation processes for magnesium alloys. Section 2.2 presents the general fatigue properties observed in magnesium, focusing on cyclic damage accumulation and the role of microstructure on fatigue crack initiation and fatigue crack propagation, as well as methods for characterizing these behaviors.

2.1. Metallurgy of Magnesium

2.1.1. Physical Metallurgy of Rare-Earth Magnesium Alloys

Magnesium is rarely used in structural engineering applications without being alloyed with other elements. Commonly, other metals such as aluminum, manganese, zinc, zirconium, and rare earths are added to produce alloys with the mechanical properties necessary for structural applications [15]. The properties of many cast and wrought magnesium alloys can be improved through age hardening, which involves solution treatment to produce a single phase, followed by subsequent quenching and aging at relatively low temperatures to produce distributed precipitates in the magnesium matrix. Rare earth elements, when alloyed with magnesium, can produce a significant age-hardening response.

Magnesium forms solid solutions with many of the rare earth (RE) elements. Aging of these alloys leads to precipitation within grains, contributing to improved creep resistance and improved strength (Figure 2.1). The mechanical properties of Mg-RE alloys can further be improved by the addition of zirconium, frequently used as an alloying element to produce grain refinement in alloys that do not contain aluminum or manganese. Strength in the Mg-RE-Zr alloy system can further be improved with the addition of Zinc. Common cast and wrought alloys using these elements include the ZE alloys. Further improvements to this system can be made by utilizing yttrium as the RE alloying element. Yttrium features a particularly high solid solubility in magnesium (12.5%), resulting in an increased capacity for age hardening (Figure 2.2). This results in improved room-temperature strength and high-temperature creep resistance [15]. The most successful alloys in this group have been the WE54 and WE43 alloys, utilizing a Mg-Y-Nd-Zr system [16].

Precipitation in Mg-Y-Nd is complex, involving formation of the following metastable phases from the supersaturated solution: ordered G.P. zones, hexagonal close packed (hcp) β’’ ($Mg_3(Nd,Y,Zr)$), globularly shaped orthorhombic β’ ($Mg_{12}NdY$), face-centered cubic β_1 $\{1\bar{1}00\}$ plates ($Mg_3(Nd,Y)$), and finally larger face-centered cubic β $\{1\bar{1}00\}$ plates ($Mg_{14}Nd_2Y$) (Figure 2.3a,b) [16,17]. Researchers have also noted the formation of metastable β’’’ precipitates in rare-earth strengthened magnesium alloys [18,19]. It has been noted that the significant improvement in hardness and strength seen in Mg-Y-Nd alloys is due to the formation of β_1 prismatic plates, and the role they serve to impede dislocation movement and slip along the basal plane in the magnesium matrix [20]. In deformation through either basal slip or twinning, precipitate plates formed on prismatic planes of the magnesium matrix serve as the strongest barrier to deformation, as compared to basal plates or spherical particles (Figure 2.3c,d) [16].

2.1.2. Description of Microstructure

Alloys in the Mg-RE system are utilized in both cast and wrought conditions. In the as-cast conditions, α-grains are surrounded by a well-developed grain boundary network (Figure 2.4a) [15,21]. Aged alloys exhibit strengthening precipitates within the matrix. An investigation of cast Mg-Nd2.8-Gd1.5-Zr0.5-Zn0.2 revealed a microstructure of equiaxed grains populated with Mg/Nd-Gd intermetallic compounds, with a $Mg_{12}Nd_xGd_{(1-x)}$ eutectic network forming at grain boundaries. Solution treatment and aging to a T6 temper resulted in dissolution of the intermetallic compound and the formation of β'' and β' precipitates in the matrix, although the grain boundary eutectic network was not completely dissolved during the solution treatment [22]. In wrought alloys, the microstructure depends heavily on the thermo-mechanical processing of the particular condition being characterized. Commonly, hot working produces an elongated grain structure, occasionally decorated with smaller, equiaxed recrystallized grains [15]. A study of the effects of T5 and T6 tempers on hot rolled WE43 found that the deformed grain morphology remained after a T5 temper, while a T6 temper resulted in a fully recrystallized grain structure. TEM observation revealed the presence of strengthening precipitates in the matrix, with increased precipitate size in the T6 tempered material, as compared to the T5 temper [23]. An investigation by Marrow et al. revealed larger scale precipitation along grain boundaries and in the matrix in T6 tempered WE43 [24].

2.1.3. Deformation Processes of Magnesium

Although magnesium alloys offer increased weight-saving possibilities as compared to other structural metals, they often exhibit reduced ambient temperature formability and significant anisotropy. As a hexagonal material, magnesium only exhibits one close-packed plane system, which fails to provide the five independent slip systems necessary to meet the Von

Mises requirement for the homogenous plastic deformation of crystals [25]. This results in greater anisotropy and a higher potential for the development or strengthening of deformation-induced crystallographic texturing, as well as necessitating additional deformation mechanisms and the activation of less-favorable slip systems [26].

In general, hcp materials feature easy glide along the $\langle 11\bar{2}0\rangle$ direction, although the plane of easiest slip varies depending on the c/a ratio. In magnesium alloys, the principal slip system lies in the basal plane ($\{0001\}\langle 11\bar{2}0\rangle$), which only provides two independent slip systems. Although deformation on non-basal slip systems is possible, they exhibit lower levels of activation and often fail to activate during room-temperature deformation. Many variables can affect the activation of non-basal slip, including alloy composition, texture, grain size, and temperature. Non-basal slip systems present in magnesium include the prismatic $\{10\bar{1}0\}\langle 11\bar{2}0\rangle$ (2 independent slip systems), the pyramidal $\{10\bar{1}1\}\langle 11\bar{2}0\rangle$ (four independent slip systems) and the pyramidal <c + a> $\{11\bar{2}2\}\langle 11\bar{2}3\rangle$ (five independent slip systems) (Figure 2.5). Although literature values vary, the critical resolved shear stress (CRSS) required for the room-temperature activation of non-basal slip has been reported to be significantly higher than that for basal slip [27,28]. Further hindering the formability of magnesium is the fact that only the pyramidal <c + a> slip system can accommodate deformation with components in the *c*-direction of the unit cell. In addition to the activation of non-basal slip systems, the Von Mises criterion is met through the activation of deformation twinning. In hcp materials, extension twins activate on $\{10\bar{1}2\}$ planes in $\langle 10\bar{1}\bar{1}\rangle$ directions (Figure 2.5), and can further help accommodate deformation with components in the *c*-direction of the unit cell. Although twinning helps to meet the Von Mises criterion, there are limits to its effectiveness as a deformation mode. Due to the nature of twinning, shear can only occur in one direction, rather than forward and backward like slip [29].

Furthermore, as twinning requires a reorientation of the crystal lattice, the amount of strain accommodated by twinning is directly related to the volume of the lattice that has twinned and is limited by the volume of crystal that can feasibly undergo twinning. Finally, as twinning involves a sudden reorientation of the crystal lattice, which introduces internal stresses that may lead to failure [30]. The activation of twinning and the difficulty in activating additional slip systems play an important role in determining deformation-induced crystallographic texture.

Crystallographic texture in polycrystalline materials is of substantial importance. In metals, texture can be developed during thermal-mechanical processing. Crystallographic texture develops as a result of the balance between deformation mechanisms that contribute to plastic deformation. In a study of rolled α-titanium, the competition between twinning or basal slip as the dominant deformation mode at different levels of strain produced significantly different crystallographic textures [31]. In magnesium, texturing can result in significant anisotropy and limited formability in the final product [32]. During rolling of hcp materials, generally a strong [0001] fiber texture tends to develop as the majority of grains align such that their basal planes lie parallel to the sheet plane [33]. While it has been shown that grain growth or recrystallization during annealing of conventional wrought magnesium alloys generally have only a moderate effect on texture reduction, it has been found that the addition of RE elements can lead to significantly weaker textures as a result of recrystallization [32,34–37]. Ball and Prangnell first noted weakened texture in a RE containing magnesium alloy WE54 following extrusion, which they attributed to recrystallization and particle stimulated nucleation [38]. Mackenzie et al. observed the development of non-basal texturing in the recrystallization of extruded WE43. They postulated that the presence of RE elements resulted in the formation of recrystallized grains oriented such that their basal poles were 45° from the extrusion axis [39].

In a study on the role of yttrium in the texture evolution of magnesium alloys, Farzadfar et al. observed a significant retardation of dynamic recrystallization during uniaxial hot compression in a Mg-2.9Y alloy coupled with a weakening of a strong basal texture during subsequent annealing [34]. Even wrought magnesium alloys with more dilute concentrations of RE elements exhibit a weakening of basal texture. In a study of micro-alloyed magnesium alloys, Stanford et al. noted a decrease in $[10\bar{1}0]$ extrusion texture strength with an accompanying appearance of a $[11\bar{2}1]$ texture peak with increasing RE content (Figure 2.6), coupled with increasing ductility [37].

Many studies have focused on determining how differences in microstructure as a result of composition and processing impact mechanical properties and the complex deformation response of magnesium. Minor differences in microstructure can have significant effects on a variety of mechanical properties, including the mechanisms that govern strain localization, crack initiation, and microstructural-scale fatigue crack growth.

2.2. Fatigue of Magnesium Alloys

Magnesium alloys are increasingly being considered in structural applications due to their excellent properties, such as low density and high specific strength. These lightweight alloys are particularly attractive in applications where reductions in weight can result in significant improvements to fuel efficiency [1]. However, the fatigue behavior in magnesium alloys has not been investigated as fully as in other structural alloy systems, and the roles of microstructure on fatigue mechanisms are not yet well understood, especially in the VHCF regime, where local microstructure controls crack initiation and early propagation behavior.

Both cast and wrought magnesium alloys are utilized in fatigue applications, but frequently display significantly different fatigue properties. Wrought magnesium alloys are free from most defects found in cast magnesium parts, which often act as crack initiation sites in fatigue. Additionally, wrought alloys benefit from increased strengthening as a result of the fabrication process [40]. Consequently, wrought magnesium alloys often display superior fatigue properties [41], but may also suffer from asymmetry of yield behavior as a result of texturing arising from deformation processing.

Fatigue failure can occur in many different forms, and generally occurs under cyclic loads whose peak values are much lower than loads traditionally deemed safe based on static fracture analysis [42]. The fatigue response of an alloy is comprised of different behavioral regimes, including crack initiation, short crack growth, and long crack growth behaviors, which together determine the total fatigue life of a structure. In each area, fatigue behavior is dependent on a variety of factors, including microstructure, mechanical loading conditions (frequency, load ratio, load level, temperature), and environment. The first stage of fatigue occurs before crack initiation, and involves the initial movement and generation of dislocations, as well as the initiation of cyclic hardening or softening [43]. This small-scale accumulation of cyclic damage leads to the initiation of microscopic cracks. Following crack initiation, microscopic cracks grow and coalesce into dominant cracks, leading to crack propagation. Following stable crack propagation, structural failure eventually occurs. Fatigue life in the VHCF regime is dominated by crack initiation and microstructurally small crack growth, and variation in these behaviors can have a significant effect on total component lifetime [2]. Even at nominally elastic strain levels, cyclic damage can accumulate and lead to crack initiation and failure beyond the high cycle fatigue (HCF) regime, i.e., 10^7 cycles, which is considered a fatigue limit for many non-ferrous materials [3–5]. For magnesium alloys in general, fatigue lifetime data beyond 10^7 cycles is sparse.

2.2.1. Very High Cycle Fatigue Behavior

Researchers have recently questioned the concept of the “fatigue limit” in the context of VHCF [44]. Studies at 30 Hz [45] and at ultrasonic frequencies [46,47] have indicated that the assumption of a fatigue limit may not be valid for all magnesium alloys. Even at nominally elastic strain levels, cyclic damage can accumulate and lead to crack initiation and failure beyond the 10^7 cycles (HCF regime), which is often considered a working fatigue limit for many non-ferrous materials [3,4,48]. In a study of die-cast AE42 and AM60 alloys, failures were observed in the VHCF regime, with AE42 exhibiting no fatigue limit [49]. Both alloys showed a tendency for cracks to initiate from within the sample, rather than on the surface. It is postulated that casting pores served as crack initiation sites, with the majority of fatigue life corresponding to the crack propagation stage. Similarly, in a VHCF study of extruded AZ31 a fatigue limit was not observed [50]. A study of the fatigue behavior of as-extruded AZ31, AZ80, and ZK60 in the VHCF regime found that the S-N curves exhibited no apparent fatigue limits (Figure 2.7) [46]. In a comprehensive study of AZ alloy fatigue lifetime behaviors in the VHCF regime, many alloys exhibited no fatigue limit (Figure 2.8) [51]. Despite the excellent mechanical properties of the WE43 magnesium, little research has been conducted into its fatigue behavior. Gu et al. investigated the fatigue behavior of wrought WE43 in the HCF regime in both laboratory air and simulated body fluid and found an apparent fatigue limit of 100 MPa in laboratory air [52]. Despite their findings, WE43 fatigue data in the VHCF regime is lacking, and the identified fatigue limit may not hold for higher cycle testing. In general, data on the fatigue behavior of magnesium alloys in the VHCF regime is sparse. Due to the fact that fatigue lives in the HCF and VHCF regimes are dominated by crack initiation and crack propagation, differences in crack initiation and crack propagation can result in significantly different fatigue lives. Accurate prediction of fatigue lives requires an understanding of the interaction between local microstructure and mechanisms of fatigue crack initiation and propagation.

2.2.2. Damage Accumulation and Fatigue Crack Initiation

While the exact point at which crack initiation occurs is still debated, crack initiation is generally defined as the number of cycles necessary to generate the smallest detectable crack [53]. Additionally, crack initiation can refer to the period when a site of cyclic damage begins to behave as a propagating crack. Using this definition, crack behavior will be determined by local microstructural features. When the crack length is on the order of the microstructural length scale, accurate prediction of fatigue life requires an understanding of the micro-scale mechanistic responses to cyclic stress during initiation and small-scale crack growth. Furthermore, crack initiation mechanisms are dependent on fatigue regime, with different initiation mechanisms and their microstructural dependencies operating in low cycle fatigue and in the VHCF regime. This work will focus predominantly on fatigue behavior in the HCF and VHCF regimes. In the VHCF regime, it has been suggested that, while the strain level is too low to develop persistent slip bands (PSBs), a small fraction of grains exhibit microstructurally irreversible slip [5]. This irreversible slip then accumulates at favorable microstructural locations at the surface, resulting in localized surface roughening and eventual crack initiation [54]. As strain accumulates more rapidly at specific microstructural configurations or features, these mechanisms and microstructural features must be studied in order to understand initiation behavior in magnesium alloys.

Fatigue cracks in magnesium have been observed to initiate by a number of mechanisms. Crack initiation in cast magnesium alloys is often related to the presence of pores or internal defects, which is one of the sources of the lower fatigue resistance of cast magnesium as compared to wrought alloys [55–59]. In fatigue, when pores or defects act as crack initiation sites, the crack initiation stage of fatigue is often negligible, and the fatigue life is dominated by the crack propagation stage, as observed by Caton in a cast aluminum alloy [60]. In a study investigating the fatigue properties of as-cast and extruded AZ61 magnesium alloys, Sajuri et al. found that casting defects significantly degraded fatigue properties in the as-cast condition (Figure 2.9). Furthermore, fatigue life of the as-cast alloy was found to be essentially equal to the crack growth life [57]. Wrought magnesium alloys are essentially free from casting defects, and therefore demonstrate superior fatigue properties [40,41].

In the HCF regime, observed crack initiation mechanisms include cyclic slip deformation active near grain boundaries and in grain interiors [2,61,62], stress concentrations related to twin boundaries [2,63], as well as stress concentrations around inclusions in many cases (Figure 2.10) [59,64–68]. In a study of rolled AZ31, Tokaji et al. found that crack initiation occurred at the specimen surface in both an intergranular and transgranular manner, as well as at subsurface microstructural sites due to cyclic slip deformation [61]. Bernard et al. observed crack initiation in an extruded AZ61 alloy to be the result of decohesion along multiple persistent slip bands which then coalesced to form dominant fatigue cracks [62]. Nascimento et al. linked crack initiation in an extruded ZN11 alloy to cyclic slip deformation and the interaction between slip bands and Mg-Nd-Zn particles, while initiation in an extruded AZ31 alloy was linked to stress concentrations at twin boundaries as a result of dislocation blocking [2]. In a study of rolled AZ31 magnesium, Uematsu et al. observed crack initiation to occur through basal slip at a stress concentration induced by the formation of a secondary twin within a primary twin band (Figure 2.11). Additionally, they observed crack initiation along a grain boundary at a microstructural site where the angle of basal slip, primary, and secondary twins were close to the angle of the grain boundary (Figure 2.12) [63].

While many studies of crack initiation in magnesium alloys have focused on the low and HCF regimes, information on crack initiation mechanisms for magnesium in the VHCF regime is generally lacking. In VHCF of non-magnesium alloys, researchers have observed a variety of crack initiation mechanisms. Studies have shown in a range of alloys that stress-life (S-N) plots exhibit two distinct regions with two apparent asymptotes, an apparent HCF fatigue limit at moderate strain amplitudes and a VHCF fatigue limit at lower strain amplitudes (Figure 2.13). These distinct regions occur as a result of competition between two failure modes, with one failure mode active at shorter lifetimes, and a second failure mode creating a secondary fatigue limit at higher lifetimes [26,48,69,70]. In a study of fatigue in high strength low alloy steels, Wang et al. observed that failures in the gigacycle regime were dominated by subsurface crack initiation at inclusions, while failures below 10^7 cycles were dominated by surface initiation [26]. Similar results in a beta titanium alloy were observed by Chandran and Jha, who further linked the variation in fatigue life to environmental effects accelerating crack initiation and growth at surface initiation sites [70]. In materials where inclusions or pores do not cause initiation, initiation tends to occur at microstructural sites where the accumulation of irreversible slip is favored. Szczepanski et al. observed crack initiation in Ti-6246 at surface locations featuring larger than average primary alpha, α_p, grains, which occurred by cyclic strain localization on basal and prismatic planes [71]. Fractography of crack initiation sites revealed the presence of many facets with orientations favorable for slip. Huang et al. found that in gigacycle fatigue of a bearing steel, subsurface crack initiation occurred at large, single grains (Figure 2.14) [72]. They further observed that, for subsurface initiation sites, 90% of the total lifetime was devoted to initiation of the crack. In a study of VHCF of polycrystalline copper, Stanzl-Tschegg and Schönbauer observed strain localization and PSB formation below the conventional "PSB threshold" along with the formation of numerous non-propagating small cracks [73]. They found that an approximate 100% increase in strain amplitude was necessary for the formation of a propagating crack, indicating that sub-PSB threshold crack growth may not be possible in some materials.

Although investigations of crack initiation in the VHCF regime for magnesium are rare, both cast and wrought alloys have been studied. In cast alloys, crack initiation in the VHCF regime has overwhelmingly been tied to the presence of casting defects like porosity [49,56,74–77]. In wrought alloys, a wider variety of initiation mechanisms has been observed. In a number of studies, crack initiation occurred due to stress concentrations around inclusions [46,78,79]. Cracks have also been observed to initiate through cyclic slip deformation along persistent slip bands [47,80] and twin boundaries [47,50,81] as well as at both surface and near-surface sites exhibiting oxide films [82]. In a study of extruded GW123K and AZ31 magnesium alloys, Yang et al. observed the initiation of numerous cracks along twin bands in the AZ31 alloy, while the GW123K alloy exhibited crack initiation along persistent slip bands in the absence of crystallographic twins (Figure 2.15) [47]. In a study of VHCF properties of extruded AZ80 magnesium alloy, Shiozawa et al. also observed crack initiation along twin boundaries, with facet-like regions oriented favorably for slip present at the initiation sites (Figure 2.16) [81]. Xu et al. observed both surface and near-surface initiation during VHCF of a Mg-Zn-Y-Zr alloy, with oxide films present at each initiation site, but absent elsewhere on the fracture surface. Crack initiation was attributed to an interaction between single slip and environment, resulting in oxide film formation and subsequent retardation of cyclic slip (Figure 2.17) [82]. In addition to crack initiation, crack propagation often forms a significant portion of VHCF lifetime.

2.2.3. Fatigue Crack Propagation

Fatigue crack growth is strongly affected by the deformation characteristics and microstructure of the material, as well as the loading conditions. In magnesium, as in most ductile metals, fatigue crack growth is believed to occur through localized deformation near the crack tip facilitated by crystallographic slip. In general, linear elastic fracture mechanics divides fatigue crack growth into two stages, discussed below.

During Stage I fatigue crack growth, crack propagation occurs predominantly through single slip along the direction of the primary slip system (Figure 2.18). Single slip along the dominant slip system results in a “zig-zag” crack path, with reorientation of the crack occurring at grain boundaries. Stage I crack growth occurs when the crack is small and the plastic zone size at the crack tip is comparable to or smaller than the grain size. This stage of crack growth generally corresponds to slow growth rates near the crack propagation threshold, with high crack closure levels and significant sensitivity to local microstructure.

At higher stress intensity levels, the plastic zone size at the crack tip is larger and the plastic zone samples multiple grains. Corresponding crack growth occurs through simultaneous or alternating crystallographic slip along two slip systems, and generally results in a crack path that is normal to the far-field loading axis (Figure 2.18). This period of crack growth is known as Stage II and corresponds to low levels of crack closure and reduced sensitivity to microstructural features. Stage II crack growth is also known as the Paris regime of crack growth, which refers to stable fatigue crack growth for a certain range of the stress intensity factor ΔK between stage I and stage III crack propagation. In this range, Paris et al. showed that the increment of fatigue crack growth, da/dN, could be related to the stress intensity factor range ΔK by the power law relationship

$$\frac{\mathrm{d}a}{\mathrm{d}N} = C(\Delta K)^m \tag{2.1}$$

where *C* and *m* are scaling constants that are influenced by variables like microstructure and environment [83,84].

2.2.4. Fatigue Striations and Beach Marks

In many alloys, fracture surfaces corresponding to stage II crack growth exhibit features known as fatigue striations (Figure 2.19). Fatigue striations have been described as “ripples” on the fracture surface, and were first observed by Zapffe and Worden in a study of steel and aluminum alloys [85]. Fatigue striations are essentially registrations of the crack front from prior cyclic loading. In the Paris regime of fatigue crack growth, it has been shown that the spacing between fatigue striations correlates with the experimentally measured per cycle crack growth rate [86]. Although not all alloys form fatigue striations, they have been observed in many pure metals and alloys.

Conceptual models of the formation mechanism for fatigue striations have focused on plastic blunting of the crack tip. Laird et al. first showed that in high-strain cyclic loading of a ductile metal, crack tip blunting occurred during tensile loading, and formation of a *ductile fatigue striation* and re-sharpening of the crack tip occurred on unloading or compressive loading (Figure 2.20) [87]. This explanation was further refined in a study by McMillan et al. showing the formation of fatigue striations exhibiting a “saw tooth” profile, and linking the formation of individual teeth to single loading cycles (Figure 2.21) [88]. Researchers have also observed striations not formed due to duplex slip, but rather during stage I crack growth. These *brittle* *striations* have been observed on crystallographic {100} facets in high strength aluminum alloys, and have been postulated to form either through interrupted cleavage fracture, environmental interactions with the fracture surface [89], or through a process similar to the formation of ductile striations through crack tip blunting [90].

The one-to-one correspondence of individual cycles and fatigue striations has been questioned for fatigue crack growth at low ΔK levels and with low crack growth rates [91]. In a study of fatigue crack growth in a 2024-T3 aluminum alloy, Broek et al. found that, at crack growth rates below 3×10^{-8} m/cycle, striation spacing exceeded the average crack growth rate, which they attributed to non-uniform crack growth at low ΔK [92]. Riemelmoser et al. have proposed that there is a minimum value for striation spacing, and that it is limited by the spacing between slip lines [93]. Underlying the issue of the one-to-one correspondence is the idea that fatigue crack propagation may not always occur on a cycle-by-cycle basis. In studies of cyclic crack growth in aluminum and steel alloys, researchers observed striation spacing that exceeded fatigue crack growth rates at low ΔK values (Figure 2.22). Many of these researchers concluded that crack growth at low ΔK values was intermittent, and that thousands of cycles may be necessary to advance a fatigue crack by an additional increment [94–96]. This would result in the formation of a single striation during the increment of crack advancement, and a number of load cycles with no corresponding fatigue striations.

Striations are not the only fracture surface features that register the position of the crack front during cyclic loading. Studies have shown that cyclic changes in environment or loading conditions during crack initiation and propagation can result in the formation of periodic patterns called beach marks or marker bands on the fracture surface [97–100]. The difference between beach marks and striations is that striations generally correspond to single loading cycles and occur as a result of crack advance by cyclic slip, while beach marks correspond to multiple load cycles, and are visible due to different fracture surface morphologies produced by changes in test conditions. While striations provide some insight into local crack growth behavior, beach marks can provide information on fatigue crack propagation on a more macroscopic scale. Beach marks have been used to visualize subsurface fatigue crack growth and characterize crack growth rates [12,101] as well as in post-mortem determination of Paris law constants [99]. In general, these indicators of fatigue crack history can provide information about fatigue crack growth behavior beyond surface observations.

2.2.5. Short Crack Growth

The practice of characterizing fatigue crack growth rates has long relied on laboratory fatigue tests containing "long" cracks that are typically multiple millimeters in length. Pearson first observed the phenomena that crack propagation rates for small fatigue flaws in two aluminum alloys did not correlate with conventional long crack data [102]. A number of studies have since shown that, when characterized using linear elastic fracture mechanics (LEFM), "small" fatigue flaws (less than several millimeters) exhibit crack growth rates significantly higher than corresponding long cracks, in terms of the stress intensity parameter ΔK [60,103–106]. It is now commonly accepted that short cracks can propagate at stress intensity factors below the long crack threshold, and will propagate at faster rates than long cracks with equivalent stress intensity factors (Figure 2.23) [42]. Suresh and Ritchie [105] suggested the following definitions by which short cracks can be broadly classified:

1) Microstructurally small cracks: fatigue cracks for which the crack size is comparable to the scale of the characteristic microstructural dimension, such as grain size.

2) Mechanically small cracks: fatigue cracks in which the near-tip plastic zone is comparable to the crack size, or cracks which are engulfed by the plastic strain field of a notch.
3) Physically small cracks: fatigue cracks which have a short length (typically < 1-2 mm), regardless of the scale of characteristic microstructure or plastic zone size.
4) Chemically small cracks: fatigue cracks which exhibit anomalies in propagation rate below a certain crack size as a result of environmental stress corrosion fatigue effects on crack dimensions. These cracks may not necessarily be physically small cracks.

It is worth noting that small cracks may exhibit characteristics of multiple types. In this dissertation, cracks which are microstructurally small, mechanically small, and/or physically small will be considered. The terms "small" and "short" are used, as in much of the literature, synonymously.

The cause of the small crack phenomenon is not yet completely understood and may vary depending on the material system under consideration. Three explanations for the difference in growth rates between short and long cracks that are commonly proposed are the absence of crack closure, a breakdown in metallurgical similitude, and plasticity effects. These concepts are explained below.

It has long been recognized that, in the fatigue of conventional long cracks, crack closure or crack tip shielding essentially reduces the driving force for crack propagation. This shielding of the crack tip from the full cyclic load can occur through a number of mechanisms, including plasticity-induced crack closure, corrosion effects, and rough fracture surface morphology (Figure 2.24) [105]. Elber first noted crack closure under cyclic tension in a fatigue study of aluminum, and found that plastically deformed material formed ahead of the crack tip resulted in a wake of permanently deformed material along the fracture surface [107]. This permanently deformed material on the crack faces contacts as the tensile load is reduced, before the zero load point is reached, essentially reducing the effective stress intensity range or driving force for crack growth. In addition to plastic deformation, fracture surfaces may make contact during cyclic loading as a result of the formation of corrosion products or oxides on the fracture surface, or as a result of excessively rough fracture surface morphology in which protruding features may make contact with the opposing crack face. As short cracks exhibit shorter wakes and reduced areas of fracture, they experience reduced levels of crack closure. This can be a significant factor for *physically* small cracks.

The characterization of fatigue crack growth using linear elastic fracture mechanics is based on the assumption of microstructural similitude. This implies that, for cracks of varying length in varying specimens, conditions at the crack tip will be similar between cracks with similar values of characterizing parameter, such as ΔK, within a single material and environmental system. Microstructural similitude is based on the idea that a crack front encounters a large number of microstructural units, such as grains or dendrites. The growth of the crack is therefore averaged over the large number of microstructural units exhibiting characteristics representative of the average material response to far-field loading. Small fatigue cracks may often sample only a small number of microstructural units. As a result, the propagation behavior of the crack will vary significantly depending on the microstructural characteristics of the few grains or microstructural barriers, such as grain boundaries, encountered during early crack growth. As cracks generally nucleate in grains favorably oriented for slip and subsequent crack propagation, early crack growth of small cracks is typically rapid. The breakdown in microstructural similitude is particularly significant for *microstructurally* small cracks.

One of the assumptions of the linear elastic parameter ΔK is that plastic yielding ahead of the crack tip is small relative to the length of the crack. In small cracks, this assumption is violated as the plastic zone is comparable to the size of the crack, resulting in the accelerated crack growth characteristic of the small crack phenomenon when using the ΔK parameter to correlate crack growth rates. Elastic-plastic characterization and a consideration of increased plasticity at the crack tip offers a possible means of accounting for the apparent differences in crack growth rates of long and short fatigue cracks [42]. Plasticity effects are especially important for *mechanically* small cracks.

The small crack phenomenon represents an important technical issue because the direct application of conventional long crack data to design against failure in components that may contain short flaws can lead to dangerous overestimation of fatigue lives. For example, designers may assume that small flaws with ΔK below the long crack threshold ΔK_{TH} will not experience crack propagation and subsequent fatigue failure. However, the small crack phenomenon indicates that rapid crack growth may still occur at these flaws. It is important to note that fatigue cracks, especially in the VHCF regime, spend the vast majority of their crack propagation lives as short cracks. The small crack phenomenon can result in significantly fewer "safe" loading cycles than might be predicted for VHCF cracks using traditional long crack growth data, as small cracks have been shown to propagate more rapidly than long cracks at a similar stress intensity. To further complicate the issue, crack growth in the VHCF regime frequently consists of predominantly microstructurally small crack growth, in which variation in local microstructure can have significant impact on crack growth rates and behavior.

Understanding of the interactions between microstructure and short crack growth is clearly critical in order to design safe and efficient components. A number of studies have been conducted on a variety of magnesium alloys in order to identify the mechanisms governing crack growth, as well as the effects of local microstructure.

An investigation of cast AM60B cycled in water vapor revealed strong interaction of microstructurally short cracks with the local microstructure, with preferential propagation through dendritic cells and decreased crack growth rates as cracks approached dendrite boundaries [108]. In a study of high pressure die cast AM50 and AM60 alloys, microstructurally short crack growth was intergranular along eutectic/dendrite interfaces [109]. A study of three-dimensional short crack growth in the magnesium alloy Elektron 21 (Mg-2.5Nd-1.3Gd-0.5Zr-0.31Zn) found that short crack growth occurred preferentially along basal planes, with crack retardation at highly misoriented grain boundaries [13]. Nan et al. observed stress-level dependent crack arrest at phase boundaries in extruded AZ31, indicating a strong interaction between the microstructurally small crack and local microstructure [110]. In general, short crack growth in magnesium is characterized by strong interaction with microstructural features, although propagation modes and interaction characteristics vary widely across the spectrum of magnesium alloys. Some models of these interactions between short fatigue cracks and microstructural barriers will be discussed in the next section.

Observed short crack propagation rates vary highly with stress intensity factor, and include ranges of 1×10^{-9} to 1×10^{-5} meters per cycle in AM60B (Figure 2.25) [108], 4×10^{-9} to 4×10^{-8} meters per cycle in Elektron 21 [13], 1 x 10-10 to 1 x 10-6 meters per cycle in extruded AZ31 [110], to 4×10^{-7} to 1×10^{-4} meters per cycle in extruded AZ61 [67]. The significant variation in reported crack growth rates indicates a strong sensitivity to the individual characteristics of the studied alloys and testing conditions, such as composition, microstructure, load ratio, and environment. Although many studies have theoretically and experimentally investigated the characterization and modeling of short fatigue cracks [111,112], understanding of short crack growth behavior remains far from complete.

2.2.6. Interaction of Fatigue Cracks with Grain Boundaries

One of the reasons for the breakdown in microstructural similitude observed in the growth of short cracks is the strong effect local microstructural features, such as grain orientation, size, and the presence of grain boundaries, have on short crack growth. Grain boundaries are well known to be significant barriers to cyclic short crack growth [104,113,114], with the level of misorientation between grains playing a prominent role in magnitude of the barrier effect [115–117]. The models that describe this interaction will be described briefly below.

During Stage I crack growth, cracks are presumed to grow through the emission of dislocations from the tip of the crack along the active slip plane, which is also the plane of crack growth. This crack propagation mode has been thoroughly described by Bilby, Cottrell and Swinden, and is known as the BCS model [118]. In the BCS model, per cycle crack advancement is governed by the crack tip sliding displacement (CTSD) that occurs as a result of the dislocations emitted from the tip of the crack (Figure 2.26). Cyclic crack growth rate can be expressed by the CTSD in a power law relation, similar to the Paris law:

$$\frac{\mathrm{d}a}{\mathrm{d}N} = C(\Delta CTSD)^n \qquad [2.2]$$

where *C* and *n* are material dependent parameters. The BCS model represents crack growth in a single grain, such that the crack and its accompanying plastic zone have no interaction with boundaries. In the case where the plastic zone of a crack encounters a grain boundary, dislocation blocking and subsequent changes in the crack tip opening displacement occur. Zhang and Edwards observed a retardation of crack propagation rates in aluminum as the plastic zone of short cracks encountered grain boundaries, requiring the development of plastic deformation in the next grain to continue fatigue crack propagation [119,120]. It has also been observed that the strength of grain boundaries as barriers to crack propagation increases with increasing misorientation between adjacent grains [104,119]. The analytical models of Tanaka, Navarro, and de los Rios describe this barrier strength as a function of the crystallographic misorientation across the boundary, using distributed dislocation theory [121,122], and are summarized in [123].

There are a number of factors that affect the interaction between a fatigue crack and a grain boundary. These are either crack parameters, such as the length of the crack, the stress intensity factor, and the distance between the crack tip and the grain boundary, or boundary parameters, such as the misorientation between adjacent grains or the orientation of the boundary relative to the crack and sample surface. Crack parameters relate to the stress field at the tip of a fatigue crack, while boundary parameters relate to the resistance of a grain boundary to crack propagation.

Various models have been used to characterize the interaction between grain boundaries and damage mechanisms, based on a variety of boundary parameters or boundary parameter-derived metrics. Much of the literature indicates that, although experimental characterization can be difficult, the degree of alignment between active slip systems in adjacent grains is a critical factor in determining the ease of slip transfer, and therefore crack propagation, across grain boundaries [115,124]. The models of Tanaka, Navarro, and de Los Rios describe crack retardation and arrest at grain boundaries as a result of misorientation between slip systems in adjacent grains but fail to take into account grain boundary orientation. Zhai et al. [117] used electron backscatter diffraction (EBSD) to characterize the crystallographic orientation of grains in the neighborhood of a short crack and to investigate the effects of local crystallographic orientation on crack growth retardation in aluminum, and found that misorientation between favored slip planes across grain boundaries was a key parameter controlling crack retardation and deflection. Based on the results of their study, they developed a 3D crystallographic model for the resistance of a grain boundary to crack propagation using a geometric representation of crack deflection at a grain boundary (Figure 2.27). In the model developed by Zhai et al., ease of crack propagation across a grain boundary is directly dependent on the geometric relations of the preferred slip planes in each grain compared to adjacent grains and the grain boundary orientation, known as tilt and twist misorientation angles. During crystallographic crack growth across a grain boundary, the crack must reorient, requiring fracture between the two slip planes along the grain boundary, unless the slip planes are coincident at the boundary (Figure 2.28). Additional energy is needed for the creation of further free surfaces due to this fracture of this area, bounded along the grain boundary by the twist misorientation angle, which represents the primary resistance to crack propagation in the model. The model also incorporates the tilt misorientation component of crack deflection at the grain boundary, or the angle between the traces of the two preferred slip planes on the sample surface, which can act to reduce the driving force at the tip of the crack. The Zhai model, while qualitative, has been successful in the interpretation of 3-D crack behaviors such as crack deflection, branching, and retardation and arrest at grain boundaries. King et al. have used the tilt and twist model to evaluate short crack growth in magnesium alloy Elektron 21, using X-ray diffraction contrast tomography to provide information on grain and boundary orientation in three dimensions [116]. They found that Stage I crack propagation retarded at grain boundaries with large misorientations of the basal plane. Schaef and Marx et al. studied the effects of both crack and boundary parameters on short crack growth in a Ni Superalloy, using focused ion beam micronotches oriented to lie along (111) slip planes [125,126]. They observed a clear deceleration in crack growth rate as crack tips approached a grain boundary, followed by a rapid increase in growth rate when the cracks propagated across the grain boundary (Figure 2.29). It was noted that interaction between fatigue cracks and grain boundaries was strong as long as the cracks were short, and that cracks below 120 µm in length exhibited no crack arrest. Furthermore, they confirmed the occurrence of stepped fracture along grain boundaries, as postulated in the Zhai model [127], indicating that orientation differences between adjacent grains is the determining factor in the resistance of the grain boundary to crack propagation. Due to the fact that the full grain boundary orientation must be known to enable the calculation of twist misorientation angle, the Zhai model of tilt and twist is less useful when the complete 3-dimensional orientation of grain boundaries are unknown. In practice, use of the Zhai model when grain boundary orientations are unknown requires the assumption of grain boundaries oriented perpendicular to the sample surface, which in real materials is frequently not the case.

Investigation of grain boundaries using tilt and twist requires more detailed knowledge of grain boundary orientation than is frequently available and, thus, parameters for the study of grain boundary interaction with damage mechanisms have been developed that can be evaluated using surface EBSD data only [124]. Luster and Morris investigated slip transfer across grain boundaries using a geometric compatibility factor *m'*, defined as

$$m' = \cos\kappa\cos\phi \qquad [2.3]$$

where κ is defined as the angle between slip vectors from two adjacent grains, and ϕ is the angle between slip plane normal in those grains, with a low *m'* indicating higher difficulty of slip transfer [128]. They found that *m'* could be used to predict the activation of slip systems at grain boundaries or dislocation pileups in two-phase Ti-Al alloys. In a study of fatigue crack initiation and growth in lamellar Ti-6Al-4V, Pilchak et al. found that cracks tended to initiate and easily grow from boundaries exhibiting high values of *m'* and therefore easy slip transfer [129]. The geometric compatibility factor is convenient as it requires information that can be found using methods that are commonly available and that often allow for rapid investigation, but it fails to take into account the effect of the grain boundary orientation on grain boundary barrier strength and is divorced from actual crack propagation mechanisms at the grain boundary. In general, studies of slip transfer and crack propagation criteria highlight the difficulty in predicting crack retardation and arrest when using two-dimensional characterizations of microstructure, and point toward three-dimensional microstructural characterizations and computational modelling as necessary tools to more accurately understand how microstructure will affect local stress states and fatigue behavior.

Based on the models of Zhai, Wen, and Wilkinson, as well as the experimental results presented in Chapter 5, Panwar et al. [130] have developed a combined grain boundary interaction model that takes into account the coupling between tilt and twist misorientation, nominal Schmid factor, and a critical crack transmission stress. In this model, this critical crack transmission stress is given by,

$$S \geq \frac{k_l}{M_{Leading}\sqrt{r_0}}\left[\frac{1-e^{-\left(\frac{1-\cos\beta}{\alpha_1}+\frac{\sin\alpha}{\sin\alpha_0}\right)}}{1-e^{-\left(\frac{1}{\alpha_1}\right)}}\right] \qquad [2.4]$$

Here, M is the nominal Schmid factor in the Leading Grain, k is a locking parameter from the Hall-Petch relationship for tensile yield strength, r_O is included to prevent a stress singularity (typically 0.1 to 1 μm is used), α is the twist misorientation angle, β is the tilt misorientation angle, α_O is half of the maximum twist misorientation angle, used to normalize the function, and α_1 is a weighting parameter applied to scale the effect of twist misorientation in relation to tilt orientation. The Panwar model can be used to model the level of retardation in fatigue crack growth at grain boundaries as a function of varying microstructural parameters, such as tilt and twist misorientation (Figure 2.30).

2.2.7. 3D Characterization of Fatigue Crack Growth

Understanding of the structure-properties relationship of fatigue behavior with local microstructure requires accurate characterization of that microstructure. As a result of efforts to provide more complete descriptions of microstructure, characterization methods that provide quantitative microstructural information in three dimensions are gradually being developed and adopted for the analysis of mechanical properties. Traditionally, techniques to characterize fatigue behavior have focused on observations of the specimen free surface, resulting in 2-D measurements that fail to sufficiently describe important fatigue and geometric properties. These include complex fracture surface morphologies, variation in local crack growth rates and the true size, shape, and crystallographic orientations of grains below the specimen surface. Many studies have focused on characterization methods beyond surface observation to gather this information [12,131–139].

The analysis of fracture surfaces provides some understanding of three-dimensional fatigue crack growth beyond the two-dimensional information available from surface observations. Identification of the crystallographic orientation of fracture surface facets is necessary to gain an understanding of fracture mechanisms. Techniques for determining the crystallographic orientation of fracture facets can be divided into two categories as either direct or indirect methods. Direct methods involve capturing crystallographic information directly from the fracture facet using diffraction from either electron beams [138] or X-rays [132], and hence require that each facet to be characterized be aligned normal to the incident electron or x-ray beam. Researchers have developed a number of procedures to determine fracture facet orientation, generally based on stereographic facet-orientation fractography [139,140]. The efficacy of this method is dependent on the surface roughness of the fracture facet, with rougher surfaces preventing accurate characterization of crystallographic orientation, often as a result of the plastic deformation that accompanies fracture.

Indirect methods involve characterization of the spatial orientation of a fracture facet, coupled with characterization of the crystallographic orientation of the grain relative to some other reference frame, generally a prepared metallographic surface intersecting the fracture surface [133–138]. The spatial reference frame of the facet normal must then be related to the crystallographic reference frame gathered from the prepared surface to determine the crystallographic orientation of the facet. Because orientation data is collected from a prepared surface, indirect methods can generally only be used to characterize grains that are adjacent to a free surface, although interior grains can be characterized through destructive serial sectioning or FIB sectioning [134,141]. In practice, fractographic determination of the crystallographic orientation of facets is limited to the investigation of discrete points on a fracture surface and cannot provide broad or high-resolution data for an entire fracture surface. These techniques provide little information beyond crack path crystallography.

Subsurface fatigue crack growth behavior can be further investigated through the use of marker bands, beach marks, and striations [12,99,142,143]. As each of these features records the crack front, if the number of cycles elapsed in each feature is known, local subsurface crack growth rates can be determined. Marker bands frequently use a designed loading spectrum to imprint patterns on the fracture surface to more accurately indicate the location of the crack front at specific points during the fatigue test. Until recent advances in three-dimensional characterization of fracture surface topography, analyses of crack propagation using these features have been based on two-dimensional projections of the fracture surface, and have failed to account for the true three-dimensional nature of crack propagation [12].

With advances in synchrotron radiation techniques in recent years, nondestructive and high-resolution characterization of three-dimensional microstructures and fatigue cracks has become possible [144–147]. X-ray tomography provides a way of investigating three-dimensional microstructure, and, through repeated characterization, can be used to track changes in microstructure over time. As such, it has become a useful tool for studying cyclic damage accumulation and fatigue crack growth [14]. Ludwig et al. [148] were some of the first to use X-ray tomography to study the interaction between microstructure and fatigue cracks. In their study, X-ray tomography was used to characterize the grain structure of a polycrystalline volume of an aluminum alloy along with the three-dimensional shape of a fatigue crack, using liquid gallium to highlight grain boundaries through absorption contrast. In combination with crystallographic characterization of the sample surface through EBSD, X-ray tomography provided information on the three-dimensional morphology of a microstructurally short fatigue crack. Additional studies have focused on using X-ray tomography to characterize three-dimensional fatigue behavior in a number of materials, including various aluminum alloys [149–

153], cast iron [24], and titanium fiber composites [154]. Researchers have also attempted the *in situ* characterization of fatigue damage evolution using interrupted tomographic imaging [24,151,155,156].

Although X-ray tomography can provide information on the three-dimensional morphology of a fatigue crack through absorption contrast, it cannot provide information on grain shapes and crystallographic orientations in most materials. By combining X-ray tomography with three-dimensional X-ray diffraction microscopy or diffraction contrast tomography (DCT), the relationship between crack morphology and local three-dimensional microstructure (including grain morphology and crystallographic orientations) can be investigated. More detail on the X-ray techniques used to characterize three-dimensional microstructure can be found in [145,157,158]. Herbig et al. [159] have combined in situ characterization of three-dimensional fatigue crack growth through repeated phase contrast tomography with grain orientation characterization through DCT in a beta titanium alloy. The characterization technique allowed for the visualization and analysis of local subsurface crack growth and crystallographic orientation of the fracture surface (Figure 2.31). King et al. [13] used the same techniques to study microstructurally short fatigue crack growth from focused ion beam notches in magnesium alloy Elektron 21, and found that crack propagation occurred preferentially along basal planes and exhibited retardation at certain grain boundaries (Figure 2.32). Similar insight into microstructurally small fatigue crack behavior has also been achieved in a post-mortem study of an aluminum alloy by Spear et al. [12]. Three-dimensional crack morphology was determined through X-ray tomography, while crystallographic information was investigated using near-field high-energy X-ray diffraction microscopy (HEDM). Subsurface local crack growth rates were determined post mortem by means of marker bands on the fracture surface produced using a modified loading spectrum. In the study, both intergranular and transgranular crack propagation were observed, with the latter occurring on a wide variety of crystallographic planes (Figure 2.33), indicating a complex interaction between microstructure and fatigue behavior.

2.2.8. Environmental Effects

Fatigue behavior in magnesium can be very sensitive to environment. This sensitivity can manifest as variations in fatigue lifetime or crack propagation behavior. In a study of fatigue behavior in a rare-earth magnesium alloy in laboratory air and vacuum, fatigue life increased in vacuum as a result of increases in the duration of both the crack initiation and propagation stages of fatigue [160]. Significantly decreased fatigue crack propagation rates were observed in dry air as compared to fatigue in laboratory air and distilled water in a study of wrought magnesium alloys AZ31 and AZ61 [161]. Tokaji et al. observed different fracture surface morphologies in specimens fatigued in dry air, laboratory air, and distilled water, and postulated that different fracture mechanisms were active in each of the three environments. Similar results were reported in a study of fatigue crack propagation rates in AZ61 in which controlled humidity levels ranged from 20% to 85% relative humidity (Figure 2.34) [162]. Accelerated crack rates in higher humidity environments in the study were attributed primarily to hydrogen embrittlement and secondarily to anodic dissolution at the crack tip.

Additional studies of fatigue in magnesium alloys in corrosive aqueous NaCl environments have shown that aggressive environments can have complex effects on fatigue behavior. Rozali et al. observed decreased fatigue crack growth rates in a 3.5 mass% NaCl environment as compared to fatigue in low humidity environments, possibly as a result of oxide-induced crack closure [163]. Gu et al. observed significantly reduced HCF fatigue lifetimes for both AZ91D and WE43 cycled in simulated body fluid, with crack initiation occurring at corrosion pits in the sample surface (Figure 2.35) [52]. A study of corrosion fatigue on various magnesium alloys indicated that corrosion effects were less significant in extruded alloys than in cast alloys. It was also observed that different magnesium alloys displayed different sensitivities to the tested corrosive environments, indicating a complex relation between alloy composition, environment, and fatigue response [45].

2.2.9. Ultrasonic Fatigue

In this dissertation, ultrasonic fatigue methods are used as the primary approach to attaining cycle counts in the VHCF regime and in conducting in situ SEM fatigue studies. The technique is particularly attractive for studies in the high and very high cycle fatigue regimes as the high cycling frequency of approximately 20 kHz allows for significant increases in testing speeds as compared to conventional hydraulic testing equipment (usually 10-50 Hz). The mechanics of ultrasonic fatigue are detailed in [164].

Ultrasonic fatigue testing has been used since the 1950s [164,165] to provide a time-efficient means for investigating VHCF, and has been utilized to investigate a wide range of materials including steels [166,167], aluminum alloys [3,168], nickel-base superalloys [4,9], titanium alloys [10,169] and magnesium alloys [11,46,56,74]. Progress in the use of the ultrasonic technique for understanding fatigue behavior has been reviewed by Bathias [6], Stanzl-Tschegg [7], and Mayer [8]. Over the past forty years ultrasonic fatigue has been extended to enable VHCF in crack growth studies [170,171] and has been combined with other techniques including synchrotron imaging [9]. Despite these advances, the data acquired from ultrasonic fatigue has largely been limited to the determination of total fatigue life, crack growth rates, and deformation processes that are inferred from post-failure surface microscopy or fractography. Observations regarding crack initiation and ultimate failure have conventionally been linked to microstructural characteristics in a "before-and-after" methodology through electron microscopy and crystallographic mapping techniques like EBSD. Attempts have been made beyond the "before-and-after" methodology to characterize fatigue damage as a function of ongoing cyclic loading using *ex situ* imaging of developing cracks in an interrupted but ongoing loading sequence. Stanzl-Tschegg et al. [5] used high resolution SEM and atomic force microscopy (AFM) imaging in combination with interrupted ultrasonic loading to investigate fatigue damage in copper polycrystals in the VHCF regime. *Ex situ* techniques can require a significant amount of time but provide useful information regarding development and progression of fatigue damage. Geathers et al. and Adams et al. have used a unique combination of scanning electron microscopy and ultrasonic fatigue, which will be discussed in more depth in the next chapter, to investigate cyclic damage accumulation and crack propagation *in situ*, as well as the effect of environment of fatigue crack propagation in titanium and magnesium [10,11].

2.2.10. Summary

This section summarizes the following key portions of the literature review for this dissertation: very high cycle fatigue behavior or magnesium alloys, fatigue crack initiation mechanisms in relation to microstructure, microstructurally small fatigue crack growth and its interaction with grain boundaries, and the three-dimensional characterization of fatigue behavior and microstructure. Identification of open questions from these areas is also discussed.

There have been several studies that show fatigue failure can occur in the VHCF regime, beyond the conventionally assumed non-ferrous fatigue limit of 10^7 cycles. In this regime, local microstructure controls crack initiation and early propagation behavior, and variation in these behaviors can have a significant effect on total fatigue life. Despite this, the fatigue behavior of magnesium alloys has not been investigated as fully as in other structural alloy systems, and the roles of microstructure on fatigue mechanisms are not yet well understood. For magnesium alloys in general, fatigue lifetime data beyond 10^7 cycles in sparse. Studies of VHCF behavior in magnesium have generally focused on aluminum and zinc bearing alloys, and have shown that most exhibit no fatigue limit [46,50,51]. Characterizations of fatigue behavior in WE43 have been limited to a study of the role of environment on HCF behavior [52], and an investigation, conducted as part of this thesis work, into the role of heat treatment on VHCF behavior [11].

Studies have shown that fatigue crack initiation mechanisms in the VHCF regime are closely tied to microstructure. In cast magnesium alloys, crack initiation has been overwhelmingly linked to casting defects like porosity [49,56,74–76]. In wrought alloys, initiation behavior varies widely. Initiation has been observed at surface sites near grain boundaries, twin boundaries, along persistent slip bands and at inclusions [46,47,50,81]. Subsurface crack initiation has also been observed and linked to environmental interactions and cyclic slip deformation in favorably oriented grains [11,82]. With the wide variation in initiation behaviors observed in different alloys, it is clear that microstructure plays a critical role in determining fatigue crack initiation locations and lifetimes. Questions still remain as to the role of microstructure in determining crack initiation behavior in WE43, and how initiation behavior affects total fatigue life.

Crack growth in the VHCF regime frequently consists of predominantly microstructurally small crack growth, in which variation in local microstructure can have significant impact on crack growth rates and behavior. As with fatigue crack initiation behavior, fatigue crack propagation behavior in magnesium has been shown to be strongly dependent on microstructure and varies depending on the alloy being studied. Both intergranular [109] and transgranular [13] modes of crack propagation have been observed, and many researchers have noted the strong impeding effect grain boundaries can have on crack propagation rates. Grain boundaries exhibiting high misorientation have been shown to impede slip transfer and fatigue crack propagation in a number of materials [115,117,125,126], including magnesium [13]. Despite this, there is still disagreement in the literature on which crack or boundary parameters are critical in determining the interaction between cyclic damage and grain boundaries [115,124]. Investigation of many significant boundary and crack parameters is hampered by the fact that three-dimensional characterization of the microstructure may be required for their determination. In addition, studies of fatigue behavior are frequently limited in that cracks are conventionally studied using only surface observations, even though the majority of crack propagation occurs below the sample surface, where observation is challenging. Characterization of subsurface crack propagation requires the use of in-situ three-dimensional characterization or post-mortem investigation using fracture surface markings like striations or beach marks. In general, studies of slip transfer and crack propagation criteria highlight the difficulty in predicting crack retardation and arrest when using two-dimensional characterizations of microstructure and crack propagation, and suggest an increased need for three-dimensional characterization of the interaction between fatigue cracks and grain boundaries.

Recent advances have been made in the field of three-dimensional characterizations of microstructure and fatigue behavior. Improvements in synchrotron radiation sources have allowed the use of X-ray tomography, X-ray diffraction microscopy (HEDM), and X-ray diffraction contrast tomography (DCT) for both in-situ and post-mortem characterization of microstructure and fatigue behavior. Herbig et al. [159] and King et al. [13] have characterized microstructure through DCT in conjunction with in-situ characterization of fatigue crack propagation through repeated phase contrast tomography in titanium alloy Ti 21S and magnesium alloy Elektron 21, respectively. Their approach allowed for the analysis of local crack growth rates of short fatigue cracks, as well as determination of three-dimensional fracture surface morphology and the shape and crystallographic orientation of grains surrounding the crack, but required a significant amount of time for mechanical testing and X-ray characterization. Spear et al. [12] have developed a methodology for reducing the time required for characterization by investigating crack propagation in an Al-Mg-Si alloy in a post-mortem manner using marker-bands to visualize the advance of the crack front, while characterizing the surrounding microstructure using HEDM. The use of these methods allows for a more complete investigation of the three-dimensional evolution of small fatigue cracks within the local microstructural environment, but the number of studies utilizing these characterization techniques is limited, in large part by the difficulty and time required.

The interaction between microstructure and fatigue crack initiation and propagation behaviors is critical in gaining an understanding of VHCF behavior, and the identification of critical microstructural parameters is still ongoing. Studies of fatigue behavior and the effects of microstructure are particularly limited in magnesium alloys, considering the high variability of behavior observed in different alloys and the difficulty in comprehensive characterization of microstructure. Questions still remain regarding the determining role of microstructure in crack initiation, as well as the critical boundary parameters governing the interaction between short fatigue cracks and grain boundaries. These questions, and efforts to characterize these behaviors, are discussed further in this thesis.

Figures

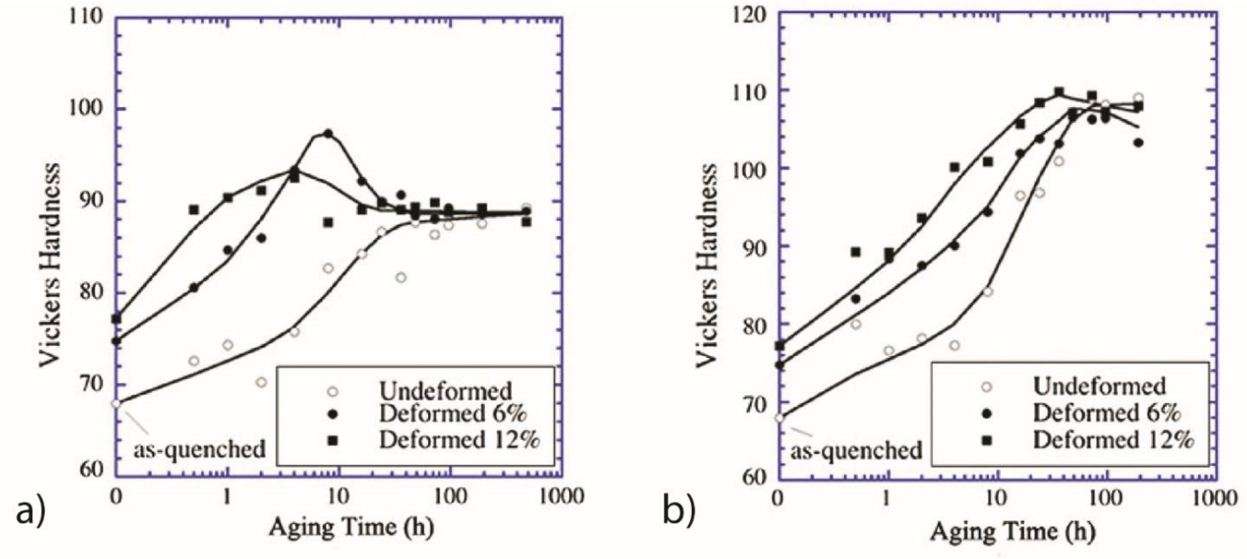

Figure 2.1: Age-hardening response of RE Mg alloy WE54 at (a) 523 K (250 °C) and (b) 473 K (200 °C) [16].

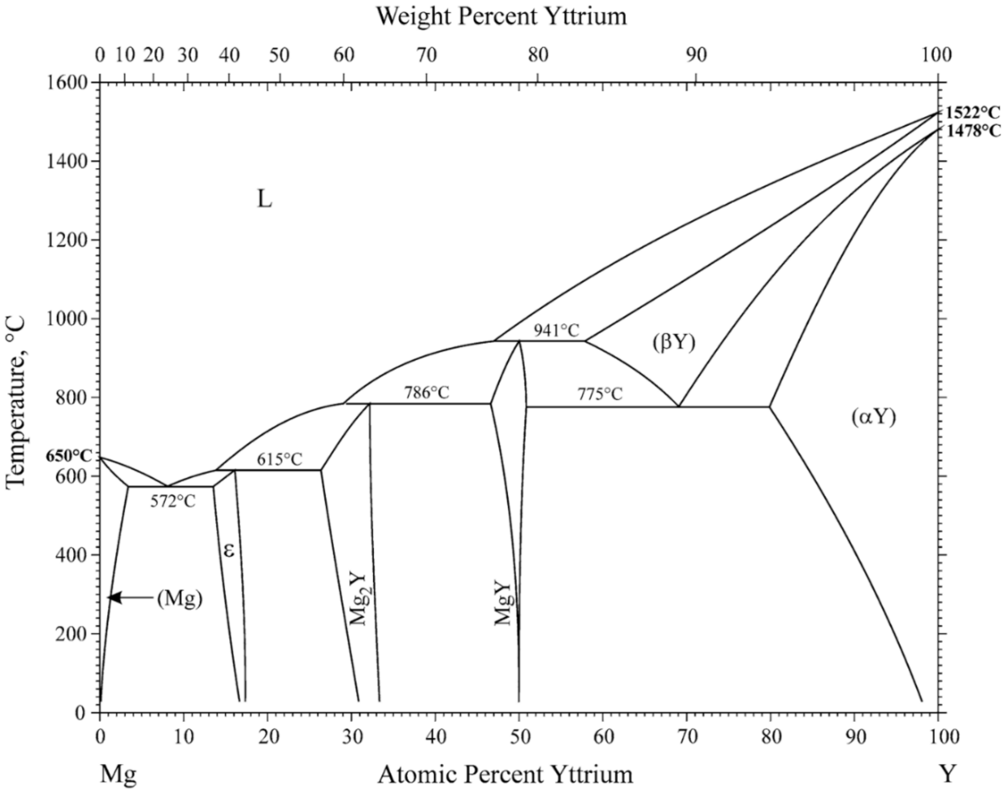

Figure 2.2: Mg-Y binary phase diagram illustrating the potential for precipitation strengthening of RE containing magnesium alloys [172].

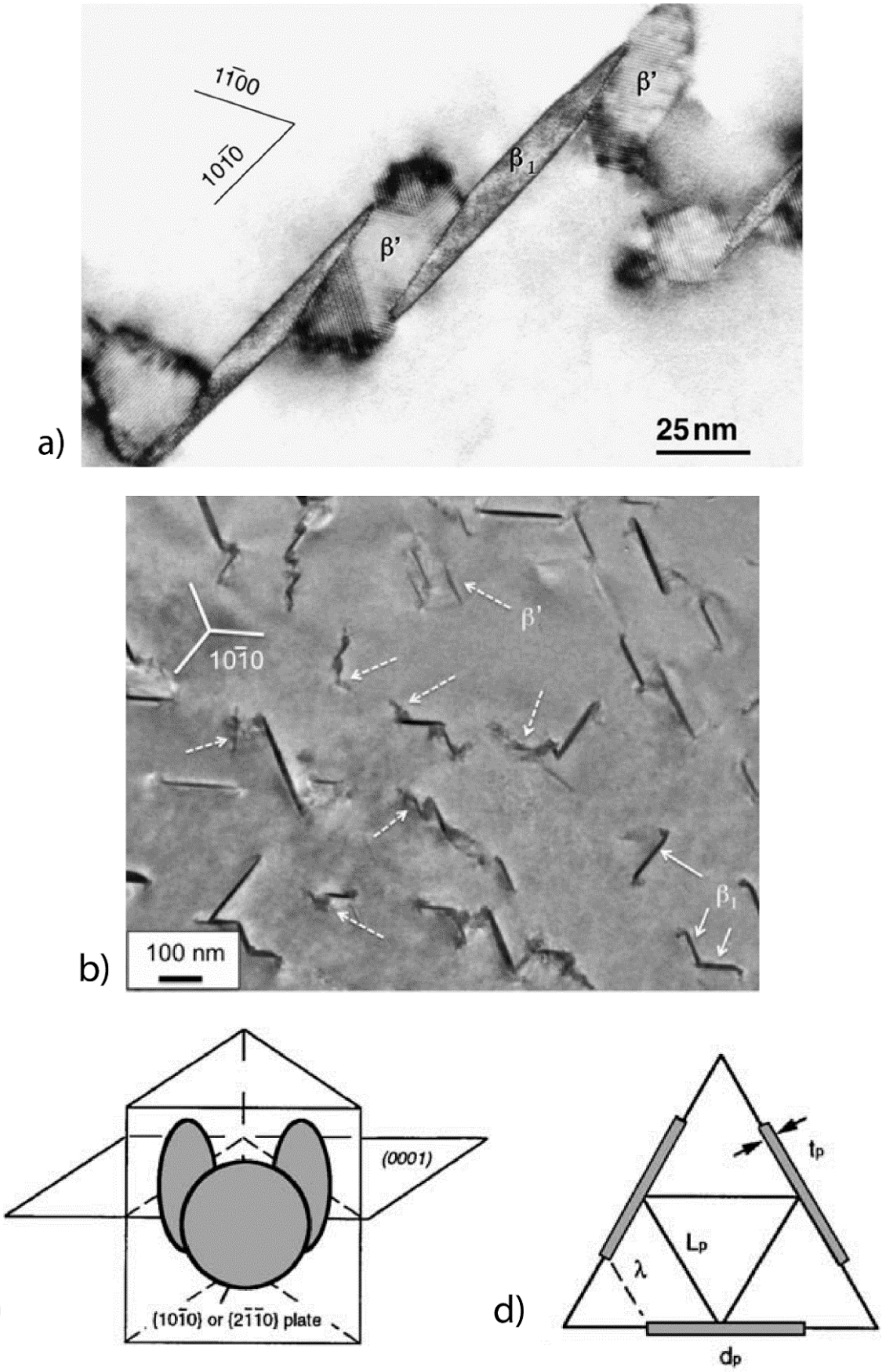

Figure 2.3: TEM images of RE β’ and β1 precipitates in (a) peak-aged WE54 [173] and (b) peak-aged WE43 [17]. (c) Diagram of $\{10\bar{1}0\}$ or $\{2\bar{1}\bar{1}0\}$ β1 precipitate plates in a volume of Mg matrix, and (d) a projection of prismatic plates onto the (0001) basal slip plane [20].

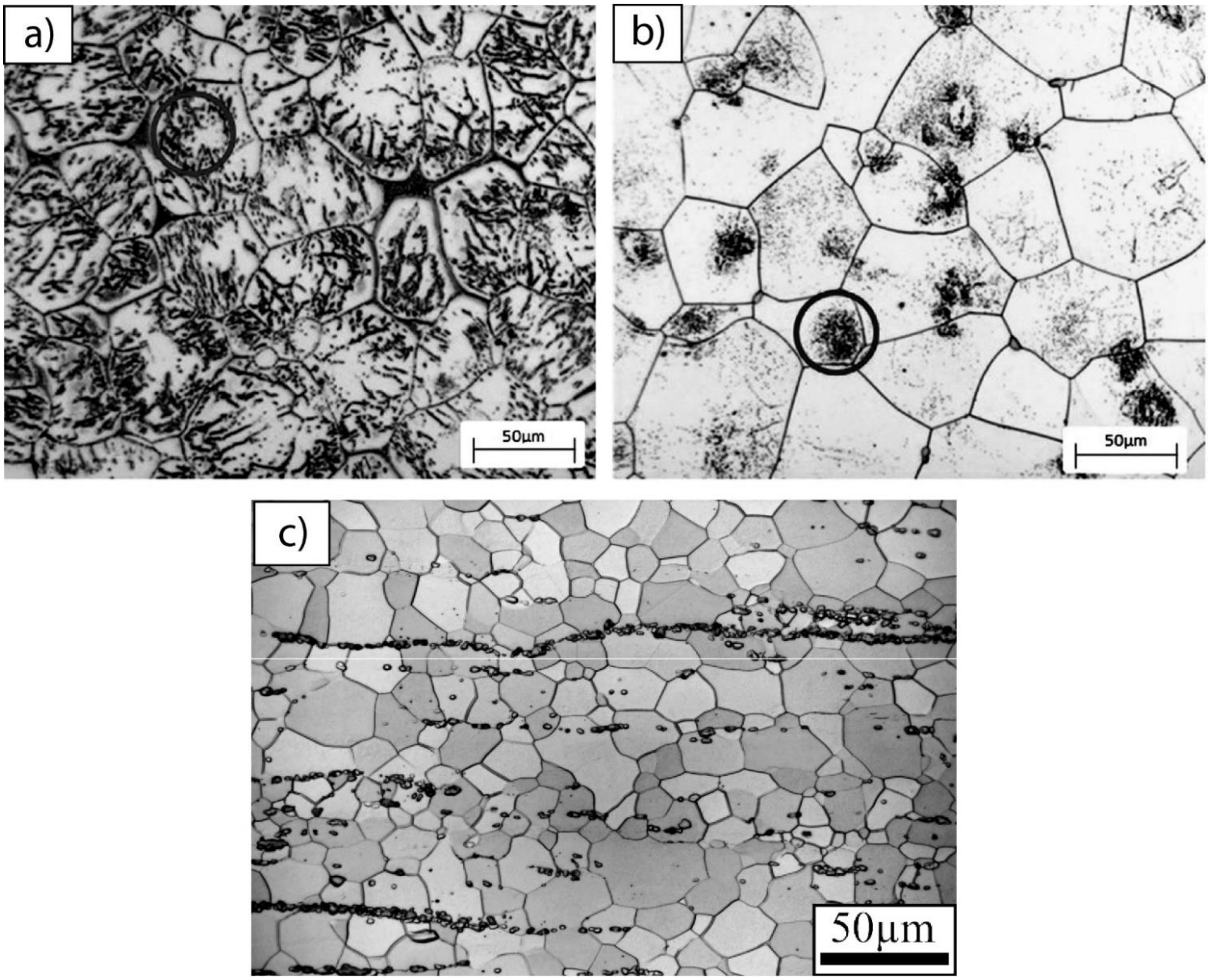

Figure 2.4: Optical micrographs of the (a) as-cast and (b) T6 condition of the rare earth containing magnesium alloy Elektron 21 and (c) hot-rolled and annealed magnesium alloy WE54 [22,174].

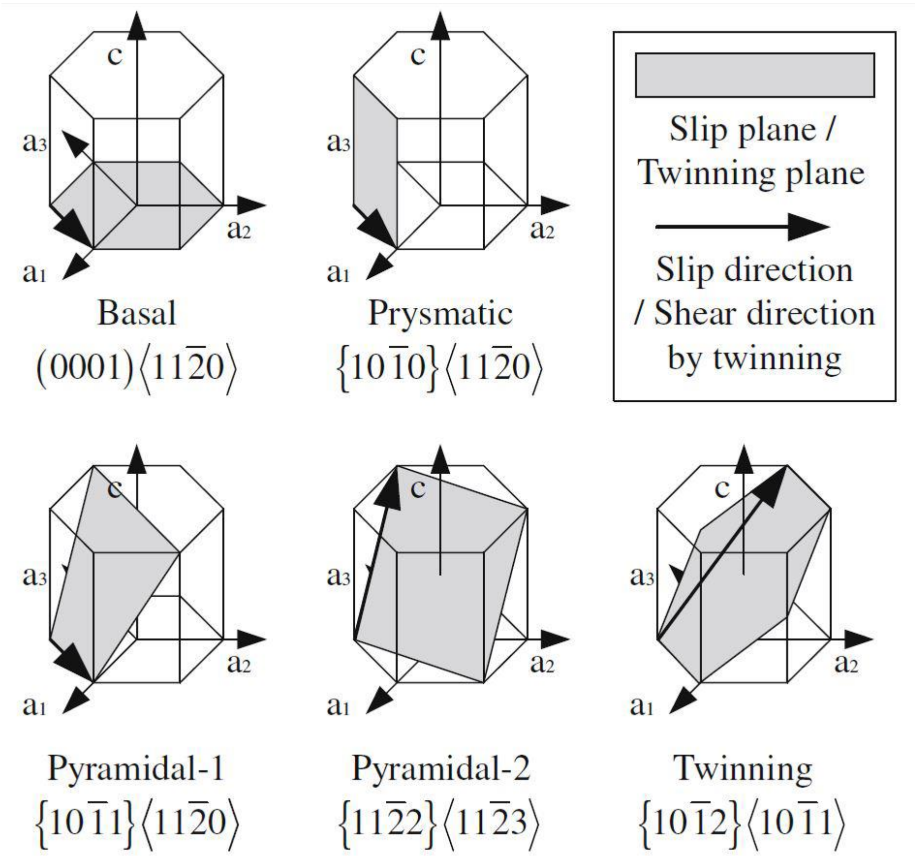

Figure 2.5: Slip systems of hcp magnesium are shown. Plastic deformation is controlled by slip on the basal $\{0001\}$, prismatic $\{10\bar{1}0\}$ and pyramidal $\{10\bar{1}1\}$ crystal planes, while deformation along the c axis occurs through pyramidal <c+a> $\{11\bar{2}2\}$ slip in addition to $\{10\bar{1}2\}\langle\bar{1}011\rangle$ extension twinning [175].

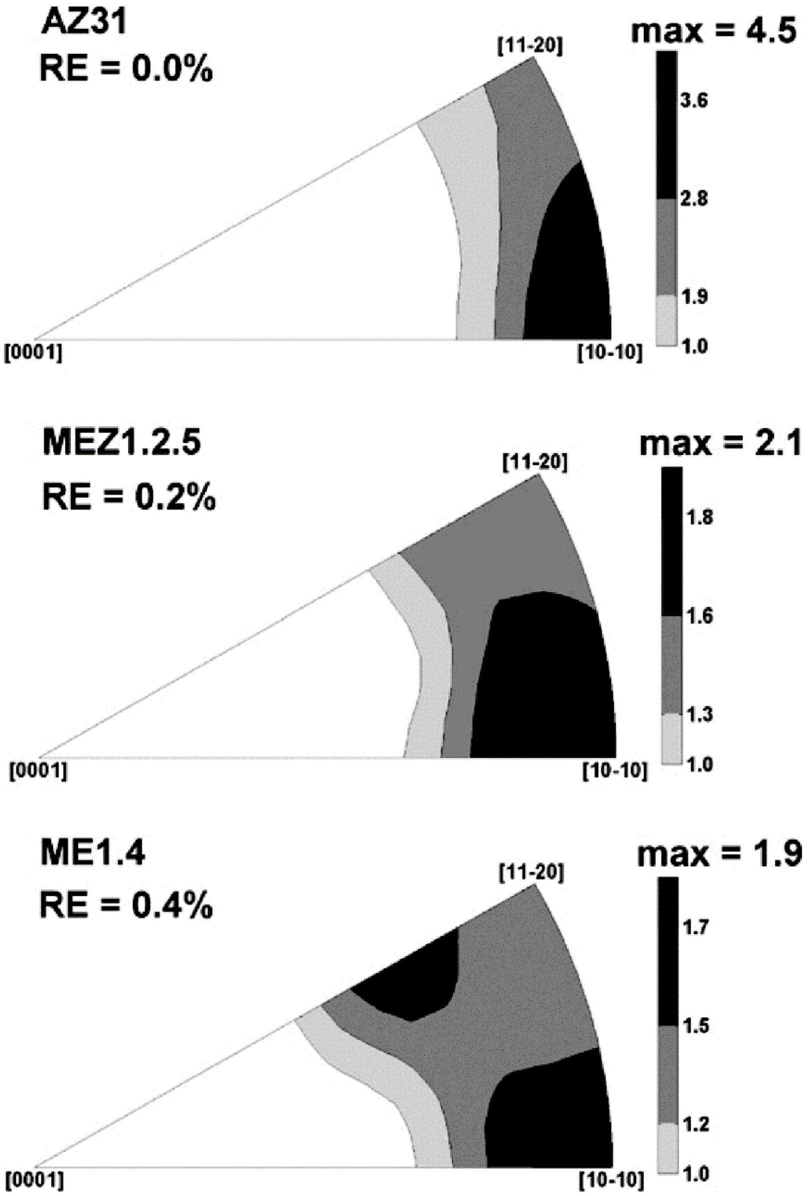

Figure 2.6: Inverse pole figures of extruded magnesium alloys, along the extrusion direction. The strength of the $[10\bar{1}0]$ pole decreases with increasing rare earth content, and at the higher alloying level of 0.4% RE, a second peak at approximately $[11\bar{2}1]$ becomes evident [37].

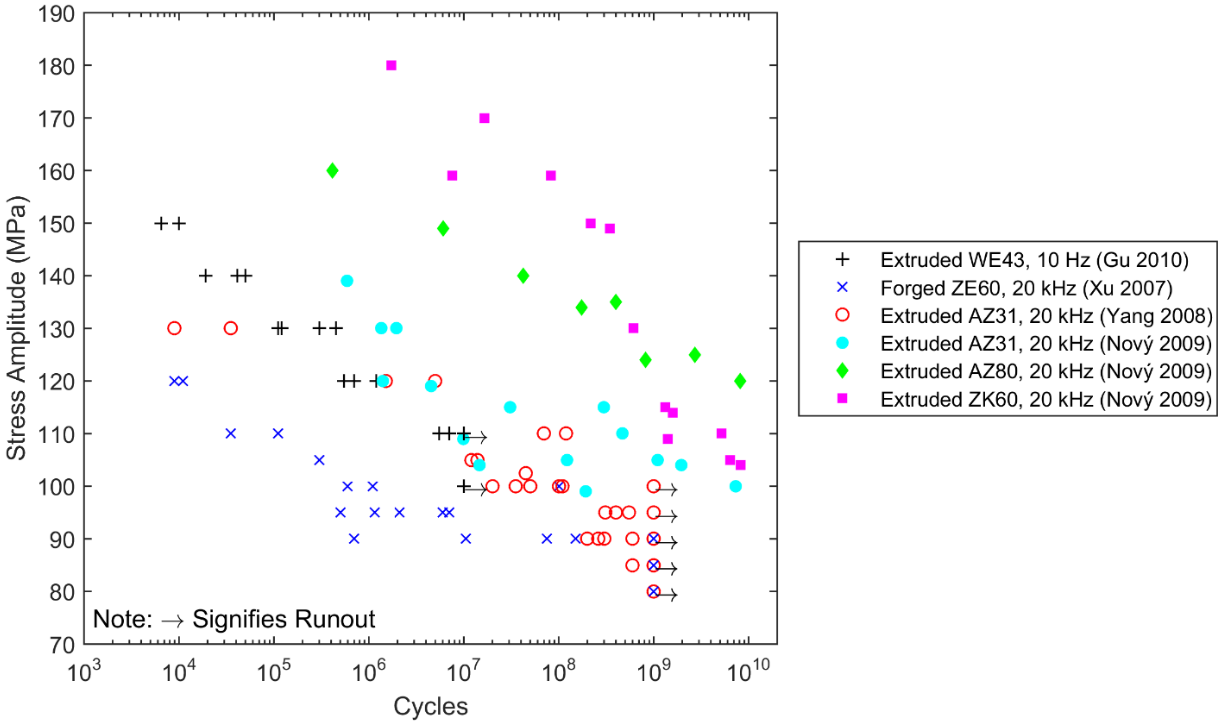

Figure 2.7: Fatigue lifetime behaviors in the HCF and very high cycle fatigue regimes for a variety of magnesium alloys investigated in literature [46,50,52,82].

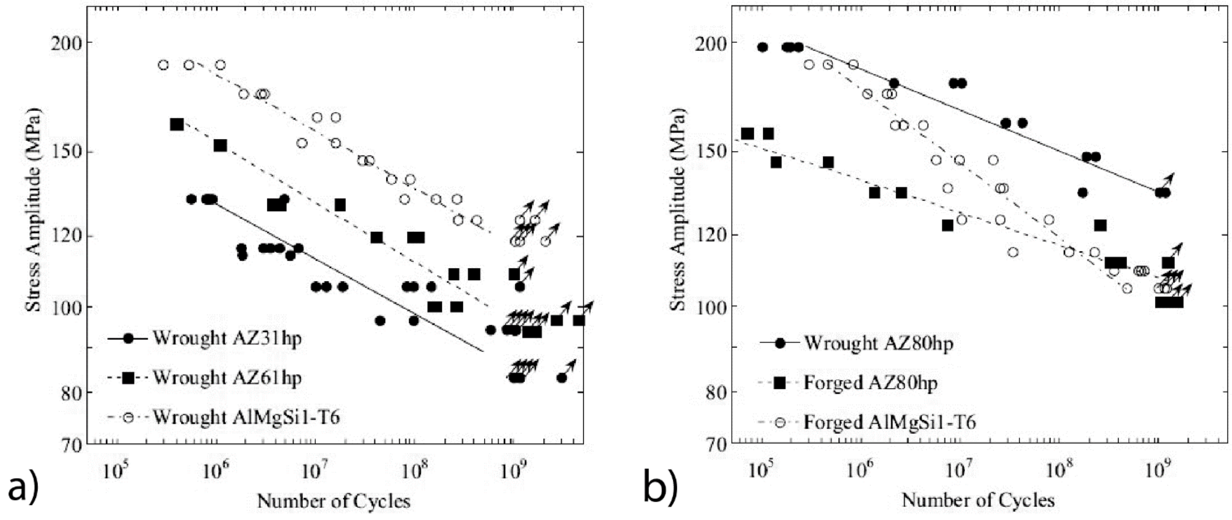

Figure 2.8: VHCF behavior for a variety of AZ alloys all lacking the conventionally assumed fatigue limit [51].

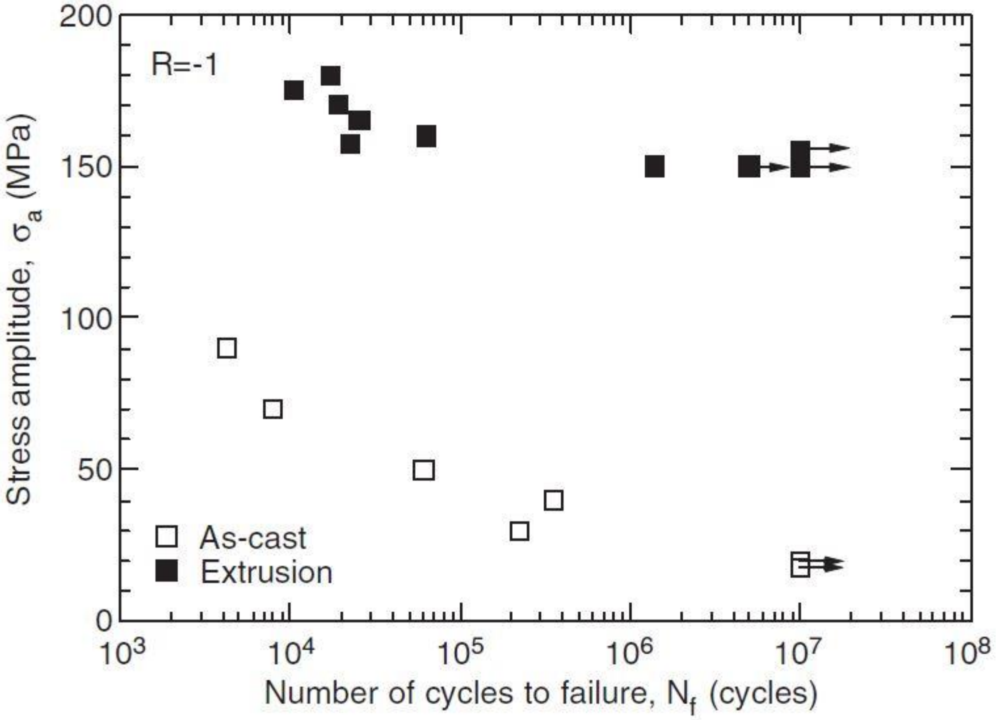

Figure 2.9: Fatigue life behavior of as-cast and extruded conditions of the magnesium alloy AZ61 illustrates the significant improvement in fatigue properties observed in wrought magnesium alloys as compared to cast alloys [57].

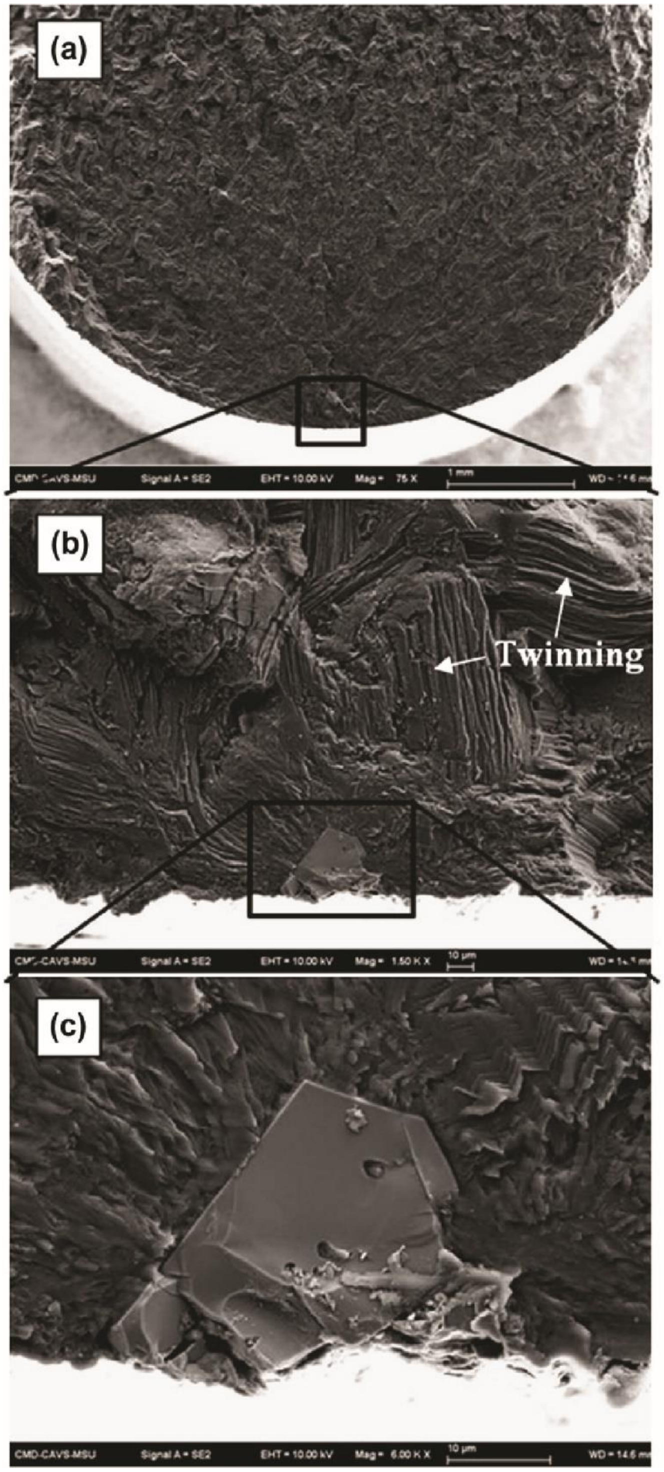

Figure 2.10: Post-mortem characterization of fatigue failure in magnesium alloy AM30 showing (a) crack propagation through glide twinning and (b),(c) initiation at an intermetallic particle [68].

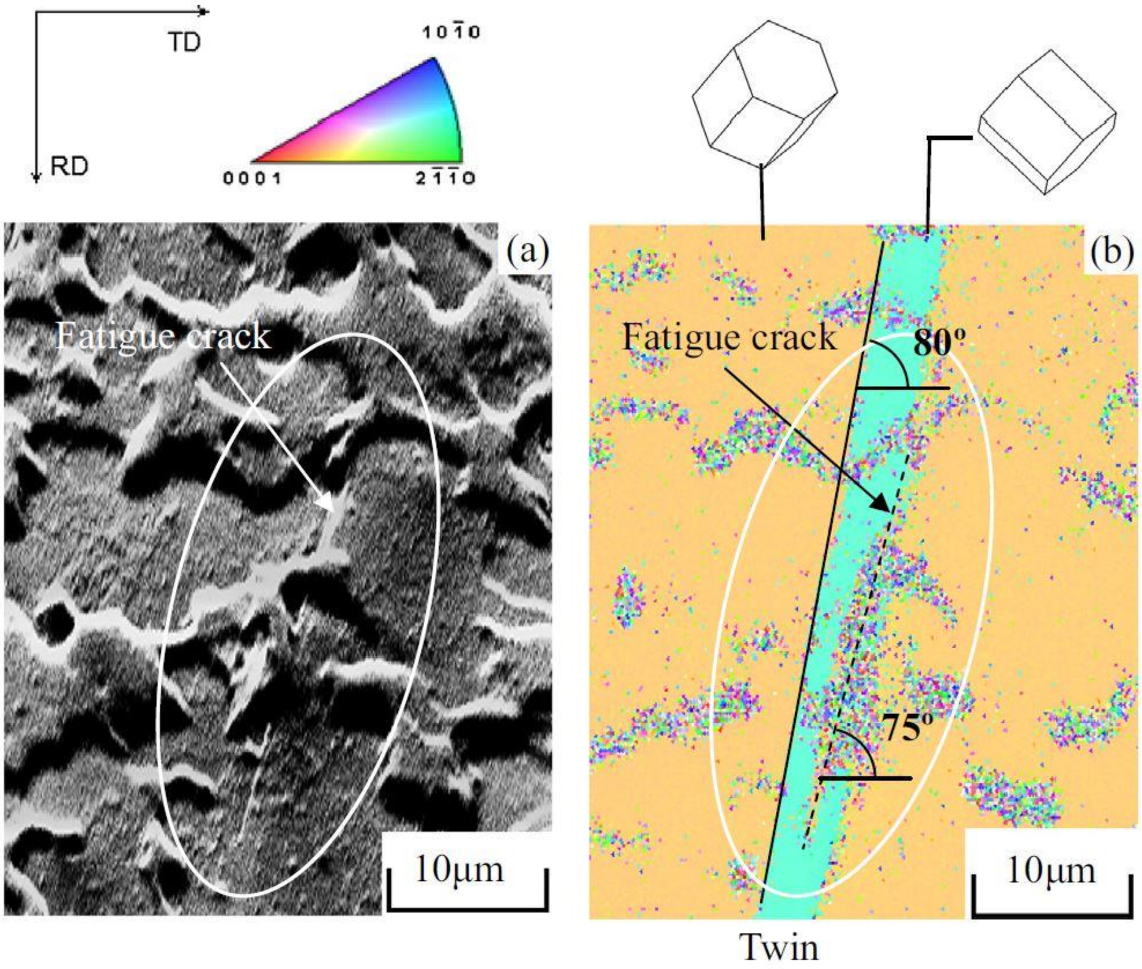

Figure 2.11: (a) SEM and (b) EBSD micrographs showing short fatigue crack initiated at a twin boundary at 8% of total life [63].

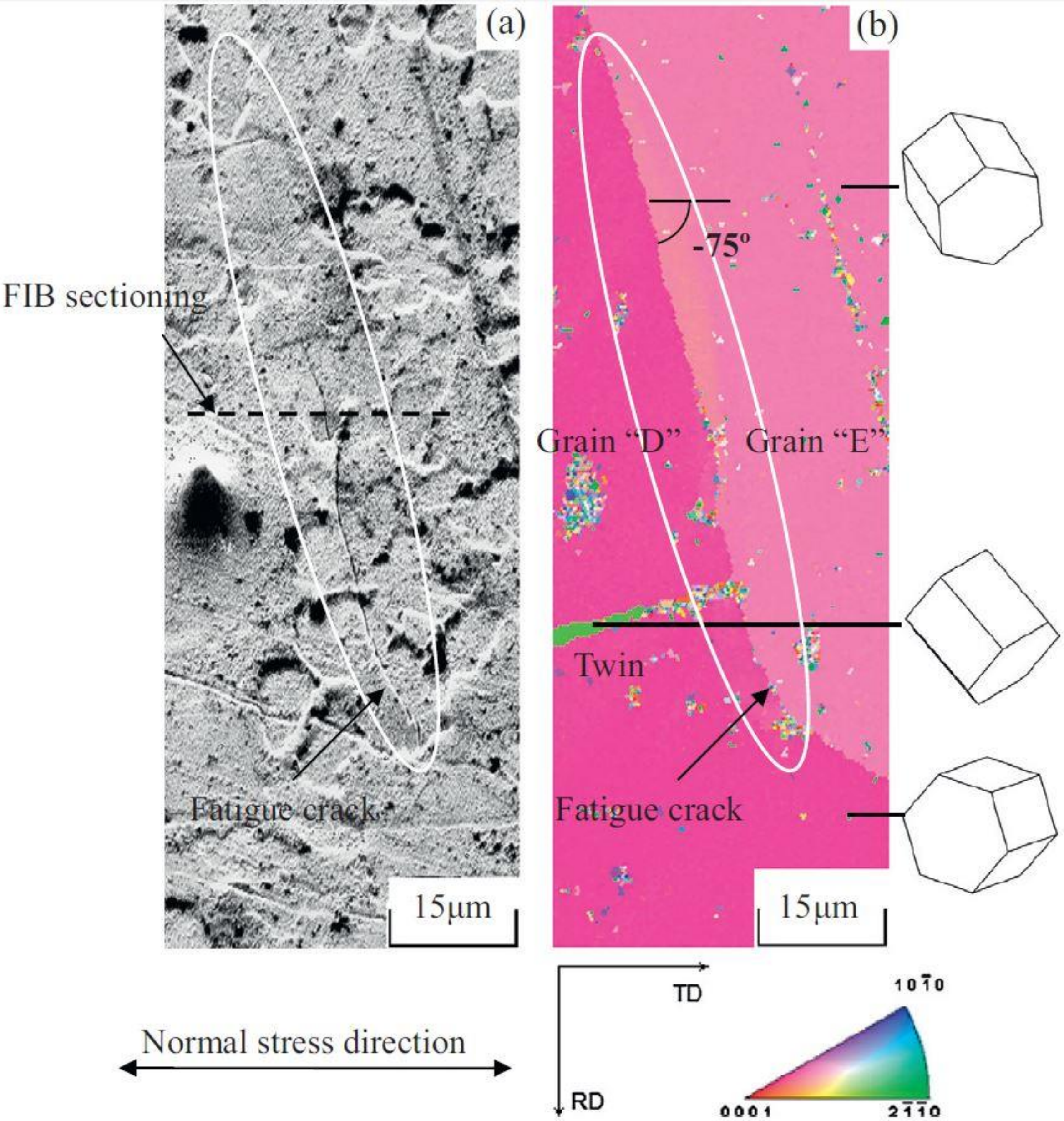

Figure 2.12: (a) SEM and (b) EBSD micrographs showing short fatigue crack initiated along a grain boundary at 8% of total life [63].

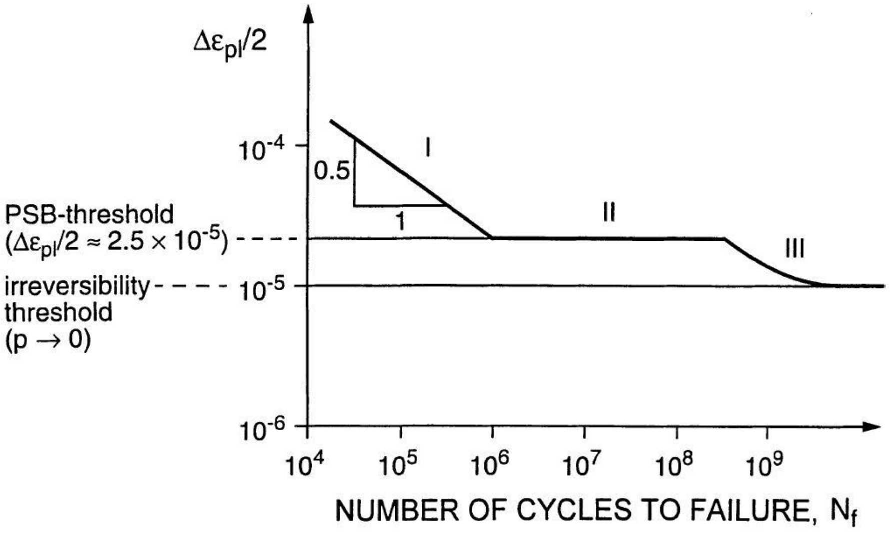

Figure 2.13: Schematic fatigue life curve with a plastic strain fatigue limit in the HCF regime (II), terminated by a further decrease of fatigue life with decreasing strain amplitude below the persistent slip band threshold in the VHCF regime (III) [48]

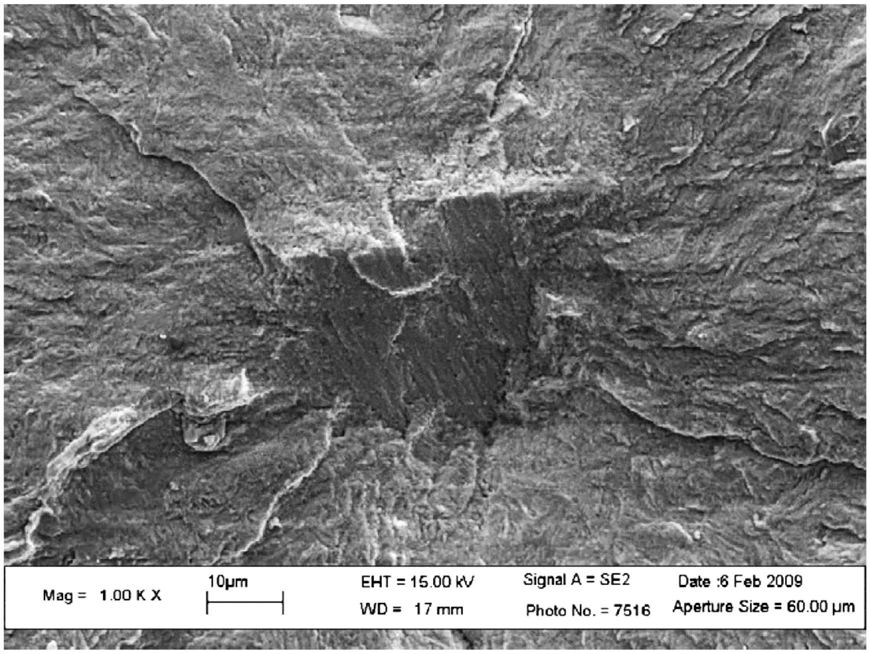

Figure 2.14: Subsurface fatigue crack initiation during gigacycle fatigue of a bearing steel at a supergrain surrounded by a fine granular area, observed by SEM [72].

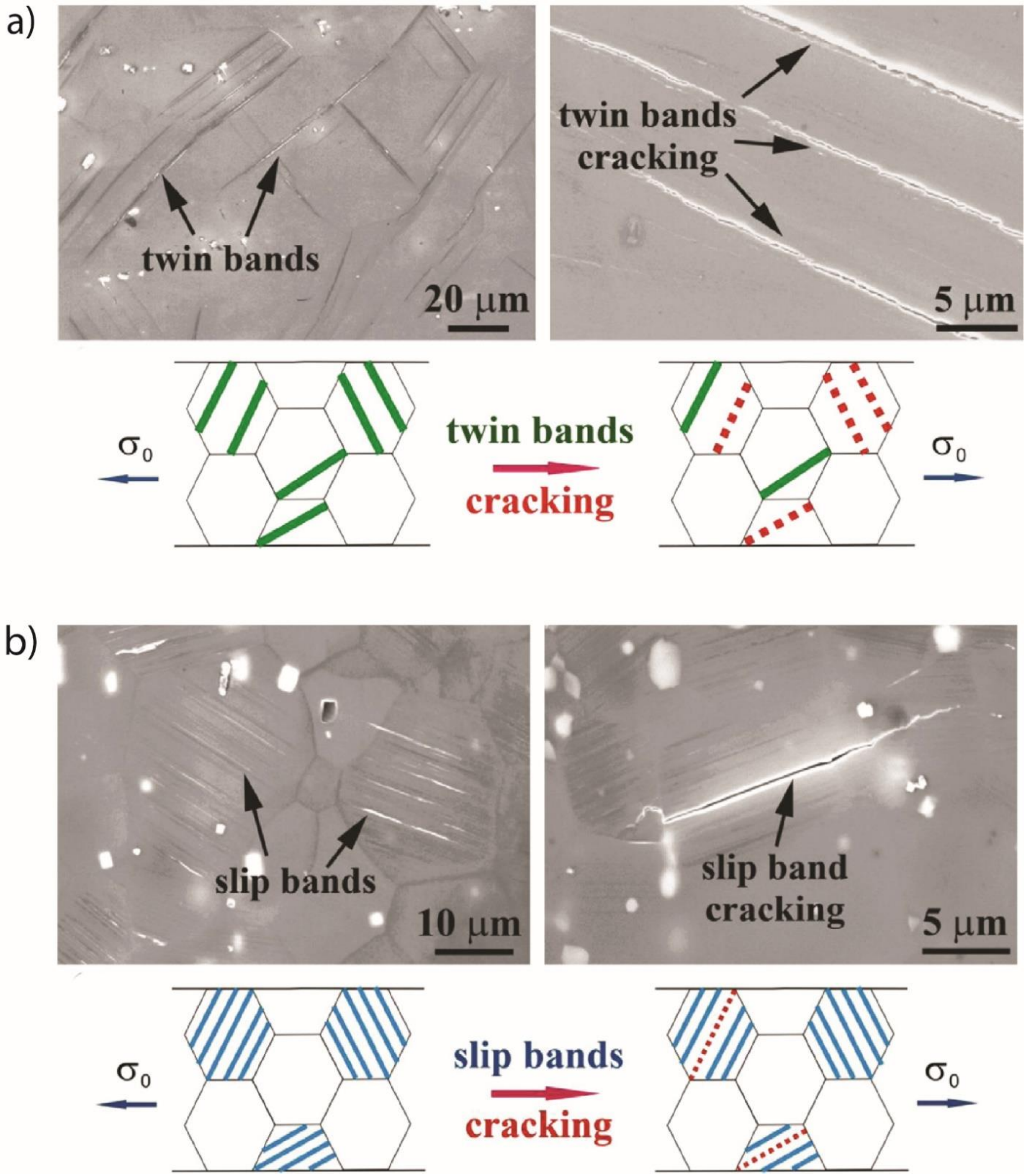

Figure 2.15: Low and high magnification images and schematic diagrams for fatigue crack initiation in (a) magnesium alloy AZ31 along grain boundaries and in (b) magnesium alloy GW123K along slip bands, with cracks indicated by the dotted lines [47].

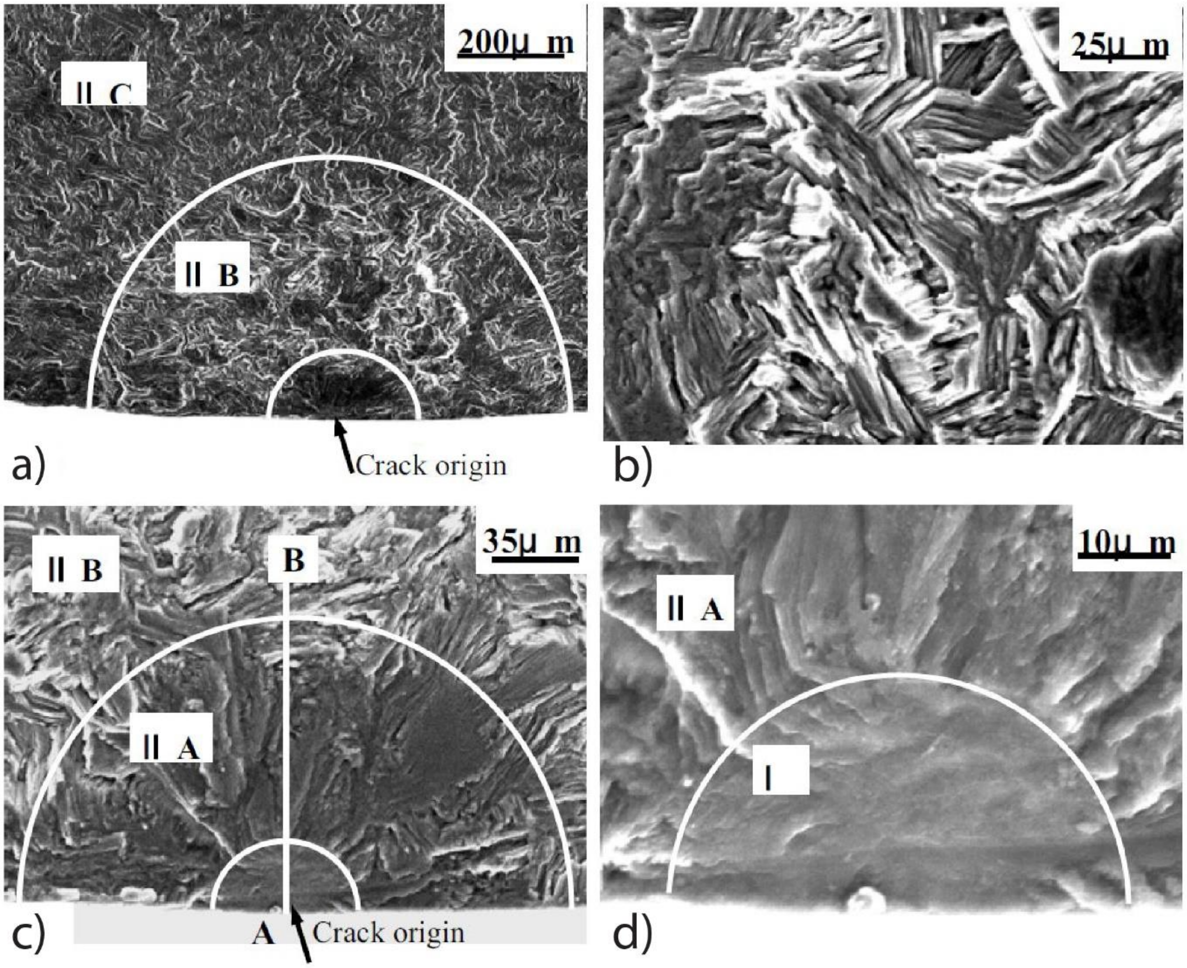

Figure 2.16: SEM observation of fracture surface of an AZ80-T5 specimen that failed at a low stress amplitude level through crack initiation at a twin boundary; (a) Macroscopic view around crack initiation site; (b) higher magnification of region IIB; (c),(d) magnified view of crack origin [81].

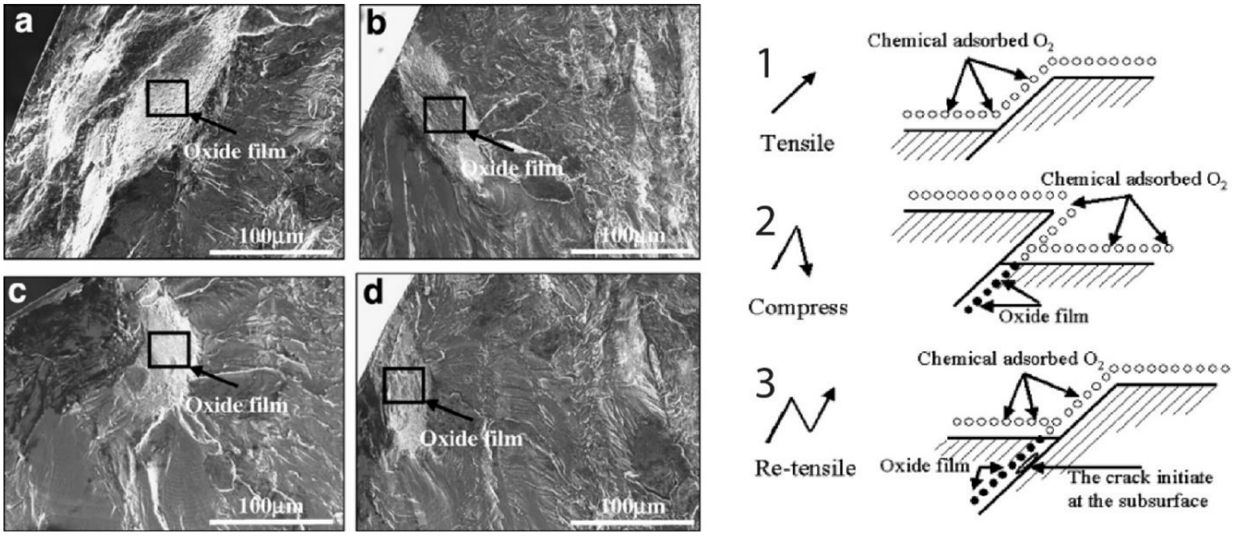

Figure 2.17: Subsurface VHCF crack initiation at oxide films in a forged Mg-Zn-Y-Zr magnesium alloy, and a schematic illustration of the initiation process due to the interaction between single slip and environment [82].

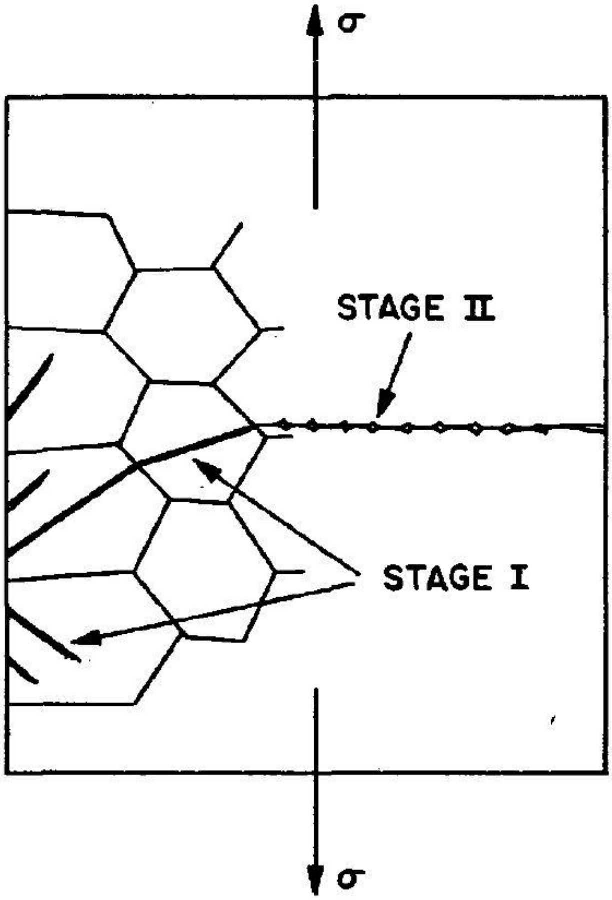

Figure 2.18: Schematic of single-slip Stage I and dual-slip Stage II crack propagation [90].

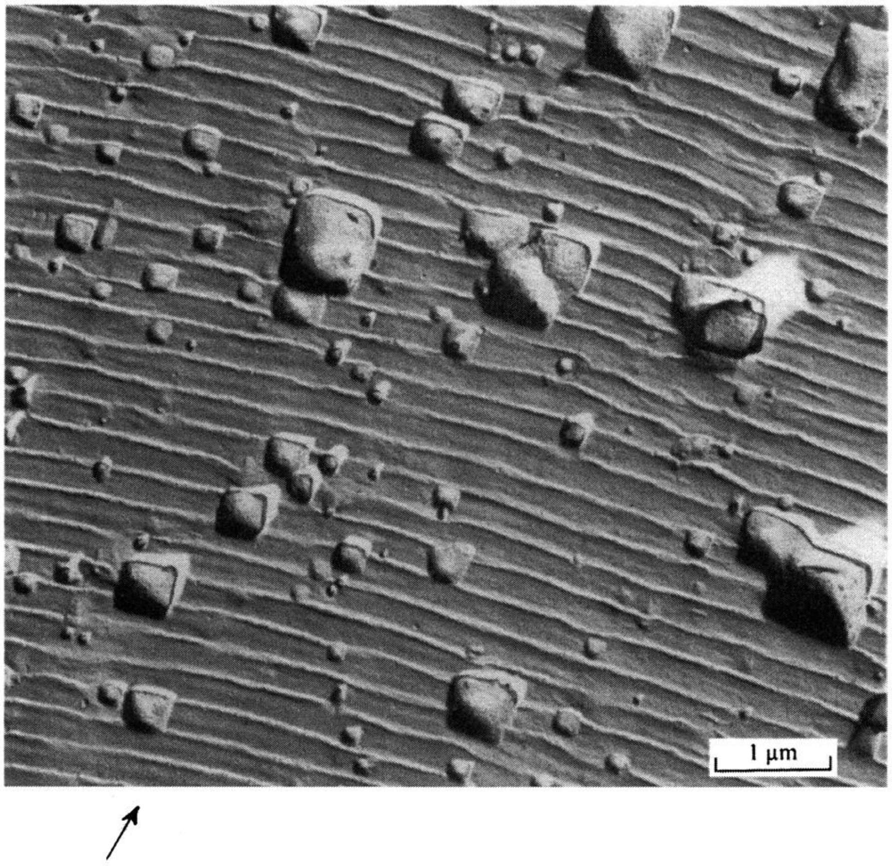

Figure 2.19: Fatigue striations on an etched fracture surface in aluminum alloy 2024-T3. The arrow indicates the direction of crack propagation [42].

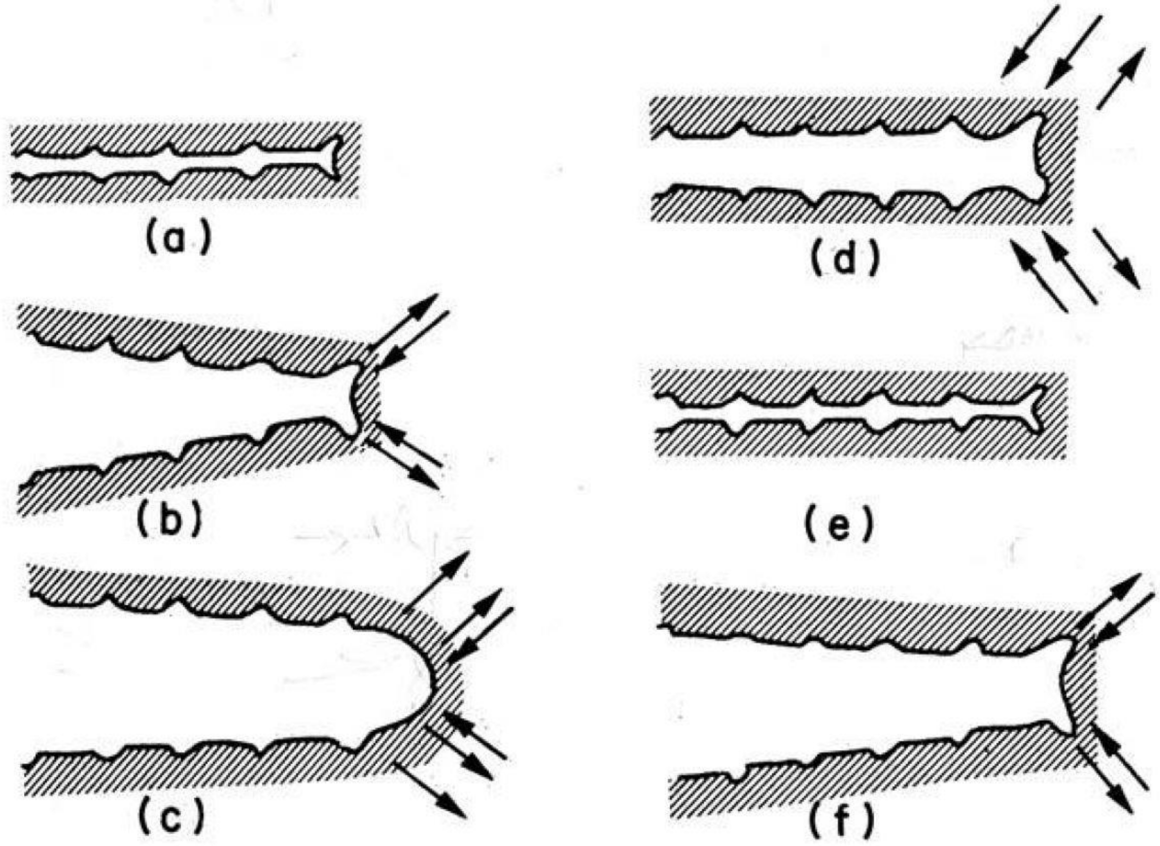

Figure 2.20: The plastic blunting process of fatigue crack propagation in stage II crack growth: (a) zero load, (b) small tensile load, (c) maximum tensile load, (d) small compressive load, (e) maximum compressive load, and (f) small tensile load. Repeated blunting of the crack tip has been postulated as one of the possible mechanisms of fatigue striations [90].

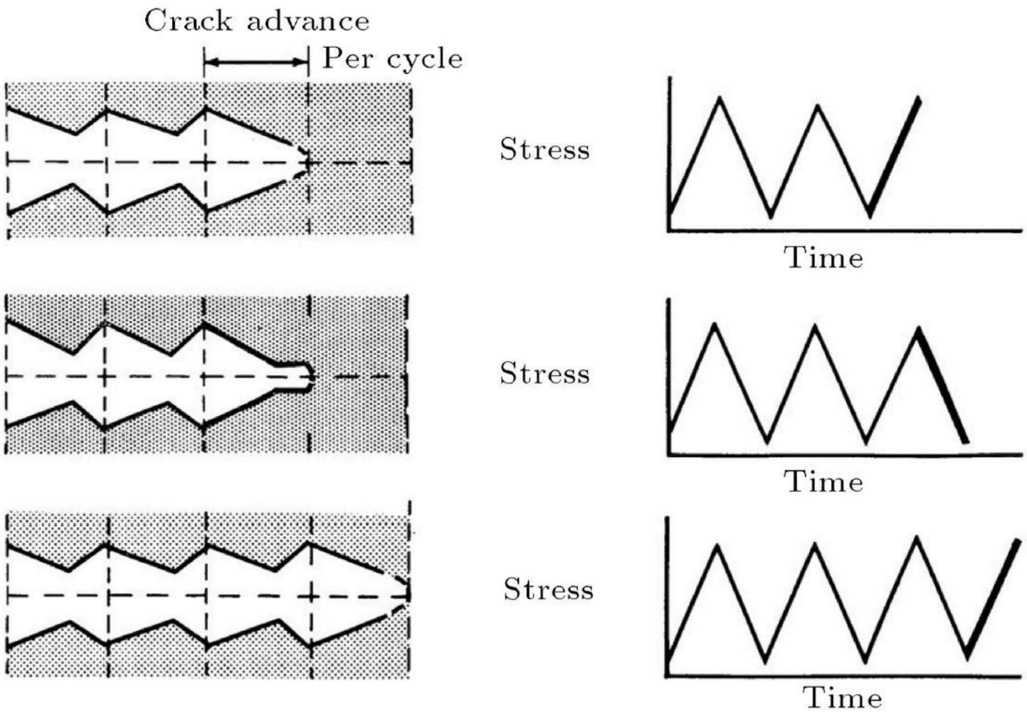

Figure 2.21: Schematic showing formation of saw-tooth striations during crack propagation. This model links individual striations to single loading cycles [88].

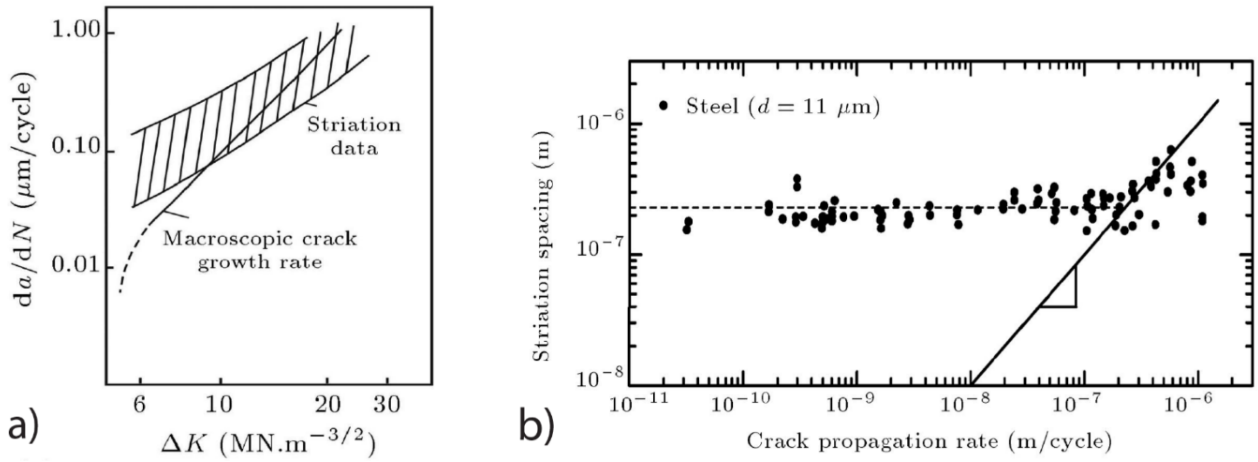

Figure 2.22: Comparisons of striation spacing and crack growth rates for (a) 7010 aluminum and (b) steel indicate that striations may not always occur on a one-to-one basis with loading cycles, especially at lower crack growth rates [94,96].

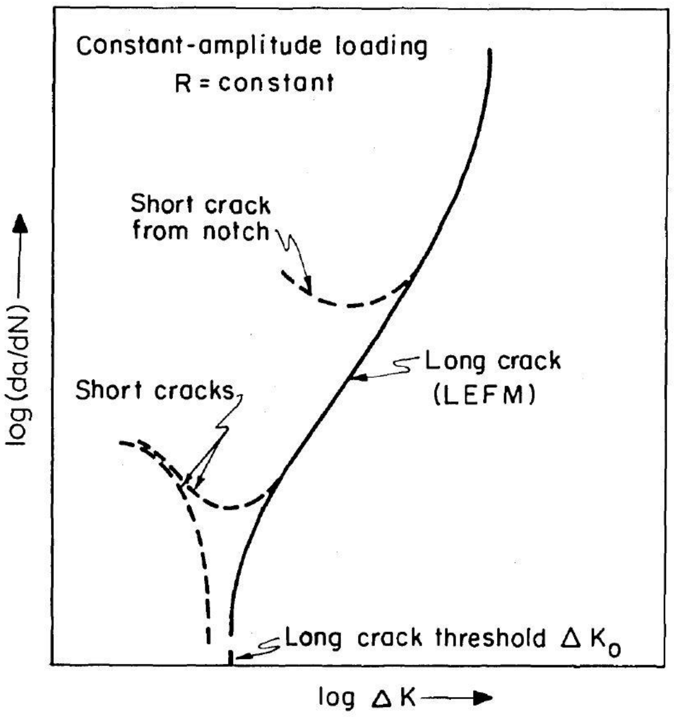

Figure 2.23: Typical fatigue crack growth rates (d*a*/d*N*) for long and short cracks as a function of stress intensity factor range ΔK. Comparatively rapid crack growth rates for short cracks illustrates the short crack phenomenon [105].

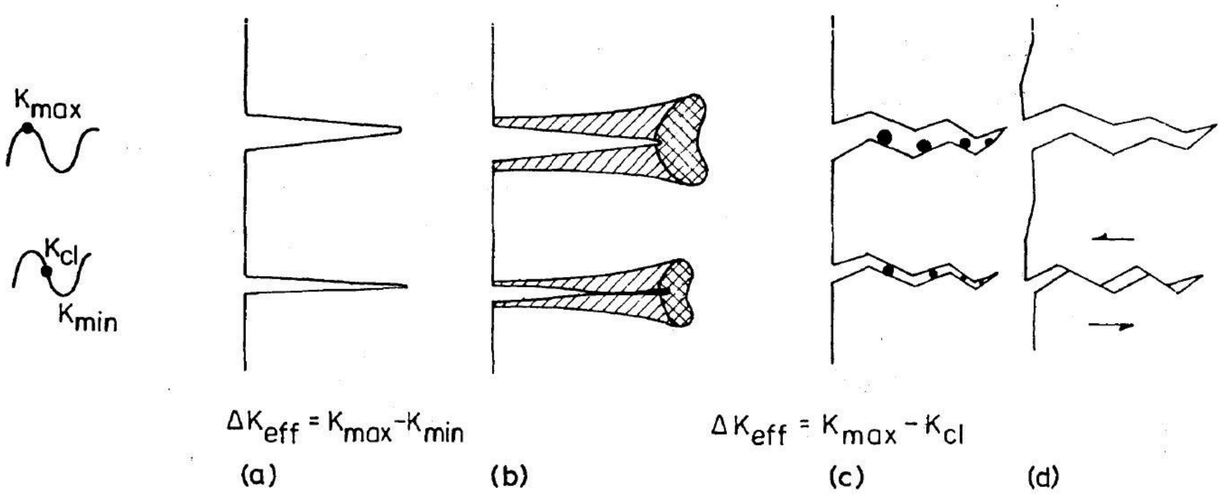

Figure 2.24: Schematic illustration of possible mechanisms of fatigue crack closure at near-threshold stress intensities: (a) no crack closure, closure induced by (b) cyclic plasticity, (c) corrosion deposits, and (d) rough fracture morphology. ΔK_{eff} is the effective stress intensity range, defined by $K_{max} – K_{cl}$, where K_{cl} is the stress intensity at which the two fracture surfaces come into contact ($K_{cl} \geq K_{min}$) [176].

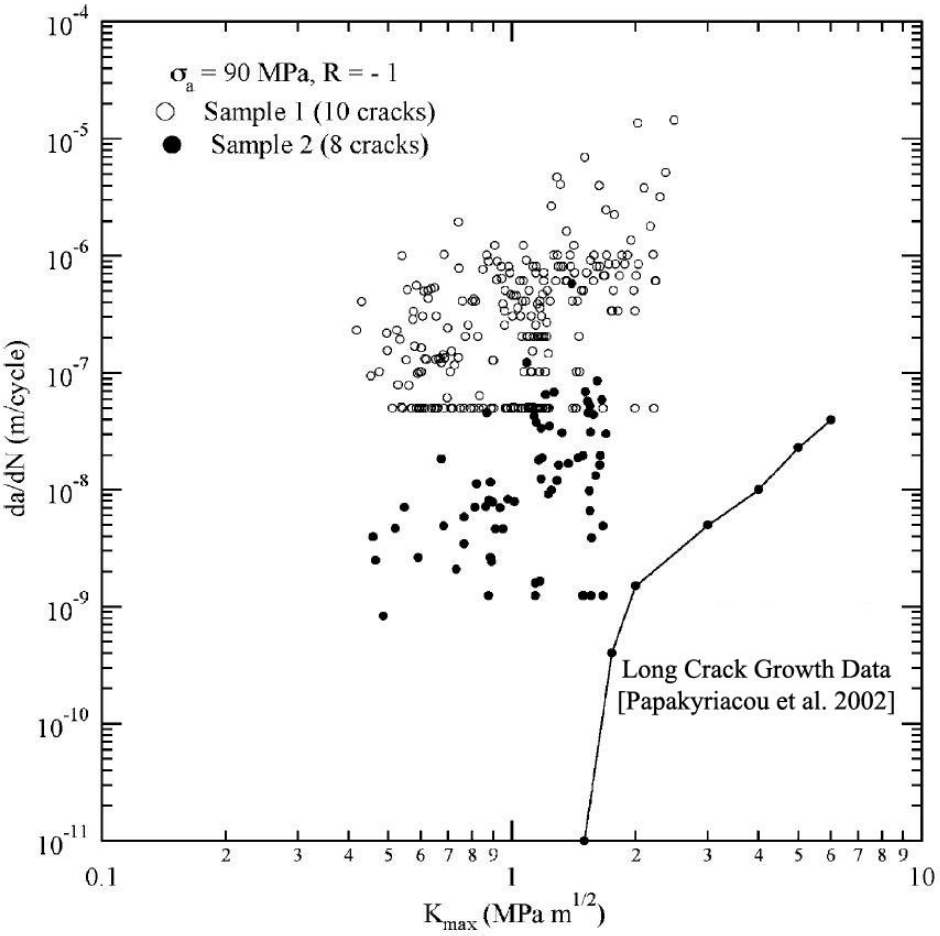

Figure 2.25: Plot of microstructurally small crack growth rates in cast AM60B magnesium showing the occurrence of accelerated crack growth and high sensitivity to microstructural features [108]. Includes long crack data for AM60hp from [177] for reference.

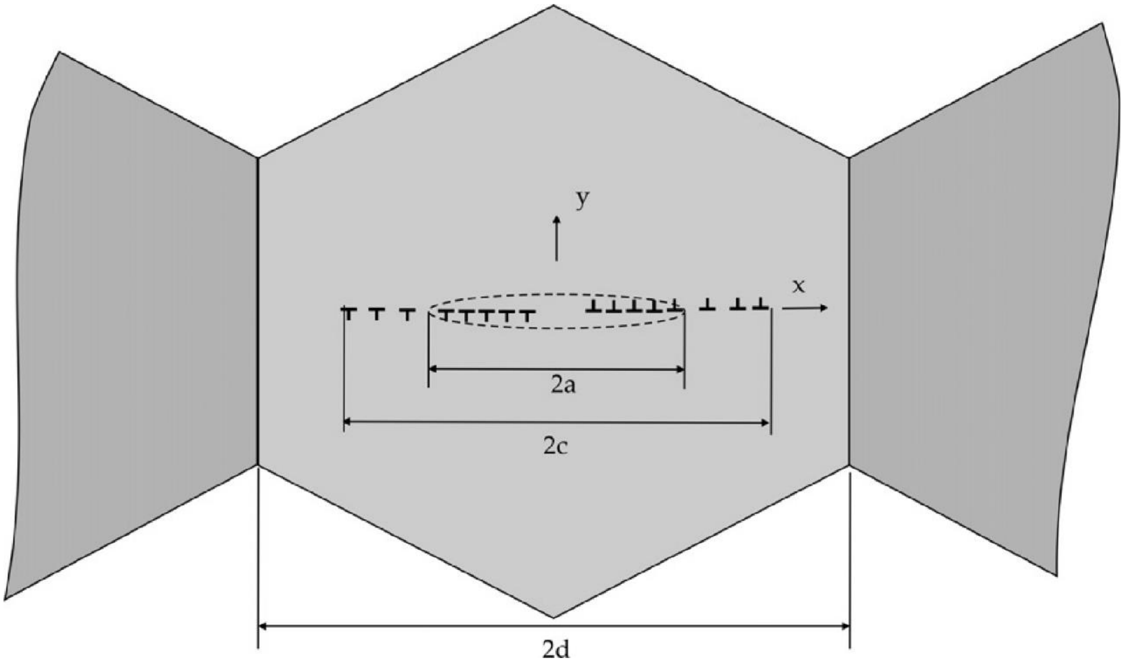

Figure 2.26: BCS model of a crack propagating through the emission of dislocations in stage I inside a single grain [125].

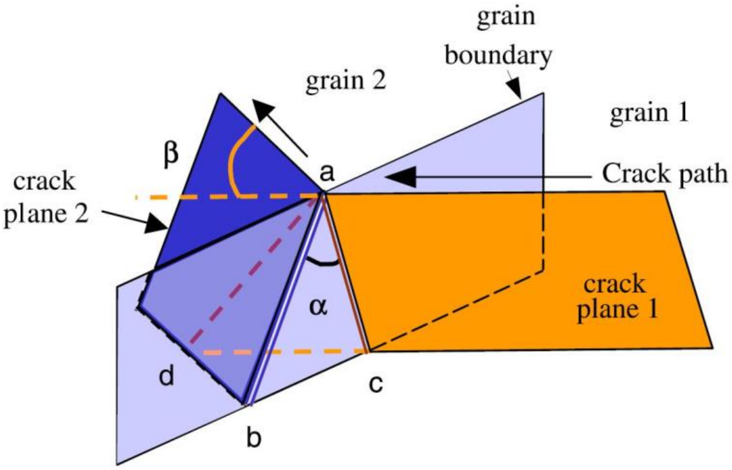

Figure 2.27: A crystallographic model for crack retardation at a grain boundary. While tilt angle, β, has some effect, the twist angle, α, is the dominating factor controlling crack behavior at the grain boundary [127].

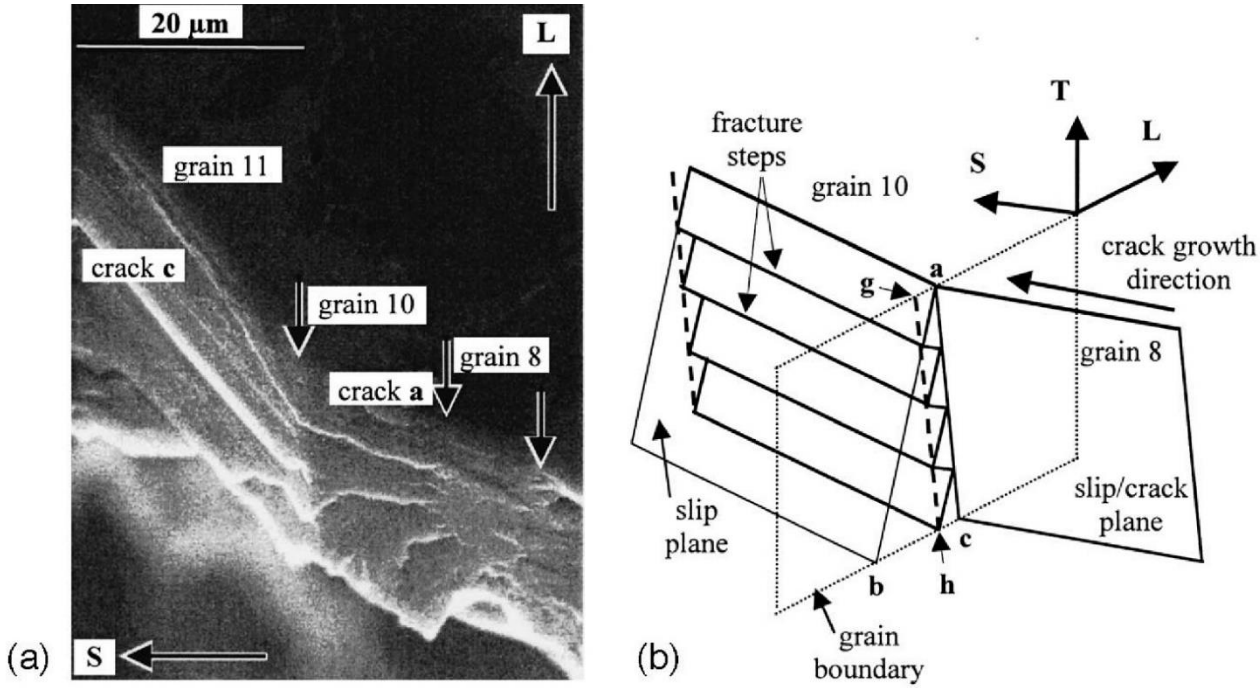

Figure 2.28: (a) A fatigue fracture surface from an Al-Li 8090 alloy showing the presence of fracture steps, postulated to occur as a result of (b) slip plane misalignment at the grain boundary [117].

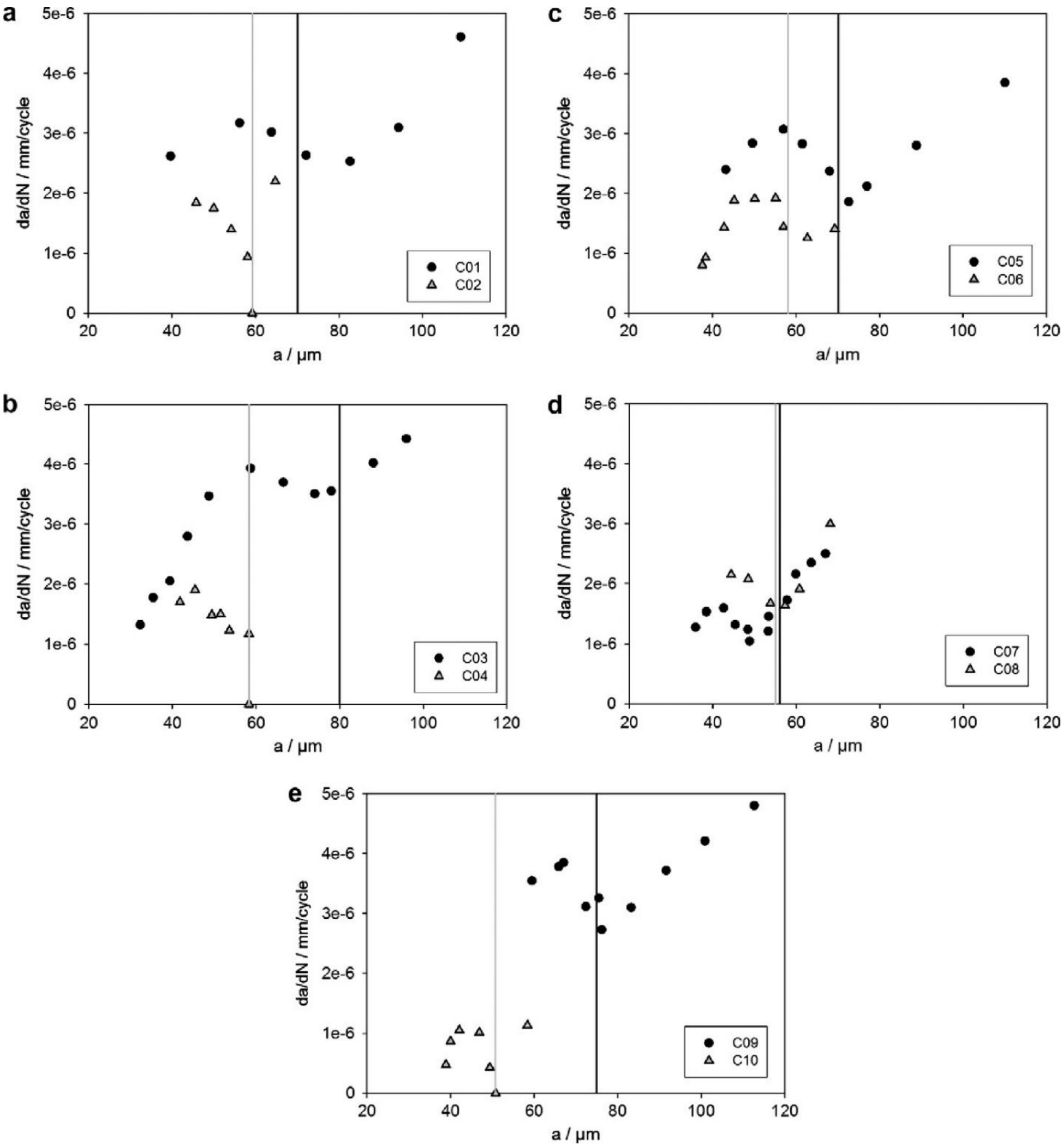

Figure 2.29: Crack propagation rates for a number of cracks in a coarse-grained Ni superalloy showing the effect of grain boundaries on crack growth rates. Vertical lines represent the location of grain boundaries relative to the crack initiation point [125].

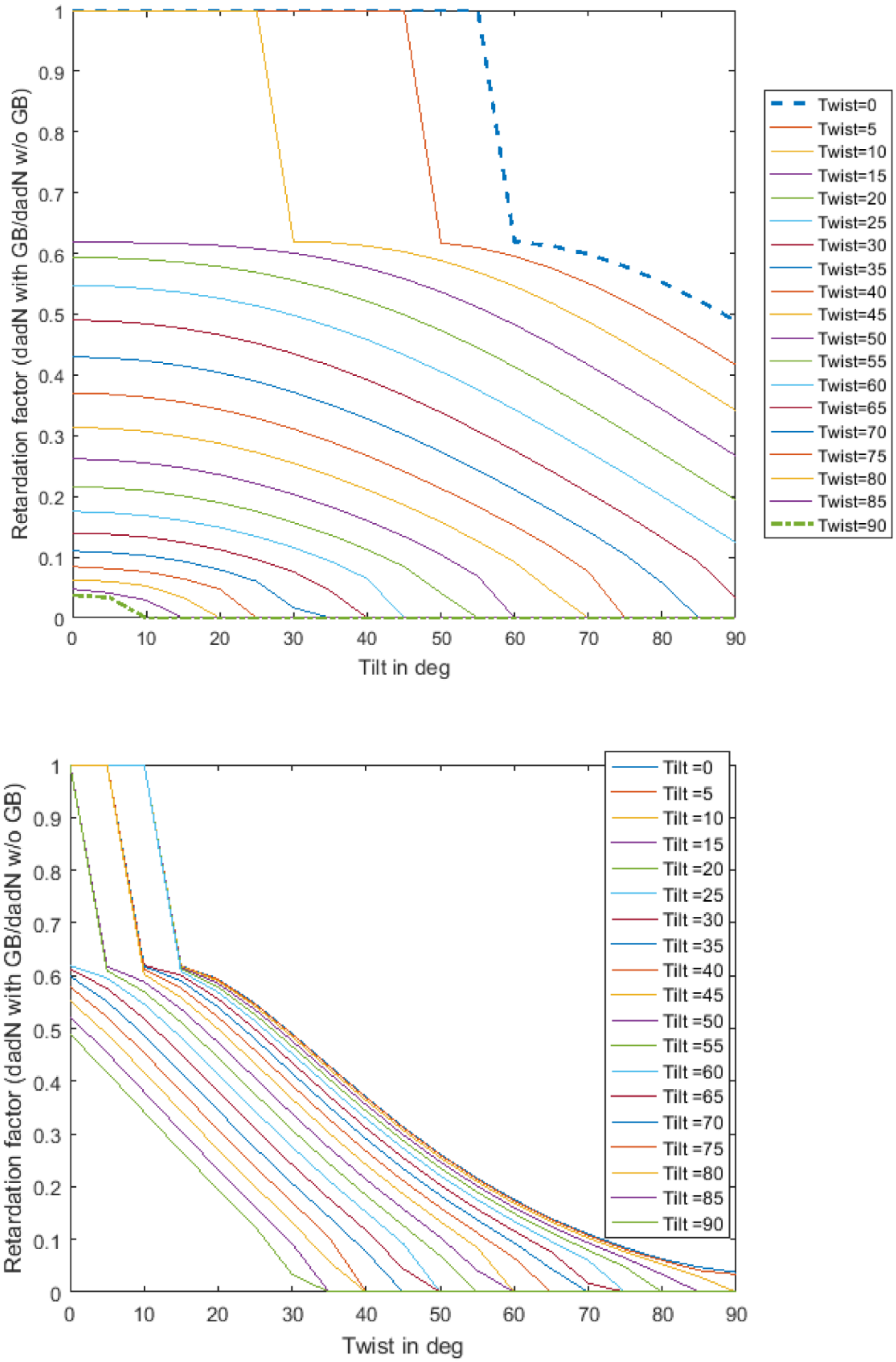

Figure 2.30 - Retardation in fatigue crack growth due to fatigue crack-grain boundary interaction as modeled by the Panwar model. Varying levels of retardation are shown with variation in tilt and twist misorientation across grain boundaries [130].

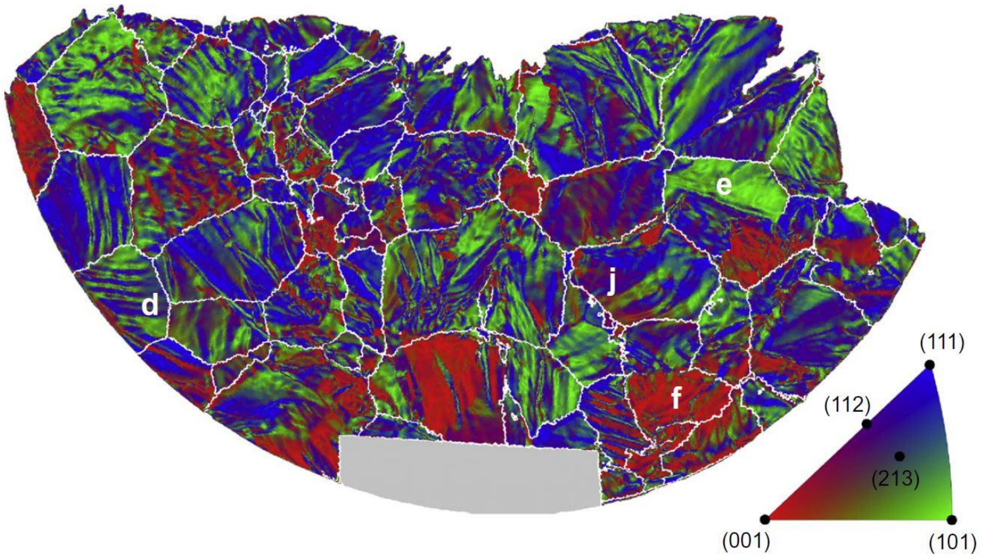

Figure 2.31: View along the loading axis of the fracture surface of beta titanium alloy Ti21S showing grain boundaries in white. The triangle colors represent the orientation of the fracture surface in the crystallographic system as defined in the stereographic triangle on the left [159].

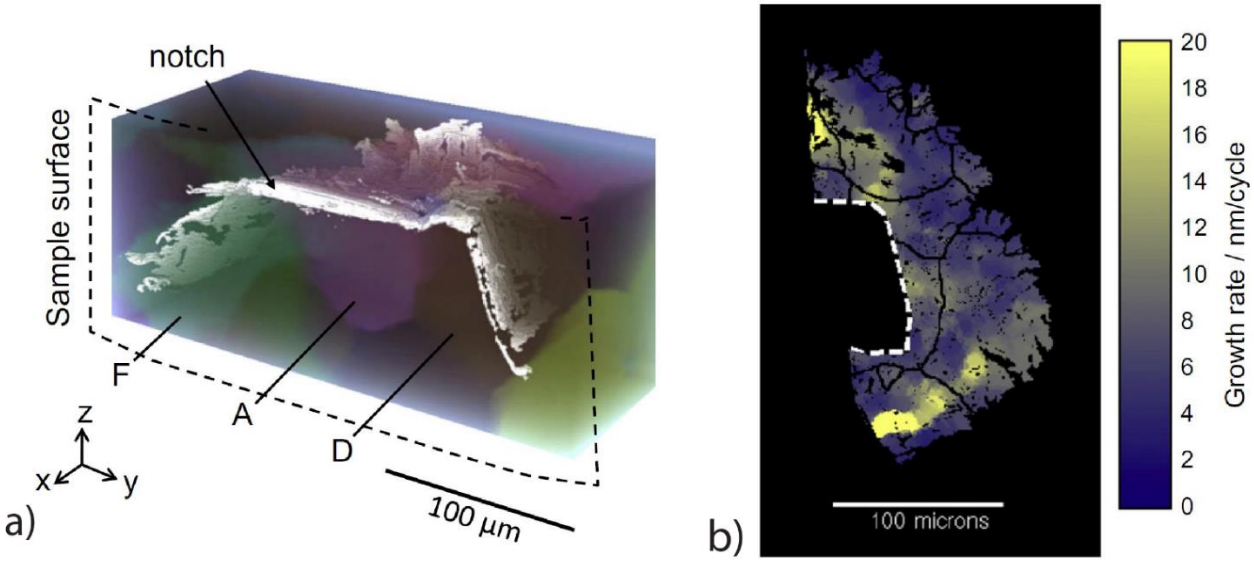

Figure 2.32: (a) 3D rendering of crack growth in magnesium alloy Elektron 21, characterized using X-ray diffraction tomography and DCT. The crack is represented in white and individual grains are colored. (b) Local crack growth rates across the fracture surface were highly sensitive to microstructure [13].

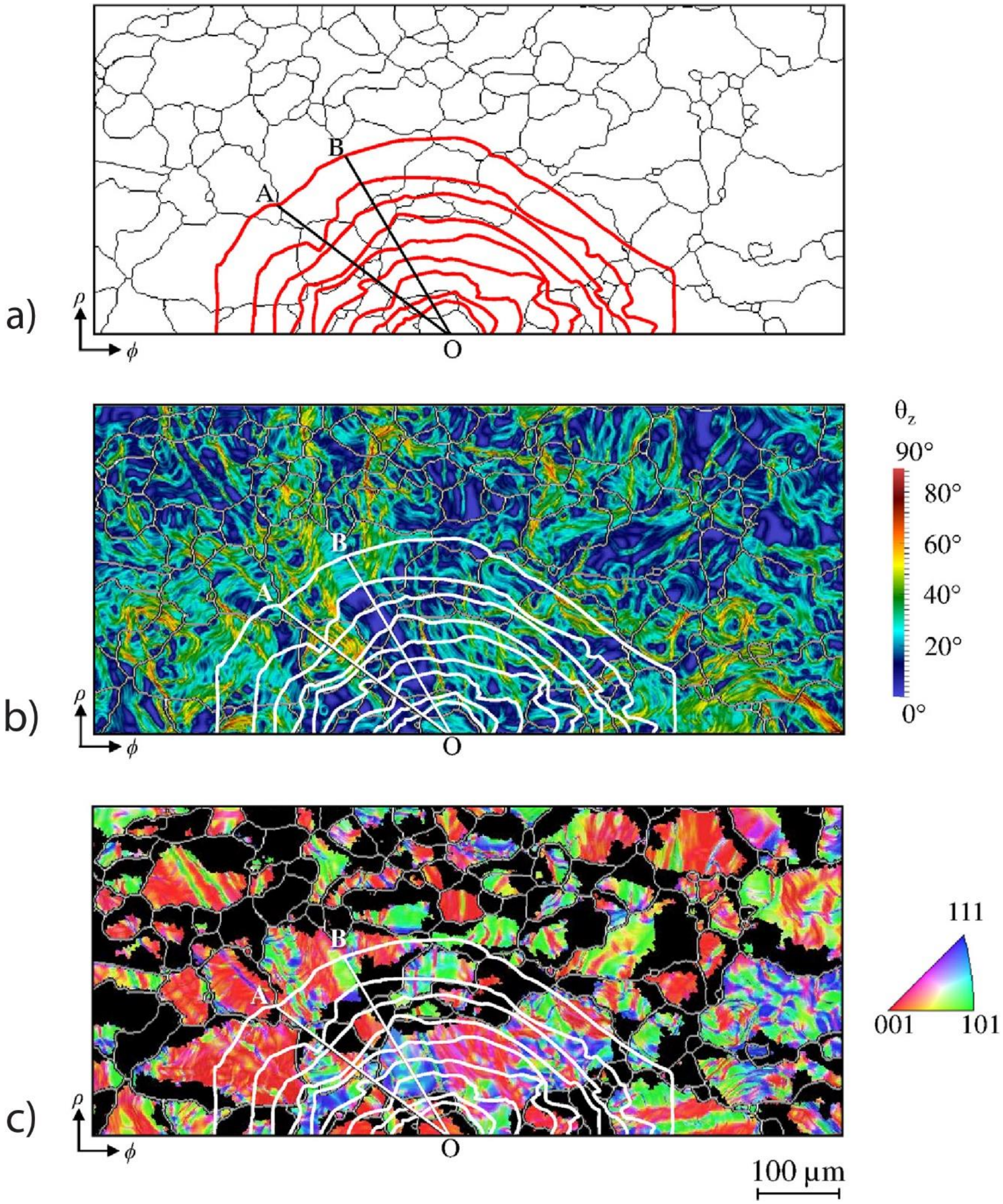

Figure 2.33: Maps of a fatigue fracture surface from an Al-Mg-Si alloy characterized using X-ray tomography and HEDM showing (a) grain boundaries and marker bands, (b) the angle between the local crack surface normal and the global loading direction, and (c) crack surface crystallography representing the local crack surface normals. Black regions correspond to intergranular crack growth [12].

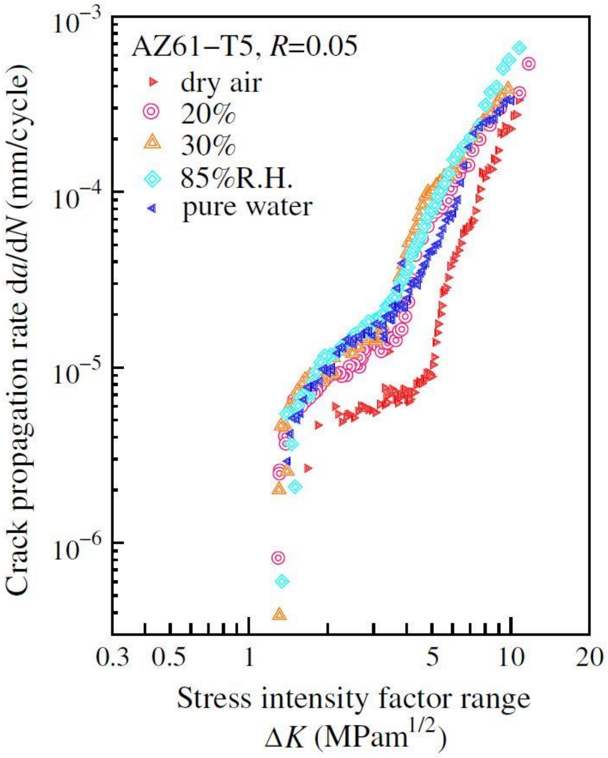

Figure 2.34: Increased fatigue crack growth rates in T5 AZ61 magnesium alloy due to increasing levels of relative humidity in the testing environment. Fatigue crack propagation in dry air is noticeably slower [162].

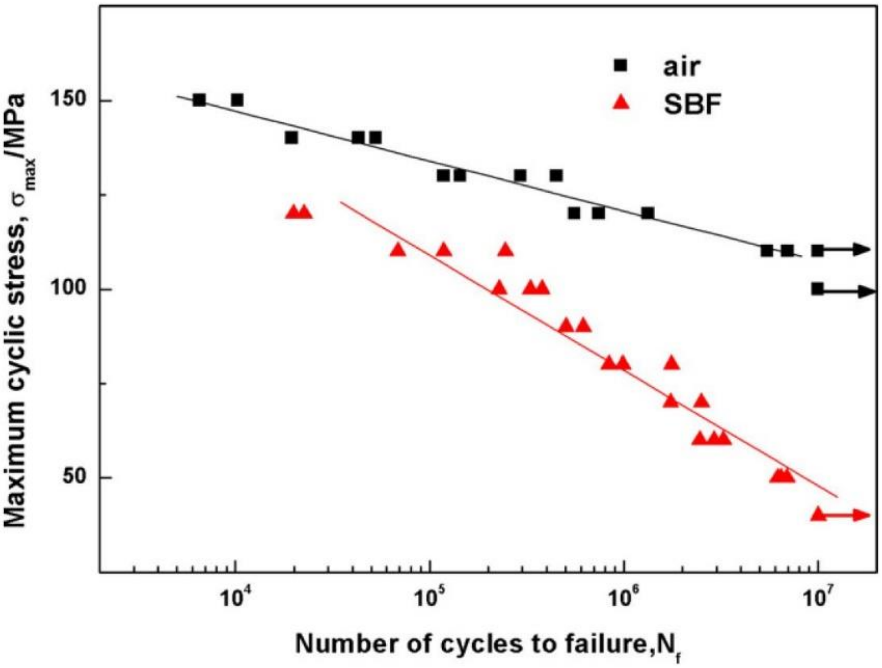

Figure 2.35: Fatigue lives of extruded WE43 magnesium tested in laboratory air and simulated body fluid. The environment composed of simulated body fluid resulted in significantly reduced fatigue strength [52].

CHAPTER 3

MATERIAL AND EXPERIMENTAL PROCEDURES

This chapter describes the WE43 alloy investigated and the experimental techniques used in this study. Section 3.1 describes the properties of the magnesium alloy employed in this work. Section 3.2 describes the microstructural characterization techniques that were used. Section 3.3 describes the fatigue specimens used in fatigue life studies, fatigue crack growth studies, and thin foil fatigue crack growth studies, including the design and preparation of specimens for testing. The techniques and procedures used for ultrasonic fatigue testing are described in Section 3.4, including descriptions of the experimental setups employed for fatigue life studies, fatigue crack growth studies in laboratory air, and the ultrasonic fatigue and scanning electron microscopy (UFSEM) system used for in situ studies. Finally, Section 3.5 covers the experimental setup for the X-ray characterization of microstructure and fatigue behavior, including X-ray tomography and far- and near-field high-energy X-ray diffraction.

3.1. Material

Magnesium alloy WE43 was prepared by Magnesium Elektron Ltd. as 26 mm thick hot-rolled plate. The alloy had a nominal composition (wt.%) of 3.7-4.3 Y, 2.3-3.5 Rare Earths, 0.2 minimum Zr, and Mg (balance). Table 3.1 shows the material composition as measured by inductively coupled plasma-mass spectrometry (ICP-MS) conducted by NSL Analytical Services. WE43 was provided in the T5 condition, consisting of hot-rolling at a proprietary temperature and subsequent aging at 204° C for 48 hours. Further heat treatment was conducted in our laboratory to produce underaged and peak-aged (T6) microstructures. Solution treatment of the as-received alloy was conducted at 525° C for 8 hours. Subsequent aging at 250° C for 4 hours and 16 hours was used to produce the underaged and peak-aged conditions, respectively. Grain size was characterized using the line intercept method and electron backscatter diffraction (EBSD) mapping in a Tescan Mira3 scanning electron microscope (SEM) with EDAX OIM Data Analysis software (Figure 3.1). Average grain diameters measured using both techniques are detailed in Table 3.2. An investigation of tensile behavior performed by A. Githens revealed notable differences in the mechanical properties of the three conditions (Table 3.3), with the T5 condition exhibiting yield and tensile strengths significantly higher than those of either the underaged or T6 conditions [178]. In these tests, the tensile loading direction was parallel to the rolling direction, which was the same orientation used in all fatigue tests.

The crystallographic texture produced by each heat treatment was investigated using EBSD (Figure 3.2). Each of the three conditions featured a medium strength basal texture, with 2.90, 4.10, and 3.35 multiples of random distribution (m.r.d.) observed in the T5, underaged, and T6 conditions, respectively. Basal poles were aligned perpendicular to the rolling plane, i.e. parallel to the normal direction (ND) of the plate.

Table 3.1: Chemical composition (wt./at.%) of WE43 alloy used in this study.

	Y	Nd	Gd	Zr	Zn	Mg
ICP-MS Characterization	3.74/1.08	2.10/0.37	0.52/0.08	0.45/0.13	0.02/0.01	Balance

Table 3.2: Average grain diameter of WE43 microstructural conditions as measured by the line intercept method and EBSD area averaging.

Microstructural Condition	Line Intercept Average Grain Diameter (μm)	Number of Line Sampled Grains	EBSD Average Grain Diameter (μm)	Number of EBSD Sampled Grains
T5	13 ± 2	543	13 ± 7	3172
Underaged	107 ± 15	199	112 ± 55	524
T6	121 ± 11	174	114 ± 58	840

Table 3.3: Mechanical properties of WE43 determined through tensile testing [178].

Microstructural Condition	Elastic Modulus (GPa)	Tensile Yield Strength (MPa)	UTS (MPa)	Percent Elongation
T5	43.5	265	335	19
Underaged	43.5	139	235	15
T6	43.5	159	243	15

3.2. Microstructural Characterization

3.2.1. Metallographic Sample Preparation

Metallographic samples were prepared in order to characterize the microstructure of each of the heat treatments of WE43 magnesium. Samples were sectioned from the plate of magnesium and characterized in the normal (ND), rolling (RD), and transverse (TD) directions. The planes of RD represent planes normal to the fatigue specimen loading direction. Sectioned samples were mounted in slow-set epoxy and ground using silicon carbide papers of successively finer grit up to a grit of 1200. Polishing was completed using 6, 3, and 1 μm diamond suspensions on Buehler microcloth polishing pads, followed by a final polish using Buehler Masterpolish, a weakly basic polishing suspension containing a mixture of alumina and colloidal silica on a Buehler chemomet polishing cloth. To highlight grain boundaries, specimens were lightly etched for 3-5 seconds by submersion using an etchant composed of 5 ml nitric acid, 15 ml acetic acid, 20 ml distilled water, and 60 ml ethanol.

3.2.2. Optical Microscopy

Light optical microscopy was completed using a Nikon inverted optical microscope to examine the microstructure. Digital images were acquired at various magnification and were used to determine the average grain size and grain morphology.

3.2.3. Scanning Electron Microscopy

Scanning electron microscopy (SEM) was used to characterize the microstructure of the three conditions, as well as complete investigations of the free and fracture surfaces of fatigue specimens. Characterizations were completed using a Tescan Mira 3 FEG-SEM. Electron backscattered diffraction (EBSD) techniques were performed in order to gain information about crystallographic orientations and texturing. EBSD scans were carried out at 30 kV with scan step sizes of approximately 0.5 µm and 5 µm for characterization of the T5 and solution treated conditions, respectively. SEM was further utilized in the post-mortem characterization of fatigue damage and fracture surfaces, as well as in-situ characterization of fatigue crack propagation, as detailed in Section 3.4.

3.3. Fatigue Specimens

3.3.1. Specimen Design

Fatigue specimens were designed to resonate at a frequency of 20 kHz. Fatigue specimen drawings are shown in Appendix A. Specimen design was determined using numerical techniques to solve a wave equation of the form shown in Equation 3.1, in which u represents the displacement in the longitudinal direction, A represents the cross-sectional area, and ρ and E represent the density and elastic modulus of the specimen, respectively. Equation 3.1 is solved iteratively using a Matlab program to determine the three portions of the fatigue specimen: the gage section, the curved shoulder region, and the grip section.

$$\ddot{u} + \left(\frac{\dot{A}}{A}\right)\dot{u} + \omega^2\left(\frac{\rho}{E}\right)u = 0 \qquad [3.1]$$

Figure 3.3 shows a characteristic plot of the strain and displacement along an ultrasonic fatigue specimen. The strain is nearly constant through the specimen gage (0 - 6 mm), and then decreases rapidly in the shoulder and grip sections. The center of the specimen corresponds to a displacement node, while the ends of the specimen correspond to strain nodes, and maximum displacement.

3.3.2. Specimen Preparation

Cylindrical fatigue specimens were used for both fatigue life (S-N) tests and short fatigue crack growth tests. Specimens were machined from blanks extracted from rolled plate, with the longitudinal axis of the specimens aligned with the rolling direction of the plate. Final machining of the cylindrical specimens was completed by low stress grinding to minimize compressive residual stresses. The specimen gage is nominally 4 mm in diameter and 7.5 mm in length.

The majority of fatigue life specimens were prepared by electropolishing to remove remaining surface compressive residual stresses. The electrolyte used was 3 parts orthophosphoric acid to 5 parts ethanol. Electropolishing was conducted at room temperature with no agitation of the electrolyte, using a stainless-steel beaker as the cathode. The power supply was set to control the potential at 12 V, and the current was allowed to fluctuate with the condition of the electrolyte. Approximately 50 µm of material was removed from the surface during 30 – 45 minutes of electropolishing. Some specimens were tested as machined with a low-stress ground surface, which was found to produce no difference in fatigue behavior but provided an inferior surface for investigation of surface crack propagation.

3.3.3. Fatigue Crack Growth Specimens

Smooth bar fatigue specimens utilized in fatigue life tests were modified for use in short fatigue crack growth studies. Flats were machined on opposing sides of the gage section of the specimens to maintain symmetry and to prevent any bending stresses from developing. These flats facilitated microstructural characterization using EBSD techniques and enabled observation of fatigue crack growth. The gage flats were then prepared by hand grinding with SiC paper and polishing with diamond solution, followed by electropolishing.

To investigate short crack growth behavior, micro-notches were machined in the gage-flats to act as crack-initiation sites, using an FEI Quanta 200 3D focused ion beam (FIB) equipped with a gallium ion source operating at 30kV and a probe current of 5.0 nA. Notches were machined perpendicular to the loading direction at the centerline of the specimen and each had a length of 100 µm, a width of 6 µm, and an approximate depth of 40 µm. In most cases, three notches, centered about the midsection of the gage length and separated by 2mm, were machined in each specimen. These notches were placed without regard to the local microstructure, although surrounding microstructure was characterized using EBSD techniques.

For short fatigue crack growth tests targeted at investigating the role of grain boundaries on crack propagation, FIB micro-notches were placed at specific microstructural sites and aligned to be parallel to basal slip planes in three dimensions (Figure 3.4). This was achieved by first characterizing the flats in the gage section microstructurally using EBSD. Next, large grains with high nominal basal Schmid factors and interesting grain boundary characteristics were selected as locations for the micro-notch, with the notch entirely contained within the favorably oriented grain (on the sample surface). (Note: we adopt here the nomenclature “nominal” Schmid factor in recognition of the fact that the Schmid factor provided by standard orientation imaging analysis software assumes that the stress field is uniaxial. In polycrystals, adjacent grains may alter the stress state, so this assumption is not necessarily accurate, however in the absence of more detailed crystal plasticity simulations of the actual stress fields it is a helpful means to identify grains and phenomena of interest.) Orientation of the basal system was determined through EBSD determination of Euler angles, and the sample was oriented during machining of the FIB notch such that the basal system was parallel to the FIB micro-notch.

3.3.4. Thin Foil Specimens

In order to investigate the role of grain boundaries on short fatigue crack growth without the effect of subsurface microstructure, dog-bone-shaped thin sheet fatigue samples were fabricated by electrical discharge machining. The foil specimens were flat coupons 30.5 mm in total length, with a gage section 1.6 mm long and 2 mm wide. A drawing of the specimen is available in Appendix A. The longitudinal direction of the specimens was aligned with the rolling direction of the WE43 plate. Specimens were hand-polished to approximately 200 µm using Sic paper, then further thinned to approximately 150 µm through electropolishing, using the same electrolyte used to prepare cylindrical samples. The sample surface was then characterized using EBSD. An edge notch perpendicular to the tensile axis was produced at the center of the gage section of each fatigue specimen through FIB machining.

3.4. Ultrasonic Fatigue Testing

Ultrasonic axial fatigue tests were performed in laboratory air and *in situ* in a Tescan Mira-3 FEG-SEM using ultrasonic fatigue equipment operating at 20 kHz. The ultrasonic instrumentation used in this study was designed at BOKU Vienna. Cylindrical specimens were fatigued at a stress ratio of R = -1 (fully reversed loading), while thin foil specimens were fatigued at a stress ratio of R = 0.1.

3.4.1. Experimental Setup for Ultrasonic Fatigue Testing in Laboratory Air

Fatigue testing in laboratory air was conducted using the experimental setup shown in Figure 3.5. Imaging of crack growth specimens was accomplished using a Navitar 12X Ultrazoom lens system equipped with a 5X Mitutoyo infinity corrected objective and a 5-megapixel CCD (Point Grey GRAS-50S5C) in combination with a Questar positioning stage. The ultrasonic fatigue system used in this setup is described in detail in [9], and specific components are identified in Figure 3.5. A summary of the ultrasonic system follows. The ultrasonic pulse that drives fatigue in the specimen when in resonance is generated by a piezoelectric transducer at the top of the load frame. The signal from the piezoelectric transducer is then amplified when passing through the amplification horn before entering the fatigue specimen further down the load line. The components of the system are machined from commercially available Ti-6Al-4v that are tuned to resonance using the equations described in Appendix B. The frequency of the acoustic signal can be adjusted until the fatigue sample is in resonance. Ultrasonic fatigue tests are displacement controlled, within a closed feedback loop using a displacement transducer or Hall Effect sensor. The control unit of the ultrasonic fatigue system sends a command voltage to the ultrasonic transducer to produce an acoustic pulse and monitors the displacement measured by the Hall Effect sensor. The control unit then adjusts the power sent to the ultrasonic transducer until the measured displacement matches the user specified amplitude at the control unit. Once the specimen is in resonance and the displacement matches the selected amplitude, the voltage supplied to the ultrasonic transducer is reduced to a point that is sufficient to maintain resonance in the specimen. The system is able to perform these adjustments in a specified duty cycle consisting of repeated loading blocks interrupted by pauses to reduce specimen heating. Additional cooling is provided by forced air directed at the gage of the fatigue specimen. Thermocouples were used to verify that the specimen surface temperature did not vary by more than ± 5° C.

Due to slight variations in the dimensions of fatigue specimens and the connections between components in the ultrasonic load line, the system must be calibrated before each fatigue test. Kyowa strain gages with a gage length of 1 mm were applied to each fatigue specimen using cyanoacrylate based strain gage cement to measure the cyclic strain applied during fatigue loading. Specimens were then cycled at low amplitudes, well within the elastic regime of loading, to determine the slope of the line relating the supplied command voltage to measured strain. As fatigue testing was conducted at stresses in the range of approximately 0.4 to 0.75 of the yield stress, it is assumed that the cyclic loading was nominally elastic. The testing amplitude for the command signal could then be determined by extrapolation from the linear curve created using low amplitude loading.

3.4.2. Experimental Setup for *In Situ* Ultrasonic Fatigue Testing

High spatial resolution (≈ 5 nm) imaging of fatigue damage at the microstructural length scale in vacuum and laboratory air was accomplished using a unique combination of ultrasonic fatigue instrumentation and scanning electron microscopy, termed UFSEM and shown in Figure 3.6. The ultrasonic fatigue instrumentation operates on the principles described in [164], and the

UFSEM system is detailed in [10] and summarized here. The load line components of the system are machined from Ti-6Al-4V and are tuned to a resonance frequency of 20 kHz. The components include an ultrasonic transducer that produces a sinusoidal displacement using a piezoelectric material stack, an amplification horn that magnifies the displacement from the transducer and a lambda rod to extend the length of the load line. The ultrasonic load line is mounted to a custom-built SEM chamber door designed to fit with the Tescan Mira-3 microscope, although the system has also been used with SEM chamber doors designed to fit with a Philips XL30 ESEM and a FEI Quanta 3D ESEM. The system is controlled by instrumentation that monitors and maintains the amplitude and frequency of the displacement signal in a closed loop system. Rather than a Hall Effect sensor, a piezoelectric film sensor (Measurement Specialties, Inc. Model DT1-028K) is used to measure the displacement response in the load train, and provides a smaller, more manageable footprint in the SEM chamber. The fatigue specimen is positioned in the SEM chamber using a McAllister Technical Services MB1500 manual manipulator stage with five translational adjustments. The multiple degrees of freedom of the manipulator stage enabled the observation and tracking of multiple microstructural features or fatigue cracks during a fatigue test.

As in conventional ultrasonic fatigue testing, heating of the specimen is a concern when investigating fatigue using the UFSEM system. Aside from duty cycle loading, no auxiliary cooling methods were used during *in situ* testing. In tests conducted in both laboratory air and vacuum, a duty cycle of 200 ms / 9000 ms pulse/pause was used to allow significant time for heat to dissipate. Thermocouples were used to monitor specimen temperature, which was maintained within approximately 5° C of room temperature.

Installing ultrasonic fatigue instrumentation in the Tescan Mira-3 SEM enables the *in situ* investigation of fatigue crack propagation in vacuum, or the *ex situ* characterization at the microstructural scale of fatigue in laboratory air. When conducting ultrasonic fatigue in laboratory air, cycling was conducted using the UFSEM system with the SEM chamber vented to laboratory air. Following a number of duty cycles, testing was paused to allow imaging in the SEM, after which the SEM chamber was vented and testing continued in laboratory air. This approach greatly expedites the high resolution characterization of crack growth in that the fatigue specimen does not have to be removed from the ultrasonic fatigue instrument prior to observation in the SEM.

3.4.3. Fatigue Life Tests

All fatigue life tests were conducted using the ultrasonic instrumentation discussed in Section 3.4.1, operating at a testing frequency of approximately 20 kHz and at a stress ratio of $R = -1$, at room temperature in laboratory air. Intermittent cycling of 200 ms / 5000 ms pulse/pause, in addition to forced air cooling, was used to minimize the heat generation associated with high frequency loading. Fatigue specimens were cycled until failure or to 10^9 cycles, which was considered a runout. In a number of cases, underaged and T6 specimen runouts were stepped in increments of 10 MPa to make efficient use of specimens. Failures resulting from step tests were tracked separately and fatigue results both with and without step tests were analyzed.

Following failure, fatigue crack paths and fracture surfaces were characterized at high spatial resolution using scanning electron microscopy in order to investigate microstructural features leading to crack initiation and modes of crack propagation.

3.4.4. Fatigue Crack Growth Tests

Fatigue crack growth tests were conducted using both the ultrasonic fatigue instrumentation discussed in Section 3.4.1 and the UFSEM system detailed in Section 3.4.2. Fatigue tests in both cases were conducted using fatigue equipment operating at 20 kHz with a load ratio of -1 at room temperature in laboratory air.

Surface images of fatigue crack growth were captured using two different methods. For *in situ* tests conducted using the UFSEM system, micrographs of crack progression were captured using secondary electron imaging in the Tescan Mira-3 microscope. Fatigue crack growth tests conducted using the ultrasonic fatigue equipment detailed in Section 3.4.1 were imaged using the Navitar optical system equipped with a 5-megapixel CCD. Diametrically opposed flats in the specimen gage were used to simplify imaging of the fatigue cracks and to ensure that the specimen surface and focal plane of the telescope remain co-planar. Cycling was paused every 25,000-30,000 cycles, depending on the fatigue crack growth rate, to observe fatigue damage and crack progression, and to capture micrographs for calculation of crack growth rates. Images were captured until the crack grew beyond the edge of the gage flat, which was approximately 2.5 mm in width. In both cases, higher resolution micrographs of the crack path and fracture surfaces were captured post mortem using a Tescan Mira-3 FEG-SEM.

Fatigue crack growth data is presented in the typical double logarithmic plot of dc/dN vs ΔK format. The surface fatigue crack growth rate, dc/dN, was calculated using a seven-point sliding polynomial method [179], and the stress intensity factor range, ΔK, was calculated using the equations of Newman and Raju [180] for a surface crack in a finite elastic plate, where c/a was assumed to be unity.

The fatigue crack growth behavior is assumed to follow a power law equation, where the fatigue crack growth rate, *dc/dN*, is related to the cyclic stress intensity factor ΔK by the power law equation given by Equation 3.2:

$$\frac{dc}{dN} = C(\Delta K)^m \qquad [3.2]$$

where *C* and *m* are constants affected by various factors including material, environment, and test conditions like microstructure, temperature, and load ratio.

3.4.5. Foil Crack Growth Tests

The ultrasonic fatigue equipment detailed in [9] and summarized in Section 3.4.1 incorporates hydraulic cylinders which are used to enable fatigue investigations at positive mean stresses. The two hydraulic cylinders have a combined load capacity of 22 kN and provide both the loading force and guide the upper and lower platens. The load line used for positive mean stress testing includes a lambda rod with a flange at a zero displacement node at the end of the load line. The load line is connected to the upper and lower platens by spherical bearings to minimize bending strains by allowing self-alignment.

Ultrasonic fatigue systems generally place fairly strict limitations on specimen dimensions and geometry. In order to study thin foil specimens, a “carrier” specimen was designed for resonance at 20 kHz and machined from titanium alloy IMI 834, to which a foil specimen could be rigidly attached at the specimen shoulders as seen in Figure 3.7. Drawings for the carrier and foil specimens are included in Appendix B. During resonance, the carrier specimen vibrates with a displacement node at the center of the gage, and displacement maxima at the ends of the sample. Cyclic loads are applied to the foil specimen via the displacement of the carrier specimen at the shoulder connections and are adjusted by varying the displacement amplitude of the carrier. Strains for foil specimens of varying thickness were determined through both a finite element analysis of the carrier/foil assembly and by applying strain gages to the gage sections of both the carrier and foil specimens.

Fatigue tests for foil specimens were conducted with a load ratio of 0.1 with a maximum stress in the foil of 60 MPa. Intermittent cycling of 100 ms was utilized to allow for frequent documentation of fatigue crack propagation. Images of crack propagation were captured using the Navitar optical system equipped with a 5-megapixel CCD. Following calculation of fatigue crack growth rates, the stress intensity factor range, ΔK, was calculated using the equations of Newman and Raju [180] for an edge-cracked finite plate.

3.5. X-Ray Characterization

To gain more understanding of the role of three-dimensional microstructure on short crack growth behavior, a short crack growth test was conducted using a cylindrical fatigue sample. The sample was then characterized post-mortem by imaging the crack path and fracture surfaces using scanning electron microscopy, followed by X-ray computed tomography and high-energy X-ray diffraction (HEDM) characterization of a reduced section of the specimen. The X-ray measurements were performed at the 1-ID beamline of the Advanced Photon Source (APS) at Argonne National Lab.

3.5.1. Sample Preparation for X-Ray Characterization

The three-dimensional characterization of short fatigue crack behavior was accomplished by first characterizing fatigue crack propagation in two cylindrical fatigue specimens. Following fatigue failure and characterization of the crack path and fracture surfaces, the sample was sectioned on a slow-speed metallographic saw to produce a strip 1 mm wide by 0.5 mm thick from both the top and bottom halves of the specimen. The strips were centered about the site of crack initiation, which was clearly identified by the presence of the FIB micro-notch and the appearance of distinct fracture features. The two strips were then mounted back-to-back to produce a 1 mm by 1 mm specimen featuring the initiation site on both mating sides of the fracture surface. The 1 mm specimen was extracted from the larger fatigue specimen to ensure that an entire volume containing the fatigue crack surface could be characterized using synchrotron X-rays.

3.5.2. X-Ray Tomography

Following SEM-based imaging of the crack path and fracture surfaces, the sectioned specimen was mounted such that the loading axis was perpendicular to the incident X-ray beam. Approximately 1800 tomograms were collected over a 360° rotation of the specimen. Filtered back-projection was used to reconstruct a set of two-dimensional images representing slices through the z-axis (vertical) of the specimen. Noise was then filtered from these 2-D images using an inverse Fourier Transform technique written in Matlab. The sample was reconstructed in 3-D using Avizo [181] to produce a three-dimensional representation of the fracture surface. Spatial resolution of the tomographic reconstruction was 1.5 µm. The reconstruction of the fatigue fracture surface was later meshed using triangular facets to quantify crack-surface crystallography.

3.5.3. Far-Field High-Energy X-Ray Diffraction

Following tomographic characterization, far-field HEDM data was collected in a volume that spanned 800 µm along the z-axis (vertical) (Figure 3.8). An 800 µm tall box X-ray beam was used to define the measurement volume for the dataset. The measurements were made over a 360° rotation with a 0.25° interval. Analysis of the diffraction data was conducted using the HEXRD code [182] to provide a characterization of grain centroids and crystallographic orientations. The set of indexed orientations is further utilized during the reconstruction of near-field HEDM data to reduce the number of orientations that must be simulated.

3.5.4. Near-Field High-Energy X-Ray Diffraction

The experimental setup for near-field HEDM was first presented by Poulsen [183] (Figure 3.9). Forward modeling techniques applied to the experimental data yield three-dimensional maps of crystallographic information from the characterized specimen. For each cross-section of the specimen illuminated by the line-focused monochromatic (50 keV) X-ray beam (approximately 0.004 x 1.3 mm^2), diffraction spots from grains satisfying the Bragg condition were imaged for rotations through 180° about the z-axis, with images collected over 0.25° integration intervals. This procedure was repeated at two different detector positions to aid in the forward modeling reconstruction. The specimen stage was then translated vertically 12 μm along the rotation axis, and a new set of diffraction images was collected from the newly illuminated plane of the specimen. This process was repeated over the height of material to be measured. Individual diffraction spots provide information on the parent grain including crystallographic orientation, spatial position, and grain geometry, allowing for the non-destructive characterization of three-dimensional microstructure and crack behavior. Near-field HEDM data was analyzed using the IceNine data reduction code [157].

Figures

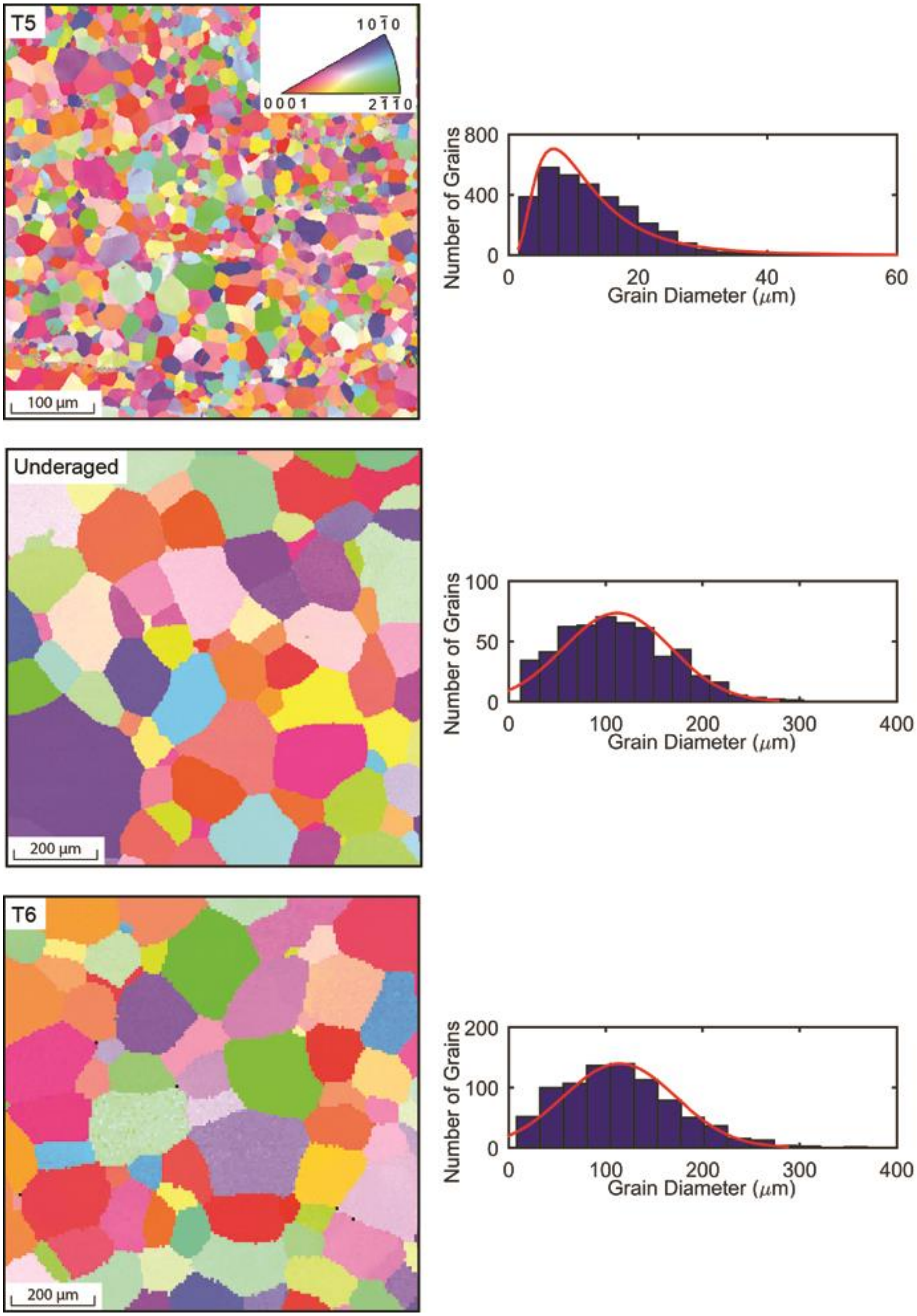

Figure 3.1: Characteristic microstructures and grain size distributions of the T5, underaged, and T6 conditions of WE43 magnesium.

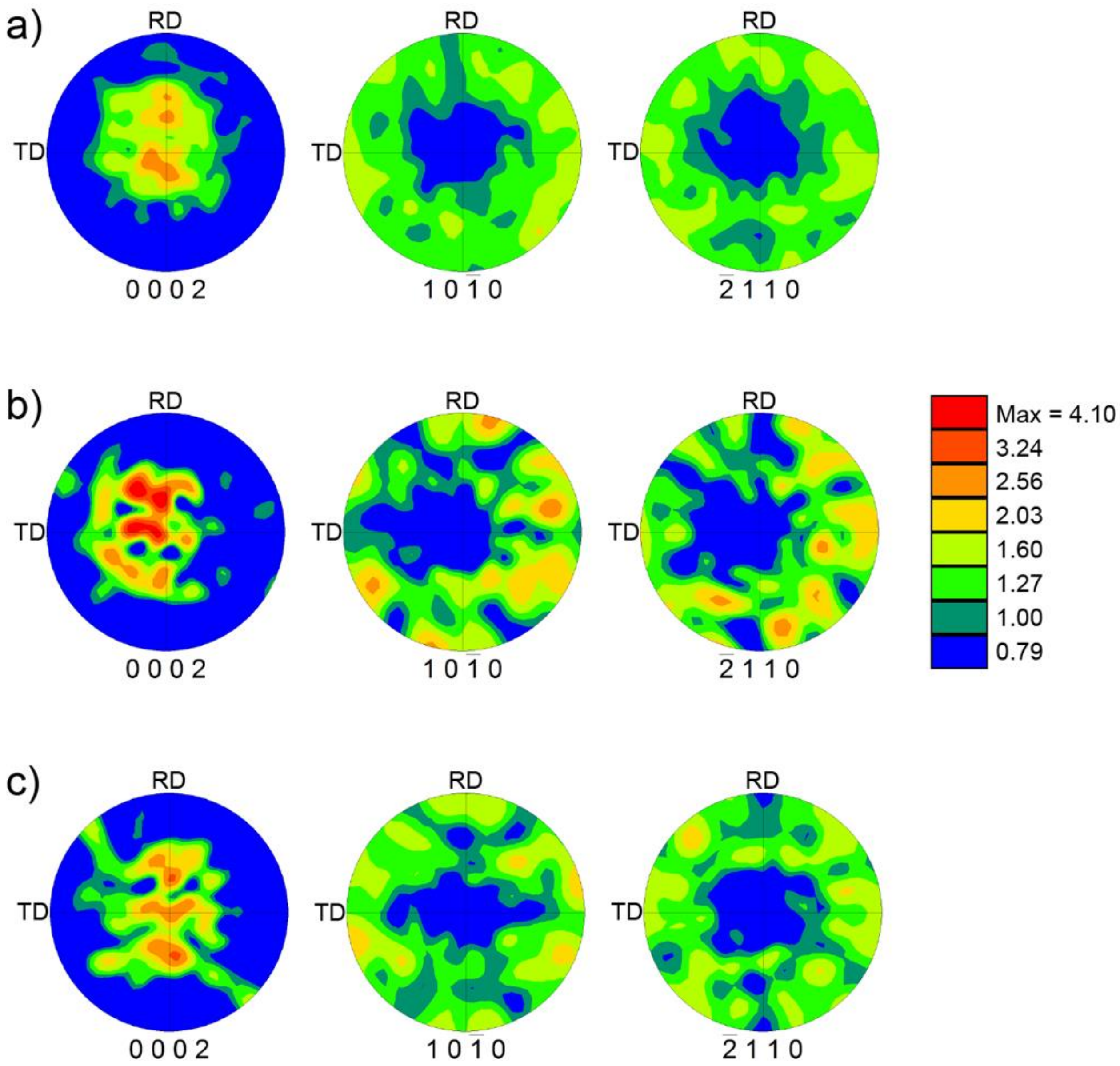

Figure 3.2: Crystallographic texture maps from the a) T5, b) underaged, and c) T6 conditions of WE43 magnesium showing a clustering of basal poles around the normal direction of the rolled plate.

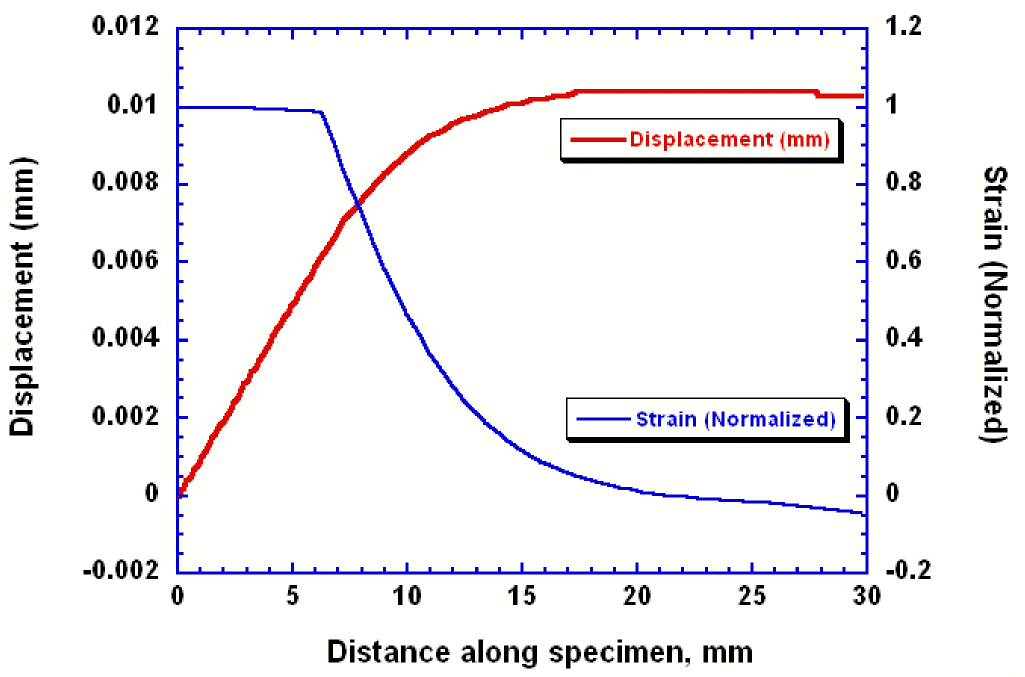

Figure 3.3: A plot of strain and displacement as a function of position along the loading axis of a generic ultrasonic fatigue sample, illustrating the concentration of strain along the gage section [169].

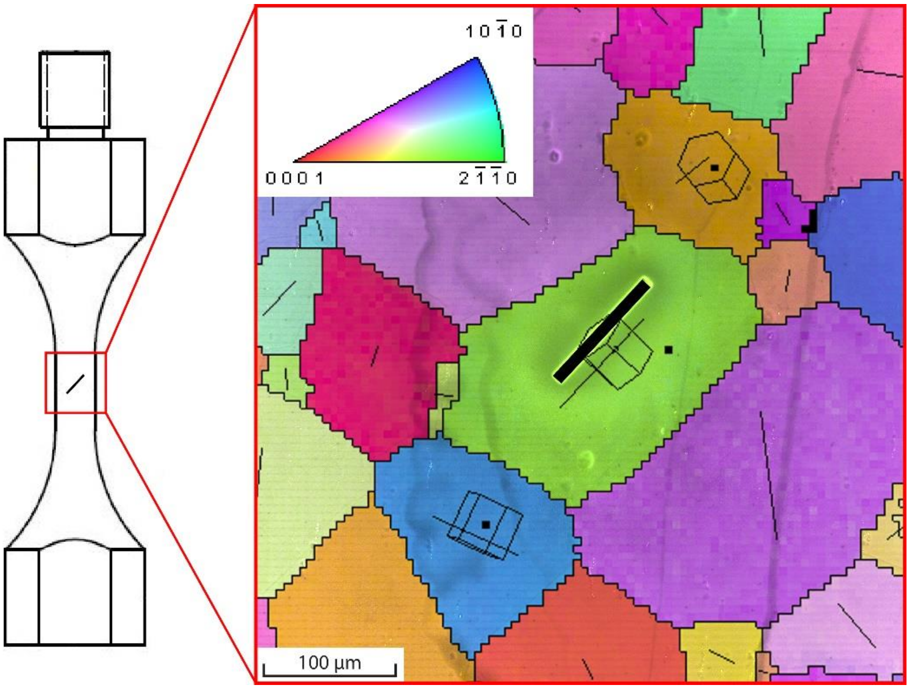

Figure 3.4: Diagram showing placement of focused ion beam notch parallel to basal slip planes. FIB micronotches are used as a crack initiation site in ultrasonic fatigue short crack growth tests.

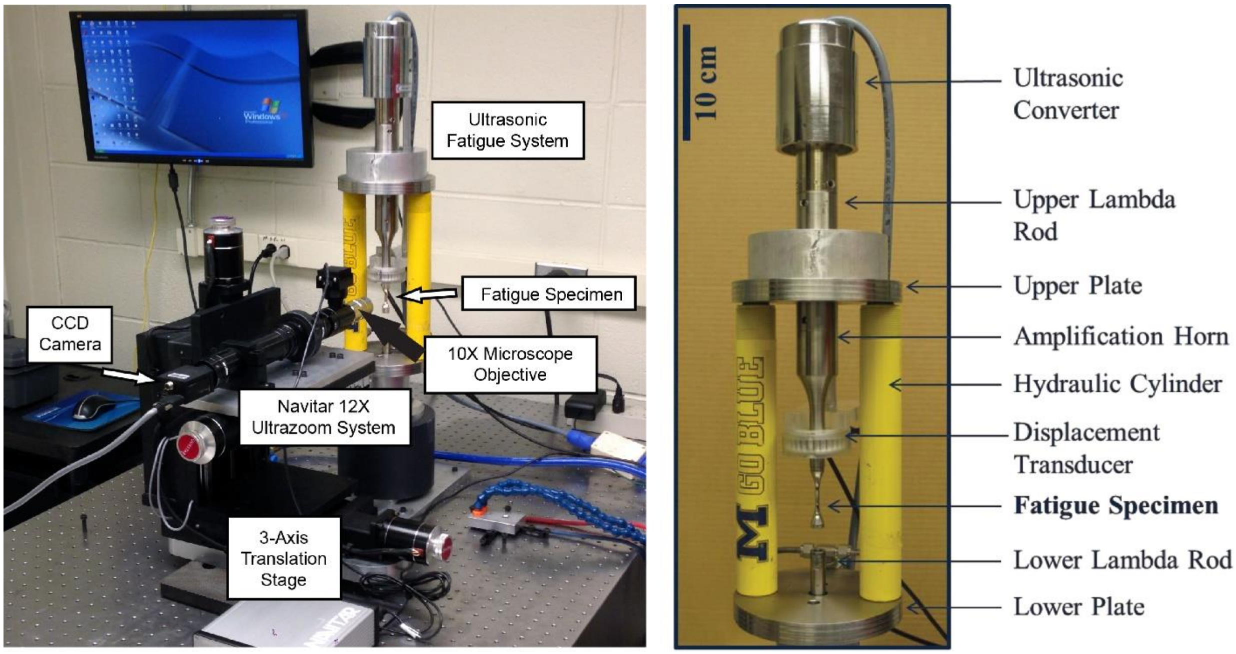

Figure 3.5: Ultrasonic fatigue instrumentation configured for fatigue life and short crack growth tests in laboratory air. The use of hydraulic cylinders allows for testing at positive stress ratios.

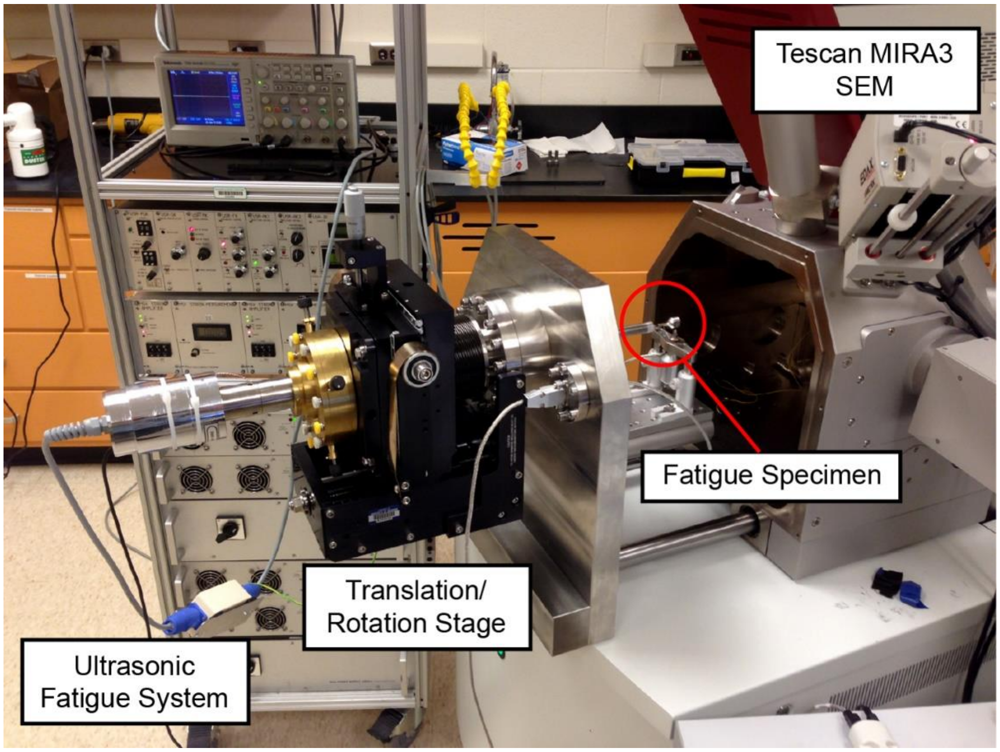

Figure 3.6: Integrated ultrasonic fatigue and scanning electron microscopy system (UFSEM) for *in situ* fatigue investigations and fatigue in vacuum [11].

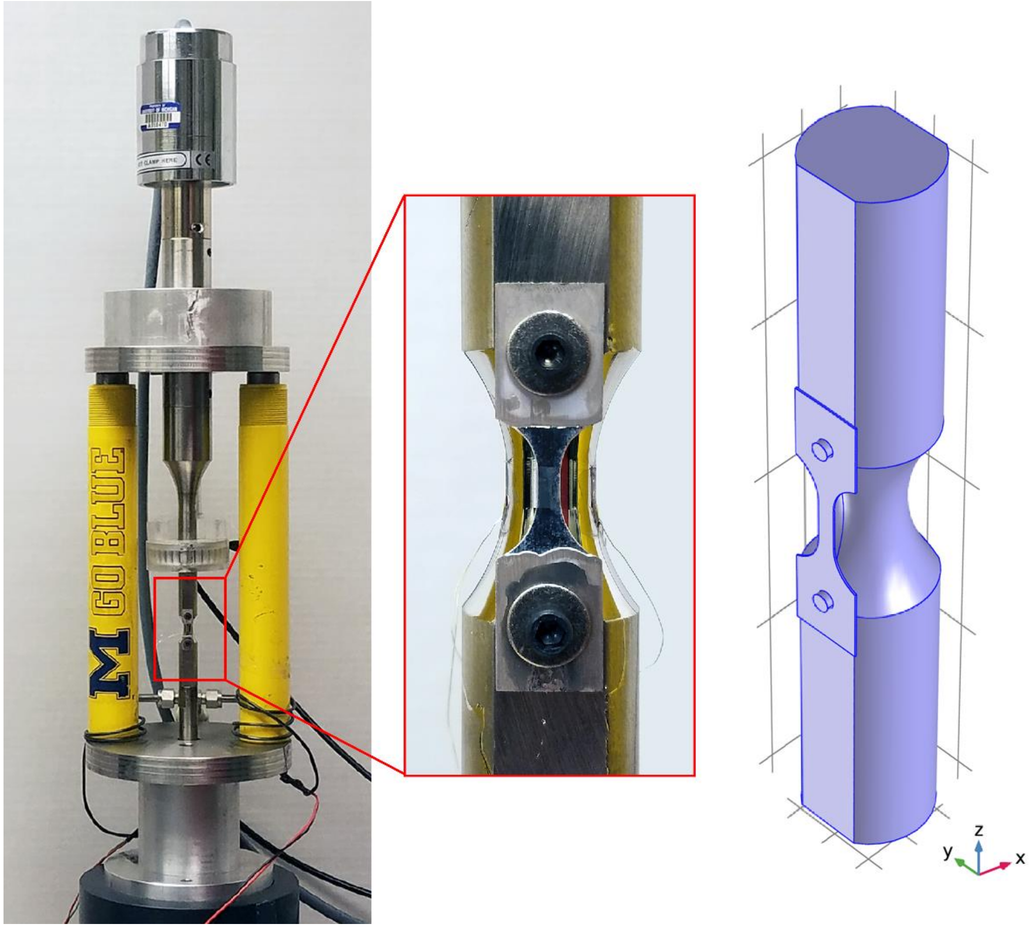

Figure 3.7: Ultrasonic fatigue instrument configured for positive R ratio thin foil short crack growth tests. The foil specimen is attached to the shoulders of the carrier specimen, as detailed in [9].

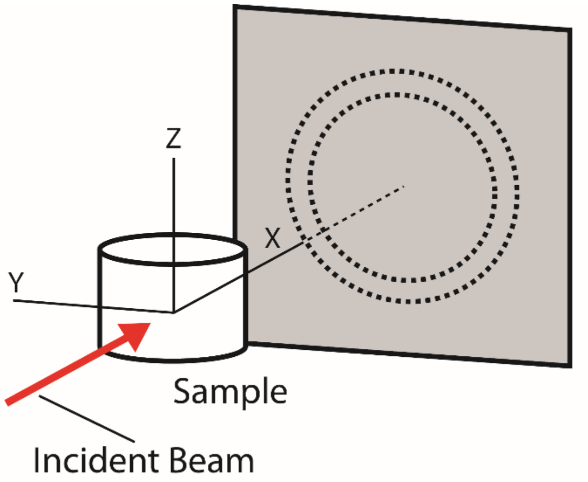

Figure 3.8: Schematic describing the geometry of the far-field high-energy X-ray diffraction experimental setup. The X-ray beam passes through a rotating specimen and produces diffraction spots on a detector, approximately following the Debye-Scherer rings.

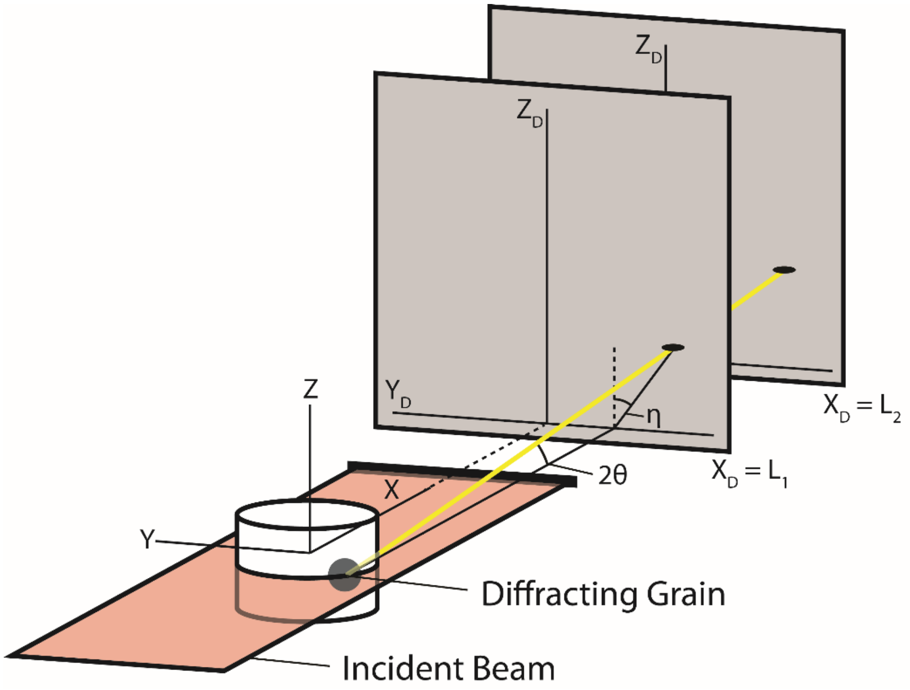

Figure 3.9: Schematic describing the geometry of the near-field high-energy X-ray diffraction experimental setup. The line-focused X-ray beam produces diffraction spots on detectors at two distances. Diffraction spots can then be used to reconstruct the three-dimensional microstructure of the specimen.

CHAPTER 4

THE EFFECTS OF HEAT TREATMENT ON VERY HIGH CYCLE FATIGUE BEHAVIOR

This chapter describes the results of experiments designed to investigate the role of microstructure on crack initiation and short crack growth and subsequent fatigue life in the VHCF regime. Three microstructural conditions were examined: as-received (T5) WE43 with a relatively fine grain size, a solution-treated and underaged condition and a solution treated and peak-aged (T6) condition. The latter two treatments produced a large-grained, precipitation strengthened microstructure. Ultrasonic axial fatigue and scanning electron microscopy techniques (UFSEM) were used to investigate natural crack initiation as well as fatigue crack growth behavior emanating from focused ion beam micro-notches. Crack growth in vacuum was also investigated using the UFSEM system described in Chapter 3. These experiments led to observations and insights into microstructural and environmental influences on both initiation and crack growth in magnesium alloys during ultrasonic fatigue. Section 4.1 presents the characterization of the microstructure and mechanical properties. Section 4.2 provides an overview of specimen preparation, while Section 4.3 describes the results of fatigue life tests for the three heat treatments of WE43. Section 4.4 describes crack initiation behavior from fatigue life tests, and Sections 4.5 and 4.6 present the short fatigue crack growth, including observations on crack path morphology for laboratory air and vacuum. Section 4.7 presents an investigation of fractographic information gathered from both natural crack initiation and short crack growth tests. Section 4.8 presents a discussion of the results of this study and Section 4.9 summarizes the findings.

4.1. Material and Microstructural Characterization

Magnesium alloy WE43 was supplied by Magnesium Elektron Ltd. as hot-rolled plate in the T5 condition. Further heat treatment was conducted in our laboratory to produce underaged and peak-aged (T6) microstructures, specifically solution treatment at 525 °C for 8 hours, followed by aging at 250 °C for 4 hours for the underaged condition and 16 hours for the T6 condition. Grain size was measured by standard methods using electron backscatter diffraction (EBSD) mapping. Solution treatment increased the average grain size from 13 μm in the T5 condition to approximately 113 μm in the underaged and T6 conditions. The three conditions of WE43 exhibit significant differences in mechanical properties (Table 4.1), with the T5 condition exhibiting yield and tensile strengths significantly higher than those of either the underaged or T6 conditions [178].

Table 4.1 - Mechanical and microstructural properties of WE43 Magnesium

Microstructural Condition	Elastic Modulus	Tensile Yield Strength	UTS (MPa)	Percent Elongation	Grain Size (μm)
T5	43.5	265	335	19	13 ± 7
Underaged	43.5	139	235	15	112 ± 55
T6	43.5	159	243	15	114 ± 58

Each condition is primarily strengthened through the development of rare-earth-containing precipitates. Fine β' precipitates are present in the matrix of all three conditions, while coarser β_1 and β_1/ β precipitates are found respectively in the underaged and T6 conditions as plate-like structures along prismatic planes [184]. In order to investigate the strengthening effect of the rare-earth precipitates in the different heat treatment conditions of WE43, hardness testing was conducted using a Hysitron Triboindenter. Nanohardness indents of approximately 1 µm in width were produced using 2000 µN of force in the center of grains, away from grain boundaries to reduce the effects of grain boundary strengthening. Significant differences in matrix hardness were observed for the three heat treatment conditions (Table 4.2), although not as significant as observed differences in macroscopic tensile properties (Table 4.1), indicating that both precipitation strengthening and grain size effects contribute to the notable difference in mechanical properties. The difference in hardness observed between the peak-aged and T5 conditions indicates that residual deformation in the T5 condition may also contribute to observed differences in mechanical properties.

Table 4.2 - Hardness of WE43 magnesium conditions as measured using nanoindentation

Microstructural Condition	Hardness (GPa)
T5	1.58 ± 0.10
Underaged	1.35 ± 0.22
T6	1.19 ± 0.14

The crystallographic texture of each treatment was investigated using EBSD and detailed in Chapter 3. Each of the three conditions featured a medium strength basal texture, with 2.90, 4.10, and 3.35 multiples of random distribution (m.r.d.) observed in the T5, underaged, and T6 conditions respectively. Basal poles were aligned perpendicular to the rolling plane, parallel to the normal direction of the plate.

4.2. Specimen Preparation

Cylindrical fatigue specimens with a reduced gage section 4 mm in diameter and 7.5 mm in length were prepared with the longitudinal axis of the specimens aligned with the rolling direction of the WE43 plate. These cylindrical specimens were utilized to interrogate fatigue life in each heat treatment condition of WE43. For the investigation of short crack growth, diametrically opposed surface flats were machined into the gage sections of cylindrical specimens to allow tracking of fatigue crack growth and crystallographic analysis using EBSD. Specimen surfaces were prepared by grinding with SiC paper and polishing with diamond solution, followed by electropolishing. The majority of fatigue life specimens were prepared by a combination of low stress grinding and electropolishing, although some were prepared by low stress grinding only. Specimen design and preparation is detailed more completely in Chapter 3. Specimen drawings can be found in Appendix A.

To investigate short crack growth behavior, micro-notches were machined in the gage flats to act as crack initiation sites using an FEI Quanta 200 3D focused ion beam (FIB) equipped with a gallium ion source operating at 30kV and a probe current of 5.0 nA. Notches were machined perpendicular to the loading direction at the centerline of the specimen and each had a length of 100 µm, a width of 6 µm, and an approximate depth of 40 µm. In order to maximize the amount of data gathered from each test, three notches, centered about the midsection of the gage length and separated by a distance of 2 mm, were machined in most specimens.

4.3. Effect of Heat Treatment on Fatigue Life Behavior

To investigate the low stress, long life regimes where microstructure features dominate fatigue life, ultrasonic fatigue testing was used to perform both fatigue life studies and small crack growth measurements in a practical time frame. Fatigue life behavior was determined using ultrasonic fatigue instrumentation described in [9], operating at a testing frequency of approximately 20 kHz and at a stress ratio of R = -1 at room temperature in laboratory air. Intermittent cycling was used to minimize the heat generation associated with high frequency loading. Contact thermocouples were used to periodically measure the temperature of the specimen, and forced-air cooling was used to maintain the temperature below 35° C. Fatigue life specimens were cycled until failure or to 10^9 cycles, which was considered a runout. In a number of cases, underaged and T6 specimen runouts were stepped in increments of 10 MPa to make efficient use of specimens. Failures resulting from step tests were tracked separately and fatigue results both with and without step tests were analyzed.

The fatigue lifetime data for the three heat treatments of WE43 examined in this work are shown in Figure 4.1. For the underaged and T6 conditions, step tests were performed in an attempt to characterize the high-scatter, long-life portions of the fatigue life curve characteristic of the VHCF fatigue regime. Test runouts and fatigue failures from these step tests are marked in Figure 4.1. The T5 curve includes specimens with either low-stress ground only or low-stress ground plus electropolished surfaces, while all underaged and T6 fatigue specimens received a final electropolish. Surface preparation appeared to play no role in fatigue life, even though all failures initiated at surface sites for the T5 condition. In the underaged and T6 conditions, 4 of 16 fatal cracks initiated at subsurface sites with subsurface initiation occurring in the lower stress, longer life regime (Table 4.3). The fatigue strengths at $N = 10^9$ cycles are 110 MPa for the T5 condition and 65 MPa for both the underaged and T6 conditions. In each condition, the S-N curve appears to have a generally continuously decreasing trend without a horizontal asymptote. The fatigue ratios (σ/σ_{UTS}) for the T5, underaged, and T6 conditions at 10^9 cycles are 0.33, 0.28, and 0.27, respectively. Ogarevic and Stephens have reported that the fatigue ratio at $N=10^8$ cycles for wrought magnesium alloys in fully reversed loading at conventional frequencies was between 0.25 and 0.5, with higher ratios for higher strength alloys [185]. These results indicate that each of the three conditions of this alloy feature fatigue strength ratios at the lower end of this previously reported range.

Table 4.3 - Subsurface fatigue life failures

Microstructural Condition	Maximum Stress (MPa)	Lifetime
Underaged	75	8.91×10^7
Underaged	85	7.34×10^7
T6	75	2.61×10^7
T6	85	6.47×10^7

The underaged and T6 conditions exhibited nearly identical fatigue behavior, with both conditions having approximately 40 MPa lower fatigue strength than the T5 condition. This strongly suggests that the increase in grain size for the underaged and T6 microstructure and changes in precipitate structure for both conditions from the T5 condition exert more influence on fatigue life than the modest differences in precipitate structure between the two aged conditions. This raises a key question as to whether these differences in fatigue life can be attributed to differences in short crack growth rates and/or crack initiation lifetime. These possibilities are addressed in the studies described in the following sections.

4.4. Crack Initiation Behavior

Fatigue crack initiation sites produced in the un-notched fatigue life specimens were examined by fractography using the Tescan Mira3 SEM to better understand the role of microstructure in crack initiation. Additionally, the spatial orientation of fracture facets present at or near crack initiation sites was characterized using a quantitative tilt fractography technique described in detail in [140], which is based on the photogrammetric analysis of two fractographs of a facet taken at two different tilt angles.

4.4.1. Surface Crack Initiation

For fatigue failures in the T5 material, shown in Figure 4.1, all specimens failed from surface initiated cracks and in almost all cases, facets were found at or near the initiation site (Figure 4.2a,b). These facets were occasionally characterized by roughness on the fatigue facet surface (Figure 4.2a). However, many smooth, featureless facets were also observed (Figure 4.2b). Chemical analysis (energy-dispersive spectrometry, or EDS) showed no presence of oxide films or other inclusions at these sites, indicating that the surface roughness may be the result of crack face contact during fully reversed loading. In addition to large single facets, groupings of multiple favorably oriented facets were also observed at initiation sites in samples from the T5 condition. Two of ten initiation sites had no facets associated with them. Again, chemical analysis of these sites showed no presence of oxides or inclusions. Rough surfaces were observed on both faceted features and non-faceted features.

Evidence of other non-fatal crack initiation sites were observed on the surfaces of failed T5 fatigue specimens, but the cyclic damage and fatigue crack propagation had not progressed beyond one or two grain diameters. These very short non-fatal cracks occurred both away from grain boundaries (Figure 4.2d), and at or very near grain boundaries (Figure 4.2c), with the latter locations dominating. Non-fatal cracks initiated at or near grain boundaries either arrested at triple points or propagated through triple points into neighboring grains along predominantly basal crystallographic slip planes. Cracks that initiated in grain interiors formed through slip accumulation along predominantly basal crystallographic planes, and often arrested at grain boundaries.

Crack initiation behavior in unnotched fatigue specimens in the underaged and T6 conditions was essentially identical, with both surface and sub-surface initiation observed for fatal cracks in both heat treatments. Large facets were present at most surface crack initiation sites (Figure 4.3). In contrast with the T5 condition, faceted surface initiation sites in the coarse-grained conditions were always limited to a single initiating feature, and in some cases, the initiation site could be narrowed to only a portion of a single facet (Figure 4.3a,b). In these cases, micro-beach marks, discussed in Chapter 6, and other indicators of crack propagation were used to identify the region of initiation. Very short non-fatal cracks along grain boundaries were generally observed to lie along curved boundaries, and to only propagate along a portion of that boundary before growing tangentially into the grain interior along a crystallographic slip plane (Figure 4.3c). Although transgranular slip was occasionally observed, no non-fatal cracks were observed that initiated along those slip planes away from grain boundaries.

The projected diameters and orientations (angle of the plane normal relative to the loading direction) of facets found at or near the initiation sites for the T5, underaged, and T6 condition fatigue life specimens were analyzed and the results are shown in Figure 4.4. The largest facet dimension was larger than the average grain diameter for the majority of the facets that were measured. For the T5 condition, these facets were generally oriented for high resolved shear stress, with plane normals forming an average angle of 48° ± 10° with the loading direction (Figure 4.4a). Figure 4.4b shows projected diameters and orientations for initiating facets in the coarse-grained heat treatment conditions. In these conditions, approximately sixty percent of the facets were larger than the average grain size at their largest dimension and exhibited an average size of 155 ± 84 µm. Their orientations, while still favorable for slip, tended to lie closer to the generalized fracture plane with an average angle of 34° ± 9° formed between facet normals and the load direction.

4.4.2. Subsurface Crack Initiation

In the coarse-grained underaged and T6 conditions, four of sixteen fatigue samples failed by subsurface crack initiation and subsequent fatigue crack growth (Figure 4.1). Subsurface initiation occurred only at the lowest stresses (75 and 85 MPa) at relatively long fatigue lifetimes ($>10^7$) and even at these low stresses some specimens failed from surface initiated fatigue cracks. The measured fatigue lives from specimens with subsurface initiation sites was not significantly different from specimens that failed by surface-initiated cracks. As noted previously, subsurface initiation was absent in the T5 condition, at all stress levels and lifetimes investigated. Interestingly, the features associated with subsurface initiation and early fatigue crack growth are quite similar to the fracture surface morphology observed in crack propagation tests in vacuum (Figure 4.10), as presented in Section 4.5.2.

Typical examples of subsurface crack initiation sites are shown in Figure 4.5. The region of initiation and very early crack growth was characterized by a relatively planar fracture surface, with surface roughness on facets (Figure 4.5a). At each initiation site, a single initiating feature could not be identified, although large facets were found at each initiation zone. Occasionally, multiple large facets were found grouped in formations with high relative tilt (Figure 4.5b) or with very similar orientations, forming a "superfacet" (Figure 4.5a). These facets exhibited both smooth, relatively featureless surfaces and surface roughness characteristic of fatigue crack growth in vacuum. Facets measured at subsurface initiation sites exhibited an average projected diameter of 177 ± 87 μm, well above the average grain size of 114 μm in the underaged and T6 conditions. Subsurface facets are oriented for high resolved shear stress, with plane normals forming an average angle of 44° ± 10° with the loading direction (Figure 4.4c).

On average, subsurface facets were slightly larger than those present at surface initiation sites and were oriented slightly more favorably for high resolved shear (e.g., 44° versus 34°).

4.5. Fatigue Crack Growth Behavior

To allow for the study of short crack growth behavior in WE43 magnesium, FIB machined micronotches were centered about the gage midsection to act as crack initiation sites. In the work in this chapter, no attempt was made to locate the notch tips in specific microstructures, and therefore, potential notch tip initiation sites sampled a variety of microstructural neighborhoods. Notch tip microstructural neighborhoods were characterized prior to fatigue using EBSD. Crack growth tests were conducted at a frequency of approximately 20 kHz and at a stress ratio of R = -1 at room temperature in laboratory air, with a constant maximum stress of 85 MPa, which, assuming the notch to be a sharp crack, produced an initial stress intensity factor, ΔK, of 0.75 $\mathrm{MPa \cdot m^{1/2}}$. Observations of fatigue crack growth were made using a Navitar 12x Ultrazoom lens system equipped with a 10x Mitutoyo infinity corrected objective and a 5-megapixel CCD (Point Grey GRAS-50S5C). Cycling was paused every 25,000 to 30,000 cycles to observe fatigue damage and crack progression, and to capture micrographs for calculation of crack growth rates. Stress intensity factors were calculated using the equations of Newman and Raju [180] for a surface crack in a finite elastic plate, where c/a was assumed to be unity. Fatigue crack growth rates were calculated using a seven-point sliding polynomial method [179].

Selected short crack growth tests were performed using the UFSEM system in both laboratory air and in vacuum at pressures at or below 2.8×10^{-3} Pa. UFSEM tests in laboratory air were conducted using the UFSEM load frame external to the SEM to allow rapid insertion of the entire system in the SEM without the need to remove the specimen from the ultrasonic fatigue instrument. This greatly facilitated high resolution examination of the crack progression through the microstructure. In situ crack growth tests (SEM vacuum of 2.8 x 10^{-3} Pa) were run at a constant maximum stress of 85 MPa in most cases. Cycling was paused every 4,000 (1 pulse) to 400,000 (approximately 100 pulses) cycles, depending on fatigue crack growth rate, to observe fatigue damage and crack progression, and to capture micrographs for subsequent determination of crack growth rates.

4.5.1. Fatigue Crack Growth in Laboratory Air

The crack growth behavior of the three microstructural conditions of WE43 is shown in Figure 4.6 for tests conducted in laboratory air using FIB micronotched specimens. In the two coarse-grained microstructures there were significant fluctuations in crack growth rates, especially at ΔK less than approximately 1.5 MPa·$m^{1/2}$, and observed behaviors included significant dips in crack growth rate and occasional crack arrests that are likely associated with microstructural features like grain boundaries. In the T5 condition, crack growth rates were relatively unaffected by local microstructure, exhibiting few resolvable crack arrests or fluctuations in crack growth rate. It should be noted that such fluctuations are much more difficult to detect in fine grain materials, as significantly more crack length measurements must be made to resolve changes in crack growth rate over such small distances, and the limit of resolvability in cycle count between measurements is controlled by the ultrasonic pulse length, with a lower bound of approximately 4000 cycles in these tests. Above 1.5 MPa·$m^{1/2}$ average crack growth rates for the three conditions converge to between approximately $1\cdot10^{-9}$ and $6\cdot10^{-9}$ m/cycle.

4.5.2. Fatigue Crack Growth in Vacuum

As subsurface crack initiation and growth essentially occur in vacuum, crack growth tests were conducted in a vacuum environment to explore potential differences in subsequent short crack propagation rates between internal initiation (vacuum) and surface initiation (air) and to investigate possible differences in fatigue behavior. The UFSEM system was used to provide the vacuum environment for a fatigue crack propagation study where periods of growth were alternately in vacuum or in air. In vacuum, stress amplitudes matching those used in laboratory air experiments (85 MPa) resulted in either crack arrest, significantly lower crack propagation rates, or minimal crack propagation leading to crack arrest (Figure 4.7). In general, crack growth rates in vacuum were nearly two orders of magnitude lower than in laboratory air. When periods of crack growth in air were followed by testing in vacuum, an immediate and significant decrease in crack propagation rate occurred. Following a return to laboratory air, crack growth resumed as if uninterrupted. Increased stress amplitudes (100 MPa) in vacuum testing were used to propagate cracks previously grown to multiple grain diameters in laboratory air at 85 MPa. Again, crack propagation rates were significantly lower in vacuum than those observed in laboratory air, even for cracks propagated in air at lower stress amplitudes.

4.6. Surface Crack Path Observations

The microstructural dependence of fatigue crack paths was studied using two approaches. The fatigue crack paths on the electropolished surface flats of the micronotched specimens were characterized from their initiation at the crack tip through their growth to final failure. EBSD was used to determine if crack paths favored specific crystallographic paths in individual grains. This was done by comparing the surface crack path with slip traces for particular slip systems.

Finally, fractography was used to characterize the fatigue fracture surface morphology as the crack propagated from the micro-notches or the natural initiation sites to final failure.

4.6.1. Characterization of Fatigue Crack Growth in Relation to Microstructure

Crack paths were investigated on specimen surfaces by correlating SEM images of the crack with EBSD scans of the local microstructure collected before fatigue testing. In each condition, surface crack propagation was found to be a mix of crystallographic transgranular growth predominantly along basal planes and non-crystallographic transgranular growth. Intergranular growth was only observed occasionally. Examples of crack path profiles for the three conditions are shown in Figure 4.8. In each condition, cracks tended to reorient at grain boundaries to follow favorable crystallographic planes, often resulting in deflection of the crack path away from the macroscopic crack plane. In the T5 condition, as a result of the fine grain size, these deflections at grain boundaries resulted in only short departures of the crack from the generalized crack plane. In the underaged and T6 conditions, the larger average grain size resulted in more significant departures from the macroscopic crack plane.

4.7. Fractographic Analysis of Fatigue Cracks

SEM fractographic examination was used to further investigate the effect of microstructure on crack growth behavior in both laboratory air and vacuum environments. An overview of a typical fracture surface for a T5 failure that propagated from a micronotch in laboratory air is shown in Figure 4.9a, where the early, intermediate and later crack growth regions of interest are indicated. In the region nearest the FIB micro-notch, transgranular facets are in evidence, as illustrated in Figure 4.9b. At an intermediate crack length ($1.8 \text{ MPa}\cdot\text{m}^{1/2} < \Delta K < 3.4 \text{ MPa}\cdot\text{m}^{1/2}$), the relatively featureless crack surfaces transitions to a rough region, characterized by transgranular propagation and the general absence of facets. In this region, evidence of parallel features indicative of tearing and shear on the order of the grain size are present (Figure 4.9c). At $\Delta K > 3.4$ MPa·m$^{1/2}$, this second region transitions to a flatter noncrystallographic transgranular morphology (Figure 4.9d). As expected, the early crack growth region (nearest the notch) exhibited the same features as those found near the natural initiation sites for surface initiated failures in laboratory air. A clear difference was observed between the morphology of fracture surfaces corresponding to fatigue in laboratory air and those corresponding to fatigue in vacuum, leading to the question of whether fatigue crack propagation from a micronotch in an in situ UFSEM test would yield fracture features similar to those observed from subsurface initiated fatigue cracks. To examine this further, a test was conducted where crack initiation and early propagation was conducted in laboratory air followed by further crack propagation under vacuum in the SEM.

Figure 4.10 shows a scanning electron micrograph of a short fatigue crack growth specimen that was first fatigued in laboratory air with a maximum stress of 85 MPa. Crack growth was continued in vacuum with an increased maximum load of 100 MPa. A clear transition between two fracture surface morphologies is visible. While fracture surfaces from fatigue in laboratory air are generally featureless, regions from fatigue in vacuum exhibit more surface roughness. The effect of environment appears to be immediate, as the fracture surface abruptly changes at the air to vacuum transition and crack growth rates immediately responded to the change in gaseous environment as described in Figure 4.7.

Although fractographic investigation can provide some insight into crack propagation mechanisms, without a record of subsurface crack propagation, it cannot provide information on local crack growth rates. While it is possible in some cases to monitor crack propagation in three dimensions [12,13], it is interesting to note that in the present study regions of the fatigue fracture surfaces for tests conducted in air were often marked with microscopic indicators of crack advancement (Figure 4.11), which we term micro-beach marks. The micro-beach marks can be used to determine local crack growth rates. As shown in Figure 4.11b, these markings correlate directly with the cyclic loading history of the ultrasonic fatigue tests, where the distance between markings is proportional to the number of cycles in a given block of the load history. These periodic features are observed most easily in the large grained underaged and T6 conditions of WE43. In the finer grained T5 condition, the marks are present but more difficult to discern. In contrast to the fracture surfaces from fatigue in laboratory air, micro-beach marks are rarely observed on fracture surfaces corresponding to fatigue in vacuum, and when present tended to be irregular and very faint. Micro-beach marks are similar in appearance to the well-studied fatigue phenomena of macroscopic beach marks or marker bands [12,97,143,186]. A calculation of crack growth rate based on the assumption that each micro-beach mark corresponded to crack growth during a single ultrasonic pulse (approximately 4000 cycles), yielded growth rates on the same order of magnitude as surface-measured crack growth rates for similar stress intensities. Thus, these micro-beach marks record both the location of the crack front on interior grains and allow the determination of short crack growth behavior relative to local microstructural features, including the calculation of local, subsurface crack growth rates in a manner similar to [99]. Figure 4.11 shows a region of markings of varying widths that correspond to sets of alternating long and short pulses used to locate successive crack fronts on SEM micrographs. These features and their use in measuring crack growth rates will be discussed further in Chapter 6.

4.8. Discussion

Fatigue strength of three heat treatments (T5, underaged, and T6) of WE43 Mg alloy in the VHCF regime scaled with yield and tensile strength in a manner similar to the behavior observed by others in the LCF and HCF regimes for similar Mg alloys. In general, fatigue lifetimes in the VHCF regime are controlled by crack initiation and short crack growth. In this work, since average short crack growth rates (da/dN) did not differ significantly for any of the three heat treatment conditions, and we, therefore, conclude that the overall VHCF S-N response arises from differences in fatigue crack initiation lifetimes. For the sake of analysis here, the primary microstructure variation among the three heat treatments is identified as grain size and matrix precipitate structure. The solution treatment applied to the as-received T5 alloy to produce the underaged and T6 microstructures increased the grain size by an order of magnitude (nominally from 13 μm to 113 μm), as well as affecting matrix precipitate structure. While a detailed analysis of precipitate structure, size, and volume fraction in the three conditions is beyond the scope of the present work, the role of microstructure variation on fatigue life can be inferred from the fractographic observations and related analyses. In the remaining discussion we examine the nature of fatigue crack propagation and initiation and the likely influences of grain size and matrix precipitate structure on fatigue lives of the three heat treatments of WE43 examined in this study.

4.8.1. Crack Growth Behavior

Although local variability in short fatigue crack growth rate was more evident in the coarse-grained microstructures, especially for ΔK less than 1.5 $\mathrm{MPa \cdot m^{1/2}}$, the average crack growth rates for the three heat treatments are similar and cannot explain the significant differences in S-N fatigue life behavior between the T5 condition and the two solution treated and aged microstructures. This is best shown by using the fatigue crack growth data to estimate fatigue lives when crack initiation lifetime is assumed to be zero. If fatigue crack behavior is assumed to follow a power law equation of the form shown in Equation 4.1, the constants *C* and *m* can be determined from a least-squares fit of crack growth data (Figure 4.6). Integration of Equation 4.1 then provides an estimate of the number of cycles to propagate a crack (propagation life) as a function of crack length (Equation 4.2), with a_i and a_f representing initial and final crack lengths respectively.

$$da/dN = C\Delta K^m \qquad [4.1]$$

$$N_{Prop} = \int_{a_i}^{a_f} \frac{\Delta K^{-m}}{C} da \qquad [4.2]$$

A representative power law equation was determined by fitting the average short crack growth data for all three conditions at ΔK values higher than 1.5 $\text{MPa}\cdot\text{m}^{1/2}$, where crack growth rates for the three conditions converged, resulting in coefficients of $C = 2.88\cdot10^{-10}$ m/cycle and $m = 2.49$. In using equation 4.2 to estimate the propagation lifetime, initial crack lengths were taken to be half the average grain size for each heat treatment condition which is 6 µm for the fine-grained T5 and 56 µm for the coarse-grained underaged and T6 conditions. A final crack length of 2 mm (half the diameter of the ultrasonic fatigue specimen) was used for all calculations. The resulting estimates in Figure 4.12 show that fatigue lives in the VHCF regime are much longer than those that would occur if crack propagation were the dominant factor. This leads to the conclusion that the VHCF lives are primarily dependent on the number of cycles to initiate a crack on the scale of the grain size. It also suggests that the variability in VHCF lives is due to variability in crack initiation lifetime. The estimates also lead to the possibility that in the

10^5 - 10^6 region, the propagation of short cracks play a significant role in determining the overall fatigue life.

While grain boundaries are well known to often be significant barriers to slip transfer during deformation [115] and grain misorientation has been shown to significantly affect the resistance of boundaries to transgranular fatigue crack propagation [13,117], the influence of grain size on short fatigue crack propagation is not resolved. For example, in a short crack growth study of cast AM60B magnesium, Gall et al. noted that although small cracks interacted observably with microstructural features such as grain boundaries, the quantitative effect on overall crack growth rate was in some cases small [108]. Ravichandran has postulated that coarse-grained materials have a better resistance to fatigue crack propagation as a result of deflections at grain boundaries and the resulting reduction in the effective Mode I stress intensity factor at the crack tip [187]. Others, however, have postulated that the increased number of grain boundaries encountered in fine-grained materials slows crack advancement as compared to coarse-grained materials [67]. Although literature characterizing grain size effects on short crack growth behavior in magnesium are limited, studies in aluminum are more extensive and corroborate the few studies in magnesium. Investigations of the effect of grain size on fatigue crack growth rates by Turnbull and De Los Rios and Zurek et al. showed very similar crack growth rates in aluminum alloys with a wide range of grain sizes [188,189]. Despite this, Turnbull and De Los Rios demonstrated that a smaller grain size still resulted in increased fatigue strength. Similarly, Yue et al. showed that even when fatigue crack growth rates were slower for larger grain sizes in a Mg alloy, fatigue lives were still much greater in a microstructural condition with a finer grain size [190]. Horstemeyer et al. showed that a variation of up to two orders of magnitude in fatigue lives of an AZ91E magnesium alloy were the result of differences in the size of crack nucleation sites [191]. The relevant conclusion from Yue et al. is that the fracture energy and fatigue crack propagation results confirm well-established principles that coarse microstructures, by imposing tortuous crack paths, exhibit higher crack resistance than those microstructures where the crack path is more closely confined to the general crack plane. On the other hand, Horstemeyer et al. show that on the basis of S-N data fine-grained material has a higher fatigue strength than coarse-grained material because of the greater difficulty of fatigue crack initiation and early growth in small grains. Fatigue strength in WE43 followed the trend established by the works of Turnbull, De Los Rios, Horstemeyer et al. and Yue et al. that fatigue strength increased with decreasing grain size, independent of short crack growth behavior. Again, this points to differences in crack initiation being responsible for the observed differences in fatigue life.

4.8.2. Effect of Heat Treatment on Fatigue Life Behavior

Given that only subtle differences in short fatigue crack growth rates were observed for the three alloys and that fatigue lives in the VHCF range must then depend on differences in crack initiation lifetime, it is of interest to consider the role of microstructure on fatigue crack initiation behavior. In the present study both grain size and precipitate structure are modified by heat treatment. It is likely that crack initiation lifetime is affected by both precipitate structure and grain size but quantifying the relative importance of each microstructural feature on fatigue crack initiation is difficult.

In the present study nanohardness measurements in the matrix, away from the influence of grain boundaries, support the hypothesis that differences in yield strength are due mainly to differences in precipitate structure produced in the different heat treatments. It must also be considered that remnant deformation may remain in the T5 condition that may also contribute to strengthening. Precipitation strengthening in WE43 occurs from the precipitation of a fine β' phase [16,184]. β' precipitates are more prevalent in the T5 condition than in the underaged or T6 conditions, which is consistent with the higher strength of the T5 condition [184]. The presence of strengthening precipitates in magnesium has also been shown to have a positive effect on stress-controlled HCF (S-N) fatigue resistance. Studies have shown that, although strengthening precipitates seem to have little effect on short crack growth behavior, consistent with the observation here, they can strongly affect fatigue strength by improving resistance to fatigue crack initiation [65,192]. In a study of an extruded Mg-10Gd-3Y alloy, Liu et al. found that short crack growth behavior was relatively unaffected by heat treatment, but that crack initiation was hindered by hardening effects from β' precipitates [192]. Similarly, in a study of aged AZ61 and AZ80, Uematsu et al. attributed increases in fatigue strength to changes in fatigue crack initiation mechanisms [65].

There is also evidence from the literature that grain size can affect crack initiation behavior. Uematsu et al. and Tsushida et al. have noted a grain size effect on fatigue behavior in magnesium alloys, with decreasing grain size leading to increased fatigue strength and fatigue lifetimes [67,193]. Li et al. noted a significant difference in fatigue strength, between two Mg-Nd alloys of very similar composition and heat treatment, that was linked to a difference in deformation mechanisms in crack initiation resulting from different grain sizes [194]. In the present study crystallographic facets were associated with the initiation sites in both fine-grained T5 and coarse grained underaged and T6 conditions. These facets were in general larger than the average grain size (Figure 4.4), indicating that strain localization along favorably oriented slip planes is likely a precursor to fatigue crack initiation in WE43. In studies of the fatigue behavior of magnesium in the HCF and VHCF regimes, both Li et al. and Shiozawa et al. attributed crack initiation to cyclic slip deformation [81,194]. Cyclic slip is most likely to occur in grains that are both favorably oriented for slip and that maximize the mean free path for slip, i.e. largest possible diameter. Yue et al. have postulated that in initiation dominated fatigue coarse-grained materials perform poorly due to the ease of initiating cracks in larger grains [190]. This is attributed to an increase in the mean free path for slip, relative to finer-grained conditions. This means that Stage I fatigue cracks can grow more extensively into the specimen along crystallographic planes before encountering obstacles like grain boundaries or developing into Stage II cracks. The role of slip length and ease of crack initiation is further amplified by considering that in the fine-grained T5 condition, more than one similarly oriented facet was often observed at initiation sites, which is consistent with other studies in the VHCF regime where the proximity of multiple favorably oriented grains is the key microstructure feature associated with crack initiation [169,195].

4.8.3. Subsurface Crack Initiation

In four of the low-stress VHCF fatigue life tests of the coarse-grained conditions, the fatal crack initiated at a subsurface location. However, the fatigue lives were not significantly different for samples that failed from surface-initiated cracks. In the specimens that exhibited subsurface initiation, crack initiation and propagation are presumably operating in a vacuum environment. It is well established that environment can have a strong effect on both fatigue crack initiation and crack propagation behavior [10,108,196–198]. Indeed, fatigue crack growth conducted in vacuum as part of this study showed significantly reduced crack growth rates or complete arrest. The fracture surfaces at subsurface initiation sites were similar in appearance to fracture surfaces observed in small crack growth tests conducted in vacuum.

Although environment has a clear effect on fatigue crack growth rate, it is unclear if environment plays a significant role in determining crack initiation mechanisms in WE43. Further study is necessary to determine the role of environment on fatigue crack initiation lives in WE43. Subsurface fatigue crack initiation in magnesium alloys has been linked to the presence of grains favorably oriented for slip, with crack initiation occurring through cyclic slip deformation to produce facets at initiation sites [61,199]. It has been noted before that generally as grain size increases, the ease of crack initiation also increases due to the increased mean free path for slip [190]. On average, facets located at subsurface initiation sites are approximately 20 μm larger than those present at surface sites. Additionally, the average orientation of subsurface facets is more favorable for high resolved shear stress (assuming a nominally uniaxial state of stress, which may not generally be the case), with an average inclination of 44° ± 10° as compared to 34° ± 9°. It is expected that the occurrence of subsurface initiation is highly dependent on the microstructure of a given specimen. Given that a large average grain size and associated mean free path for slip favor crack initiation at both surface and subsurface locations, and that surface crack initiation is much more prevalent, it is likely that subsurface crack initiation can only occur when microstructural conditions for slip are optimized at subsurface locations, as in the observed initiation sites. Thus, a competition occurs between microstructural weak links, favored surface crack initiation at large grains that are oriented with moderate favorability for slip versus subsurface initiation at even larger grains that are better oriented for slip. The lack of subsurface crack initiation in the T5 condition is most likely due to the fine-grain structure. The grain size may be too small for subsurface slip to outpace surface crack initiation. Further study is necessary to understand this competition between surface initiation and subsurface initiation, as well as the role environment plays.

In this study, although we observed that fatigue crack growth rates were significantly reduced in vacuum, we also have concluded that crack propagation does not have a major influence on VHCF lifetimes, so this effect is presumably not significant for determining the lifetime of specimens with subsurface initiation sites. The observed differences in crack growth behavior between fatigue in vacuum and fatigue in laboratory air provided insight into the occurrence of subsurface crack initiation in WE43 magnesium. In this work, fatigue in vacuum resulted in crack growth rates one to two degrees of magnitude lower than crack growth rates observed in laboratory air. At comparable stress intensity levels, crack growth essentially halted in vacuum. Furthermore, following the change of environment, no transitional effect was observed in crack growth behavior or on the fracture surface. This indicates that material at the crack tip was immediately interacting with the environment, and that WE43 is highly susceptible to environmental effects. It has been observed in both conventional and ultrasonic fatigue that fatigue behavior in vacuum may vary significantly from that observed in laboratory air in many metals [10,196,198]. Stanzl-Tschegg et al. observed both higher crack growth rates and lower crack growth threshold in a humid air environment as compared to vacuum in a crack growth study of a 2024-T3 aluminum alloy [196], and decreased crack growth rates in vacuum in a 7075-OA aluminum alloy and a Ti-6Al-4V alloy [198]. Geathers et al. observed an extreme effect of environment on short crack growth in Ti-6242S subjected to ultrasonic fatigue, with fatigue in vacuum essentially halting crack growth [10]. Studies of environmental effects on fatigue crack growth in magnesium alloys are limited. Tokaji et al. observed a significant decrease in crack propagation rates in dry air as opposed to laboratory air in magnesium alloys AZ31 and AZ61 [161]. Similar trends were reported in a study of AZ61 cycling in dry air and in a range of relative humidity [162]. Studies of steels [200,201], Superalloys [202], and titanium alloys [70] have shown that generally reduced fatigue lives for surface-initiated cracks as compared to subsurface-initiated cracks are due to the acceleration of surface crack initiation and growth by a laboratory air environment as compared to quasi-vacuum conditions in the interior of the specimen.

4.9. Summary and Conclusions

Axial ultrasonic fatigue tests have been performed on smooth, cylindrical specimens of a hot-rolled WE43 magnesium alloy in laboratory air at ambient temperature using ultrasonic fatigue equipment. The effect of heat treatment on fatigue strength in the very high cycle regime has been discussed in terms of short crack growth and fatigue crack initiation behavior in the T5, underaged, and T6 conditions. Subsurface fatigue crack initiation in underaged and T6 WE43 was investigated. The following conclusions can be made:

- Heat treatment had a significant effect on fatigue strengths at 10^9 cycles for the T5, underaged, and T6 conditions, with values of 110 MPa, 65 MPa, and 65 MPa, respectively. The underaged and T6 conditions exhibited fatigue strengths that were identical and much lower than the T5 condition, which was found to be a result of differences in grain size and the role this played on crack initiation.

- Crack initiation sites exhibited evidence of cyclic strain accumulation as a crack initiation mechanism. Crack initiation sites in each of the three conditions featured large facets oriented for high resolved shear stress.

- Heat treatment had no significant effect on average crack growth rates. Despite local variations in short crack growth rate, average crack growth rates for each of the three conditions were very similar at stress intensities greater than 1.5 $\mathrm{MPa \cdot m^{1/2}}$.

- Crack paths in each of the conditions were strongly affected by local microstructure, with cracks predominantly propagating in a crystallographic transgranular manner. Crack path deflection was observed at grain boundaries in each condition, with larger departures from the generalized crack plane observed in the coarse-grained conditions as a result of the larger average grain size.

- It appears that fatigue lives in the VHCF regime are primarily determined by the number of cycles to initiate a grain size crack. Small fatigue crack growth appears to have no significant effect on fatigue lives in this regime.

Figures

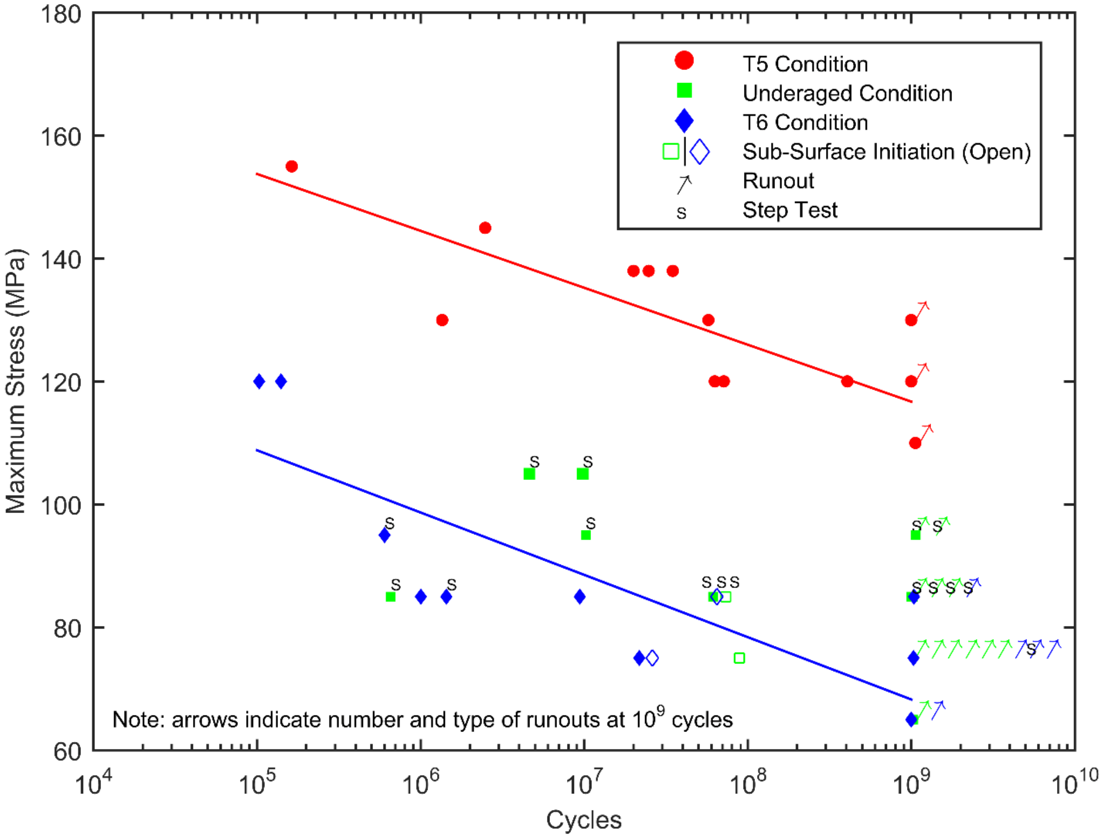

Figure 4.1 - Fatigue lifetime behavior of the three conditions of WE43, with data points from step tests indicated. The similarities between the microstructures of the underaged and T6 conditions result in little difference in fatigue lifetime behavior, which becomes more evident with the inclusion of step tests. Subsurface initiation was observed in the coarse-grained conditions at high lifetimes and is detailed in Table 4.3.

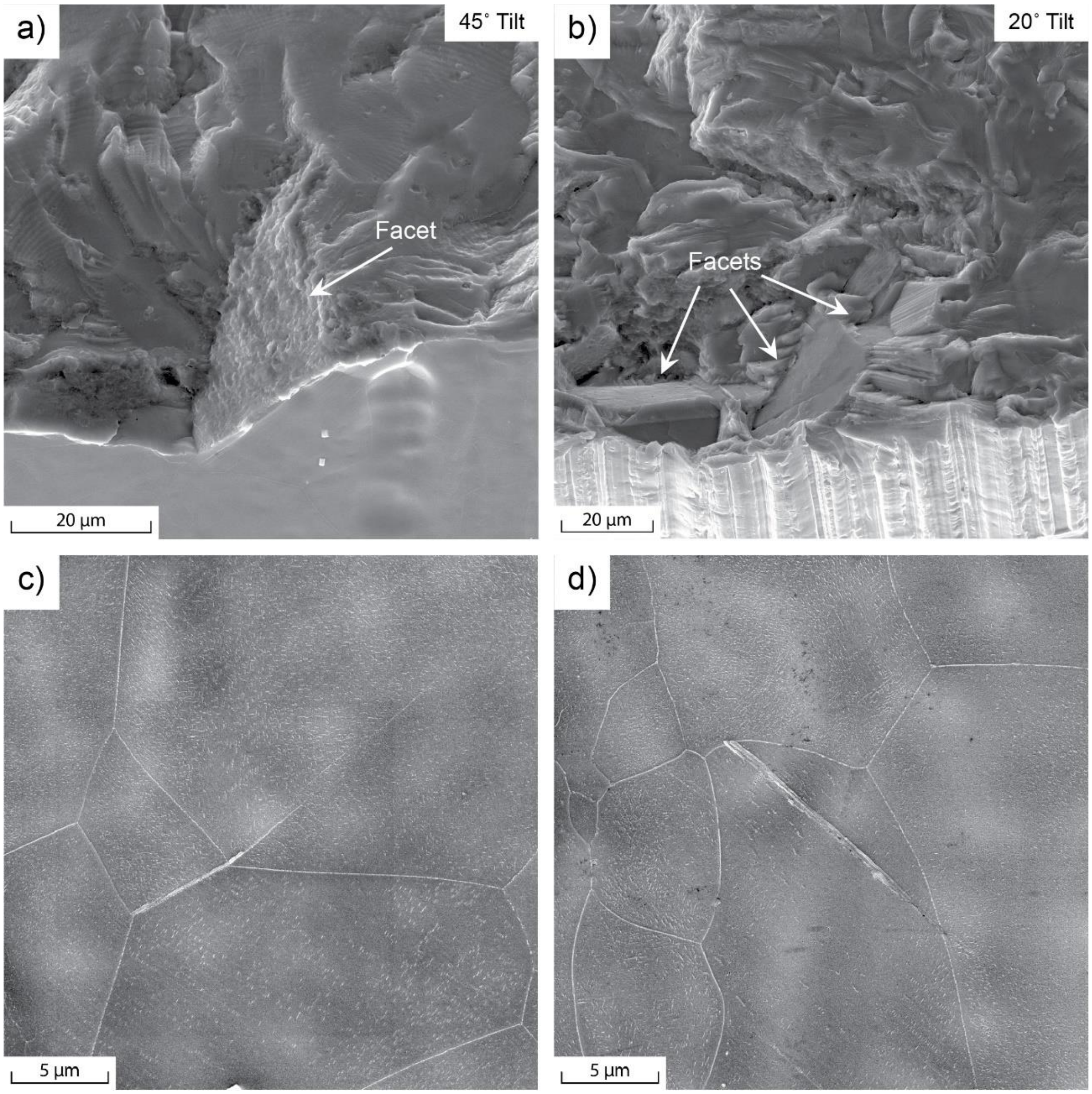

Figure 4.2 - Crack initiation sites in T5 WE43 showing a) single facets, b) groupings of multiple facets, and fatigue damage sites at c) intergranular and d) transgranular locations.

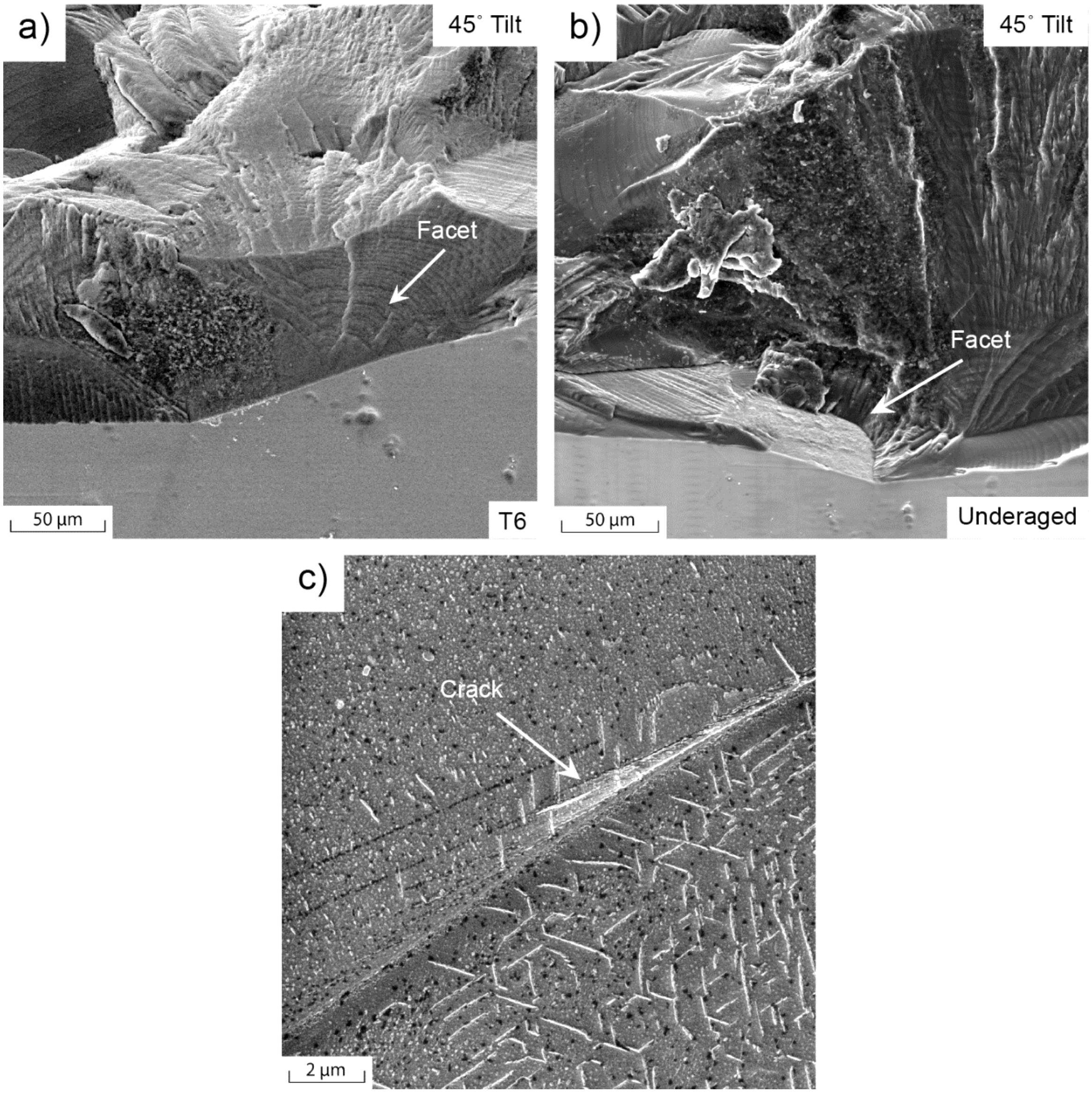

Figure 4.3 - Crack initiation sites in coarse-grained WE43 showing a), b) large single facets, and c) non-fatal crack initiation site at a grain boundary.

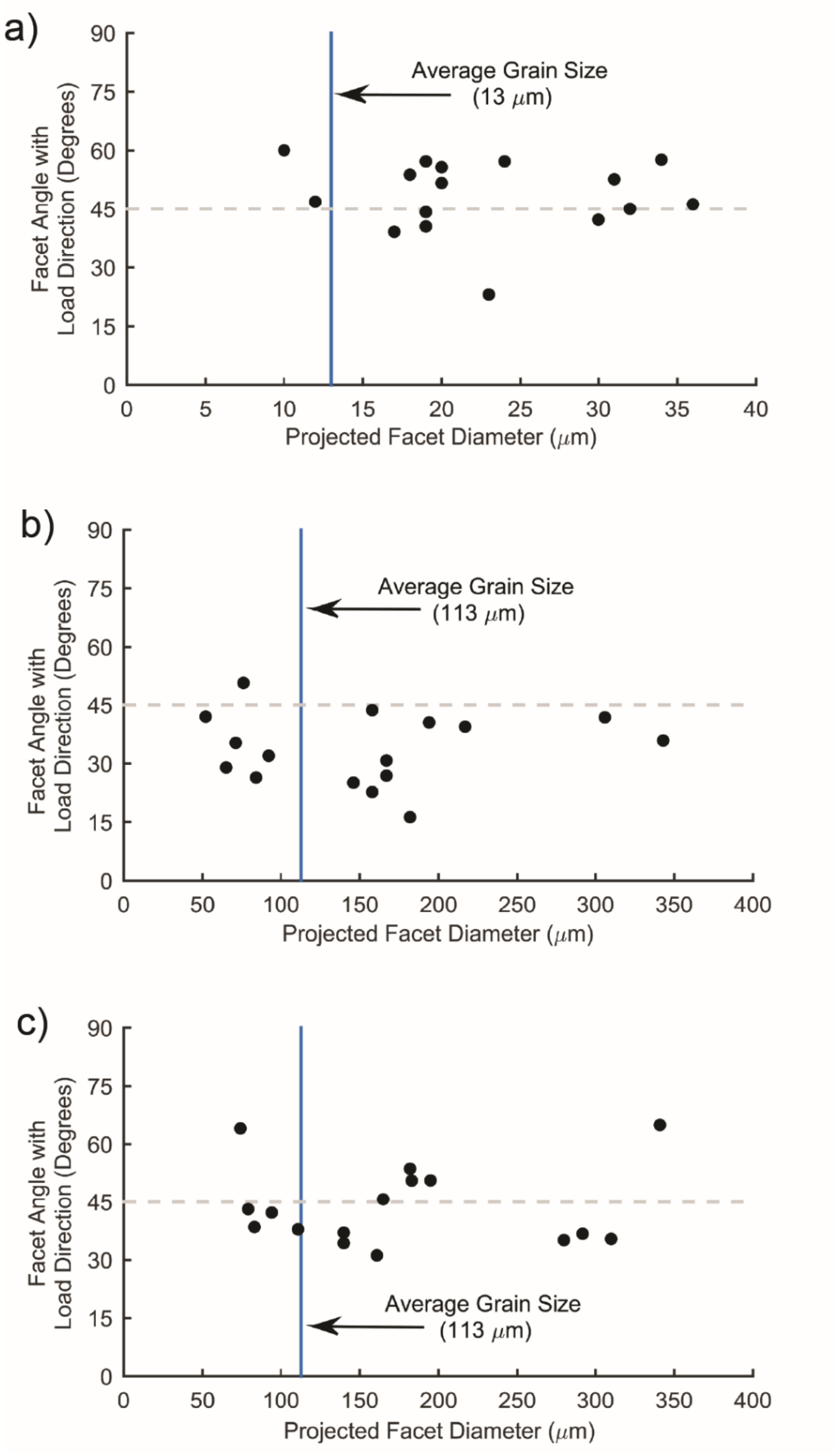

Figure 4.4 - Diameters and orientations (angle of plane normal with respect to load) of facets present at a) T5 surface initiation sites, b) underaged and T6 surface initiation sites, and c) underaged and T6 subsurface initiation sites.

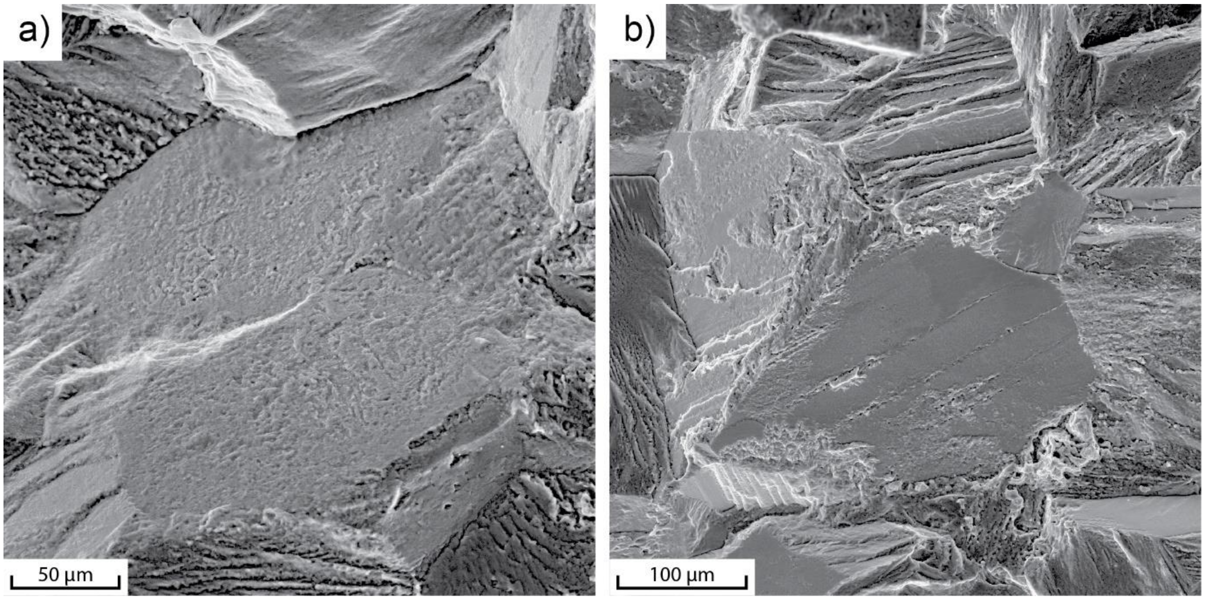

Figure 4.5 – Subsurface crack initiation sites in large-grained WE43 showing a) "supergrain" groupings of facets and b) chevron groupings of facets.

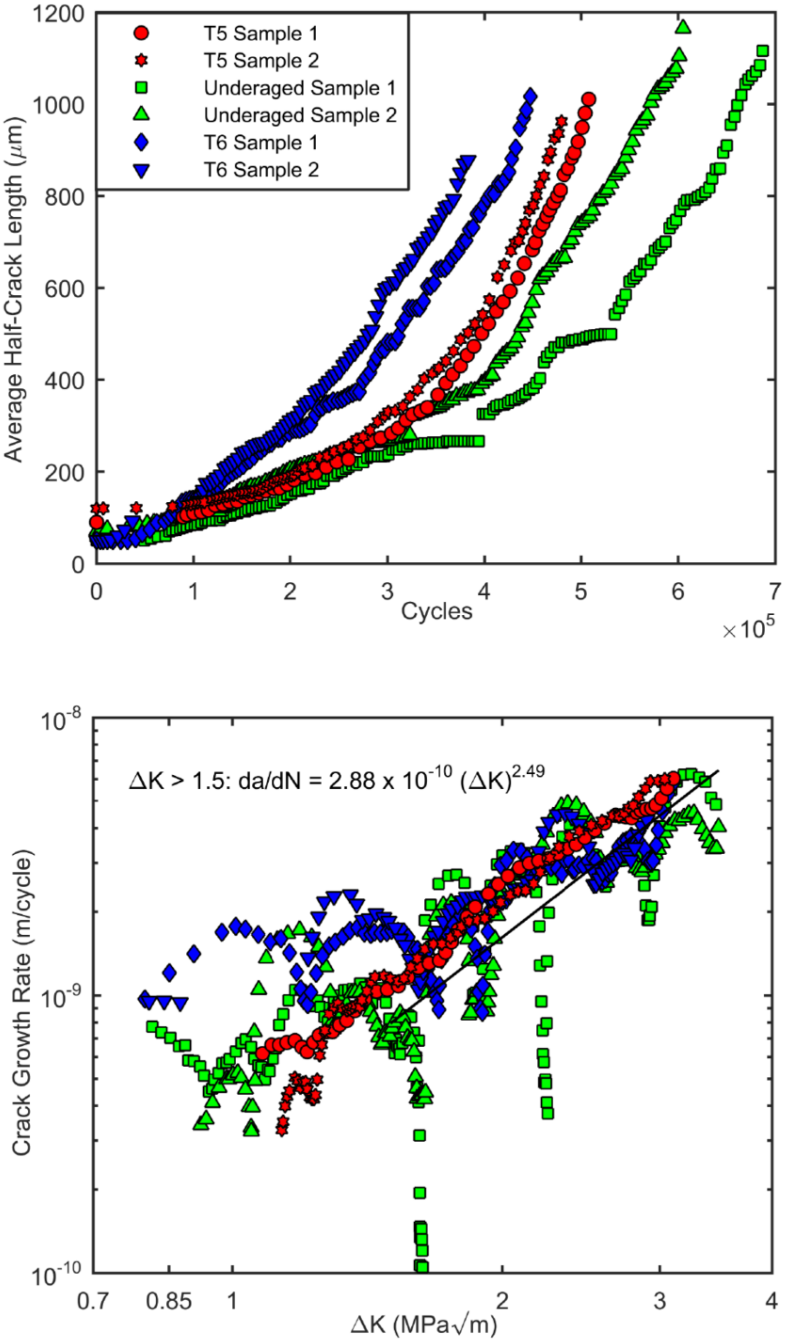

Figure 4.6 - Crack growth behavior in the three conditions of WE43 including a vs. N and da/dN vs. ΔK showing microstructural effects in the underaged and T6 conditions.

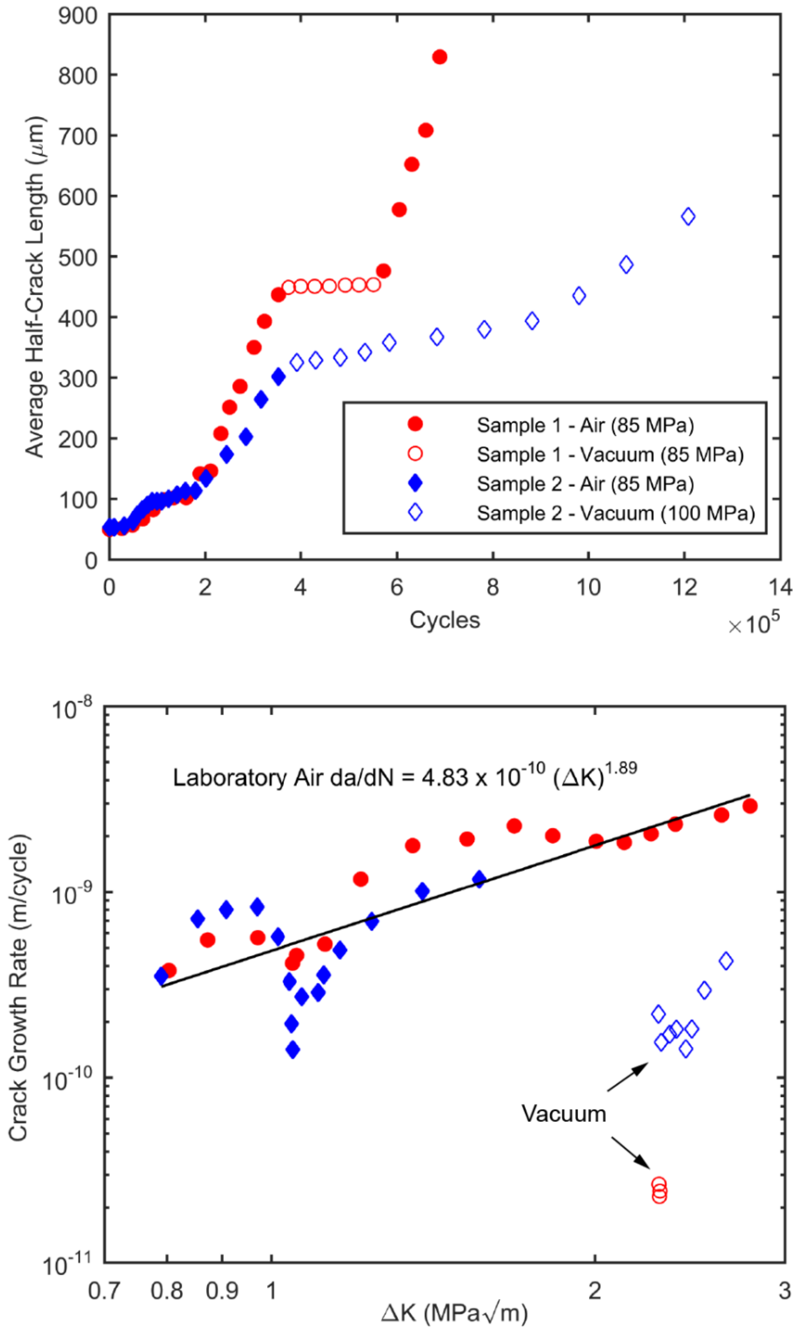

Figure 4.7 - Crack growth of underaged WE43 in vacuum results in crack arrest or significantly reduced growth rates as compared to laboratory air. Environmental transitions show immediate effects on crack growth rate.

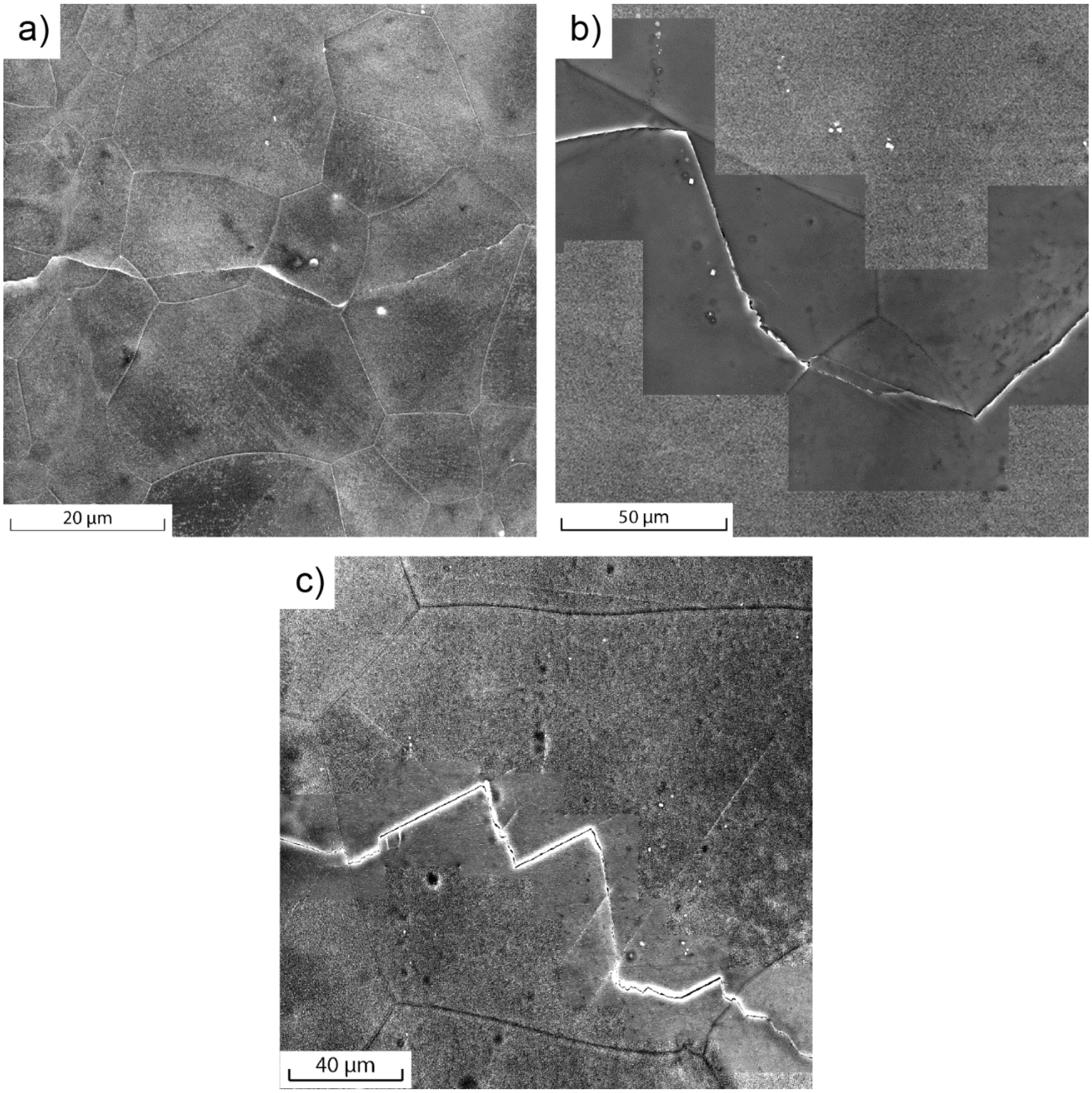

Figure 4.8 - Surface crack profiles showing apparent crystallographic propagation and deflection of short cracks at grain boundaries in the a) T5, b) underaged, and c) T6 conditions of WE43.

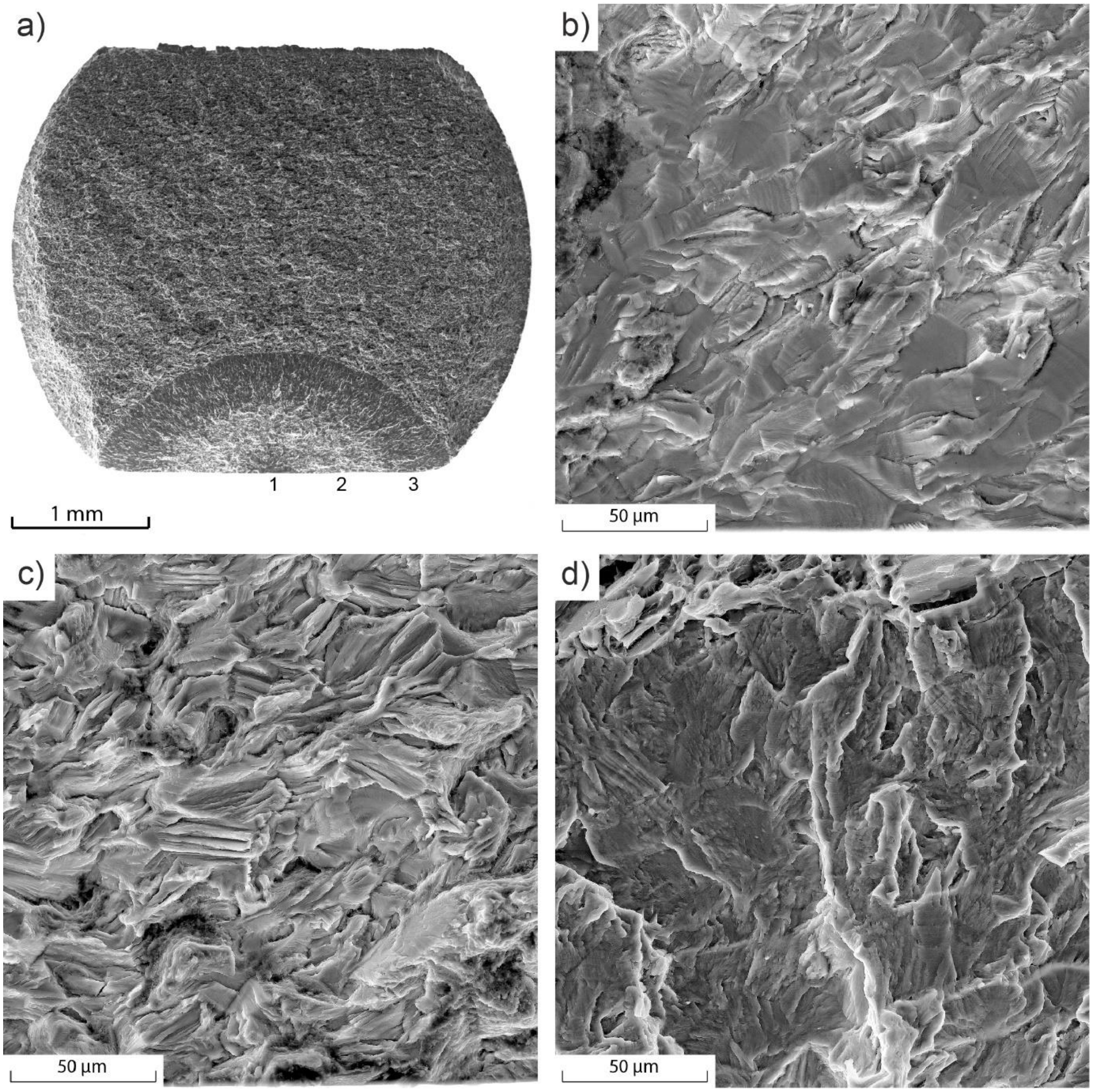

Figure 4.9 - a) Macroscopic fracture surface of a T5 specimen showing 3 regions with distinct morphologies, b) first, corresponding to marker 1, a heavily faceted region of crystallographic transgranular growth at low stress intensities, c) second, corresponding to marker 2, a rough transgranular region with lamellar structures at mid-range stress intensities, and lastly, d) smooth, non-crystallographic transgranular growth at higher stress intensities until sample failure corresponding to marker 3.

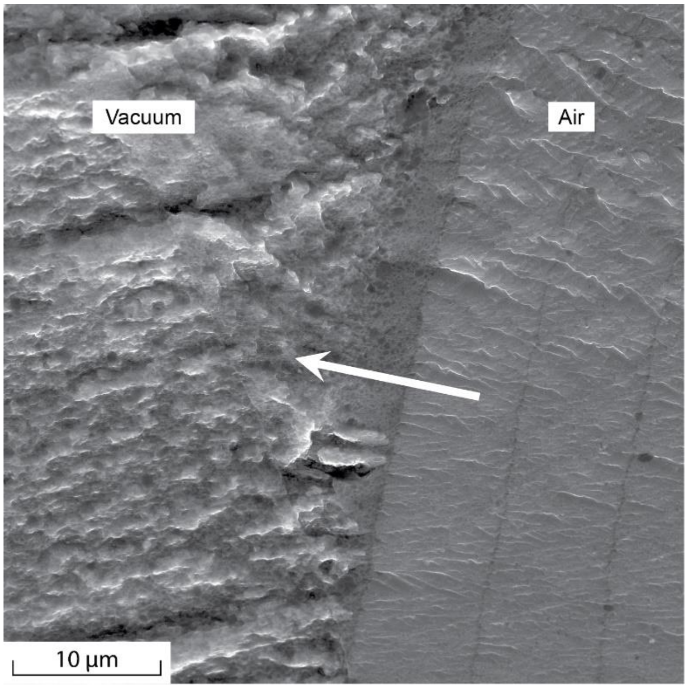

Figure 4.10 - Fracture morphology in a WE43 sample fatigued in laboratory air and vacuum, showing a notable transition in fracture surface morphology as a result of the change in environment. Crack growth is from right to left in the direction of the arrow.

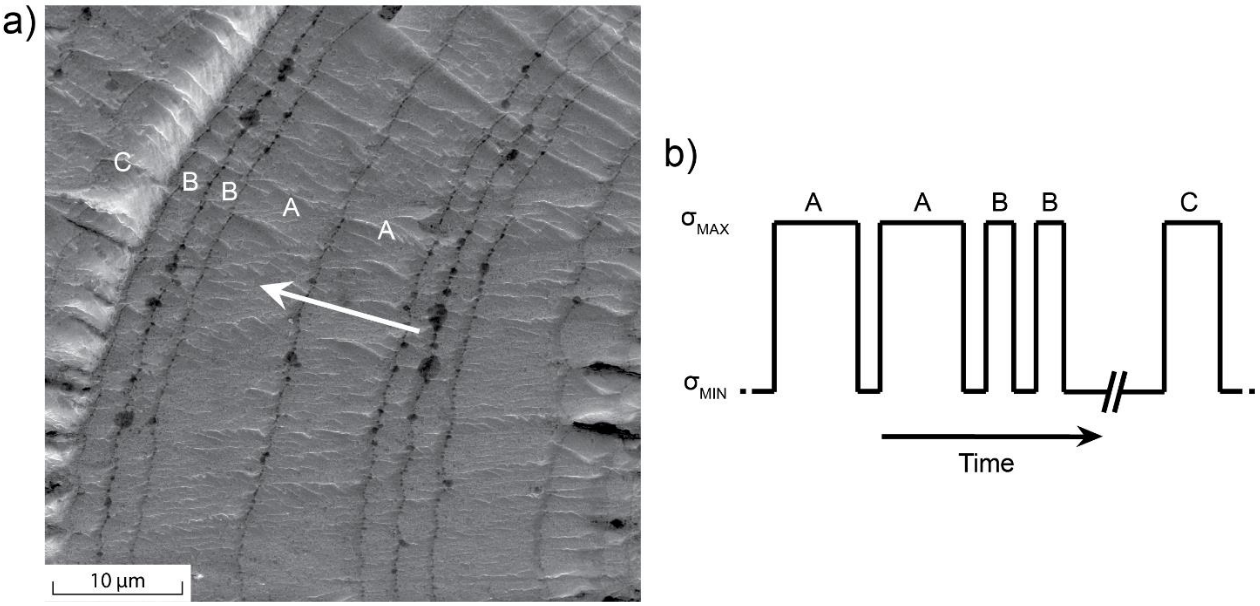

Figure 4.11 - Fracture morphology in WE43 magnesium produced by crack propagation in laboratory air showing a) micro beach marks. Crack growth is from right to left, in the direction of the arrow. B) Differing pulse lengths (A, B, and C) produce micro-beach marks of different widths. Minor pauses (<1 minute) produced the finer divisions visible between bands A and B, while a longer pause (> 15 minutes) for characterization of the crack on the specimen surface in an SEM produced the more significant division between bands B and C.

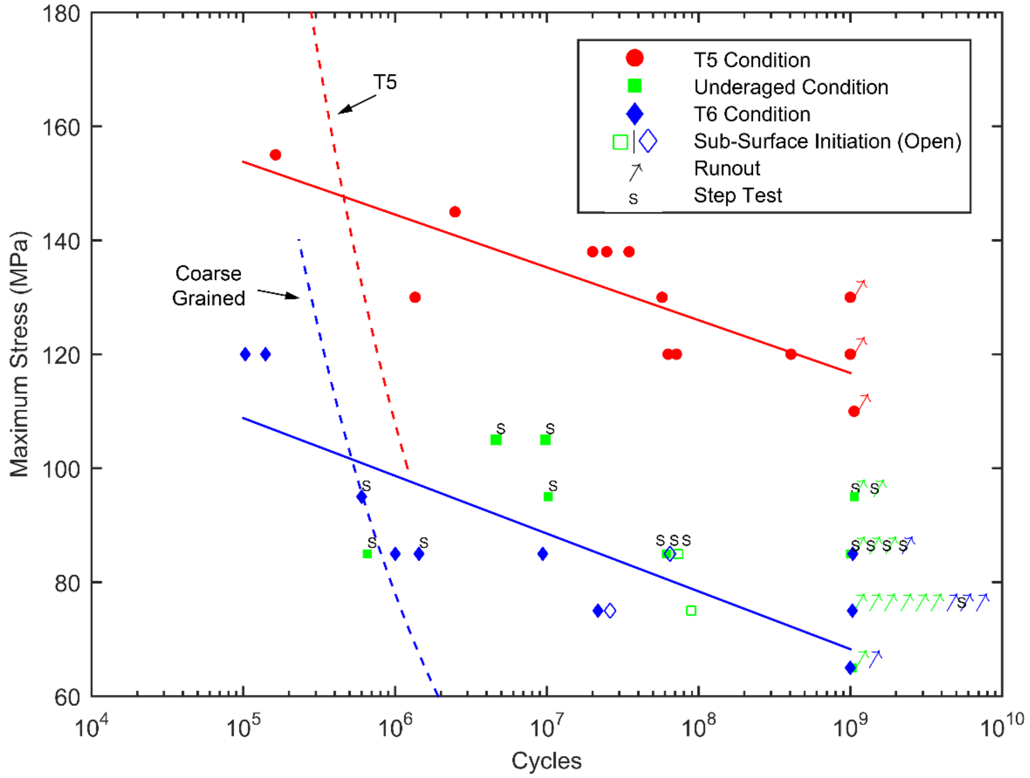

Figure 4.12 – Estimates (dashed lines) of crack growth-controlled fatigue life based on integration of a power law crack growth behavior. The initial crack length for each condition was taken to be half the average grain sizes. The low lifetime estimates indicate that propagation life does not contribute significantly to total lifetime in the VHCF regime.

CHAPTER 5

THE ROLE OF GRAIN BOUNDARIES ON FATIGUE CRACK GROWTH

5.1. Introduction

Grain boundaries have long been known to be significant barriers to crack propagation. A number of studies have been conducted to characterize this interaction, and to determine the crack and boundary parameters controlling the resistance of a grain boundary to continued crack propagation. Many of these studies have proposed models for crack-grain boundary interactions that are based on the idea that the rate of crack advance across a grain boundary is directly related to the ease of dislocation motion across that boundary along crystallographic slip planes. Different measures of crystallographic misorientation across grain boundaries are often used as metrics to explain and quantify this interaction between grain boundaries and fatigue cracks. Identification of characteristics and modes of crack propagation therefore becomes critical in evaluating the nature of cross-boundary crack propagation.

Chapter 5 discusses experiments designed to investigate the interaction between short fatigue cracks and grain boundaries, and explores the accuracy of existing geometric crack-boundary interaction models in describing the experimental results. Both cylindrical and thin foil specimens of coarse-grained WE43 magnesium were examined. The UFSEM system described in Chapter 4 was used to conduct in situ investigations of crack growth from basal-oriented FIB notches. In an attempt to move toward a two-dimensional crack growth experiment, a specially configured ultrasonic fatigue instrument [9] was used to investigate short crack growth in thin foils. In the foil specimens, the effect of grain boundaries on crack growth rate was investigated through characterization of both the surface and subsurface microstructure of foil specimens. Surface microstructure was investigated using a combination of scanning electron microscopy and electron backscatter diffraction. Subsurface characterization was achieved through three-dimensional mapping of the fracture surface using the tilt-photogrammetry software Alicona MeX™ (Alicona GmbH, Graz, Austria; http://www.alicona.com). Accurate grain boundary orientations were determined using a combination of surface and subsurface microstructural data. These experiments led to observations and insights into the role of different microstructural, crack, and grain boundary parameters in the interaction between short fatigue cracks and local microstructure. Section 5.2 provides an overview of the material used in this study, and the experimental methods used to conduct fatigue tests and characterization. The results of both the in situ and foil fatigue tests are presented in Section 5.3. Section 5.4 includes a discussion of the differences observed between the two types of tests, as well as a discussion of specific results and the efficacy of geometric models of boundary interactions with growing cracks in correctly describing those results. Finally, Section 5.5 summarizes the findings and presents conclusions.

5.2. Materials and Methods

5.2.1. Material

Magnesium alloy WE43 was prepared by Magnesium Elektron Ltd. The alloy was provided as hot-rolled plate in the T5 condition. The composition (wt%) of the alloy is 3.74Y, 2.10Nd, 0.52Gd, 0.45Zr, 0.016Zn, and Mg (balance). The as-received material had been hot rolled and then aged for 48 hours at 204° C. Additional heat treatment consisting of solution treatment and aging was conducted in our laboratory to produce coarse-grained microstructures strengthened with rare-earth precipitates. Solution treatment of the as-received alloy was conducted at 525° C for 8 hours. Aging at 250° C for 4 hours and 16 hours was used to produce the underaged and peak-aged (T6) conditions, respectively, and the resulting microstructures are described in Chapter 3. Both conditions exhibited fine β'/β''' precipitates as well as coarser β_1 precipitates [18,19,184]. Grain size was measured by standard methods using electron backscatter diffraction (EBSD) mapping in a Tescan Mira3 scanning electron microscope (SEM) with EDAX OIM Data Analysis software. The 525° C/8h solution treatment increased the average grain size from 13 µm to approximately 113 µm. The crystallographic texture of each treatment was investigated using EBSD and is detailed in Chapter 3. The two conditions featured a medium strength basal texture, with 4.10 and 3.35 multiples of random distribution (m.r.d.) observed in the underaged and T6 conditions respectively. Basal poles were aligned perpendicular to the rolling plane, parallel to the normal direction of the plate. The large grain size provided an ideal opportunity to investigate crystallographic transgranular crack growth and the interaction between short fatigue cracks and microstructural features. Mechanical and fatigue properties for this material in these conditions are discussed in greater detail in Chapter 4 and in [11].

5.2.2. Specimen Preparation

In Situ Specimen Preparation

Cylindrical fatigue specimens with a reduced gage section 4 mm in diameter and 7.5 mm in length were machined following design standards in [170] from both the underaged and T6 conditions such that the longitudinal axis of the specimens aligned with the rolling direction. To facilitate tracking of fatigue crack growth and crystallographic analysis using EBSD, diametrically opposed surface flats were machined into the gage sections. Specimen surfaces were prepared by hand grinding with SiC paper and polishing with diamond solution, followed by electropolishing in a solution of three parts by volume 85% phosphoric acid (H_3PO_4) and five parts by volume 95% ethanol for 30 minutes. Approximately 30 μm was removed from the surface by electropolishing.

To investigate crystallographic short crack growth behavior, micro-notches were machined in the gage flats to act as crack initiation sites, using an FEI Quanta 200 3D focused ion beam (FIB) equipped with a gallium ion source operating at 30kV and a probe current of 5.0 nA. FIB micro-notches were placed at specific microstructural sites and aligned parallel to basal slip planes in three dimensions. This was achieved by first characterizing the flats in the gage section crystallographically using EBSD. Next, large grains with high nominal basal Schmid factors and particular grain boundary characteristics were selected as locations for the micro-notch, with the notch entirely contained within the favorably oriented grain (on the sample free surface). We adopt here the nomenclature “nominal” Schmid factor in recognition of the fact that the Schmid factor provided by standard orientation imaging analysis software assumes that the stress field is uniaxial. In polycrystals like those investigated in this study, adjacent grains may alter the local stress state, so this assumption is not necessarily accurate. However, in the absence of more detailed crystal plasticity simulations of the actual local stress state, reference to the nominal Schmid factor can be a helpful means to identify grains and phenomena of interest. Orientation of the basal plane was determined through EBSD determination of Euler angles, and the sample was oriented during machining of the FIB notch such that the basal plane was parallel to the plane of FIB micro-notch. Each micro-notch had a length of 100 μm and a width of 6 μm, and an approximate depth of 40 μm, although this depth was affected by the inclination of the notch relative to the specimen free surface. In some cases, three notches were machined in each specimen to maximize the amount of data collected per specimen.

Thin Foil Specimens

In order to investigate the role of grain boundaries on short fatigue crack growth without the effect of subsurface microstructure, dog-bone-shaped thin sheet fatigue samples with a nominal thickness of 300 µm were fabricated from the underaged condition of WE43 by electrical discharge machining. The foil specimens were flat coupons 30.5 mm in total length, with a gage section 1.6 mm long and 2 mm wide. The longitudinal direction of the specimens was aligned with the rolling direction of the WE43 plate. Specimens were hand-polished to a thickness of approximately 200 µm using SiC paper, then further thinned to approximately 150 µm through electropolishing, using the same electrolyte used to prepare cylindrical samples. The sample surface was then characterized using EBSD. An edge notch perpendicular to the tensile axis was produced at the longitudinal center of the gage section of each fatigue specimen by FIB machining using an FEI Nova 200 nanolab SEM/FIB operating at 30kV and a probe current of 5.0 nA.

5.2.3. Experimental Procedures

UFSEM Crack Growth Testing

High spatial resolution (≈ 5 nm) imaging of fatigue damage at the microstructural length scale was accomplished using a unique combination of ultrasonic fatigue instrumentation and scanning electron microscopy, termed UFSEM. The ultrasonic fatigue instrumentation operates on the principles described in [164], and the UFSEM system is detailed in [10] and summarized here. The load line components of the system are machined from Ti-6Al-4V and are tuned to a resonance frequency of 20 kHz. The components include an ultrasonic transducer that produces a sinusoidal displacement using a piezoelectric material stack, an amplification horn that magnifies the displacement from the transducer and a lambda rod to extend the length of the load line. The ultrasonic load line is mounted to a custom-built SEM chamber door designed to fit with the Tescan Mira-3 microscope. The system is controlled by instrumentation that monitors and maintains the amplitude and frequency of the displacement signal in a closed loop system. A piezoelectric film sensor (Measurement Specialties, Inc. Model DT1-028K) is used to measure the displacement response in the load train. The fatigue specimen is positioned in the SEM chamber using a McAllister Technical Services MB1500 manual manipulator stage with five translational adjustments. The many degrees of freedom of the manipulator stage enable the observation and tracking of multiple microstructural features or fatigue cracks during a fatigue test. The UFSEM system is shown in Figure 3.6 in Chapter 3.

As in conventional ultrasonic fatigue testing, heating of the specimen is a concern when investigating fatigue using the UFSEM system. Aside from interrupted loading cycles, no auxiliary cooling methods were used during *in situ* testing. A duty cycle of 200 ms / 9000 ms pulse/pause was used to allow time for heat to dissipate. Thermocouples were used to monitor specimen temperature, which was maintained within approximately 5° C of room temperature.

The UFSEM system enables the *in situ* investigation of fatigue crack propagation in vacuum, or the *ex situ* characterization at the microstructural scale of fatigue in laboratory air. When conducting ultrasonic fatigue in laboratory air, cycling was conducted using the UFSEM system with the SEM chamber vented to laboratory air. Following a number of duty cycles, testing was paused to allow imaging in the SEM, after which the SEM chamber was vented to atmosphere and testing continued in laboratory air.

UFSEM tests were conducted at a frequency of approximately 20 kHz and at a stress ratio of $R = -1$ at room temperature, with a constant maximum stress of 85 MPa, which assuming the notch to be a sharp crack gave a K_{max} of 0.75 $MPa \cdot m^{1/2}$, calculated using the equations of Newman and Raju [180] for a surface crack in a finite elastic plate.

Thin Foil Short Crack Growth Testing

Thin foil crack growth testing was conducted using the experimental setup detailed in [9] and summarized here. The ultrasonic pulse that drives fatigue in the specimen when in resonance is generated by a piezoelectric transducer at the top of the load frame. The signal from the piezoelectric transducer is then amplified when passing through the amplification horn before entering the fatigue specimen mounted in the load line. As in the UFSEM system, the components of the ultrasonic load line, machined from commercially available Ti-6Al-4V, are tuned to resonance using the equations described in Appendix B. The control system is able to maintain resonance and control fatigue loading in a specified duty cycle consisting of repeated loading blocks interrupted by pauses to reduce specimen heating. Additional cooling is provided by forced air directed at the gage of the fatigue specimen. Thermocouples were used to verify that the specimen surface temperature did not vary by more than ± 5° C. The ultrasonic fatigue instrument is equipped with hydraulic cylinders that enable fatigue investigations at positive mean stresses. The two hydraulic cylinders have a combined load capacity of 22 kN and provide the loading force as well as aligning the upper and lower platens. The load line used for positive mean stress testing includes a lambda rod with a flange at a zero displacement node at the end of the load line. The load line is connected to the upper and lower platens by spherical bearings to minimize bending strains by allowing self-alignment.

Ultrasonic fatigue systems, such as those used here, operate in a relatively narrow range of resonant frequencies, which places fairly strict limitations on specimen dimensions and geometry. In order to study thin foil specimens with resonant frequencies much higher than 20 kHz, foils were rigidly attached to the shoulders of a titanium alloy IMI 834 “carrier” specimen designed for resonance at 20 kHz. Drawings for the carrier and foil specimens are included in Appendix A, and a schematic of the carrier and foil specimens is shown in Figure 5.1. During resonance, the carrier specimen vibrates with a displacement node at the center of the gage, and displacement maxima at the ends of the sample. Cyclic loads are thus applied to the foil specimen via the displacement of the carrier specimen at the shoulder connections and are adjusted by varying the displacement amplitude of the carrier. Strains for foil specimens of varying thickness were determined through both a finite element analysis of the carrier/foil assembly and by applying strain gages to the gage sections of both the carrier and foil specimens.

Fatigue tests for foil specimens were conducted with a load ratio of 0.1 with a maximum nominal stress in the foil of 60 MPa. A positive mean stress was applied using the aforementioned hydraulic cylinders. Intermittent loading with a 100 ms /300 ms pulse/pause duty cycle was utilized to allow for frequent measurement of fatigue crack propagation. Imaging of crack propagation was accomplished using a Navitar 12X Ultrazoom lens system equipped with a 5X Mitutoyo infinity corrected objective and a 5-megapixel CCD (Point Grey GRAS-50S5C) in combination with a Questar positioning stage. Following calculation of fatigue crack growth rates, the stress intensity factor range, ΔK (K_{max}-K_{min}), was calculated using the equations of Newman and Raju [180] for an edge-cracked finite plate, with a correction for loading under a fixed-grip condition [203].

Characterization of Fatigue Crack Growth Behavior

Surface images of fatigue crack growth were captured using two different methods. For *in situ* tests conducted using the UFSEM system, micrographs of crack progression were captured using secondary electron imaging in the Tescan Mira-3 microscope. Diametrically opposed flats in the specimen gage were used to simplify imaging of the fatigue cracks and to ensure that the specimen surface and focal plane of the microscope remain co-planar. Cycling was paused intermittently, depending on the fatigue crack growth rate, to observe fatigue damage and crack progression, and to capture micrographs for calculation of crack growth rates. Generally, images were captured until the crack grew beyond the edge of the gage flat, approximately 2.5 mm in width. Crack growth in foil specimens was imaged using the Navitar optical system equipped with a 5-megapixel CCD. Cycling was paused intermittently every 100 ms (approximately every 2000 cycles) to record crack propagation. Images were captured until crack propagation reached the approximate center of the foil and the driving force for crack growth correspondingly decreased. For both UFSEM and foil crack growth tests, higher resolution micrographs of the crack path and fracture surfaces were captured post mortem using a Tescan Mira-3 FEG-SEM.

To aid in the analysis of the interaction between fatigue crack growth and microstructural features, crack growth data is presented in a *dc/dN* vs crack length format. The surface fatigue crack growth rate, *dc/dN*, was calculated using a seven-point sliding polynomial method [179] and the crack length was measured manually using ImageJ [204].

Characterization of Grain Boundary Parameters

The effects of grain boundary misorientation on short crack growth are being studied through the combined use of ultrasonic fatigue and EBSD. Misorientation across grain boundaries is characterized in terms of tilt and twist misorientation angle [117], and the m' parameter [128]. In the model developed by Zhai et al., ease of crack propagation across a grain boundary is directly dependent on the geometric relations of the preferred slip planes in each grain compared to adjacent grains and the grain boundary orientation, known as tilt and twist misorientation angles. For crystallographic crack growth across a grain boundary, where the preferred planes in both grains are not coincident, the crack must reorient as it crosses the boundary if it is to continue to propagate along the preferred plane in the next grain. If these preferred slip planes are not coincident at the grain boundary, continued propagation requires a fracture of the material bounded by the twist misorientation angle between the two planes along the grain boundary (Figure 5.3a). Additional energy is needed for the creation of the increased free surface area associated with the fracture of this area, resulting in possible retardation of crack growth. The geometric model also incorporates the tilt misorientation component of crack deflection at the grain boundary, or the angle between the traces of the two preferred slip planes on the sample surface, which can act to reduce the driving force at the tip of the crack [117]. Luster and Morris investigated slip transfer across grain boundaries using a geometric compatibility factor m', defined as

$$m' = \cos \kappa \cos \phi \tag{5.1}$$

where κ is defined as the angle between slip vectors from two adjacent grains, and ϕ is the angle between slip plane normal in those grains, with a low m' indicating higher difficulty of slip transfer [128]. Following fatigue, the effect of grain boundaries on crack propagation is evaluated by comparing the lowest crack growth rate observed as the crack approached a boundary, da/dN_{GB}, with the approximate steady state crack growth rate in the Trailing Grain, da/dN_{SS}, using the following formula:

$$\text{Retardation Factor} = \frac{da/dN_{GB}}{da/dN_{SS}} \qquad [5.2]$$

with a minimum retardation factor of 0 indicating permanent crack arrest, and a maximum value of 1 indicating that the grain boundary has no observable effect crack growth rate.

Tilt misorientation angle and m' parameter can all be determined solely from crystallographic orientations determined from electron backscatter diffraction microscopy. Determination of twist misorientation angle, on the other hand, requires information on grain boundary orientation in three dimensions, as well as knowledge of the crystallographic orientations of the two neighboring grains.

In order to determine subsurface grain boundary orientation, the fracture surfaces of some cylindrical samples and all foil samples were characterized in three dimensions. To accomplish this, the software package MeX was used to reconstruct the fracture surface topography using tilt photogrammetry. From these reconstructed maps of the fracture surface, the trace of grain boundaries along the fracture surface could be determined in three dimensions. This information, combined with trace measurements of the respective grain boundaries on the specimen free surface, was then used to determine the orientation of a plane representing the grain boundary and containing both grain boundary trace vectors, by using the cross product:

$$\bar{n} = \overline{V_S} \times \overline{V_F} \qquad [5.3]$$

where V_S and V_F are the vectors describing the grain boundary traces measured on the free and fracture surfaces, respectively, and n is the normal vector to the grain boundary plane (Figure 5.2b). This process is detailed in Appendix C.

The requirement for two independent traces to determine grain boundary orientation limits this analysis method to boundaries and grains that intersect the specimen free surface.

While this makes the technique difficult to apply to the cylindrical specimens investigated using the UFSEM system, the foil specimens are uniquely suited to this method of grain boundary characterization. In cases where the subsurface grain boundary orientation cannot be determined, calculation of twist misorientation requires an assumption of the subsurface orientation of the grain boundary. Grain boundaries are generally assumed to be perpendicular to the specimen free surface and the accuracy of this assumption depends on a variety of microstructural factors. For example, the assumption is more likely accurate for large or columnar grains than it would be for small, equiaxed grains. The next section briefly discusses how twist misorientation may vary based on deviation of the grain boundary orientation from this assumed perpendicularity.

Variation of Twist Misorientation Angle with Grain Boundary Inclination

Twist misorientation is measured as the angle between the traces of two active slip planes from two neighboring grains along the grain boundary separating them and requires knowledge of the inclination of the boundary relative to the specimen surface. When this grain boundary inclination is unknown, it is common to approximate twist misorientation by assuming a fixed boundary inclination. The most common assumption is that grain boundary plane is perpendicular to the specimen free surface. In actual microstructure boundary inclinations may deviate substantially from perpendicularity and can result in significant variation of the actual twist misorientation angle from that calculated assuming perpendicularity. For cases in which the perpendicularity assumption does not accurately represent the actual grain boundary orientation, twist misorientation measurements can be a very inaccurate assessment of the resistance of a grain boundary to crack propagation.

The following is an example of this possible variation of twist misorientation from the measured value taken from foil specimen F1, discussed in detail later in this chapter. The first boundary to encounter crack propagation in specimen F1 is nearly perpendicular to the free surface, featuring an inclination of approximately 99° relative to the surface. This grain boundary orientation was measured on the three-dimensional surface map of the fracture surface generated using MeX, as detailed in the previous section. The measured twist misorientation across this boundary for the basal system in these two grains is 36°. Figure 5.3b illustrates how this measured twist misorientation angle would vary if the grain boundary were rotated about its free-surface trace to produce different inclinations relative to the specimen free surface. Positive and negative rotations of approximately 10° from the initial orientation would produce twist misorientation angles of approximately 0° and 54°, respectively. The severity of this variation in twist misorientation angle is dependent on the crystallographic orientation of the neighboring grains as well as the measured surface trace of the grain boundary. This case is rather severe, with twist misorientation angle ranging from 0° to a maximum of 90° in a relatively reasonable range of possible grain boundary inclination angles. Other microstructural sites may have levels of variation that are much smaller. It is clear that accurate characterization of grain boundary orientation is necessary when seeking to determine the relationship between crystallographic misorientation across grain boundaries and crack propagation behavior.

5.3. Results

5.3.1. Crack Path Crystallography

A systematic study of the crack growth rates and propagation paths in the underaged microstructure using specimen surface observations were made for foil and cylindrical specimens by comparing the crack paths to free surface traces of the basal, prismatic, and pyramidal slip systems identified in each grain using EBSD. This data is summarized in Figure 5.4, where paths of crack propagation are averaged for 5 foil specimens and compared to averaged paths of crack propagation in conventional cylindrical crack growth specimens with horizontal FIB notches (detailed in the previous chapter) and cylindrical *in situ* crack growth specimens with basal-oriented notches. For each type of specimen, surface crack propagation was found to be a mix of crystallographic and non-crystallographic transgranular growth modes, as well as intergranular growth. In some cases, transgranular growth was observed that appeared to be crystallographic in nature in that the crack path exhibited long portions of straight growth, and generally appeared to sharply transition to new orientations on reorientation of the crack, but either did not align with traces of the basal, prismatic, or pyramidal systems, or aligned closely with traces from multiple slip systems, making the identification of a single active system impossible. These regions were categorized as transgranular growth of unknown crystallographic character. In general, crystallographic transgranular growth aligned most often with basal surface traces, although crack growth aligned with both the prismatic and pyramidal systems was observed in each type of specimen. Compared to cylindrical specimens, crack growth in foil specimens exhibited much higher levels of crystallographic transgranular growth parallel to the basal system, at the expense of other growth pathways, except intergranular crack propagation, which occurred more frequently in foils than in cylindrical specimens.

5.3.2. *In Situ* Crack Growth in Cylindrical Specimens

In situ crack growth behavior in three cylindrical specimens is presented below. When discussing grain boundaries, the terms *Leading* and *Trailing* are used to describe, respectively, the grains into which the crack is growing after crossing a boundary (Leading Grains), and grains through which the crack has already propagated when encountering a boundary (Trailing Grains).

In cylindrical specimen C1 (Figure 5.5), the notch was placed in a grain with a nominal basal Schmid factor of 0.5. The left end of the notch was located 50 µm from the projected intersection point of the crack with grain boundary (GB) 1. The right end of the notch was located 54 µm from the projected intersection point of the crack with GB 2. Crack growth occurred from both ends of the notch and propagated parallel to basal slip traces on the specimen surface. Crack growth rates for each side of the crack are shown in Figure 5.6. On both the left and right sides of the crack, crack growth halted before crossing the respective grain boundaries. Due to the small final size of this crack, the specimen was not able to be opened for investigation of the fracture surface, making nondestructive subsurface characterization of grain boundary orientation impossible, so grain boundaries were assumed to lie perpendicular to the specimen free surface for determination of twist misorientation angle. Considering the basal system in both grains, boundary 1 (left side) is characterized by an m' parameter of 0.12, a tilt angle of 17°, and a twist angle of 82°. The nominal basal Schmid factor in the Leading Grain was 0.48. Boundary 2 (right side) is characterized by an m' parameter of 0.04, a tilt angle of 90°, and a twist angle of 68°. The nominal basal Schmid factor in the Leading Grain was 0.42. Figure 5.7 shows the possible variation in twist misorientation with grain boundary inclination for each of these two boundaries. Twist misorientation at GB 1 is relatively insensitive to changes in the inclination of the grain boundary, while twist misorientation at GB2 is highly sensitive to grain boundary inclination, requiring caution when using this measure.

Table 5.1 - Grain boundary misorientation parameters for in situ specimen C1

Grain Boundary	Slip System in Trailing Grain	Slip System in Leading Grain	Nominal Schmid Factor in Leading Grain	m' Parameter	Tilt Angle	Twist Angle*	Retardation Factor
1	Basal	Basal	0.48	0.12	17	82	0
2	Basal	Basal	0.42	0.04	90	68	0

*Note: Twist misorientation angles were calculated based on an assumed grain boundary orientation and may be subject to significant variability.

In specimen C2 (Figure 5.8), the notch was placed in a grain with a nominal basal Schmid factor of 0.35. The left edge of the notch was located 106 µm from the projected intersection point of the crack with GB 1. GB 2 was located 91 µm from GB 1, measured from each intersection of the crack with the grain boundaries. The right edge of the notch was located near a series of finer grains not characterized for misorientation. Crack growth rates for the left side of the crack are shown in Figure 5.9. Crack growth occurred from both edges of the notch, with the crack propagating parallel to basal slip traces through grain boundaries 1 and 2 at the left side of the notch. Each grain boundary produced little effect on crack growth rates. Grain boundaries in this specimen were characterized in three dimensions using the method detailed in Section 5.2.3. Considering the basal system in each neighboring grain, boundary 1 was characterized by an m' parameter of 0.88, a tilt angle of 19°, and a twist angle of 4°. The nominal basal Schmid factor in the Leading Grain was 0.29. Boundary 2 was characterized by an m' parameter of 0.85, a tilt angle of 23°, and a twist angle of 17°. The nominal basal Schmid factor in the Leading Grain was 0.5.

Table 5.2 - Grain boundary misorientation parameters for in situ specimen C2

Grain Boundary	Slip System in Trailing Grain	Slip System in Leading Grain	Nominal Schmid Factor in Leading Grain	m' Parameter	Tilt Angle	Twist Angle	Retardation Factor
1	Basal	Basal	0.29	0.88	19	4	0.78
2	Basal	Basal	0.50	0.85	23	17	1

In specimen C3 (Figure 5.10), the notch was placed in a grain with a nominal basal Schmid factor of 0.49. The left edge of the notch was located 41 µm from the projected intersection point of the crack with GB 1. The right end of the notch was located 69 µm from the projected intersection point of the crack with GB 2. Crack propagation for this specimen was conducted *in situ* under vacuum in the UFSEM system. Crack growth rates for each side of the crack are shown in Figure 5.11. Crack growth occurred from both edges of the notch. On the left side of the crack, propagation occurred parallel to the basal slip system through GB 1, exhibiting a retardation in crack growth rate, followed by a reduced crack growth rate after penetrating the boundary. Crack propagation from the right side of the notch propagated parallel to the basal slip system with rapidly decreasing rates before arresting. Crack propagation in this specimen was measured as visible crack opening, rather than slip lines, which were often obscured by extruded material. For this reason, measured crack growth for the right side of the crack arrests well in advance of the grain boundary, despite the fact that extruded material and apparent slip reaches the boundary. Due to the small final size of the crack, the fracture surface was not opened, making subsurface characterization of grain boundary orientations impossible; grain boundaries were assumed to lie perpendicular to the specimen free surface for determination of twist misorientation angle. Considering the basal system in both grains, boundary 1 was characterized by an m' parameter of 0.08, a tilt angle of 85°, and a twist angle of 41°. The nominal basal Schmid factor in the Leading Grain was 0.46. Boundary 2 was characterized by an m' parameter of 0.51, a tilt angle of 43°, and a twist angle of 47°. The nominal basal Schmid factor in the Leading Grain was 0.49. Figure 5.12 shows the possible variation in twist misorientation with grain boundary inclination for each of these two boundaries. In this specimen, twist misorientation across GB 2 is less sensitive to grain boundary inclination, while twist misorientation across GB 1 is more sensitive to grain boundary inclination, resulting in more uncertainty when using misorientation measurements based on the assumed grain boundary orientation.

Table 5.3 - Grain boundary misorientation parameters for in situ specimen C3

Grain Boundary	Slip System in Trailing Grain	Slip System in Leading Grain	Nominal Schmid Factor in Leading Grain	m' Parameter	Tilt Angle	Twist Angle*	Retardation Factor
1	Basal	Basal	0.46	0.08	85	41	0.02
2	Basal	Basal	0.49	0.51	43	47	0

*Note: Twist misorientation angles were calculated based on an assumed grain boundary orientation and may be subject to significant variability.

5.3.3. Crack Growth in Thin Foils

While *in situ* crack growth testing results in micrograph recordings of crack propagation with high spatial resolution, the effects of local microstructure and grain boundaries on fatigue crack growth behavior in these specimens can be difficult to determine. This arises, in part, because the influences of subsurface grains on surface-measured crack growth rates are difficult to adequately characterize in these bulk specimens. In an effort to minimize this complication, fatigue behavior was investigated in a number of thin foil specimens, where the cross-sectional width was generally dominated by only one or two grains. In each case, the first few grain boundary characteristics have been detailed here.

Foil Specimen F1: Grain boundary misorientation parameters determined for each grain boundary in foil specimen F1 (Figure 5.13) are shown in Table 5.4. Crack growth rates for this crack are shown in Figure 5.14. Crack propagation in specimen F1 was characterized by predominantly crystallographic transgranular growth along the basal and pyramidal systems, with periods of significant crack retardation at grain boundaries.

The intersection of the crack with GB 1 was located 81 μm from the edge of the notch and was characterized by basal crack growth in both the Trailing Grains and Leading Grains. This boundary produced a retardation in crack growth rates.

The crack intersection with GB 2 was located 108 μm from that of GB 1 and was characterized by a significant retardation. In the Trailing Grain, crack propagation was parallel to the basal system and in the Leading Grain crack propagation occurred along a pyramidal plane. Two pyramidal slip planes produced surface traces close to the surface crack path, so the misorientation parameters for both in relation to the basal system in the Trailing Grain are listed in Table 5.4. Similar to GB 1, GB 2 also produced a significant retardation in crack growth rates. Crack growth rates in the Leading Grain were also reduced as compared to crack growth rates in Trailing Grains, and the fracture surface featured significant roughness (Figure 5.2a).

The crack intersection with GB 3 was located 89 μm from that of GB 2, and featured crack propagation parallel to the pyramidal system in both the Trailing and Leading Grains. In the Leading Grain, only one variant of the pyramidal slip system resulted in slip traces parallel to the crack path, and misorientation parameters for this variant were determined for the two possible pyramidal variants in the Trailing Grain. GB 3 produced no retardation of crack growth rates, and crack growth rates accelerated in the Leading Grain as crack propagation transitioned from the pyramidal plane to cracking on the basal plane approximately 70 µm into the Leading Grain.

The crack intersection with GB 4 is located 113 µm from that of GB 3, and surface crack propagation was characterized by noncrystallographic transgranular growth in the Trailing Grain, followed by basal crack growth in the Leading Grain. Investigation of subsurface behavior through fractography indicated that the noncrystallographic growth in the Trailing Grain was a minor surface phenomena and subsurface growth was dominated by basal crack growth. Therefore, crack misorientation parameters for basal crack growth in both the Trailing and Leading Grains is presented. GB 4 resulted in no retardation in crack growth rates. Later periods of crack retardation beyond GB 4 corresponded to periods of highly inclined crack growth, crack branching, and intergranular crack propagation.

Table 5.4 - Grain boundary misorientation parameters for foil specimen F1

Grain Boundary	Slip System in Trailing Grain	Slip System in Leading Grain	Nominal Schmid Factor in Leading Grain	m' Parameter	Tilt Angle	Twist Angle	Retardation Factor
1	Basal	Basal	0.49	0.00	86	36	0.67
2	Basal	Basal	0.15	0.53	54	51	0.15
2	Basal	Pyramidal (-1011)	0.46	0.29	30	71	0.15
2	Basal	Pyramidal (01-11)	0.46	0.76	26	10	0.15
3	Pyramidal (-1011)	Pyramidal (-1101)	0.49	0.36	54	45	0.72
3	Pyramidal (01-11)	Pyramidal (-1101)	0.49	0.03	58	28	0.72
4	Basal	Basal	0.33	0.23	10	37	1

<u>Foil Specimen F2:</u> Grain boundary misorientation parameters determined for each grain boundary in foil specimen F2 (Figure 5.15) are shown in Table 5.5. Crack growth rates for this crack are shown in Figure 5.16. Crack propagation in specimen F2 exhibited a mixture of

crystallographic transgranular, non-crystallographic transgranular, and intergranular crack propagation, and grain boundaries appeared to only have a limited effect on crack propagation rate.

The intersection of the crack with GB 1 was located 46 µm from the edge of the notch and was characterized by basal crack growth in the Trailing Grain, and tortuous noncrystallographic growth in the Leading Grain. Fractography of the Leading Grain revealed a relatively small cross-sectional area as compared to neighboring grains, and a rough fracture surface. Crack growth rates show a slight reduction at this grain boundary.

The intersection of the crack with GB 2 was located 100 µm from that of GB 1, and it was characterized by a transition from rough noncrystallographic growth to intergranular crack propagation. GB 2 appeared to have little effect on crack propagation rates. This intergranular growth continues through three triple points around Grain A, before transitioning into crack propagation parallel to the basal system while approaching GB 3 in Grain B.

This basal growth led to GB 3, located 359 µm from the edge of the notch. Crack growth in the Leading Grain at GB 3 is tortuous and apparently crystallographic in nature, with the traces of multiple slip systems aligning reasonably well with the crack path. The basal-basal misorientation parameters are listed in Table 5.5. This transition appears to have little effect on crack propagation rates, although rates of crack growth in the Leading Grain are reduced as compared to those in neighboring grains.

Subsequent grain boundaries appear to have little effect on crack propagation rate. Grain boundaries GB 7, GB 8, and GB 9 have been characterized to illustrate the reduced effect tilt and twist misorientation have on crack propagation at longer crack lengths. For each boundary, no significant retardation of crack growth was observed. GB 7 was characterized by basal growth on both sides of the boundary, with a tilt misorientation angle of 37° and a twist misorientation angle of 9°. GB 8 also characterized by crack growth along the basal system on both sides of the boundary, with a tilt angle of 74° and a twist angle of only 1°. GB 9 exhibited basal growth in the Trailing Grain, followed by intergranular crack propagation, which may be explained by the high tilt and twist misorientations of 64° and 86°, respectively. Despite this high level of misorientation and accompanying transition to intergranular growth, only a very minor decrease in crack propagation rate was observed at GB 9.

Table 5.5 - Grain boundary misorientation parameters for foil specimen F2

Grain Boundary	Slip System in Trailing Grain	Slip System in Leading Grain	Nominal Schmid Factor in Leading Grain	m' Parameter	Tilt Angle	Twist Angle	Retardation Factor
1	Basal	Basal	0.28	0.02	78	46	0.47
3	Basal	Basal	0.16	0.61	46	29	0.86
7	Basal	Basal	0.49	0.73	37	9	1
8	Basal	Basal	0.45	0.04	74	1	1
9	Basal	Basal	0.09	0.24	64	86	0.71

Foil Specimen F3: Grain boundary misorientation parameters determined for each grain boundary in foil specimen F3 (Figure 5.17) are shown in Table 5.6. Crack growth rates for this crack are shown in Figure 5.18. Specimen F3 exhibited a mixture of crystallographic transgranular and non-crystallographic transgranular crack propagation, with a fairly tortuous crack path. Although crack propagation rates showed significant variability, the effect of grain boundaries was obscured due to crack branching and the small cross-sectional area of some surface-intersecting grains.

The intersection of the crack with GB 1 was located 156 μm from the edge of the notch and was characterized by pyramidal crack growth in the Trailing Grain, and basal growth in the Leading Grain. No significant effect on crack propagation rates was observed.

GB 2 appears to feature basal to basal growth, but the boundary is not discernable on the fracture surface. Crack propagation appears uninterrupted from the pyramidal-basal transition at GB 1 until GB 3, likely as a result of the grain Trailing GB 2 featuring minimal cross-sectional area. The pyramidal-basal misorientation parameters listed in Table 5.6 for GB 1 characterize the misorientation between the grain Trailing GB 1 and the grain Leading GB 2.

The intersection of the crack with GB 3 is located 204 μm from the edge of the notch, and features basal crack propagation in the Trailing Grain, and intergranular crack propagation in the Leading Grain. No significant reduction in crack propagation rate was observed at this boundary. Misorientation parameters between basal systems in the Trailing Grain and the grain neighboring the section of intergranular propagation are listed in Table 5.6. The fracture surface of subsequent grains was blocked by crack branching, making the fractographic analysis of these boundaries impossible. Subsequent crack propagation showed little effect from grain boundaries, but rates did vary from grain to grain, and were significantly affected by branching of the crack front.

Table 5.6 - Grain boundary misorientation parameters for foil specimen F3

Grain Boundary	Slip System in Trailing Grain	Slip System in Leading Grain	Nominal Schmid Factor in Leading Grain	m' Parameter	Tilt Angle	Twist Angle	Retardation Factor
1	Pyramidal (1-101)	Basal	0.46	0.56	14	65	1
3	Basal	Basal	0.11	0.82	23	33	0.67

<u>Foil Specimen F4:</u> Grain boundary misorientation parameters determined for each grain boundary in foil specimen F4 (Figure 5.19) are shown in Table 5.7. Crack growth rates for this crack are shown in Figure 5.20. Crack propagation in Specimen F4 was occurred predominantly along the basal slip system and was relatively insensitive to grain boundaries.

Early crack growth in this specimen resulted in two crack branches. Measured arrest in crack growth rates occurred at the lower, non-dominant crack branch. As the non-dominant branch was not present on the fracture surface, the boundary was not able to be characterized in three dimensions but featured a mismatch between crystallographic orientations of 171° (axis-angle misorientation). The dominant branch featured no crack arrest and appeared to be the result of crack growth reaching the specimen surface from the unobserved side of the specimen, rather than proceeding from the notch. The intersection of the dominant crack branch with GB 1 was located 156 μm from the edge of the notch and was characterized by basal crack growth in both the Trailing and Leading Grains.

The intersection of the crack with GB 2 was located 119 μm from GB 1 and featured basal crack propagation in both the Trailing and Leading Grains. No effect on crack propagation rates was observed.

The crack intersection with GB 3 was located 139 μm from that of GB 2. Subsurface investigation of GB 3 indicated that basal crack propagation from the Trailing Grain continued across the grain boundary to basal crack propagation in the Leading Grain. Subsurface investigation also revealed a period of intergranular growth not visible on the free surface. The crack growth rate exhibited a significant retardation after propagating through GB 3.

Basal growth continued to GB 4, located 143 μm from GB 3, and continued into the Leading Grain. No effect on crack propagation rates was observed. Subsequent crack propagation occurred predominantly along the basal system, and appeared to have little interaction with grain boundaries, as observed in specimen F2.

Table 5.7 - Grain boundary misorientation parameters for foil specimen F4

Grain Boundary	Slip System in Trailing Grain	Slip System in Leading Grain	Nominal Schmid Factor in Leading Grain	m' Parameter	Tilt Angle	Twist Angle	Retardation Factor
1	Basal	Basal	0.44	0.89	20	32	0.15*
2	Basal	Basal	0.47	0.70	16	33	0.75
3	Basal	Basal	0.48	0.69	25	45	0.64
4	Basal	Basal	0.43	0.49	32	29	0.85

*Note: The retardation in crack growth rate at GB1 occurred as a result of crack retardation in a non-dominant branch of the crack, which was unable to be characterized in terms of grain boundary misorientation due to crack branching. The retardation factor does not describe crack behavior in the dominant branch of the crack.

Foil Specimen F5: Grain boundary misorientation parameters determined for each grain boundary in foil specimen F5 (Figure 5.21) are shown in Table 5.8. Crack growth rates for this crack are shown in Figure 5.22. Specimen F5 exhibited a mixture of crystallographic transgranular, non-crystallographic transgranular, and intergranular crack propagation. A large number of grain boundaries were encountered by the crack, some of which led to significant retardation in crack growth rate.

GB 1 was located 71 µm from the edge of the notch and was characterized by apparently crystallographic growth in the Trailing Grain and pyramidal growth in the Leading Grain. GB 1 had no apparent effect on crack propagation rates.

GB 2 was located 62 µm from GB 1 and featured pyramidal growth in the Trailing Grain and basal growth in the Leading Grain. The grain exhibiting basal growth exhibited a much larger cross-sectional area than was evident from free-surface observations, and the crack exhibited accelerated crack growth rates during propagation across this grain.

GB 3 was located 15 µm from GB 2 and exhibited a transition from basal crack propagation to crystallographic crack growth. Crack propagation in the Leading Grain closely matches surface traces from the prismatic and pyramidal slip systems, and is fairly tortuous in nature, indicating slip along multiple systems may be occurring. This grain also corresponds to a period of significant variation in local crack propagation rates. Misorientation parameters for both the prismatic and pyramidal systems present in the grain Leading GB 3 are presented below in Table 5.8.

GB 4 was located 161 µm from GB 3 and featured the transition of the possible prismatic or pyramidal growth in the Trailing Grain to basal growth in the Leading Grain. GB 4 also corresponded to a temporary arrest in crack propagation.

GB 5 was located 48 µm from GB 4 and appeared to feature a transition from basal growth to intergranular crack propagation, but subsurface investigation indicated that intergranular propagation was localized to the surface, and basal growth continued across the grain boundary. Subsequent grain boundaries exhibited little effect on crack propagation rates.

Table 5.8 - Grain boundary misorientation parameters for foil specimen F5

Grain Boundary	Slip System in Trailing Grain	Slip System in Leading Grain	Nominal Schmid Factor in Leading Grain	m' Parameter	Tilt Angle	Twist Angle	Retardation Factor
2	Pyramidal (1-101)	Basal	0.48	0.16	16	83	0.62
3	Basal	Prismatic (10-10)	0.49	0.05	75	3	0.50
3	Basal	Pyramidal (-1011)	0.47	0.10	84	24	0.50
3	Basal	Pyramidal (10-11)	0.47	0.01	65	32	0.50
4	Prismatic (10-10)	Basal	0.46	0.86	7	81	0.02
4	Pyramidal (-1011)	Basal	0.46	0.52	15	63	0.02
4	Pyramidal (10-11)	Basal	0.46	0.99	3	10	0.02
5	Basal	Basal	0.39	0.13	85	49	1

Crack growth rates for the *In Situ* and foil specimens are shown together in Figure 5.23. While the majority of the *in situ* cracks were of shorter length (due to early arrest), crack growth rates for specimen C2 and the foil specimens are similar at similar crack lengths (Figure 5.23a). Crack growth data for the foil specimens clearly illustrates the high local variability in crack growth rate as a result of variation in local microstructure. In Figure 5.23b, crack growth rate is compared to maximum stress intensity factor. The configuration of foil specimen attached to a carrier specimen produces a fixed specimen displacement loading condition in the foil (often referred to as fixed-grip loading). Stress intensity was calculated taking this loading condition into account [203].

5.4. Discussion

The experiments detailed above were conducted to help determine the role of local microstructure on short crack propagation, specifically the role of boundaries between grains, and the crystallographic misorientation between those grains forming the boundaries. The efficacy of different models that incorporate misorientation to predict crack arrest and retardation are discussed in the following sections.

5.4.1. Crack Growth Behavior

The interaction between cracks and grain boundaries has recently been modeled in terms of the geometric relation between active slip planes across the boundary. Identification of crack behavior and active slip systems therefore becomes critical in evaluating the nature of cross-boundary crack propagation.

Crack growth in both cylindrical and foil specimens, as described in preceding sections, is predominantly crystallographic in nature. This crystallographic transgranular crack propagation mode is well described by geometric models of the crack-grain boundary interaction based on the misalignment of crystallographic slip planes across grain boundaries such as tilt and twist misorientation [117], and the m’ parameter [128].

As discussed in Section 5.3.1, the most significant difference in crack propagation modes observed in cylindrical and foil specimens is a significant reduction in noncrystallographic transgranular growth observed in foil specimens, and an accompanying increase in crystallographic transgranular growth along basal slip planes as well as an increase in intergranular growth. With a thickness of one to two grain diameters on average (approximately 150 µm), grains in foil specimens experience significantly reduced constraint from neighboring grains during fatigue and plastic deformation, as compared to the 4 mm diameter cylindrical specimens, which is the likely cause for the observed changes in crack propagation mode in the foils. Fractographic investigation of foil specimens also indicated that many grains that exhibited rough non-crystallographic growth also exhibited relatively small cross-sectional areas on the fracture surface, as compared to neighboring grains. In foil specimens, the reduction in constraint made the crystallographic transgranular modes of crack propagation more favorable, hence their increased prevalence.

5.4.2. Effects of Microstructure on Fatigue Crack Growth

Can we use what we know from these experiments to assess current microstructural models of short fatigue crack growth and robust life predictions that use these models? The following sections discuss observed interactions between fatigue cracks and grain boundaries, evaluated using the various models of crack-grain boundary interaction which are reviewed in this chapter.

Existing Grain Boundary Interaction Models

A number of researchers have attempted to quantify the boundary and crack parameters controlling fatigue crack arrest at grain boundaries. Zhai et al. [117] investigated the effects of tilt and twist misorientation across grain boundaries on short fatigue crack growth in Al-Li alloys. They found that the microstructurally short crack growth rate appeared to be strongly influenced by tilt and twist misorientation across grain boundaries that were interacting with the crack front. They hypothesized that when none of the slip planes in a grain into which a fatigue crack attempts to grow (i.e. from the Trailing Grain to the Leading Grain) form small tilt and twist angles with the active crack plane crack arrest or severe retardation in growth will occur. In a study of slip transfer across grain boundaries in a Ti-Al alloy, Luster and Morris [128] developed a term called the m' parameter that linked the ease of slip transfer across grain boundaries to the coherency of slip planes and directions across the boundary. The m' parameter predicts that slip transfer becomes more difficult when either slip directions or slip plane normals in the Trailing Grain and Leading Grain have significant misalignment. These parameters have been discussed in more detail in Chapter 2.

Based on the work of Zhai et al. [117], two phenomenological models have been developed to understand the interaction of grain boundaries and fatigue cracks. Wen and Zhai [205] introduced a model that represents the resistance of a grain boundary to crack propagation due to twist misorientation as a Weibull-type function. The model did not incorporate other boundary or microstructural parameters such as tilt misorientation angle or Schmid factor. A second model was developed by Wilkinson [206] that incorporates the effects of adjacent grain orientations in addition to the twist misorientation. The effect of orientation is considered using the ratio of the Sachs factor of the active plane in the Leading Grain to the Sachs factor of the active crack plane in the Trailing Grain. The model also incorporates a critical crack transmission stress, or the stress required for a crack to cross a grain boundary.

Based on the models of Zhai, Wen, and Wilkinson, as well as the experimental results presented in this chapter, Panwar et al. [130] have developed a combined grain boundary interaction model that takes into account the coupling between tilt and twist misorientation, nominal Schmid factor, and a critical crack transmission stress. In this model, this critical crack transmission stress is given by,

$$S \geq \frac{k_l}{M_{Leading}\sqrt{r_0}}\left[\frac{1-e^{-\left(\frac{1-\cos\beta}{\alpha_1}+\frac{\sin\alpha}{\sin\alpha_0}\right)}}{1-e^{-\left(\frac{1}{\alpha_1}\right)}}\right] \qquad [5.4]$$

Here, M is the nominal Schmid factor in the Leading Grain, k is a locking parameter from the Hall-Petch relationship for tensile yield strength, r_O is included to prevent a stress singularity (typically 0.1 to 1 µm is used), α is the twist misorientation angle, β is the tilt misorientation angle, α_O is half of the maximum twist misorientation angle, used to normalize the function, and α_1 is a weighting parameter applied to scale the effect of twist misorientation in relation to tilt orientation. This critical crack transmission stress from the Panwar model will be compared to the relative levels of retardation at each grain boundary in an attempt to model crack retardation and arrest with varying parameters.

Role of Grain Boundary Misorientation in Crack Retardation and Arrest

For each characterized grain boundary from both *in situ* and foil specimens, the correlation of the retardation factor (the normalized reduction in crack growth rate at the grain boundary) with the Panwar model critical stress criteria, tilt misorientation angle, twist misorientation angle, nominal Schmid factor in the Leading Grain, m’ parameter, and stress intensity factor is shown in Figure 5.24. While some individual fatigue crack-grain boundary interactions appear to follow predictions based on the models and parameters, there is no overall trend or definitive correlation.

Boundary sites from *in situ* specimens generally show good agreement with model predictions of behavior for each parameter, although the number of sampled boundaries is small compared to the number of boundary sites sampled from foil specimens. Crack-grain boundary interactions from the *in situ* specimens C1 and C3 were characterized by a high level of crack retardation or arrest, while boundaries in specimen C2 exhibited very little retardation in crack growth rate. Considering the Panwar critical stress criteria, twist misorientation angle, and m' parameter, the level of crack growth retardation generally followed expected behavioral trends, although the range of the Panwar critical stress criteria is not as large as that observed in foil specimens. The relation between crack growth retardation and tilt misorientation is less conclusive, however, with low tilt angles corresponding to many levels of crack retardation. Similarly, nominal Schmid factor in the Leading Grain provides little insight into the crack-boundary interaction, as the majority of sampled boundaries tend to exhibit relatively high nominal Schmid factors in the Leading Grain.

The larger number of boundary sites from foil specimens allows for a more comprehensive characterization of the efficacy of the discussed models and parameters in describing actual fatigue behavior. For each parameter, significant scatter in the level of crack growth retardation was observed. Considering the body of grain boundary data as a whole, no clear trend was observed relative to any of the parameters. However, a few important conclusions can be drawn from the data.

Fatigue crack-grain boundary interaction sites that experienced relatively high maximum stress intensity factors (2.12 $\text{MPa}\cdot\text{m}^{1/2}$ and higher) generally exhibited lower levels of crack retardation, with crack growth rates retarding at a maximum of approximately 40% of the steady state crack growth rate, and in many cases exhibiting no retardation of growth rates. Given a simple estimation of the plastic zone size in monotonic loading for the plane stress condition:

$$r_{monotonic} = \frac{1}{2\pi}\left(\frac{K_{max}}{\sigma_{ys}}\right)^2 \tag{5.5}$$

Theoretically, the cyclic yield stress can be approximated as $\sigma_{ys}^{cyclic} = 2\sigma_{ys}$, meaning the plastic zone size for cyclic loading in the plane stress condition will be a quarter of the monotonic plastic zone size, or

$$r_{cyclic} = \frac{1}{8\pi}\left(\frac{K_{max}}{\sigma_{ys}}\right)^2 \tag{5.6}$$

For a stress intensity of 2.12 MPa·m$^{1/2}$, this corresponds to a plastic zone size of approximately 9 μm, around an order of magnitude smaller than the average grain size [207]. It is possible the increased driving force for crack propagation at higher stress intensities was enough to overcome disadvantageous grain boundary characteristics.

Based on the boundary site data, the role of nominal Schmid factor in the Leading Grain in crack arrest and retardation is unclear, but it does provide insight into crack path selection. The average nominal Schmid factor of Leading Grains at sampled grain boundaries was 0.41, indicating that the fatigue crack tended to propagate crystallographically most readily through grains with a high driving force. Crack propagation often responded to grains with low nominal Schmid factor by changing active slip systems, and at times switching to noncrystallographic transgranular or intergranular growth when faced with low driving forces for crystallographic growth, as seen at a number of the characterized boundaries. For example, at GB 3 in foil specimen F3, crack growth transitioned from basal growth to intergranular growth, likely as a result of the very low nominal basal Schmid factor (0.11) in the Leading Grain, despite the low tilt and twist misorientation angles of basal-to-basal growth. (23° and 33°, respectively).

It is important to note that the nominal Schmid factors presented here cannot be objectively compared across different slip systems when considering the driving force for crack propagation. Studies have shown that the critical resolved shear stresses for slip systems in magnesium vary widely, with the prismatic and pyramidal systems exhibiting values much larger than those observed in the basal slip system, up to multiple orders of magnitude [28]. This means that, although a particular grain may exhibit a nominal pyramidal Schmid factor that is higher than the nominal basal Schmid factor, crack growth may occur along the basal system before the stresses necessary to drive pyramidal slip are reached. This is further complicated by the fact that the uniaxial stress state assumed for the nominal Schmid factor may deviate significantly from the actual local stress state in each grain, the determination of which would require more accurate simulation through crystal plasticity finite element analysis. Despite this, nominal Schmid factor measurements for different systems gives us a starting point to understand the ease of crack propagation along different slip systems relative to neighboring grains and provides additional context to crack growth behavior across grain boundaries.

Tilt and twist misorientation, as with the other parameters, featured significant scatter in observed fatigue crack-grain boundary interaction behavior. When considered alone, tilt misorientation does not appear to have a determining effect on the level of crack growth retardation; grain boundaries with tilt misorientations ranging from minimum to maximum values exhibited both high and low levels of crack growth retardation. While twist misorientation also exhibits a high level of scatter, the average twist misorientation across boundaries where crack propagation continued across the boundary (boundaries with complete arrest excluded) was 37°, with approximately two thirds of these exhibiting twist misorientation angles below 45° (considering different possible slip systems as different cases). Foil specimen F4 provides insight into the minimum level of twist misorientation necessary to produce crack retardation or arrest. Crack propagation in specimen F4 occurred predominantly along the basal slip system. Each of the four grain boundaries detailed in the study exhibited fairly low tilt and twist misorientation angles, with a maximum observed tilt angle of 32° and a maximum observed twist misorientation angle of 45°. Additionally, crack propagation occurred through grains featuring high basal Schmid factors, with a minimum observed value of 0.43. Each of the first four grain boundaries appeared to have no effect on crack propagation rates, excluding retardation in crack growth rates that occurred as a result of crack arrest in the non-dominant branch of the crack, which was unable to be characterized in terms of grain boundary misorientation. Considering the advantageous levels of tilt misorientation and nominal Schmid factor, twist misorientation angles below 45° were inadequate to produce notable crack retardation or arrest, indicating that, in the absence of other limiting factors, twist misorientation must be higher than 45° to produce crack arrest. This critical value of twist misorientation is dependent not only the magnitude of additional factors limiting crack propagation, but also on crack parameters affecting the driving force for crack propagation, meaning the impact of twist misorientation will decrease as stress intensity factor increases.

Further insight into the coupling of tilt and twist misorientation is gained by looking at fatigue crack propagation in *in situ* specimen C3. In specimen C3, crack propagation occurred across GB 1, despite the exhibited very high tilt angle and moderate twist angle, albeit with a high level of retardation in crack growth rate. Crack arrest was observed at GB 2, despite the fact that tilt misorientation angle was significantly lower than that observed at GB 1, and twist misorientation angle was only slightly higher. In each case, Leading Grains featured high nominal basal Schmid factor. This behavior raises the critical question of how the magnitude of twist misorientation is linked to the spectrum of crack arrest, retardation, or uninterrupted crack propagation, and what quantitative level of contribution does tilt misorientation have on this effect, if any? In the case of these two boundaries, tilt misorientation appears to have a less significant contribution to crack growth rate phenomena than twist misorientation, considering that at GB 1, a tilt misorientation angle of near maximum value permits crack propagation, while at GB 2, a tilt misorientation angle of half that value results in crack arrest with only a minor increase in twist misorientation angle. This is further reflected in the complete lack of correlation between tilt misorientation and crack growth retardation seen in Figure 5.24.

Considering this unequal weighting of tilt and twist misorientation, the m’ parameter becomes an inaccurate predictor of crack arrest and retardation as it is based partially on the angle between slip plane normals, which does not deconvolute or separately weight the influence of tilt and twist angles. This is reflected in the wide scatter of crack growth retardation data relative to m’ parameter in Figure 5.24. The significant amount of scatter in the crack growth retardation data corresponding to both tilt and twist misorientation is reflected in the data corresponding to the m’ parameter. This illustrates the flaw in more complicated model parameters based on weighting the contributions of various first order parameters like tilt, twist, or nominal Schmid factor: despite weighting, scatter in first order parameters is propagated through to the higher order model of fatigue behavior. This is observed in the high amount of scatter in the data corresponding to the Panwar critical stress criteria and corresponding levels of crack growth retardation. A trend of crack propagation occurring through boundaries exhibiting lower values of the critical stress criteria is observed, similar to the trend observed in twist misorientation values, although, again, no clear relation between the critical stress criteria and level of crack growth retardation was evident.

Fractographic Investigation of Grain Boundary Characteristics

A number of grain boundaries were investigated through scanning electron fractography to determine similarities in the nature of crack propagation across the boundary relative to misorientation characteristics of each boundary. Figure 5.25 through Figure 5.28 show a selection of boundaries grouped by tilt and twist misorientation characteristics. In each case, the direction of crack propagation is from right to left, and the detailed boundary is highlighted using a dashed line.

In general, a wide variety of fracture surface characteristics are observed across all boundary types. Frequently, the Leading Grain (left side of each image) features many tearing lines in the direction of crack growth (Figure 5.25b, Figure 5.26b, Figure 5.28), indicating small-scale crack branching or stepped fracture at the grain boundary. Zhai et al. [117] hypothesized that these fracture steps form as the crack propagates across grain boundaries featuring high twist misorientation angles in order to effectively reduce the twist angle (at the grain boundary) between crack faces in the two neighboring grains, resulting in a reduced level of crack growth retardation at the grain boundary. In this study, the formation of fracture steps did not appear to vary with the degree of tilt or twist misorientation and was observed across boundaries featuring most combinations of both high and low tilt and twist misorientation.

Although the fracture surfaces surrounding some grain boundaries were more tortuous and rough, this did not appear to correlate with higher levels of crack growth retardation. For example, GB 4 in specimen F5 (Figure 5.27b) featured a significant amount of crack growth retardation (Figure 5.22), but the fracture surface in both the Leading Grain and Trailing Grain was relatively smooth. Conversely, GB 4 in specimen F4 (Figure 5.25b) resulted in no significant reduction in crack growth rate (Figure 5.20), despite the significant surface roughness in the Leading Grain.

Non-Grain Boundary Based Instances of Crack Retardation

When considering short crack growth behavior, the occurrence of crack arrest or retardation is not always associated with the interaction of the crack and a grain boundary. Crack growth rates may appear reduced when crack growth occurs along preferred crystallographic planes inclined at a steep angle relative to the loading direction, as frequently occurred in both foil and *in situ* tests in this study. Generally, these reductions in crack growth rate are minor, but tortuosity of the crack path is a necessary consideration when evaluating the effect of microstructure on crack propagation rate. Similarly, crack arrest or retardation frequently occurs in response to the branching of a fatigue crack. These crack branching events may not be clear from surface observations for many thousands of cycles, although they can have significant effects on crack growth rate before that point. Early crack growth in foil specimen F4 exhibited a significant retardation of crack growth rate and apparent arrest near the first encountered boundary, followed by rapid crack propagation due to the occurrence of subsurface crack branching which only became evident as the new crack branch breached the surface and coalesced with previous crack growth. Fractographic investigation revealed that early crack growth was apparently dominated by a large grain on the opposite face of the foil, with crack growth trailing behind on the observed front for approximately 3 grain diameters. Crack branching in specimen F3 also resulted in accelerated growth rates as a new crack branch grew past the end of the previous branch. In specimen F5 post-mortem fractography of the fracture surface revealed that a secondary crack branch had formed in addition to the observed crack, resulting in a secondary fracture surface that rejoined the initial crack. The impetus for the formation of a second crack branch is not always clear solely from surface observations. Zhai et al. [117] have proposed that a high level of twist misorientation can explain the occurrence of subsurface crack branching. They postulate that early crack propagation occurs through the generation of shallow surface cracks along slip planes featuring large Schmid factors. When these cracks are shallow on both sides of a grain boundary, the effect of crack plane twist on crack growth behavior is minimal, as the area bounded by the twist angle is small. As the crack growths deeper into the sample, the energy necessary to fracture the area bounded by the twist angle increases significantly. Zhai et al. suggest that crack branching may occur when this energy rises above that necessary to drive crack propagation along a slip plane with a lower Schmid factor and lower twist misorientation angle.

Refinement of the Grain Boundary Interaction Model

Although the discussed phenomenological models evaluated in this study are a positive step in the modeling of a complex three-dimensional problem, they fail to consider contributions from neighboring grains (beyond those which directly host the crack) to surface-measured fatigue behavior, as well as the complex coupling effects between each boundary, microstructural, and crack parameter. In this work, it is clear that both tilt and twist misorientation play a role in the resistance of a boundary to crack propagation, albeit with differing degrees. It is also clear that these parameters must be modeled together with the resolved shear stresses in Leading Grains to allow for accurate prediction of crack path and crack growth rates, arrest, and retardation. As discussed previously, nominal Schmid factor may not be an accurate enough measure of the stress state in each grain, which is intricately tied to the local microstructural neighborhood. For alloys featuring complexity beyond simple bi-crystals or large columnar grains, meaningful investigation of the crack-grain boundary interaction requires more accurate modeling of true three-dimensional microstructure, possibly through crystal-plasticity finite element analysis.

Pierson et al. [208] have had some success in modeling fatigue behavior by correlating three-dimensional crack paths with micromechanical fields derived from high-fidelity crystal-plasticity finite-element simulations of three-dimensional fatigue and microstructural data obtained using near-field high-energy X-ray diffraction microscopy. Their modeling work was based on the work of Spear et al. [12], in which a naturally initiated fatigue crack was propagated to failure under cyclic loading in an Al-Mg-Si alloy. The material volume above and below the fracture surface was characterized in three-dimensions using X-ray computed tomography and near-field HEDM, in a method described in detail in Chapter 6. Pierson et al. were able to perform correlation analysis between 88 computed micromechanical parameters, including field variables and slip-based damage metrics, to the known path of the Al-Mg-Si fatigue failure surface. They found that the gradients of micromechanical field variables generally exhibited a stronger correlation with the crack path than the field variables themselves, indicating that the fatigue crack generally sought paths of high gradient in stress, strain, or both. However, they also found that none of the considered parameters, treated independently, were sufficient to fully and accurately describe the formation of the fatigue crack surface. Their work indicates that the prediction of fatigue behavior is likely too complex a problem to be accurately modeled by a small number of parameters derived from observations of fatigue crack growth on the specimen surface. Rather, future work should focus on investigating fatigue behavior in a three-dimensional manner in combination with crystal-plasticity finite-element analyses.

5.5. Summary and Conclusions

Short crack propagation was investigated in both cylindrical and foil fatigue specimens in order to explore the interaction of a propagating fatigue crack with grain boundaries. The effect of grain boundaries on crack propagation behavior was evaluated using the geometrical models of misorientation developed by Zhai et al. [117], Luster and Morris [128], and Panwar et al. [130] and the efficacy of the models was discussed. The following conclusions can be made:

- Crack growth in both cylindrical and foil specimens was predominantly crystallographic transgranular in nature. Relative to the cylindrical specimen design, the foil specimens exhibited decreased levels of noncrystallographic growth and increased levels of basal and intergranular growth. This may be attributed to changes in the stress state in surface grains that occur because of the reduced thickness in the foil specimen.

- Investigation of crack behavior in situ and using foil specimens confirmed that tilt and twist misorientation angle often appear to have an effect on the ease of crack propagation across grain boundaries, but this is not always the case and an accurate quantitative relation between tilt and twist misorientation and levels of crack retardation or arrest has yet to be developed.

- In addition to boundary parameters like tilt and twist, both nominal Schmid factor and crystallographic plane orientation were shown to generally have a significant effect on crack path selection and crack growth rate; but, again, this was not always the case.

- The accuracy of twist misorientation measurement, and therefore any evaluation of the geometric model, is strongly dependent on accurate measurement of the subsurface orientation of the grain boundary. In some cases, relatively small levels of error in grain boundary orientation can produce large error in twist misorientation angle, depending on the crystallographic orientation of grains under consideration. Foil specimens partially simplify this issue, as a higher proportion of grain boundaries intersect the specimen free surface, allowing for determination of three-dimensional grain boundary orientation.

- Although the models evaluated in this study consider the effects of many microstructural, crack, and boundary parameters such as nominal Schmid factor, crack length, tilt misorientation, and twist misorientation, they fail to consider the effects of neighboring grains beyond those interacting with the surface-observed crack. These neighboring grains can have a strong effect not only on fatigue behavior observed on the surface, but also on the local stress state controlling fatigue behavior, which may not be adequately captured by the nominal Schmid factor. Accurate modeling of these effects requires both comprehensive three-dimensional characterization of microstructure and fatigue behavior, and a model formulation that considers this complex three-dimensional problem.

Figures

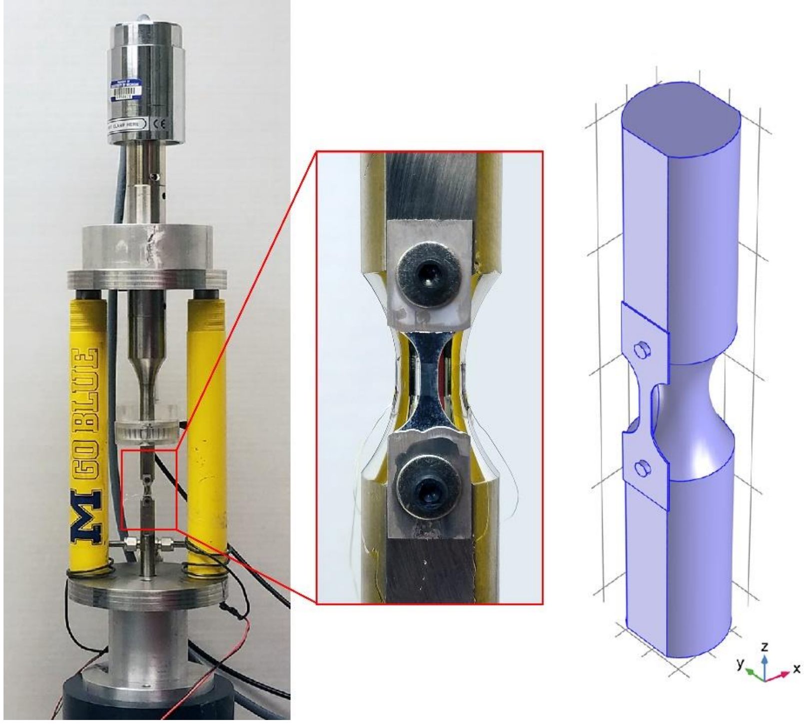

Figure 5.1 - Ultrasonic fatigue instrument configured for positive R ratio thin foil short crack growth tests. The foil specimen is attached to the shoulders of the carrier specimen, as detailed in [9].

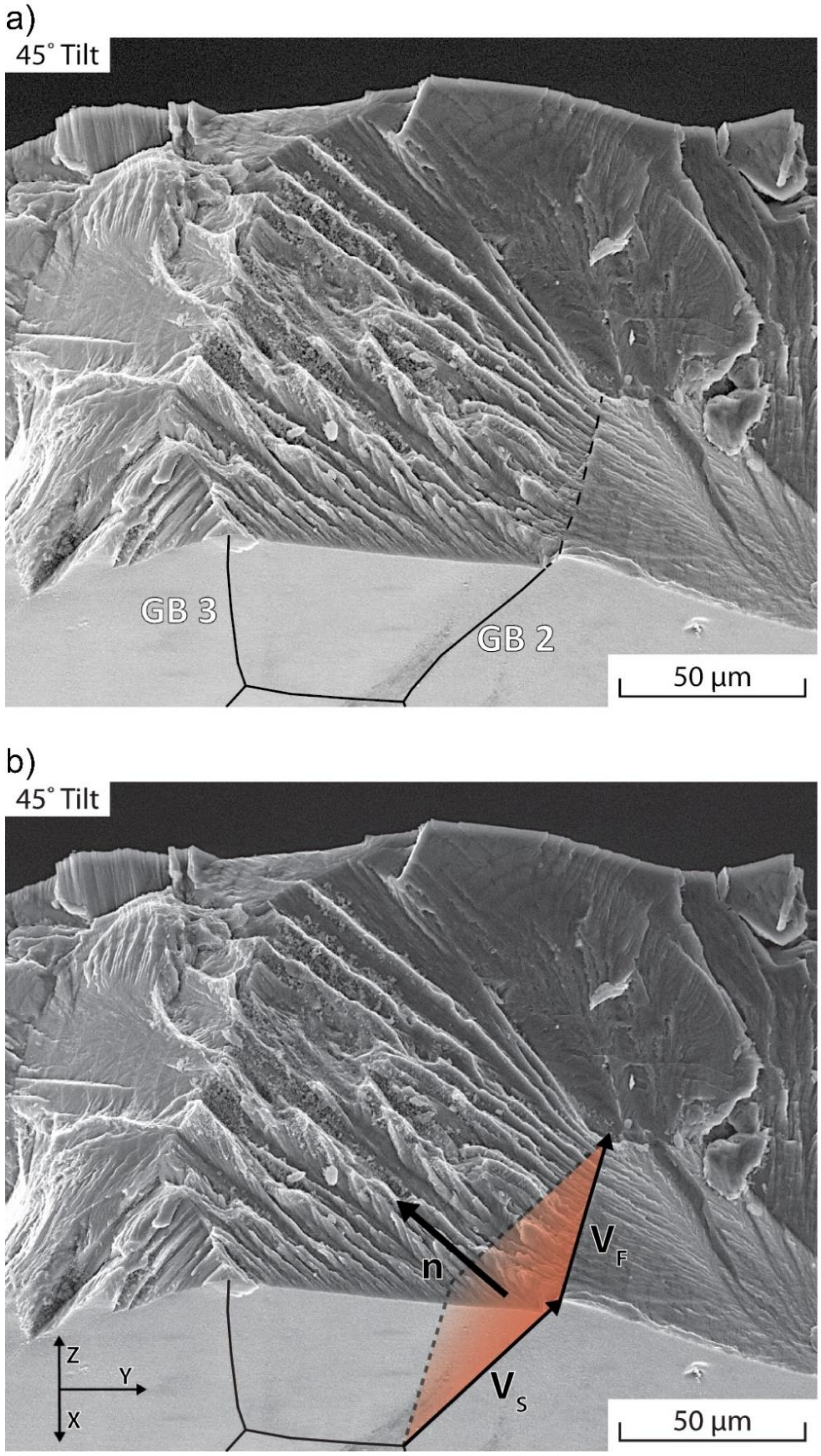

Figure 5.2 – a) Detail of rough fracture during fatigue crack growth in the pyramidal system (as identified by surface trace analysis) in the grain Leading GB 2 in foil specimen F1. b) Determination of grain boundary orientation in three dimensions using grain boundary traces measured from the free surface (VS) and the fracture surface mesh (VF).

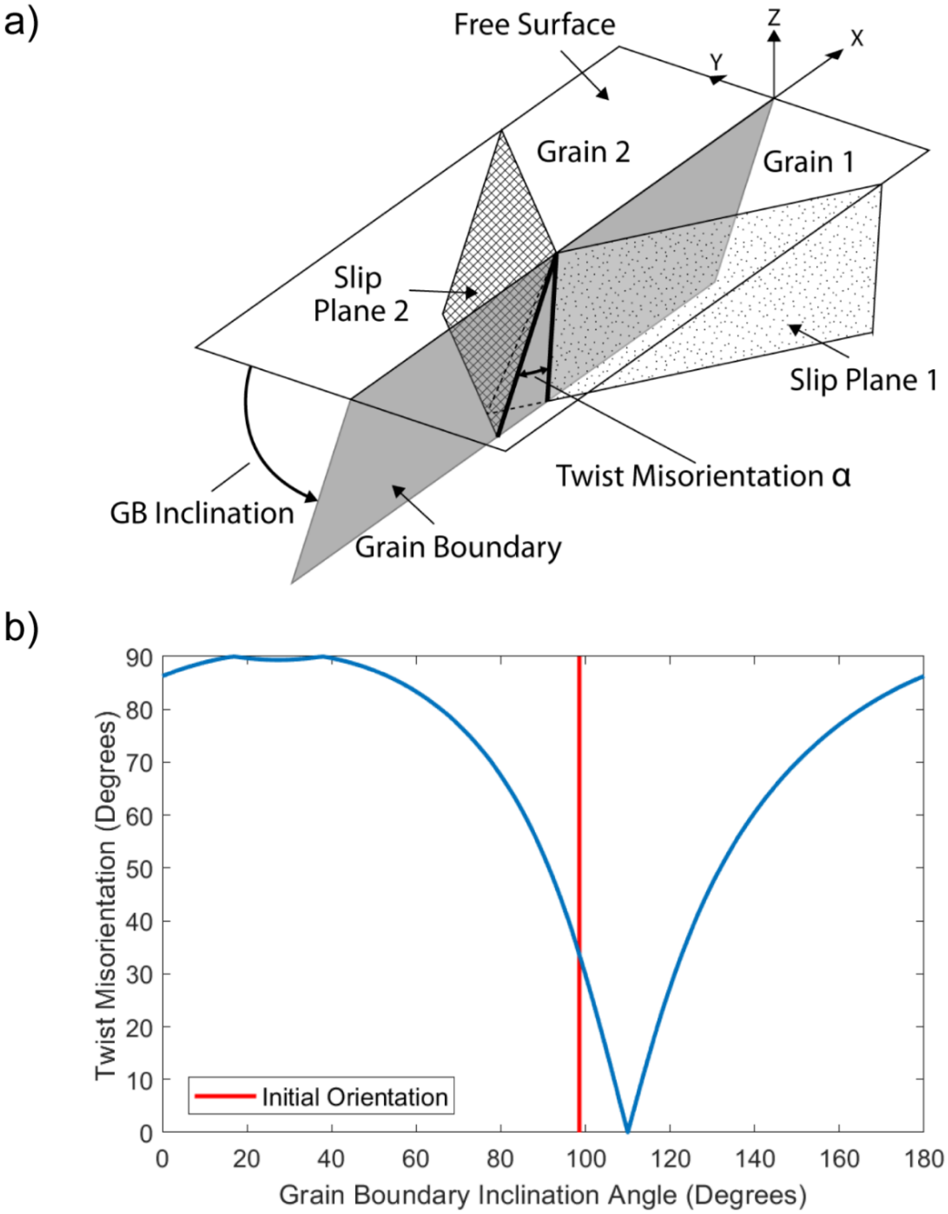

Figure 5.3 - Illustration of the effect of a) grain boundary inclination on twist misorientation angle, using b) grain boundary 1 of foil specimen F1 as an example. Minor variation in grain boundary inclination can result in significant variation in twist misorientation angle.

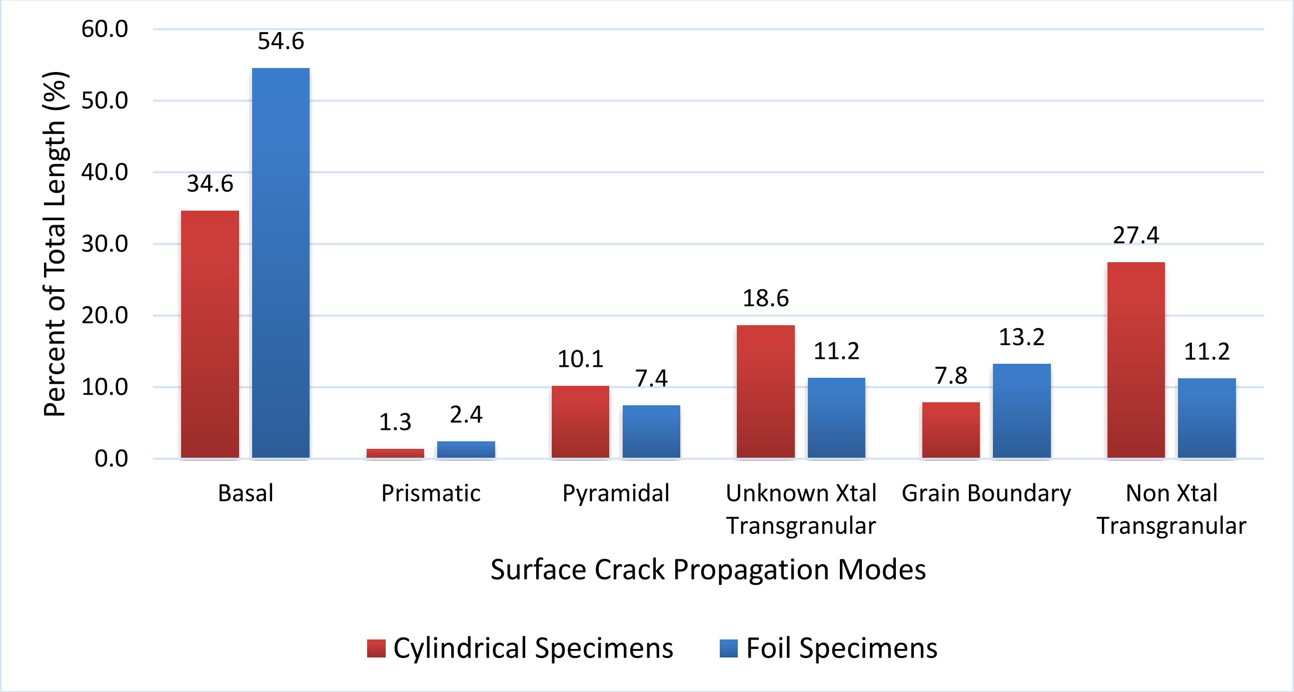

Figure 5.4 - Average surface-measured crack propagation modes for cylindrical and foil WE43 fatigue specimens

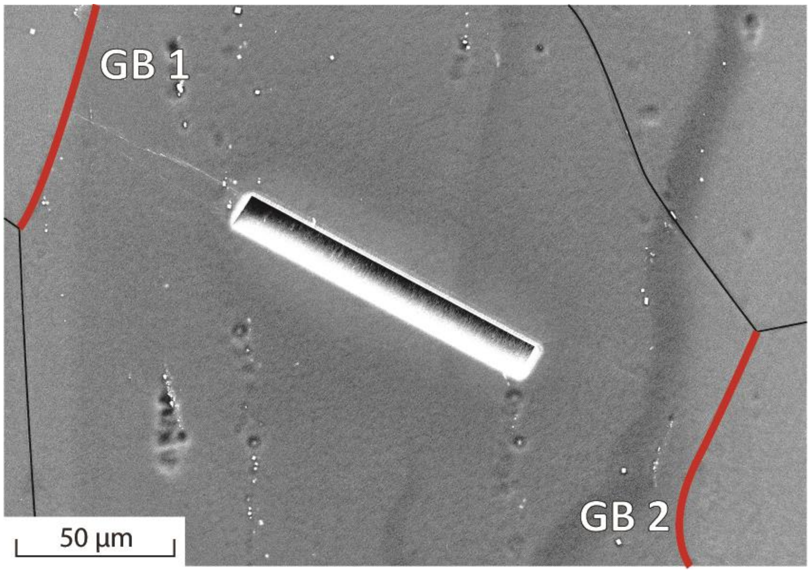

Figure 5.5 - Crack initiation site for in situ cylindrical specimen C1 exhibiting crack arrest at both GB 1 and GB 2.

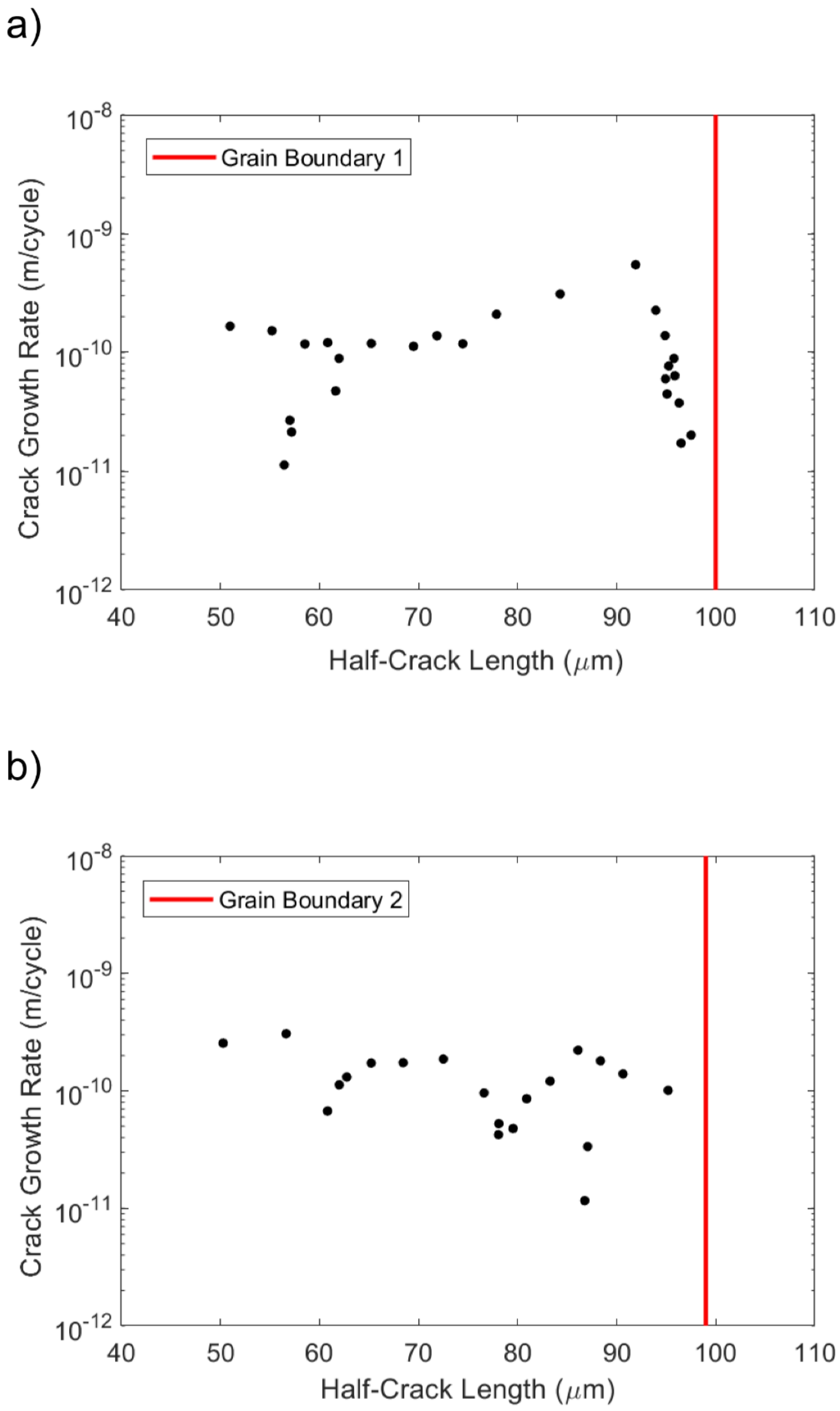

Figure 5.6 - Short crack growth in cylindrical specimen C1 showing crack interaction with grain boundaries from the a) left side and b) right side of the initiation site. In each case, retardation of crack growth rates was followed by crack arrest.

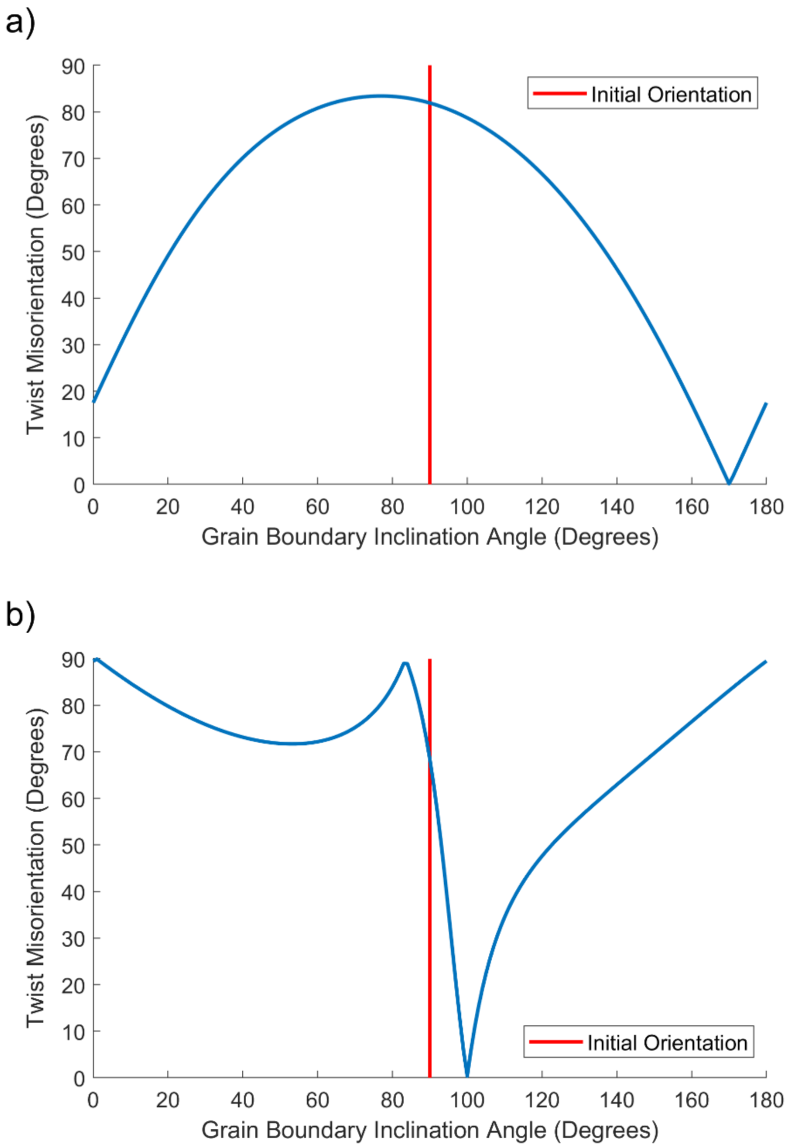

Figure 5.7 - Characterization of the possible variation in twist misorientation angle as a function of subsurface grain boundary inclination for boundaries a) GB 1 and b) GB 2 in the cylindrical in situ specimen C1, assuming an initial orientation perpendicular to the specimen free surface. In the case of GB 2, minor variation in subsurface inclination can produce significant changes in twist misorientation.

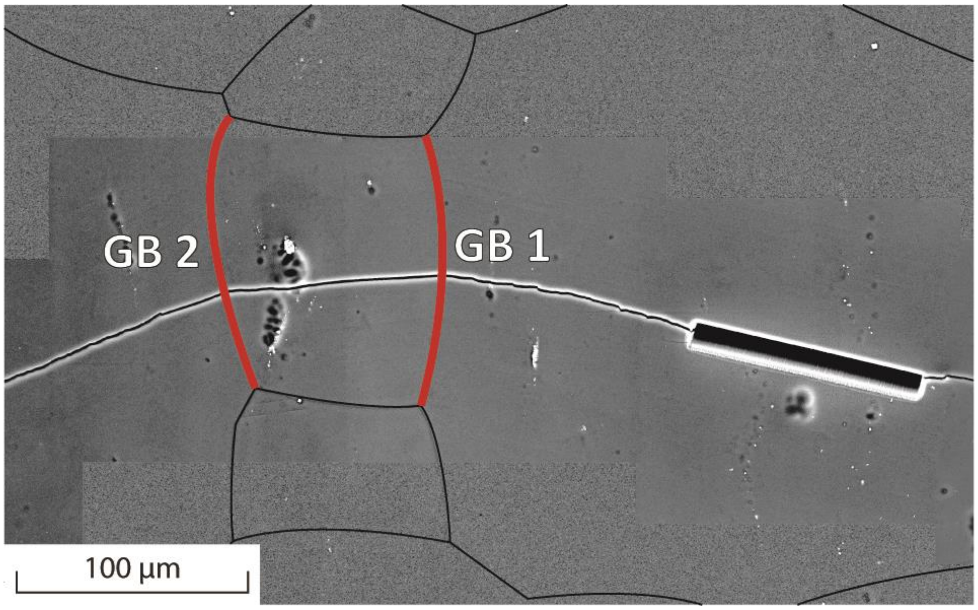

Figure 5.8 - Crack initiation site for in situ cylindrical specimen C2 exhibiting easy crack propagation through both GB 1 and GB 2 at the left side of the notch.

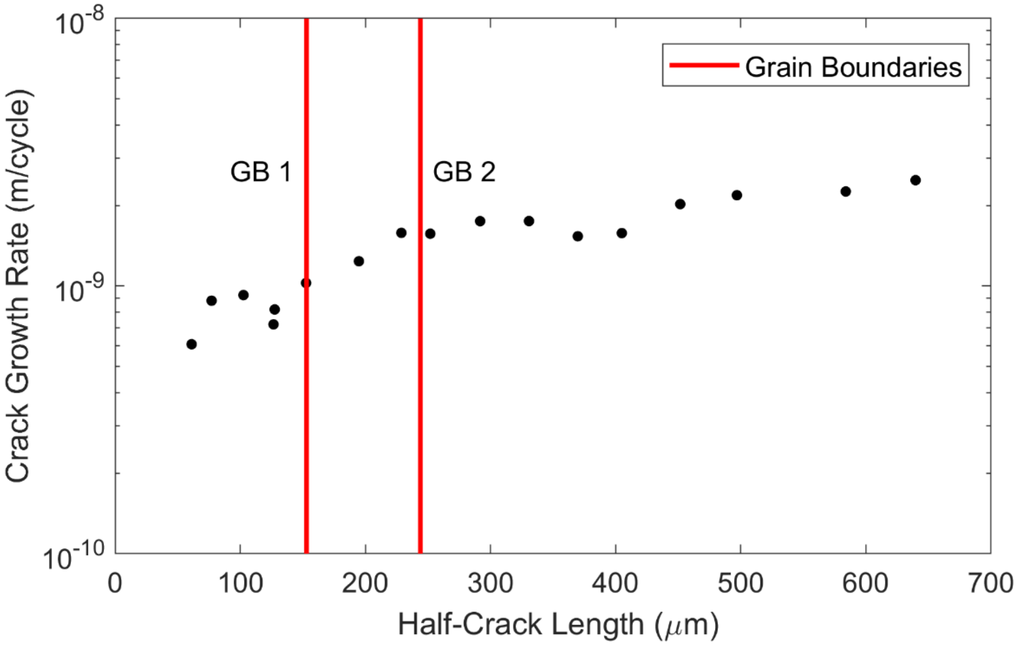

Figure 5.9 - Short crack growth from the left side of the notch in cylindrical fatigue specimen C2. Minor crack interaction with GB 1 was observed, while GB 2 had no apparent effect on crack growth rate.

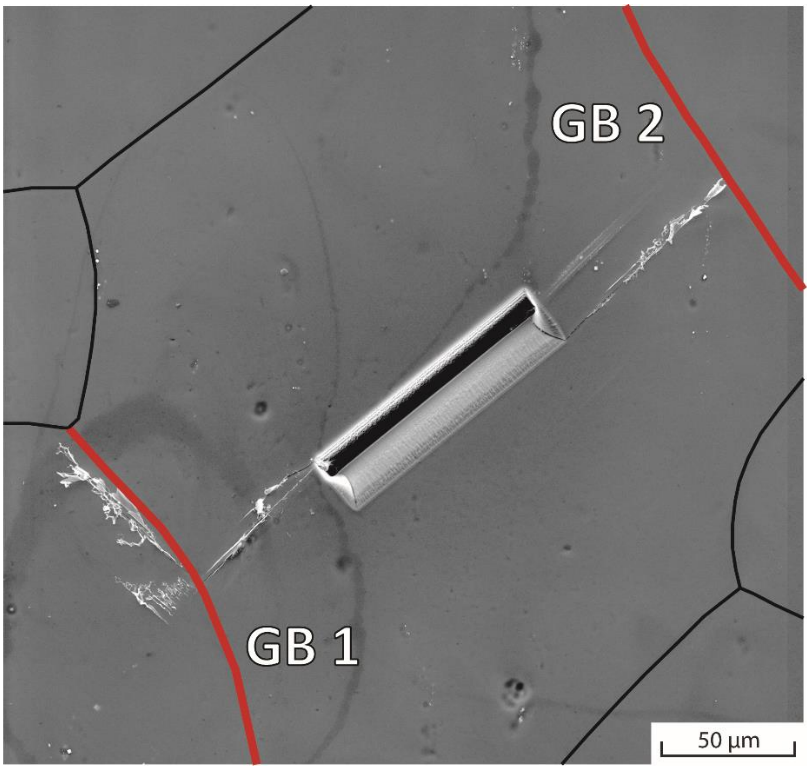

Figure 5.10 - Crack initiation site for in situ cylindrical specimen C3 exhibiting retardation of crack growth at GB 1 and complete arrest at GB 2.

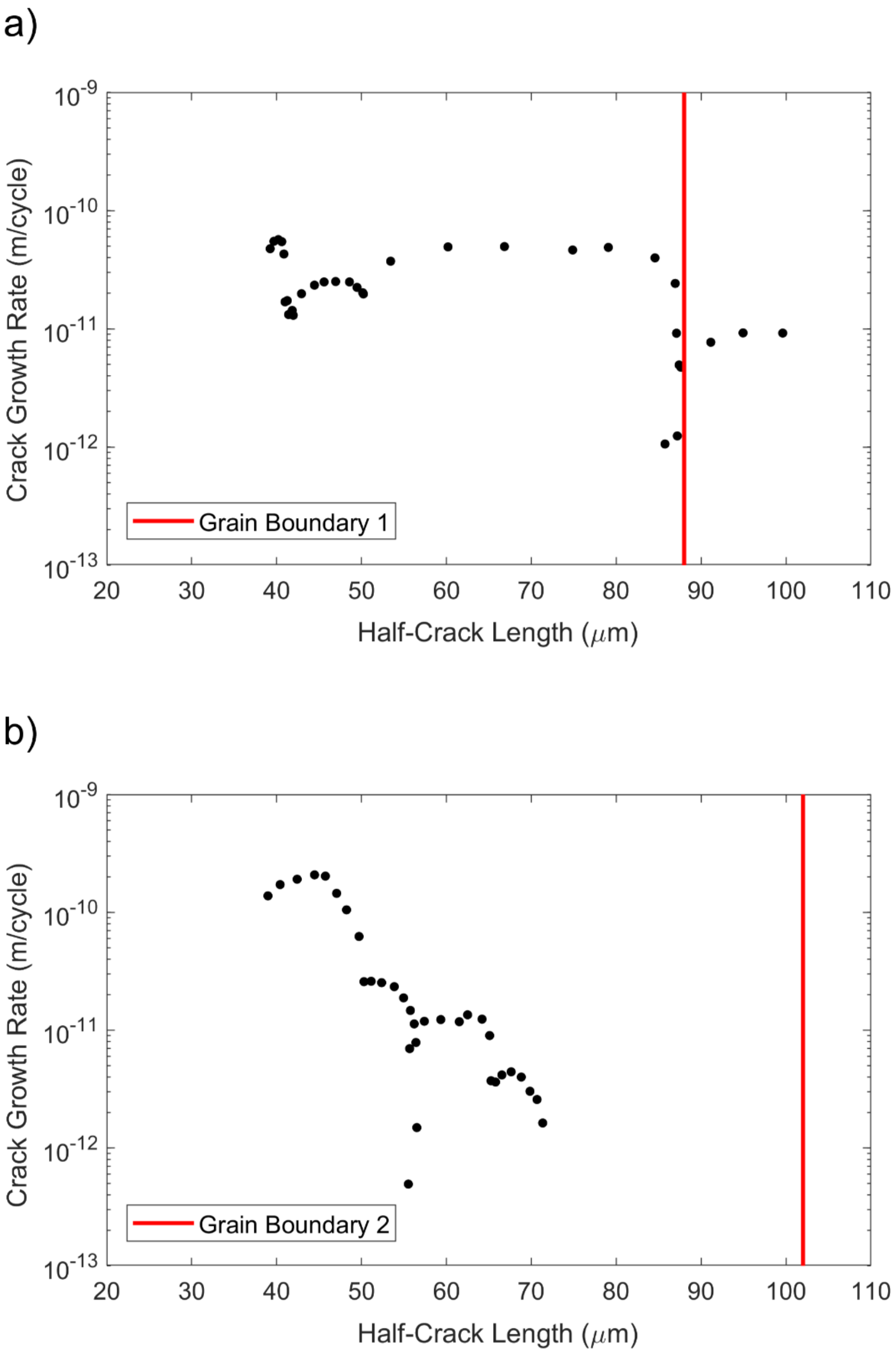

Figure 5.11 - Short crack growth in cylindrical specimen C3 showing crack interaction with grain boundaries from the a) left side and b) right side of the initiation site. At GB 1, the fatigue crack experienced retardation in growth rate, while GB 2 resulted in complete crack arrest.

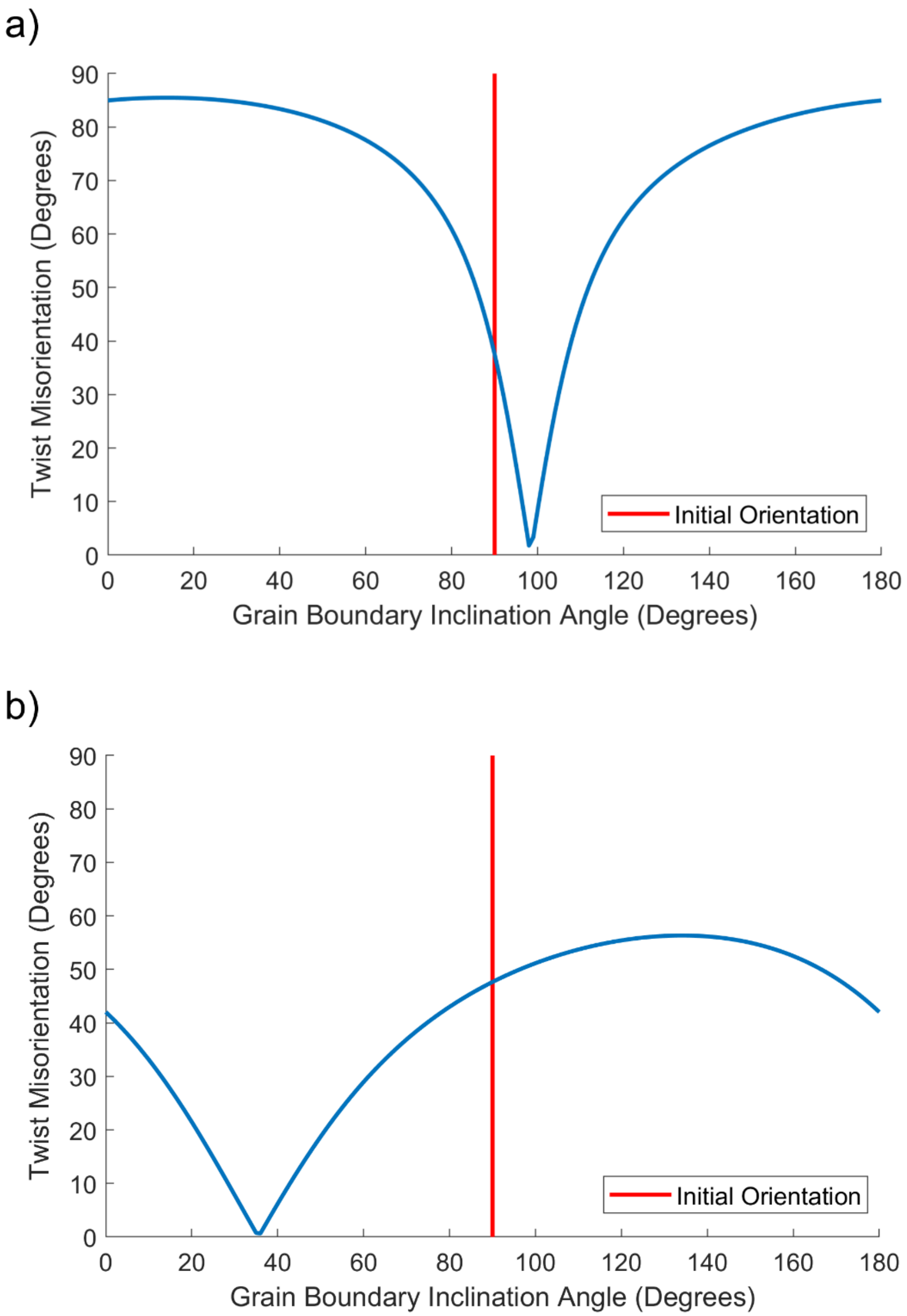

Figure 5.12 - Characterization of the possible variation in twist misorientation angle as a function of subsurface grain boundary inclination for boundaries a) GB 1 and b) GB 2 in the cylindrical in situ specimen C3, assuming an initial orientation perpendicular to the specimen free surface. In the case of GB 1, minor variation in subsurface inclination can produce significant changes in twist misorientation.

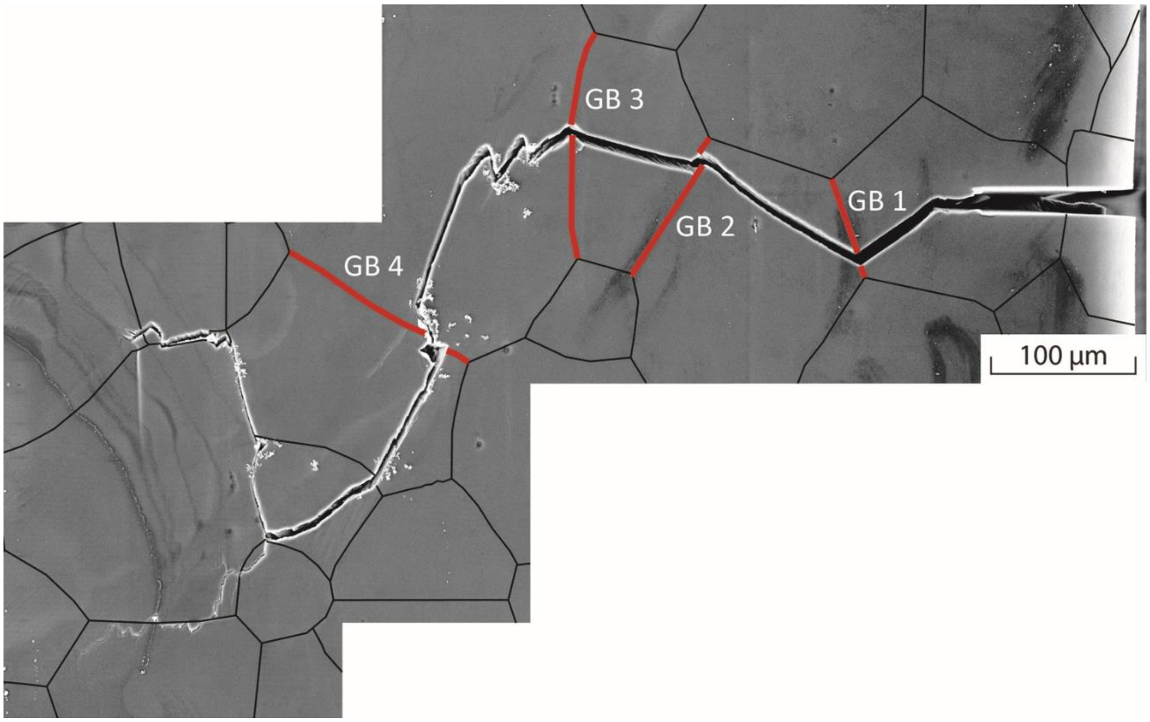

Figure 5.13 - Fatigue crack growth in foil specimen F1, exhibiting crystallographic transgranular and intergranular crack growth.

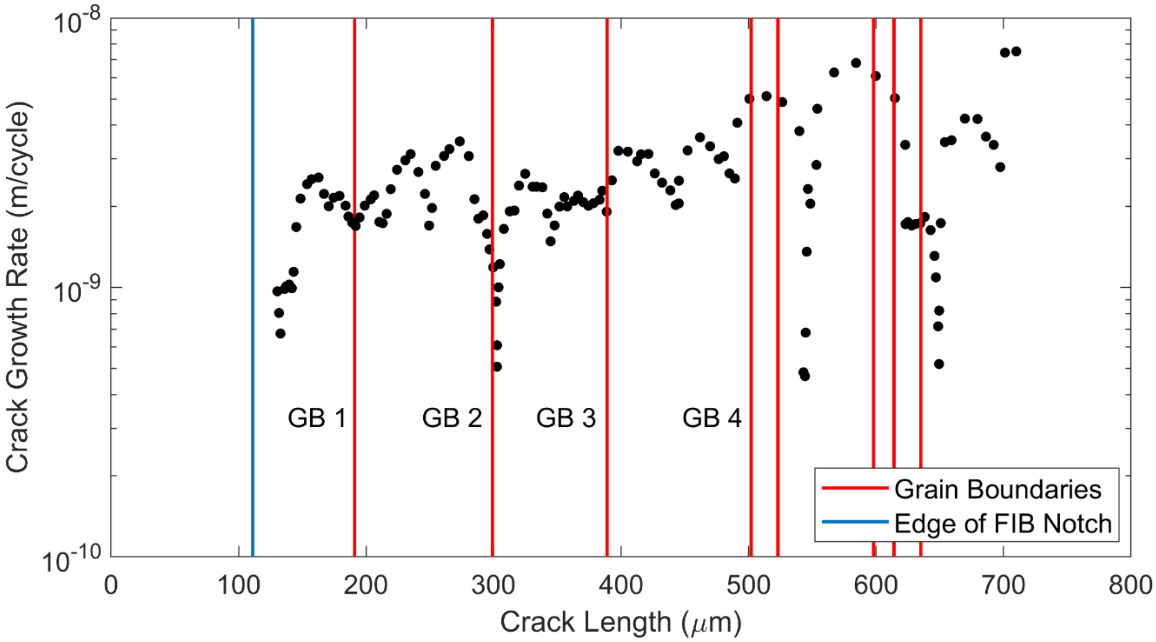

Figure 5.14 - Short crack growth in foil specimen F1 showing crack interaction with grain boundaries. Crack growth rates show retardation at boundaries GB 1 and GB 2.

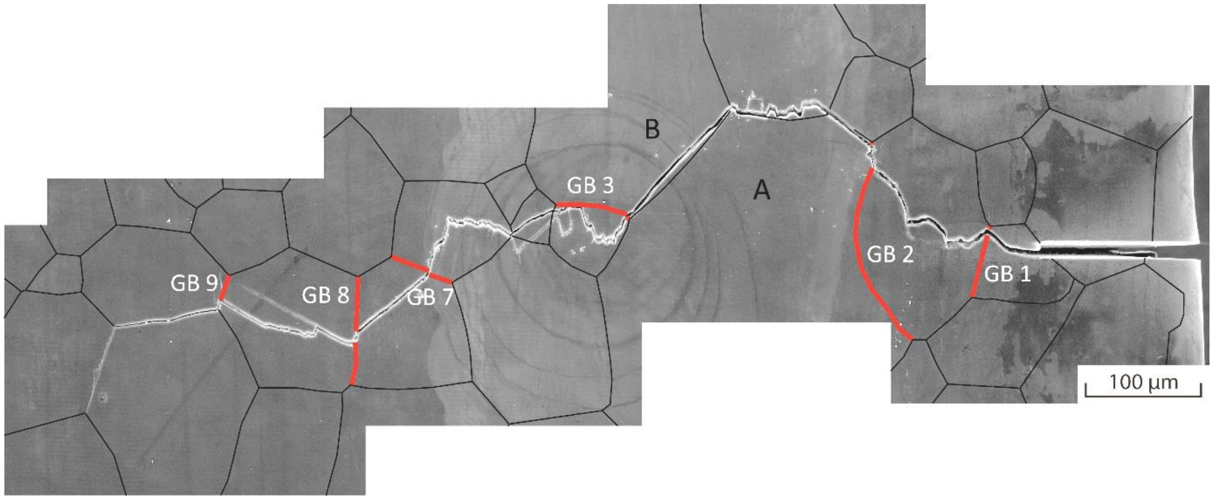

Figure 5.15 - Fatigue crack growth in foil specimen F2, exhibiting a mixture of crystallographic transgranular, non-crystallographic transgranular, and intergranular crack growth.

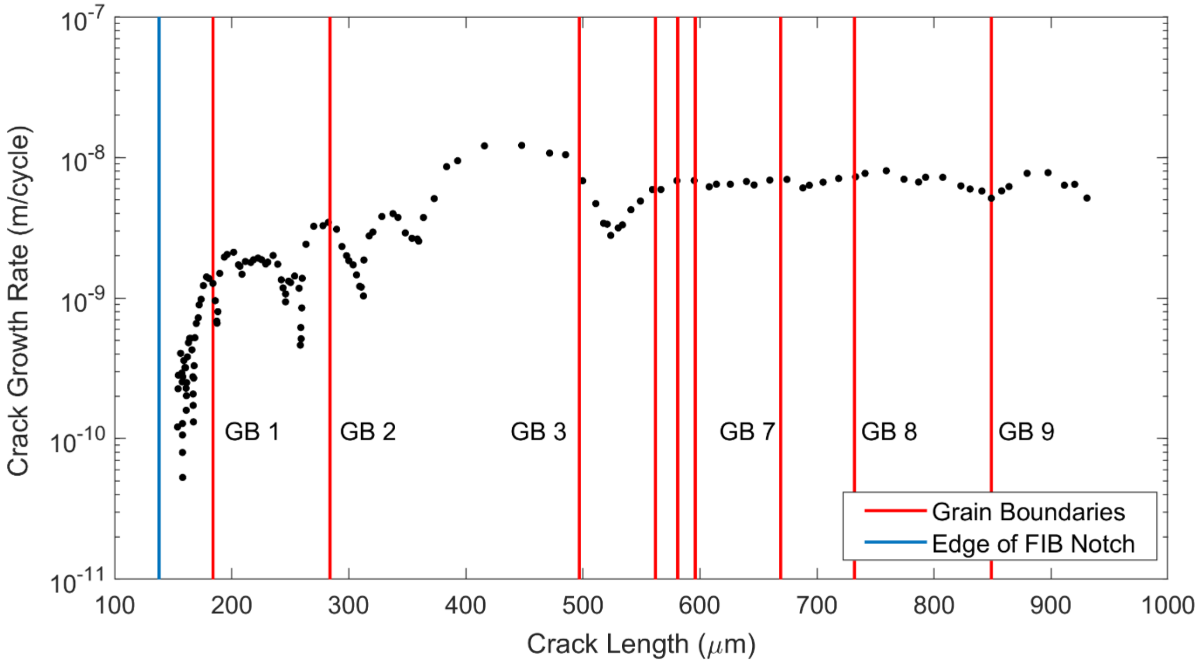

Figure 5.16 - Short crack growth in foil specimen F2 showing the interaction of the crack with grain boundaries. There was a minor retardation of crack growth at GB 1, while GB 2 and GB 3 exhibited no clear barrier to crack advance.

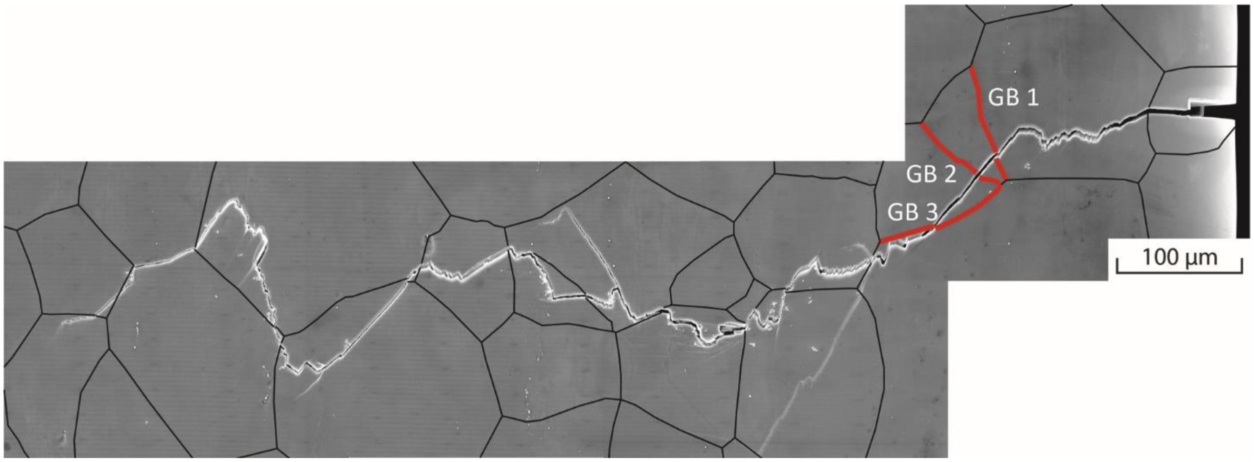

Figure 5.17 - Fatigue crack growth in foil specimen F3, exhibiting a mixture of crystallographic transgranular, non-crystallographic transgranular, and intergranular crack growth.

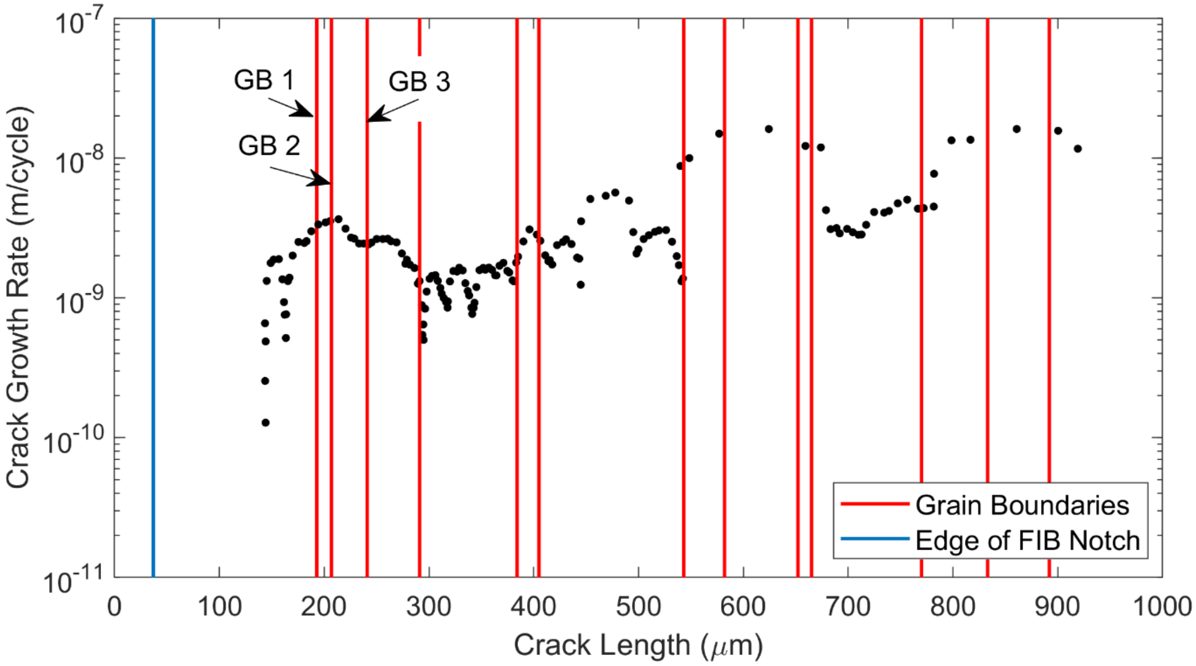

Figure 5.18 - Short crack growth in foil specimen F3 showing the interaction of the crack with grain boundaries. None of the three analyzed grain boundaries acted as significant barriers to crack propagation. Analyses of many later boundaries was precluded due to crack branching.

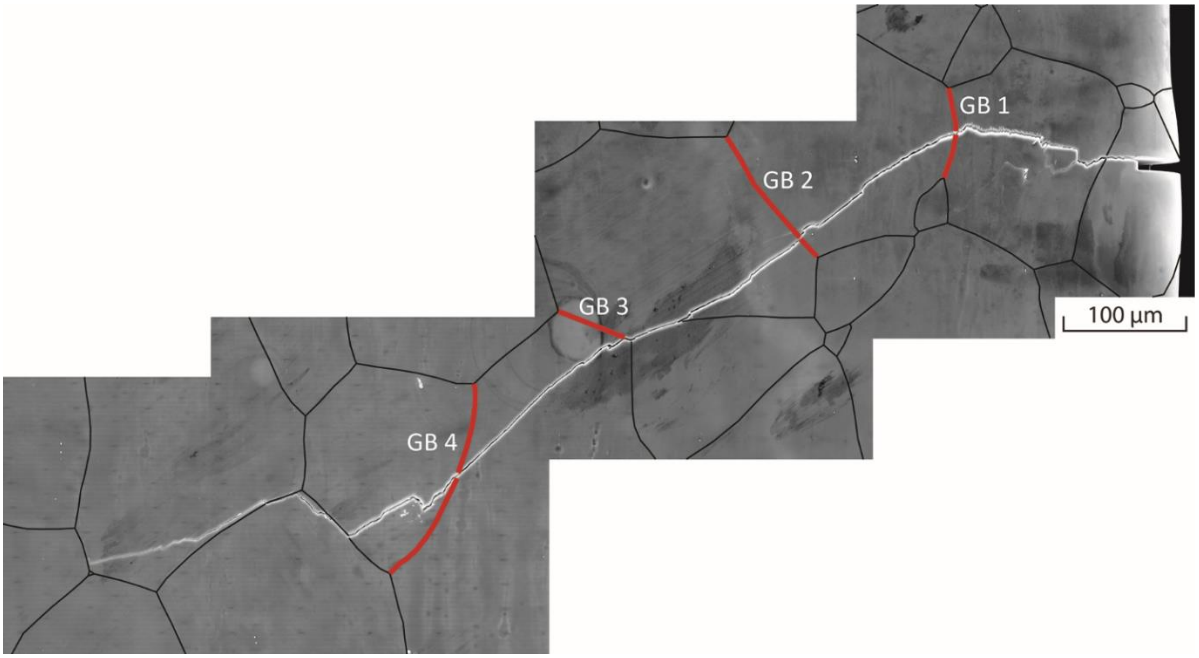

Figure 5.19 – Fatigue crack growth in foil specimen F4, exhibiting predominantly crystallographic transgranular growth along the basal slip system.

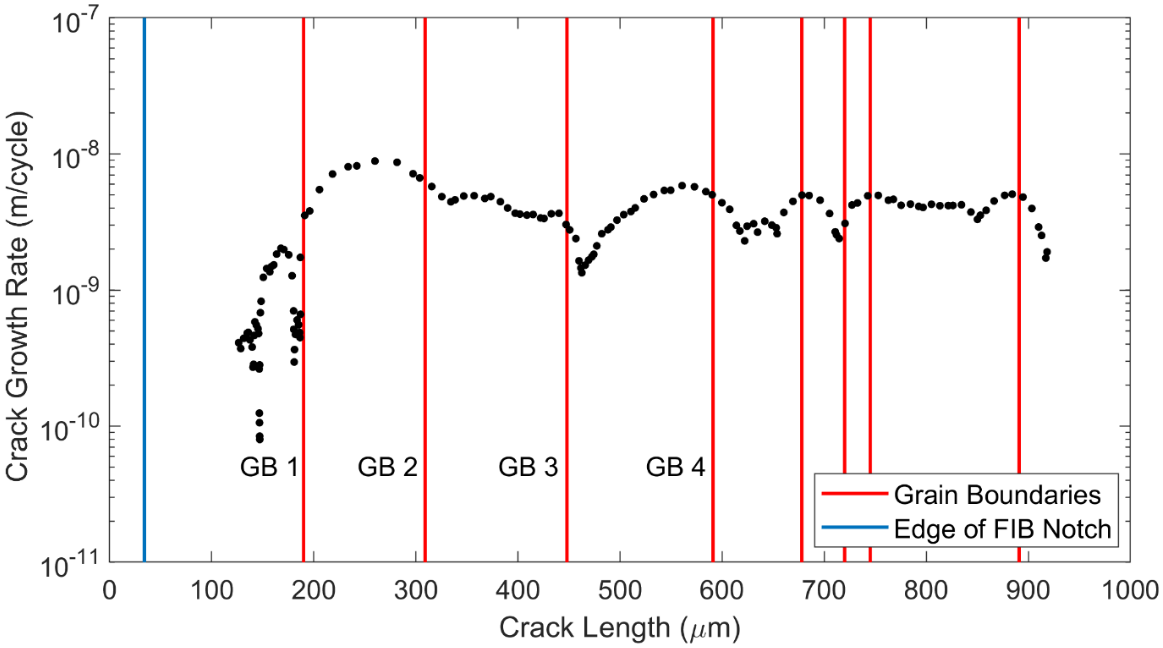

Figure 5.20 - Short crack growth in foil specimen F4 showing the interaction of the crack with grain boundaries. Of the four analyzed grain boundaries, only GB 1 exhibited a significant retardation effect on crack growth rate, which was accompanied by branching of the fatigue crack.

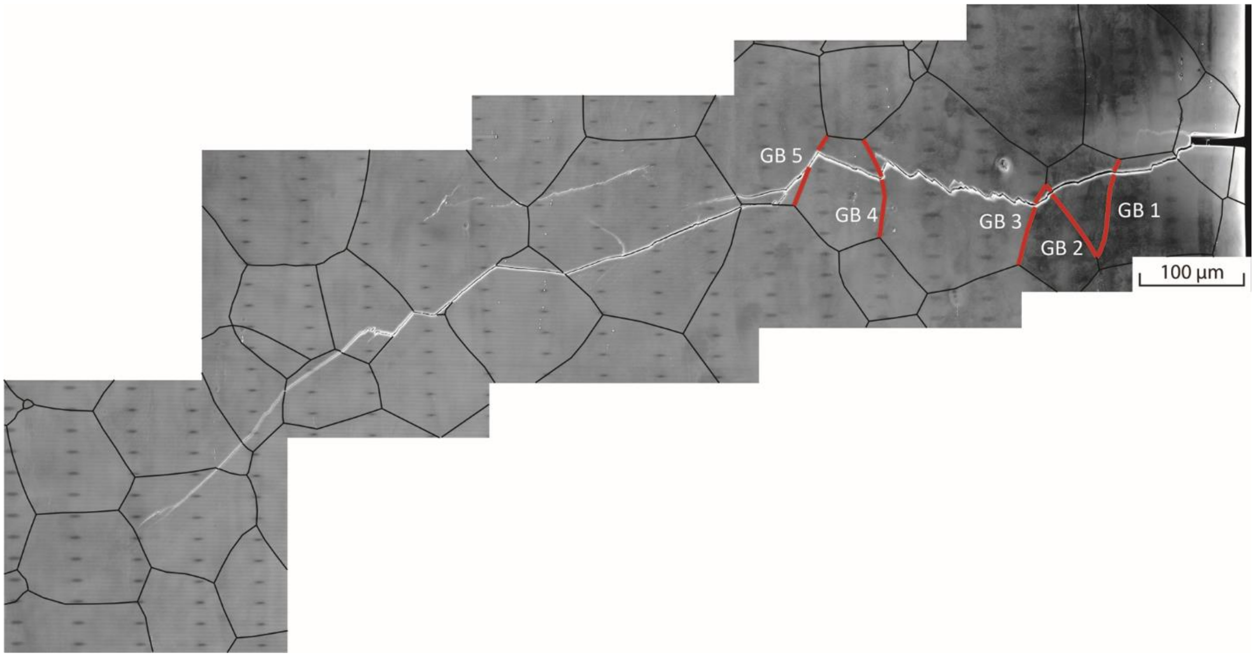

Figure 5.21 – Fatigue crack growth in foil specimen F5, exhibiting a mixture of crystallographic transgranular, non-crystallographic transgranular, and intergranular crack growth.

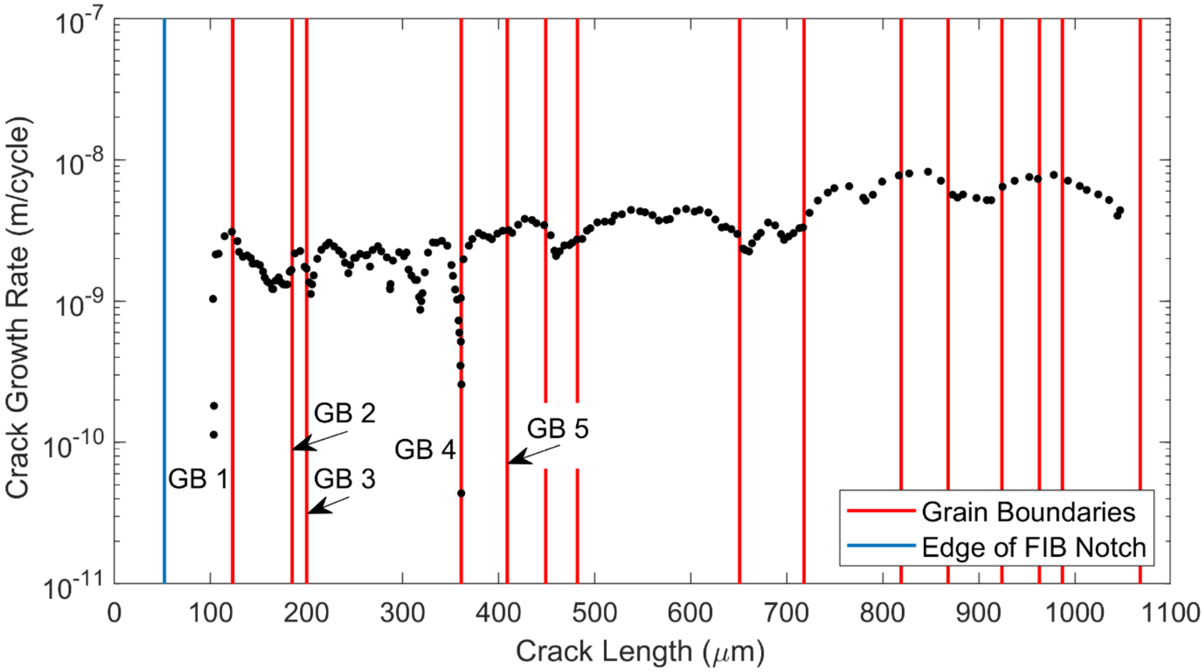

Figure 5.22 - Short crack growth in foil specimen F5 showing the interaction of the crack with grain boundaries. Crack growth was relatively insensitive to grain boundaries, although variation in active slip system and plane resulted in depressed crack growth rates in some grains and some periods of crack retardation. The interaction of the crack with GB 4 resulted in a period of crack arrest corresponding to a transition from tortuous crack growth in the pyramidal and prismatic systems to crystallographic growth on basal planes.

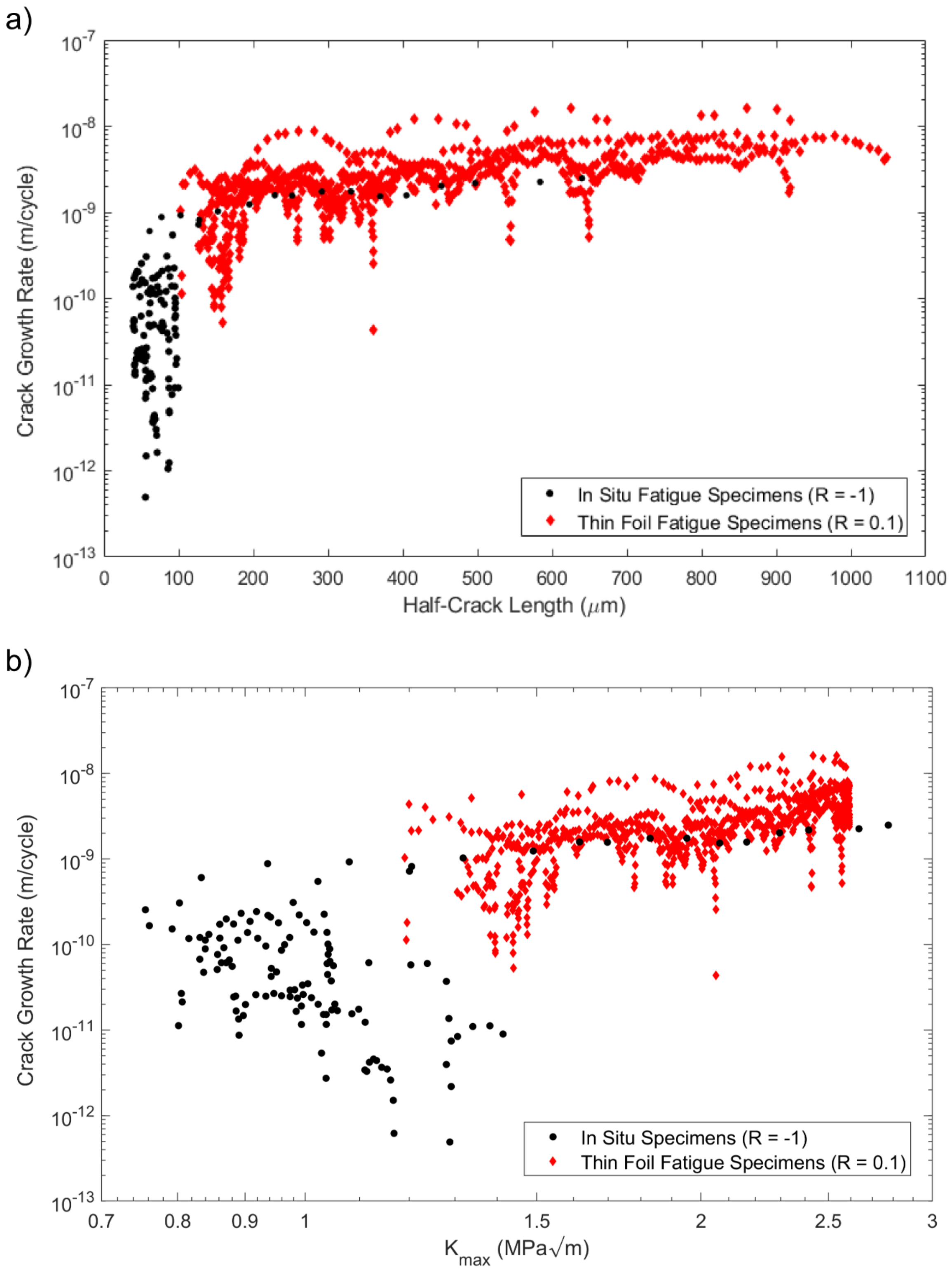

Figure 5.23 – Short crack growth behavior for *in situ* and foil specimens, comparing crack growth rate (da/dN) to a) crack length and b) maximum stress intensity factor. Displacement controlled loading and small specimen dimensions lead to compressed stress intensity factors in the foil specimens at longer crack lengths.

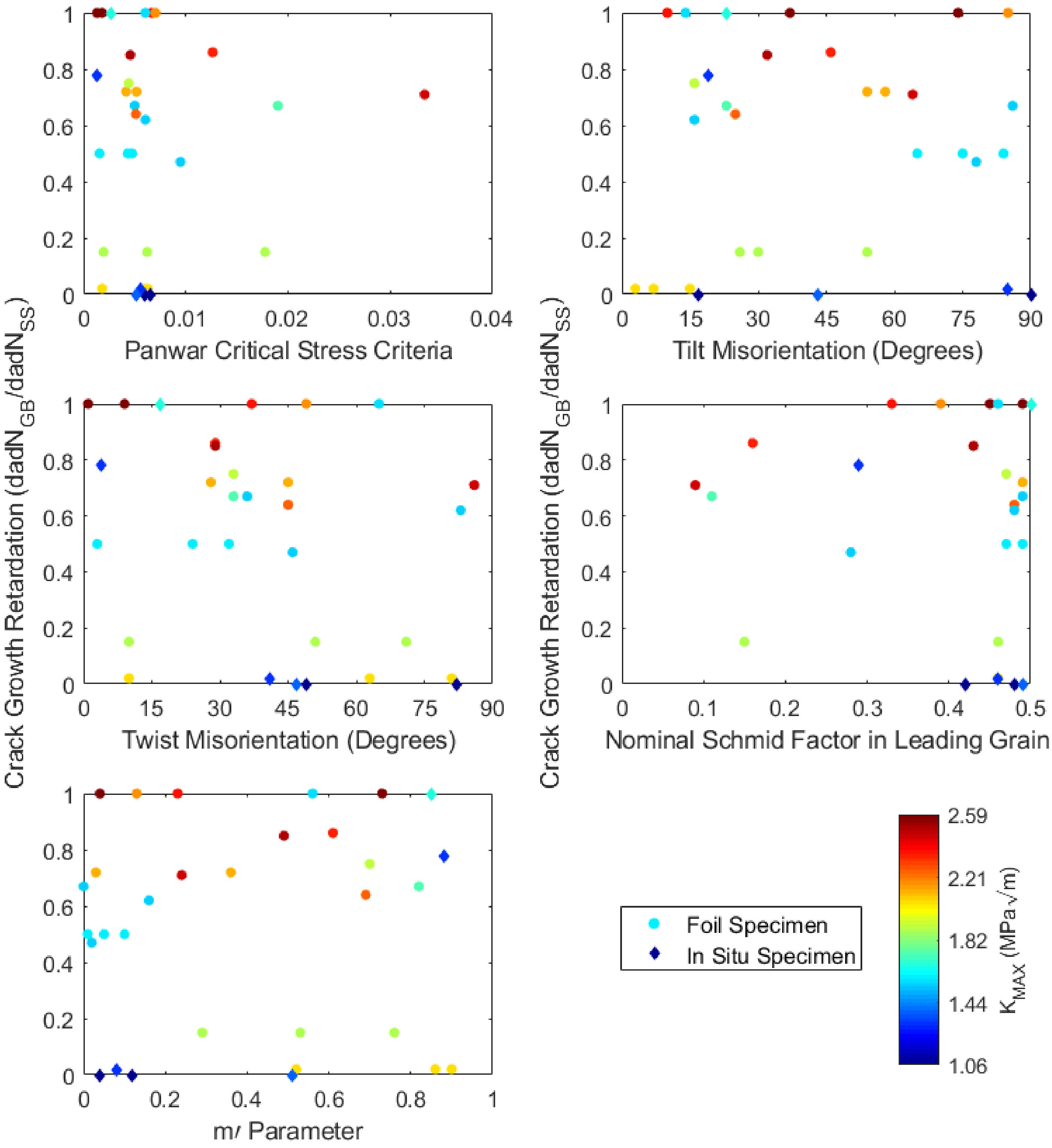

Figure 5.24 - Correlation of a variety of microstructural and model parameters with the relative retardation in crack growth rate observed at each grain boundary in foil and *in situ* specimens, along with the stress intensity of the crack for each boundary. Although these parameters have been linked to crack retardation and arrest at grain boundaries, no clear and definitive correlation is observed.

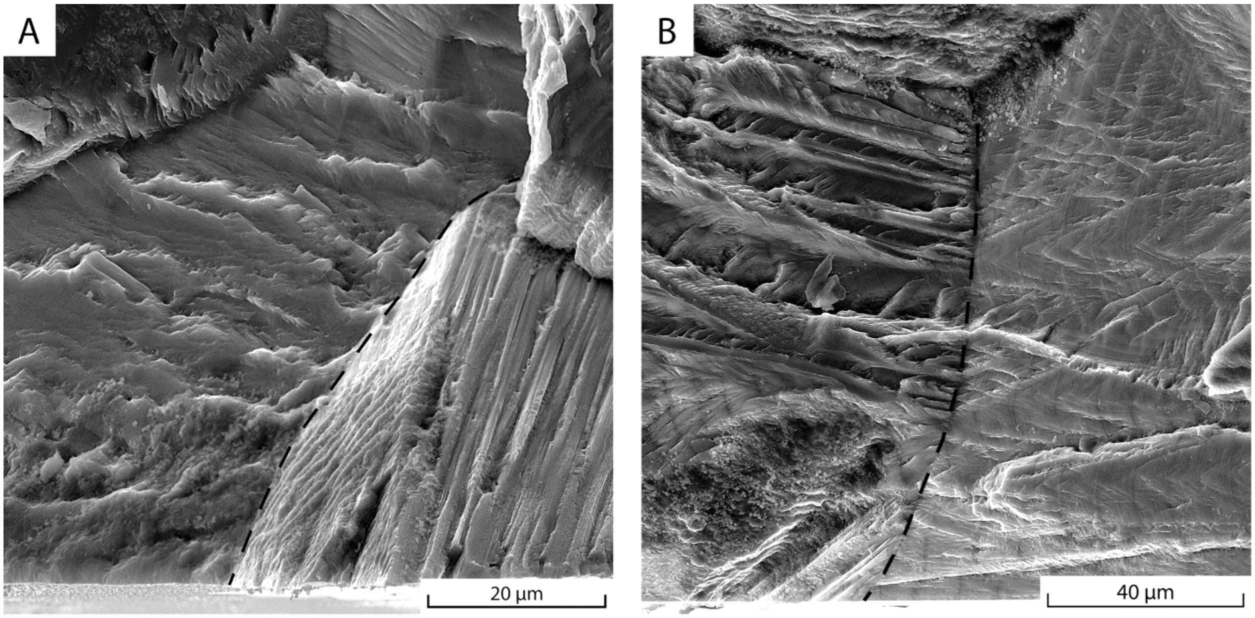

Figure 5.25 - Fractographic characterization of relatively low tilt and twist misorientation across A) GB 7 from foil specimen F2 and B) GB 4 from foil specimen F4.

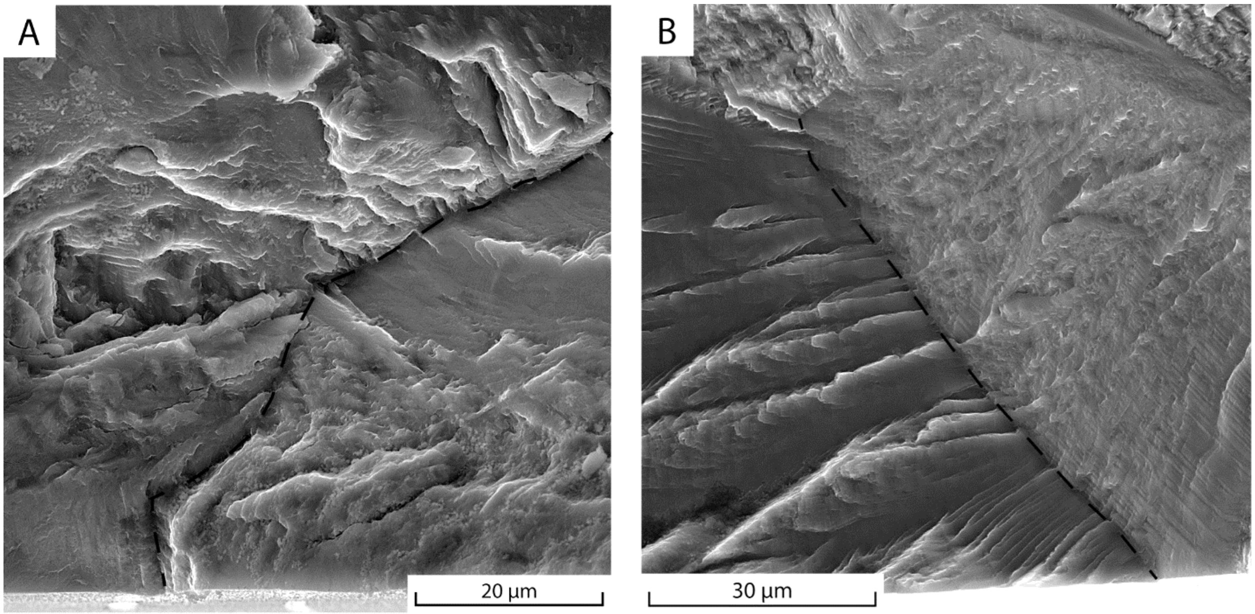

Figure 5.26 - Fractographic characterization of relatively high tilt and low twist misorientation across A) GB 8 from foil specimen F2 and B) GB 3 from foil specimen F5.

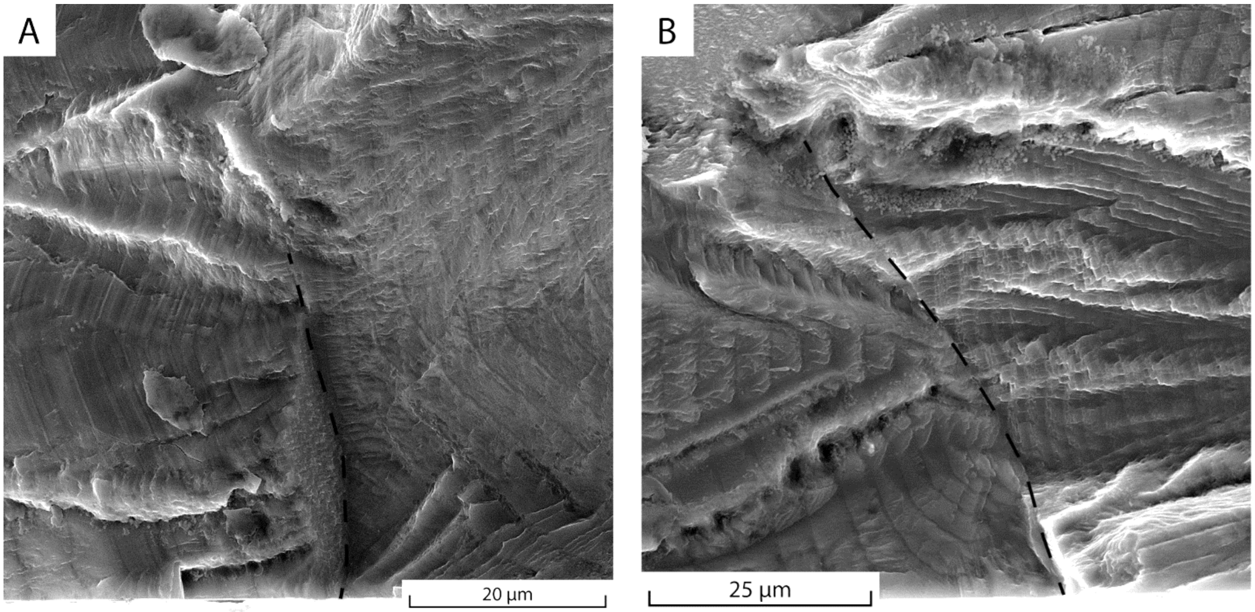

Figure 5.27 - Fractographic characterization of relatively low tilt and high twist misorientation across A) GB 3 from foil specimen F4 and B) GB 4 from foil specimen F5.

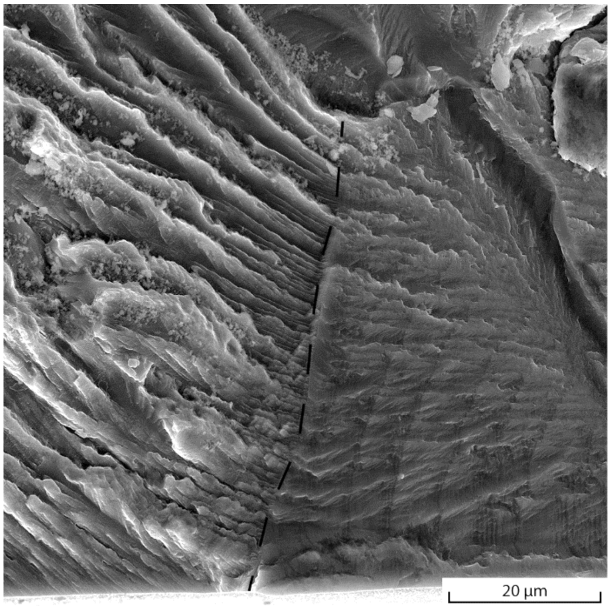

Figure 5.28 - Fractographic characterization of relatively high tilt and twist misorientation across GB 2 from foil specimen F1.

CHAPTER 6

THREE-DIMENSIONAL CHARACTERIZATION OF FATIGUE CRACK GROWTH IN WE43 MAGNESIUM

6.1. Introduction

Chapter 6 discusses an experimental methodology for interrogating short fatigue crack behavior in three dimensions and presents specific results from the fatigue of an underaged WE43 magnesium specimen. In situ fatigue testing was conducted using the UFSEM system discussed in Chapters 4 and 5 and was followed by post-mortem characterization of the fracture surface and surrounding microstructure. Micro-beach marks, discussed in Chapter 4, are used to measure and map local subsurface crack growth on crystallographic fracture facets. Following characterization of the fracture surface using scanning electron microscopy, X-ray computed tomography was conducted to produce high resolution reconstructions of the crack surface morphology in three dimensions. Near-field high energy X-ray diffraction microscopy (HEDM) was used to map grain geometries and crystal orientations in the volumes adjacent to the exposed failure surfaces. The data from high-resolution X-ray tomography and near-field HEDM were then merged to generate high-resolution maps of fracture surface crystallography. The experimental results led to insight into the evolution and variability of microstructurally small fatigue crack growth. Section 6.2 provides an overview of the material used in the study, as well as a brief review of the experimental methodology used to conduct the ultrasonic fatigue. The experimental techniques for mapping of crack growth rate using micro-beach marks, reconstruction of fracture surface morphology using X-ray tomography, and the investigation of crack surface crystallography using near-field HEDM are also described in more detail. A discussion of the technique for mapping local crack growth rate, as well as a discussion of specific results from the X-ray characterization of the fracture surface and crystallography is presented in Section 6.3. Section 6.4 summarizes the findings and presents conclusions.

6.2. Material and Experimental Methods

6.2.1. Material

Magnesium alloy WE43 was prepared by Magnesium Elektron Ltd. The composition (wt%) of the alloy is 3.74Y, 2.10Nd, 0.52Gd, 0.45Zr, 0.016Zn, and Mg (balance). The as-received material had been hot rolled and then aged for 48 hours at 204° C. Additional heat treatment consisting of solution treatment and aging was conducted in our laboratory to produce coarse-grained microstructures strengthened with rare-earth precipitates. Solution treatment of the as-received alloy was conducted at 525° C for 8 hours, followed by aging at 250° C for 4 hours to produce the underaged condition. Grain size was measured by standard methods using electron backscatter diffraction (EBSD) mapping in a Tescan Mira3 scanning electron microscope (SEM) with EDAX OIM Data Analysis software. The 525° C/8h solution treatment increased the average grain size from 13 μm to approximately 113 μm. The large grain size provides an ideal opportunity for investigating crystallographic transgranular crack growth and the interaction between short fatigue cracks and microstructural features. Mechanical and fatigue properties for this material in these conditions are discussed in greater detail in [11].

6.2.2. Specimen Preparation

A cylindrical fatigue specimen with a reduced gage section 4 mm in diameter and 7.5 mm in length was machined such that the longitudinal axis of the specimen aligned with the rolling direction of the source magnesium plate, following specimen designs outlined in [170]. To facilitate tracking of fatigue crack growth and crystallographic analysis using EBSD, diametrically opposed surface flats were machined into the gage section. The specimen surface was prepared by hand grinding with SiC paper and polishing with diamond solution, followed by electropolishing in a solution of three parts by volume 85% phosphoric acid (H_3PO_4) and five parts by volume 95% ethanol for 30 minutes. Approximately 30 µm was removed from the surface by electropolishing.

To enable the investigation of short crack growth behavior, a micro-notch was machined in the gage flat to act as a crack initiation site, using an FEI Quanta 200 3D focused ion beam (FIB) equipped with a gallium ion source operating at 30kV and a probe current of 5.0 nA. One FIB micro-notch was placed at a specific microstructural site and aligned parallel to the basal slip plane in that grain in three dimensions. This was achieved by first characterizing the crystallographic grain structure on the flats in the gage section using EBSD. Next, large grains with high nominal basal Schmid factors and grain boundary characteristics of interest were selected as possible locations for the micro-notch, with the notch entirely contained within the favorably oriented grain (on the sample free surface). Orientation of the basal system was determined through EBSD determination of Euler angles, and the sample was oriented during machining of the FIB notch such that the FIB micro-notch was parallel to basal planes. The micro-notch had a length of 100 µm and a width of 6 µm, and an approximate depth of 40 µm, although this depth was affected by the inclination of the notch relative to the specimen free surface.

6.2.3. In Situ Ultrasonic Fatigue

High spatial resolution (≈ 5 nm) imaging of fatigue damage at the microstructural length scale was accomplished using a unique combination of ultrasonic fatigue instrumentation and scanning electron microscopy, termed UFSEM. The ultrasonic fatigue instrumentation operates on the principles described in [164], and the UFSEM system is detailed in [10] and summarized here. The load line components of the system are machined from Ti-6Al-4V and are tuned to a resonance frequency of 20 kHz. The components include an ultrasonic transducer that produces a sinusoidal displacement using a piezoelectric material stack, an amplification horn that magnifies the displacement from the transducer and a lambda rod to extend the length of the load line. The ultrasonic load line is mounted to a custom-built SEM chamber door designed to fit with the Tescan Mira-3 microscope. The system is controlled by instrumentation that monitors and maintains the amplitude and frequency of the displacement signal in a closed loop system. A piezoelectric film sensor (Measurement Specialties, Inc. Model DT1-028K) is used to measure the displacement response in the load train. The fatigue specimen is positioned in the SEM chamber using a McAllister Technical Services MB1500 manual manipulator stage with five translational adjustments. The many degrees of freedom of the manipulator stage enable the observation and tracking of multiple microstructural features or fatigue cracks during a fatigue test.

The UFSEM system enables the characterization at the microstructural scale of fatigue crack growth in laboratory air. When conducting ultrasonic fatigue in laboratory air, cycling was conducted using the UFSEM system with the SEM chamber vented to laboratory air. A duty cycle of 200 ms / 9000 ms pulse/pause was used to permit imaging of crack advance and specimen cooling. Following a number of these duty cycles, testing was paused and crack advance was recorded in micrographs using the SEM, after which fatigue testing continued in laboratory air. UFSEM tests were conducted at a frequency of approximately 20 kHz and at a stress ratio of R = -1 at room temperature, with a constant maximum stress of 85 MPa.

6.2.4. Mapping of Subsurface Local Crack Growth Rate

As discussed in [11], unique indicators of crack advance have been observed in WE43 magnesium. These indicators, referred to as micro-beach marks, directly correspond to individual duty cycles (ultrasonic pulses). Their width varies with crack growth rate, and so become more widely spaced with increasing ΔK. Variations in local microstructural can result in varying local crack growth rates, which is reflected in the width of the micro-beach mark bands on the fracture surface. These indicators of crack advance provide a unique opportunity for the investigation of local subsurface crack growth. As the number of loading cycles per ultrasonic pulse is known, measurement of micro-beach mark width allows for the calculation of crack growth rate, which can then be mapped across a surface featuring multiple micro-beach marks. As micro-beach marks are a direct result of ultrasonic pulses, variation in the length of the ultrasonic loading pulse can be used to produce patterns in the marks that can be used in subsequent fractography to pinpoint crack location at specified total applied cycles.

In combination with other characterization techniques, local crack growth rates can be correlated with microstructural characteristics such as crystallographic orientation, three-dimensional crack path tortuosity, and grain boundary misorientation characteristics. In this study, micro-beach marks are used to measure local short crack growth rates on individual grain fracture facets. Tilt photogrammetry was used to determine the orientation of fracture facets featuring micro-beach marks, which were subsequently imaged using scanning electron microscopy. Beach marks on these micrographs were then digitized and fit using splines to create crack front projections. Crack growth rates are then calculated along radial directions from the beach mark initiation point. For each ray, intersection points with micro-beach marks were identified. Next, the path length between adjacent intersection points was determined. This path length was taken as *da*, while the number of loading cycled elapsed in the ultrasonic pulse was taken as *dN*. Using this method, the crack growth rate for each line segment was determined, resulting in a map of local crack growth behavior.

6.2.5. Post-mortem X-ray Tomography and High-Energy X-ray Diffraction Microscopy

Three-dimensional short fatigue crack behavior in WE43 magnesium was investigated post-mortem through the use of X-ray computed tomography and near-field HEDM, which allowed for the characterization of the volume of material immediately surrounding the specimen fracture surfaces. Measurements were performed at the 1-ID beamline of the Advanced Photon Source (APS) at Argonne National Laboratory.

Specimen Preparation

Following fatigue failure and characterization of the crack path and fracture surfaces using scanning electron microscopy, the cylindrical fatigue specimen was sectioned on a slow-speed metallographic saw to produce a strip approximately 1 mm wide by 0.5 mm thick from both the top and bottom halves of the specimen. The strips were centered about the site of crack initiation, which was clearly identified by the presence of the FIB micro-notch and the appearance of distinct fracture features. The two strips were then mounted back-to-back to produce a 1 mm by 1 mm total cross section, exposing the initiation site on both mating sides of the fracture surface. The 1 mm-wide specimens were extracted from the larger fatigue specimen to ensure that an entire cross section of the sample would be illuminated by the high-energy X-ray beam throughout a 360° rotation. For both the X-ray tomography and near-field HEDM measurements (which were conducted during the same experiment), the sectioned specimen was mounted such that the loading axis was perpendicular to the incident X-ray beam.

X-Ray Tomography

High-energy X-ray tomography data were collected to enable reconstruction of the fracture-surface morphology with high spatial resolution. A beam energy of 52 keV was used to map attenuation in the volume immediately surrounding the exposed failure surfaces. Approximately 1800 tomograms were collected over a 360° rotation of the specimen. Filtered back-projection was used to reconstruct a set of two-dimensional images representing slices through the z-axis (vertical) of the specimen. Noise was then filtered from these 2-D images using an inverse Fourier Transform technique written in Matlab. The sample was reconstructed in 3-D using Avizo [181] to produce a three-dimensional representation of the fracture surface. Spatial resolution of the tomographic reconstruction was 1.42 μm per voxel edge length. The reconstruction of the fatigue fracture surface was later meshed using triangular facets to quantify crack-surface crystallography.

Far-Field High-Energy X-Ray Diffraction

Following tomographic characterization, far-field HEDM data were collected in a volume that spanned 800 μm along the z-axis (vertical). An 800 μm tall box beam was used to define the measurement volume for the dataset. The measurements were made over a 360° rotation in 0.25° intervals. Analysis of the diffraction data was conducted using the HEXRD code [182] to provide an initial map of grain centroids and crystallographic orientations. The set of indexed orientations was used during the reconstruction of near-field HEDM data to reduce the number of orientations that must be simulated, and thereby decrease the overall computational effort during near-field HEDM reconstruction.

Near-Field High-Energy X-Ray Diffraction Microscopy

The experimental setup for near-field HEDM was first presented by Poulsen [183]. Forward modeling techniques applied to the experimental data yield three-dimensional maps of grain structure, including morphology and crystal orientation, from the characterized specimen. For each cross-section of the specimen illuminated by the line-focused monochromatic (50 keV) X-ray beam (approximately 0.004 x 1.3 mm^2), diffraction spots from grains satisfying the Bragg condition were recorded at rotation intervals of 0.25° about the z-axis throughout a 180° rotation. Diffraction spots were recorded at two different detector positions to aid in the forward-modeling reconstruction. The specimen stage was then translated vertically 12 μm along the rotation axis, and a new set of diffraction images was collected from the newly illuminated plane of the specimen. This process was repeated over the height of material to be measured. Individual diffraction spots provide information on the parent grain including crystallographic orientation, spatial position, and grain geometry, allowing for the non-destructive characterization of three-dimensional microstructure and crack behavior. Near-field HEDM data was analyzed using the IceNine data reduction code [157].

6.2.6. Quantification of Fatigue Crack Surface Crystallography

In order to determine the crystallographic nature of the fracture surface, three-dimensional data gathered from X-ray tomography and HEDM corresponding to the separate halves of the fatigue specimen were separated and reoriented. The portion of data corresponding to the top half of the fracture surface was rotated by approximately 180° about the x axis, and features on the fracture surface were used to align the two halves. This realignment results in updated spatial coordinates for both the X-ray tomography and near-field HEDM reconstructions and required an adjustment to Euler angles derived from HEDM to account for the rotation of the reference frame.

Following the alignment of the two specimen halves, crystallographic information was assigned to each triangular facet in the fracture surface mesh derived from the X-ray tomography reconstruction, in a method introduced by [12]. The method first associates triangular facets from the mesh with their corresponding grains from the HEDM data set for both the upper and lower halves of the specimen. A misorientation threshold of 30° was used to distinguish between intergranular or transgranular facets. For transgranular facets, facet crystallography was established by resolving each facet normal into the crystal reference frame of the parent grain. This method allows for the quantification of crack surface crystallography over a three-dimensional, highly-resolved fracture surface without the use of destructive characterization techniques often used to interrogate internal facets.

6.3. Results and Discussion

The following subsections provide a general discussion of the local subsurface crack growth rate mapping technique, followed by a discussion of the specific fatigue behavior of the WE43 magnesium specimen characterized in two and three dimensions.

6.3.1. Characterization of Local Subsurface Crack Growth Behavior

Conventional measurements of crack propagation using indicators of crack advance on the fracture surface (beach marks, micro-beach marks, striations, etc.), are generally limited in that analysis is most often performed on two-dimensional images of the fracture surface. Analysis of the three-dimensional fracture surface performed using two-dimensional projections can result in calculated crack growth rates that underestimate the actual crack growth rate. The size of this error is dependent on the morphology of the fracture surface. With a three-dimensional mesh of the fracture surface, this limitation can be overcome, as detailed in [12]. Despite this, X-ray mapping of fracture surfaces remains a time intensive process that is not feasibly applicable to a large number of specimens.

Further limiting surface-wide mapping of crack growth behavior is the difficulty in resolving the crack front. Micro-beach marks and loading induced marker-bands are not always distinguishable on all parts of the fracture surface, making complete and accurate reconstruction of the crack front difficult. Generally, micro-beach marks appear most frequently in areas characterized by relatively planar crystallographic transgranular crack growth.

The presence of micro-beach marks on relatively planar fracture facets permits the measurement of actual local crack growth rate, without the error associated with measurements based on two-dimensional projections. Using tilt photogrammetry, the orientation of the facet normal can be determined, allowing micrographs to be captured showing the full dimensions of the facet, rather than a projection of the skewed facet. Micro-beach marks on these facets may then be analyzed using the procedure outlined in Section 6.2.4.

In Figure 6.1, the subsurface crack growth behavior in a specimen of underaged WE43 has been measured using mapping of micro-beach marks. The scale of the micro-beach marks results in a detailed map showing variations in crack growth rate. The general increase in crack growth rate with crack length is clear, as are locations featuring a local reduction in crack growth rate. On the right side of the facet, crack growth is slowed relative to the average. This reduction in crack growth rate is accompanied by an increased number of fracture lines running in the direction of crack growth, which visibly hindered crack propagation, as seen in their effect on the crack front as recorded by micro-beach marking. Crack growth mapping also allows for the comparison of surface measured crack growth rates to subsurface crack behavior. By pairing crack growth rate information with a calculation of stress intensity factor for each segment of an individual ray taken from the rate map, the relation between surface and subsurface can be visualized and investigated. For this specimen and this specific facet, subsurface crack growth rates are very comparable to average surface measured crack growth rates in coarse-grained WE43 magnesium (Figure 6.2). Surface measurements were recorded from underaged short crack growth tests with crack growth from FIB micro-notches oriented perpendicular to the loading direction, detailed in Chapter 4. In the detailed specimen, crack propagation is from a basal-oriented FIB micro-notch. In each case, stress intensity factor was calculated for a mode I crack. At lower values of stress intensity factor, there is less agreement between local subsurface crack growth rate measurements and surface measurements. This is possibly related to the higher variability in crack growth rates observed at values of stress intensity factor below approximately 1.5 $\text{MPa}\cdot\text{m}^{1/2}$ (detailed in Chapter 4). Reduced crack growth rates in the detailed subsurface facet may also be linked to a decreased driving force for very early crack growth due to the angled FIB micro-notch.

This mapping of micro-beach marks was also applied to a facet from the underaged specimen characterized in three dimensions using high energy X-ray methods, detailed later in this chapter. Ultrasonic fatigue of the discussed specimen resulted in the formation of micro-beach mark patterns on many facets across the fracture surface, although their occurrence was insufficient to permit tracking of crack propagation across the entire fracture surface in a continuous manner. A number of sites featuring micro-beach marks are detailed in Figure 6.3. The characterized facet was located near the right side of the FIB notch, as detailed in Figure 6.3 (location 5) and Figure 6.4. There is significant variation in crack growth rate across this facet, even at different locations within the same cycle block. Higher rates of crack propagation were generally observed near the center of the facet. For this specimen and this specific facet, subsurface crack growth rates are very comparable to crack growth rates measured on the surface near the facet (Figure 6.5). This is not surprising, considering that the characterized facet is near the specimen free surface. However, it does indicate the relative accuracy of the method.

Because this method can only be applied to individual facets for which orientation is known, it lacks the flexibility of X-ray tomography mapping to characterize crack growth behavior on a larger scale across an entire fracture surface but can provide a detailed characterization of fatigue crack behavior in specific grains. When available, three-dimensional characterizations of the fracture surface can be combined with micro-beach mark characterizations of crack growth to overcome these limitations, as discussed in [12] where marker banding in conventional fatigue is used to indicate crack position at specific cycle counts.

6.3.2. Short crack growth behavior of WE43 Specimen in Two- and Three-Dimensions

In order to investigate short crack growth behavior and crack path crystallography in WE43 magnesium, fatigue testing was conducted using the UFSEM system and characterized using both traditional surface measurements as well as X-ray tomography and near-field HEDM.

Crack Initiation Site

The crack initiation site is shown in Figure 6.6. A FIB micro-notch was machined parallel to the basal slip system in grain 1 to drive crack initiation and growth along the basal system. Grains 1, 2, and 3 exhibited nominal basal Schmid factors of 0.42, 0.50, and 0.25, respectively. As outlined in Chapter 5, we adopt here the nomenclature "nominal" Schmid Factor in recognition of the fact that the Schmid factor provided by standard orientation imaging analysis software assumes that the stress field is uniaxial. In polycrystals, adjacent grains may alter the stress state, so this assumption is not necessarily accurate, however in the absence of more detailed crystal plasticity simulations of the actual stress fields it is a helpful means to identify grains and phenomena of interest. Grain boundary misorientation parameters for the boundaries separating the three grains are shown in Table 6.1, assuming crack growth occurs on the basal system in each grain. Misorientation across grain boundaries is characterized in terms of tilt and twist misorientation angle [117], and m' parameter [128]. In the model developed by Zhai et al., ease of crack propagation across a grain boundary is directly dependent on the geometric relations of the preferred slip planes in each grain compared to adjacent grains and the grain boundary orientation, known as tilt and twist misorientation angles. During crystallographic crack growth across a grain boundary, the crack must reorient, requiring fracture between the two slip planes along the grain boundary, unless the slip planes are coincident at the boundary. Additional energy is needed for the creation of further free surfaces due to this fracture of this area, bounded along the grain boundary by the twist misorientation angle (Figure 5.3a). The geometric model also incorporates the tilt misorientation component of crack deflection at the grain boundary, or the angle between the traces of the two preferred slip planes on the sample surface, which can act to reduce the driving force at the tip of the crack [117].

Luster and Morris investigated slip transfer across grain boundaries using a geometric compatibility factor *m'*, defined as

$$m' = \cos\kappa \cos\phi \qquad [6.1]$$

where κ is defined as the angle between slip vectors from two adjacent grains, and ϕ is the angle between slip plane normal in those grains, with a low *m'* indicating higher difficulty of slip transfer [128]. Surface measured crack growth behavior is discussed in the next section.

Table 6.1 - Grain boundary misorientation parameters for WE43 fatigue specimen

Grain Boundary	Slip System in Grain 1	Slip System in Neighboring Grain	m' Parameter	Tilt Angle	Twist Angle
1-2	Basal	Basal	0.87	11°	1°
1-3	Basal	Basal	0.27	79°	51°

Surface-measured Short Crack Growth

Crack growth was observed to occur from both edges of the notch. On the left side of the crack, propagation occurred parallel to the basal slip system before reaching the first grain boundary (GB 1-2), where the crack arrested temporarily, despite the very low tilt and twist misorientation angles exhibited by the grain boundary. Crack propagation from the right side of the notch propagated parallel to the basal slip system before arresting at the grain boundary (GB 1-3), which exhibited high tilt and twist misorientation angles for basal to basal crack propagation. Following crack advance across the boundary, crack propagation occurred in a noncrystallographic manner. With the exception of the first boundary encountered on each side of the crack, grain boundaries had no noticeable effect on crack propagation. Crack propagation in this specimen was predominantly crystallographic transgranular in nature (see Figure 6.7), with crack growth frequently aligning with basal slip traces. Crack growth curves for this specimen are shown in Figure 6.8.

Three-Dimensional Fatigue Behavior

Post-mortem reconstructions based on the high-energy X-ray measurements are shown in Figure 6.9. The complex morphology of the fracture surface, along with the crystallography of the fracture surface are detailed in Figure 6.10. The morphology of the fracture surface is described in terms of θ_z, or the angle between the local crack-surface normal and the global loading direction, z. Of the total fracture surface, 31.7% has a θ_z value below 30° (close to of mode I crack growth), 45.5% is inclined between 30° and 60° to the z axis, and the remaining 22.8% is inclined between 60° and 90° to the z axis, as visualized in Figure 6.11. In other words, the majority of the crack surface evolved along planes in the global reference frame that were not orthogonal to the normal loading direction. This suggests that crack growth was dominated by local microstructural or micromechanical phenomena rather than the global loading. In the map describing crack-surface crystallography (Figure 6.12), black regions correspond to intergranular crack growth while colored regions correspond to transgranular crack propagation based on a misorientation threshold of 30°. The colors shown in the crystallography map of Figure 6.10 represent the local crack-surface normals, resolved in the crystallographic reference frame, which are plotted using standard inverse pole figure (IPF) coloring. In total, 54% of the surface map shown in Figure 6.10 is identified as being intergranular, and the remaining is found to be transgranular. A wide variety of crystallographic normals is observed in grains exhibiting transgranular crack propagation, and variation is observed even within individual grains.

Figure 6.12 provides a top-down view of the crack-surface crystallography map with grain boundary traces superimposed for reference. A comparison between the y_{min} edge of the crack-surface crystallography map shown in Figure 6.12 and the crack trace shown in Figure 6.6 provides a visual registration between the surface-measured and three-dimensional data sets. Note from Figure 6.6 that the trace of the crack is very close to the grain boundary in the grain immediately to the right of the FIB-notched grain. In cases such as this, where the distance between the crack and the grain boundary is below the spatial resolution of the HEDM measurements, the crack surface in the three-dimensional data will be identified as intergranular. For this reason, the percentage of crack surface classified as intergranular is likely overestimated.

Figure 6.12 also features a section view through a region on the crack surface containing both intergranular and transgranular crack growth. For the section A-A' defined in Figure 6.12a, a trace of the high-resolution, crack-surface crystallography map is shown in Figure 6.12b. Figure 6.12c presents a cross-section view of the post-mortem HEDM data taken at the same location as section A-A'. It is possible to see from this compilation of images the locations where the crack traversed grain boundaries and either propagated within specific grains or appeared to propagate along grain boundaries (within the spatial-resolution limits of the HEDM measurements).

Features on the fracture surface with spatial dimensions smaller than the resolution of the tomographic reconstruction, such as smaller scale crystallographic facets or micro-beach marks, cannot be resolved using this technique. Due to this fact, crack surface crystallography and morphology presented in this work describe behavior averaged over the area of each triangular facet in the surface mesh, as discussed by Herbig et al [159]. While this resolution limits the analysis of crack propagation mechanisms that may be active below this length scale, these quantitative results will be useful in three-dimensional modeling of crack propagation and the interaction of cracks with grain boundaries in three dimensions.

6.4. Summary and Conclusions

Experimental methods and post-processing techniques for the two and three-dimensional characterization of short fatigue crack growth in WE43 magnesium were presented. Micro-beach marks are used to characterize local subsurface crack growth behavior on fracture facets. Post mortem characterization of the fracture surface morphology and crystallography was accomplished through the use of X-ray tomography and near-field high energy X-ray diffraction. The following conclusions can be made regarding the characterization method and results:

- Micro-beach marks provide an opportunity for the characterization of local subsurface fatigue crack growth rates on the micro-scale on individual fracture facets but requires the determination of facet orientation when not combined with three-dimensional mapping of the fracture surface.

- The combined use of X-ray tomography and near-field HEDM allows for the characterization of fracture surface crystallography over an entire three-dimensional crack surface at high resolution, a significant improvement over fractography based techniques coupled with EBSD which are generally limited to the interrogation of individual facets.

- A significant portion of subsurface crack propagation in this specimen was found to be intergranular (54%), although this was partially affected by the resolution of the HEDM data obscuring near-boundary crack propagation.

Figures

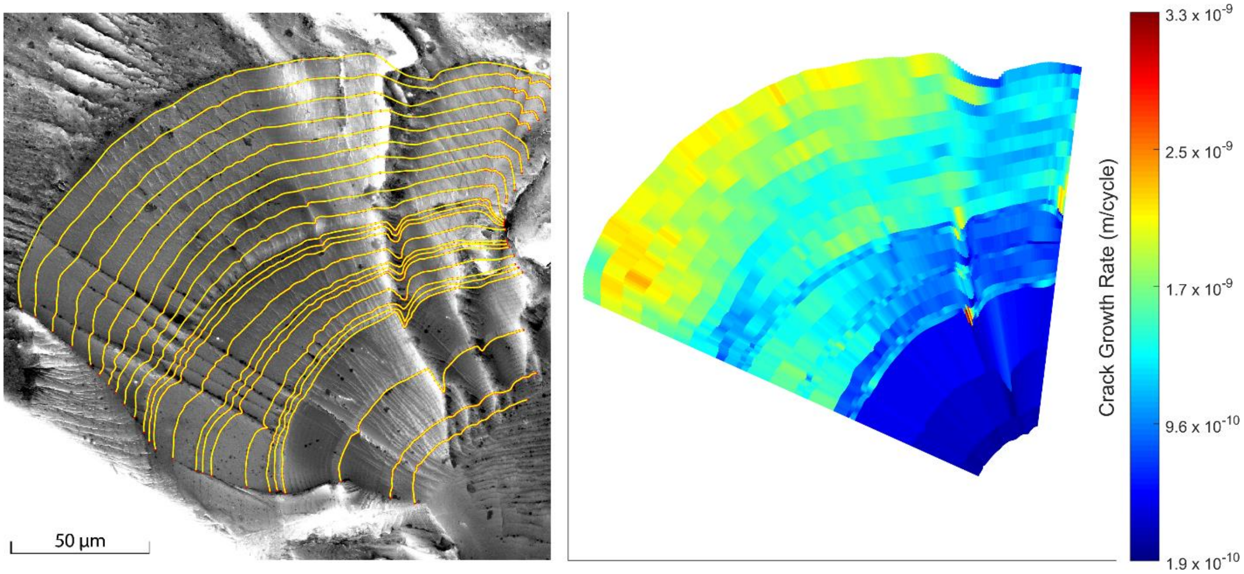

Figure 6.1 - Subsurface crack growth in a specimen of WE43. Micro-beach marks across the facet were measured and mapped to display variations in local short crack growth rate.

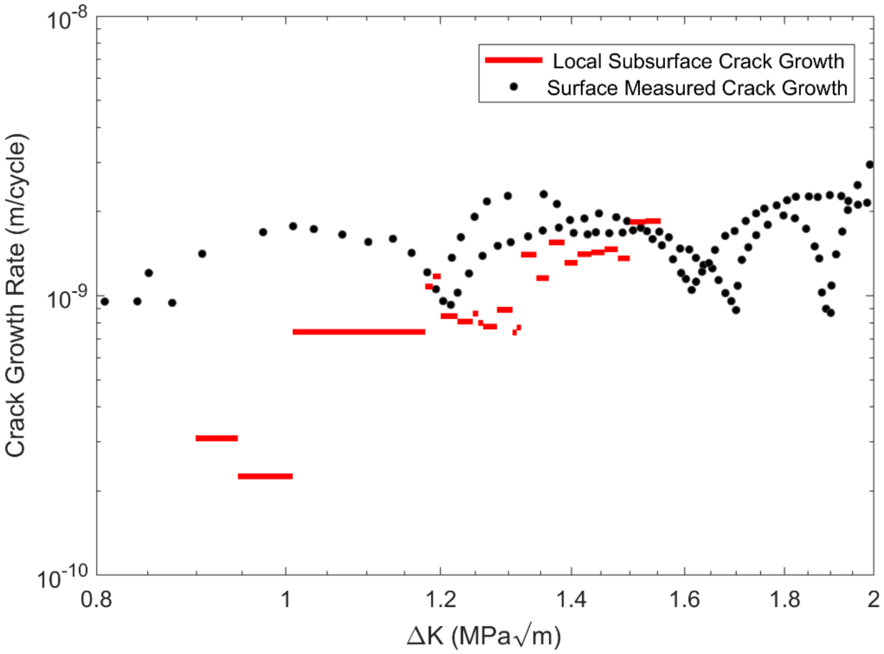

Figure 6.2 - Comparison of subsurface crack growth behavior, measured using micro-beach marks on a single fracture facet, with surface measured crack growth rates observed in coarse-grained WE43 magnesium. Crack growth rates are similar, especially at higher stress intensities.

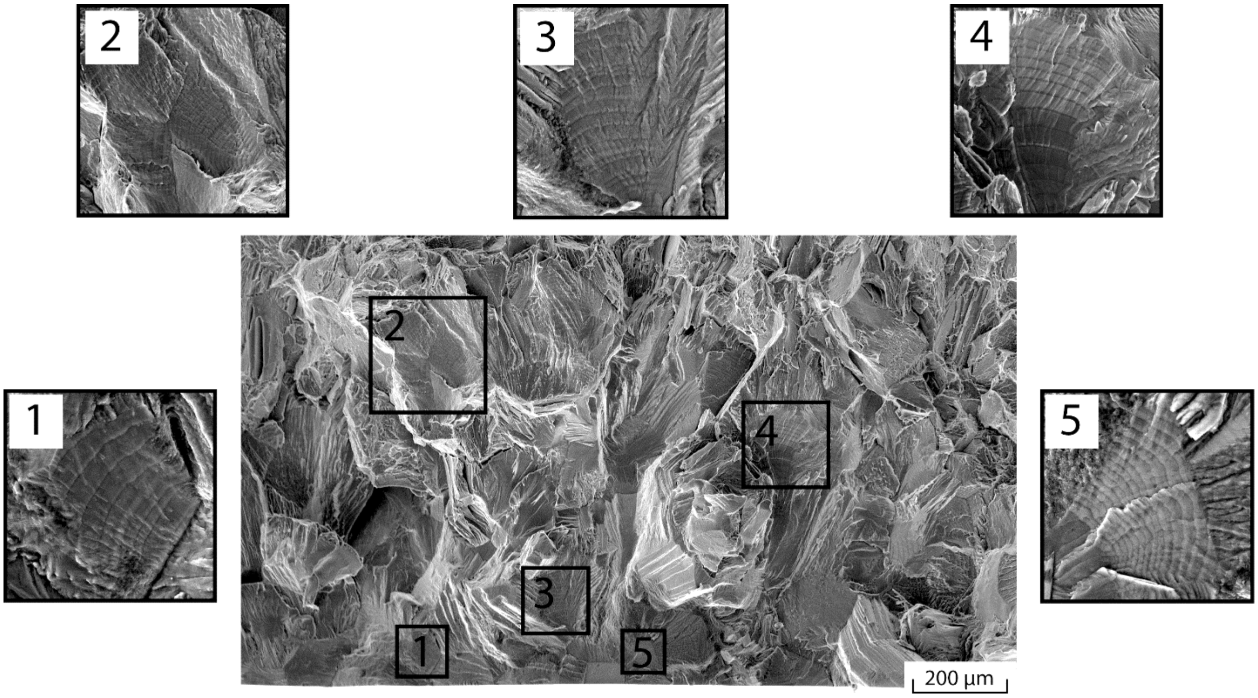

Figure 6.3 - Overview of micro-beach mark occurrence on the fracture surface of the underaged WE43 specimen tested in ultrasonic fatigue and characterized in three dimensions using high energy X-ray methods.

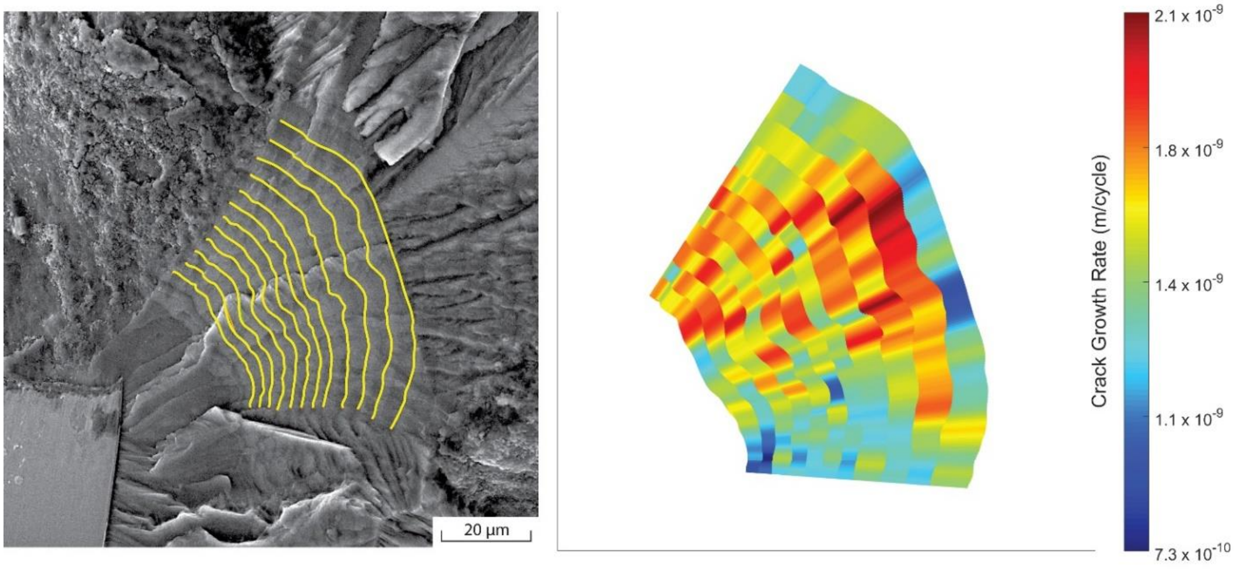

Figure 6.4 - Subsurface crack growth in a specimen of underaged WE43 characterized using high energy X-ray techniques. The characterized facet is located near the crack-initiating FIB micro-notch. Micro-beach marks across the facet were measured and mapped to display variations in local short crack growth rate.

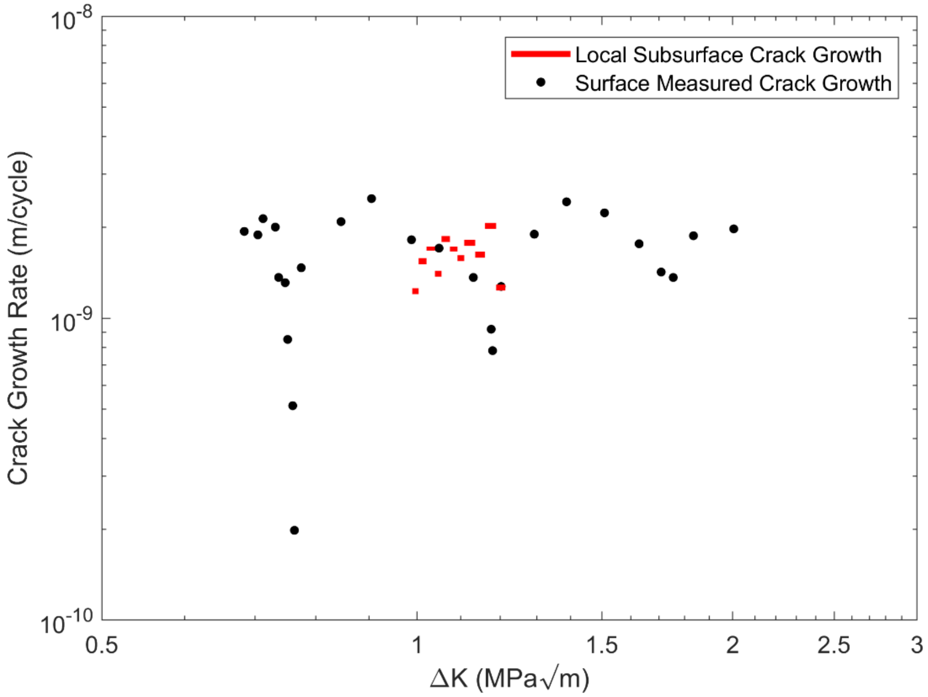

Figure 6.5 - Comparison of subsurface crack growth behavior, measured using micro-beach marks on a single fracture facet, with the surface measured crack growth from the same specimen of underaged WE43. Pictured surface crack growth rates describe crack growth from the right side of the FIB micro-notch. Surface and subsurface crack growth rates are very similar.

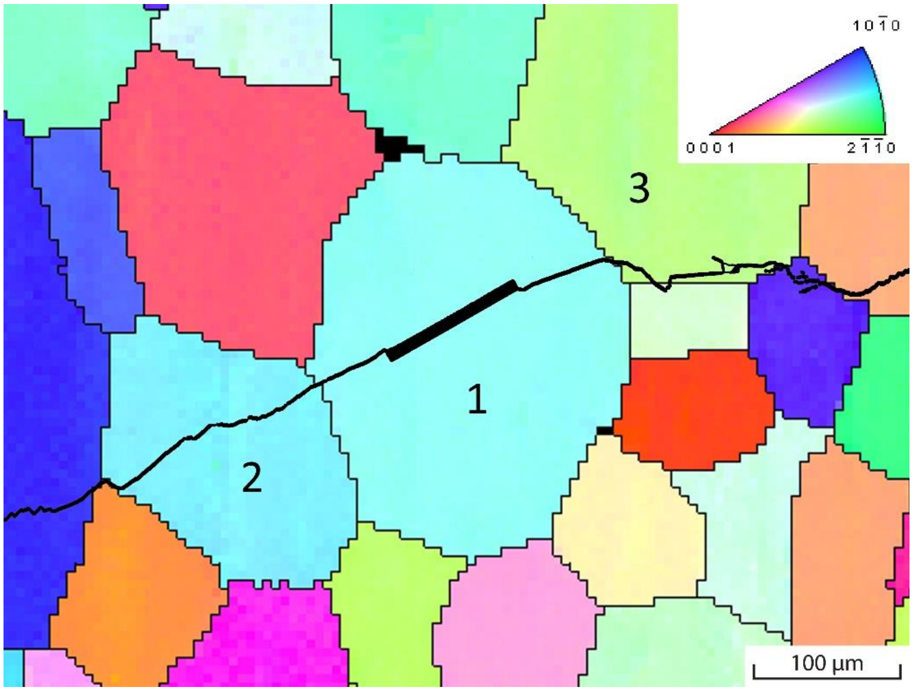

Figure 6.6 - Crack initiation site in underaged WE43 specimen. A FIB micro-notch was machined parallel to the basal system in grain 1 to induce crack initiation.

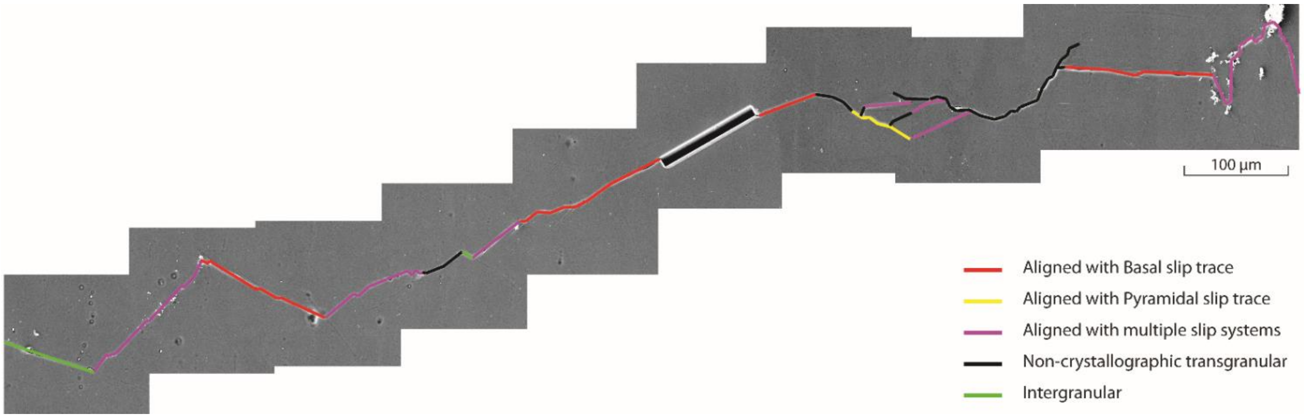

Figure 6.7 - Slip trace analysis of surface-measured crack propagation in the WE43 specimen, using crystallographic characterization through EBSD. Crack propagation was largely crystallographic transgranular in nature, predominantly parallel to the basal slip system.

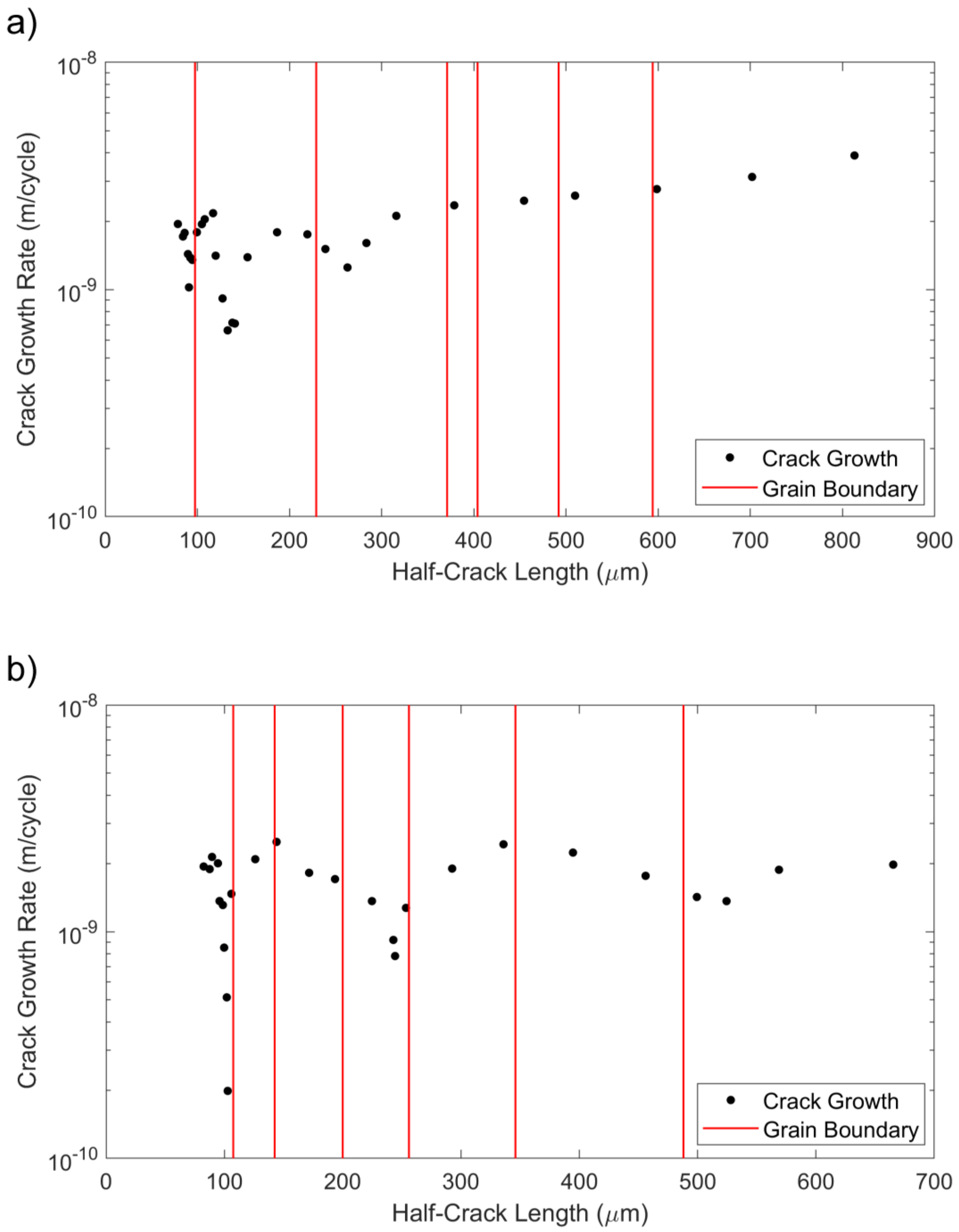

Figure 6.8 - Short crack growth in WE43 specimen showing crack interaction with grain boundaries from the a) left side and b) right side of the initiation site. On both sides of the crack, first encountered grain boundaries led to temporary crack arrest and retardation of crack growth rates.

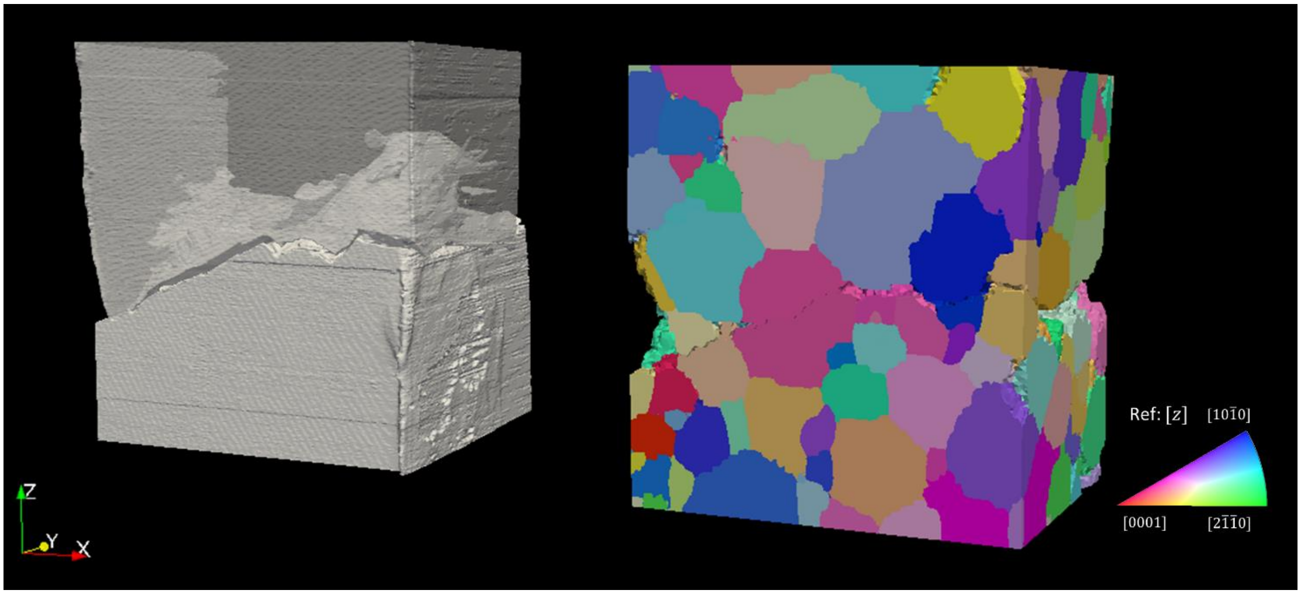

Figure 6.9 - Post-mortem reconstruction of fatigue fracture surface and surrounding grains from X-ray computed tomography (left) and near-field HEDM (right). The volumes shown are approximately 740 µm in the x direction, 540 µm in the y direction, and 1.1 mm in the z direction.

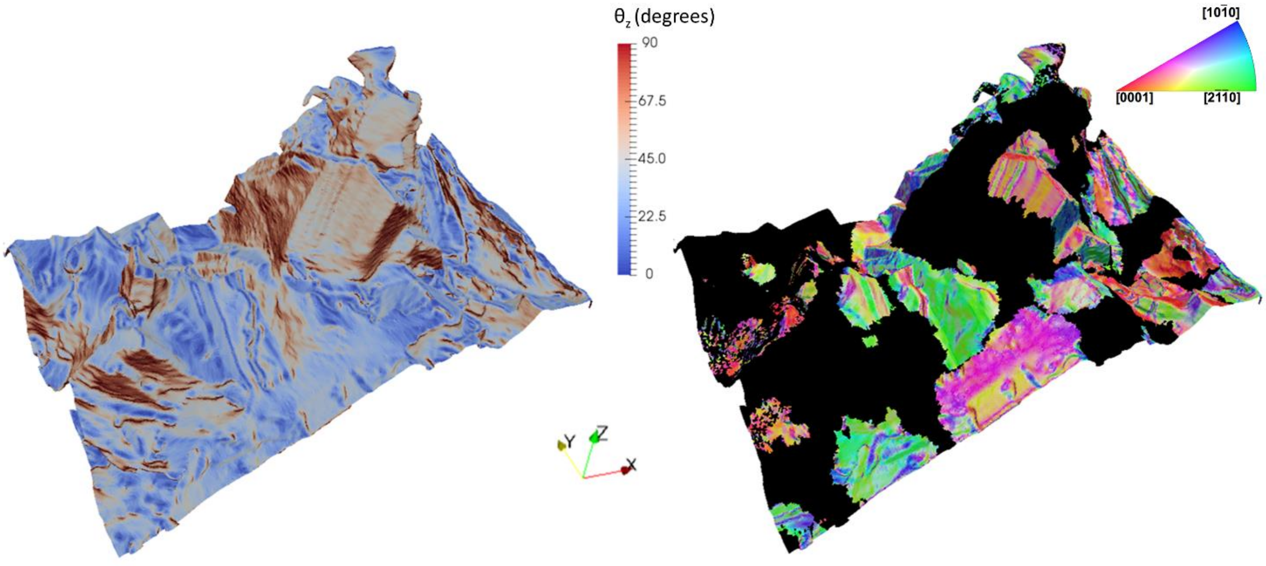

Figure 6.10 – Crack-surface morphology map plotted in terms of angle between local crack-surface normal and z-axis (left). Crack-surface crystallography map with IPF coloring plotted with respect to the local crack-surface normal (right). Black regions on the crystallography map correspond to regions of the crack surface found to be intergranular based on a misorientation threshold of 30°.

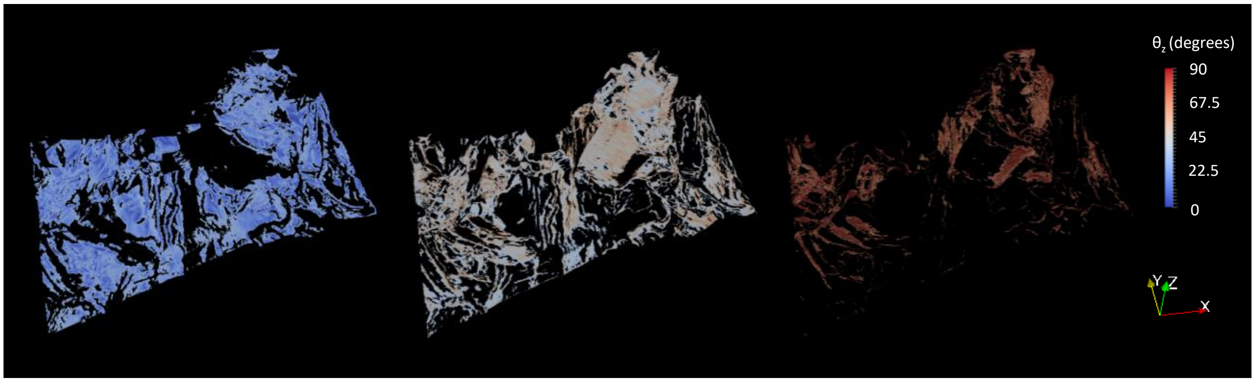

Figure 6.11 - Fracture surface thresholds based on morphology: 0°<θ_z<30° (left); 30°< θ_z <60° (middle); 60°< θ_z <90° (right).

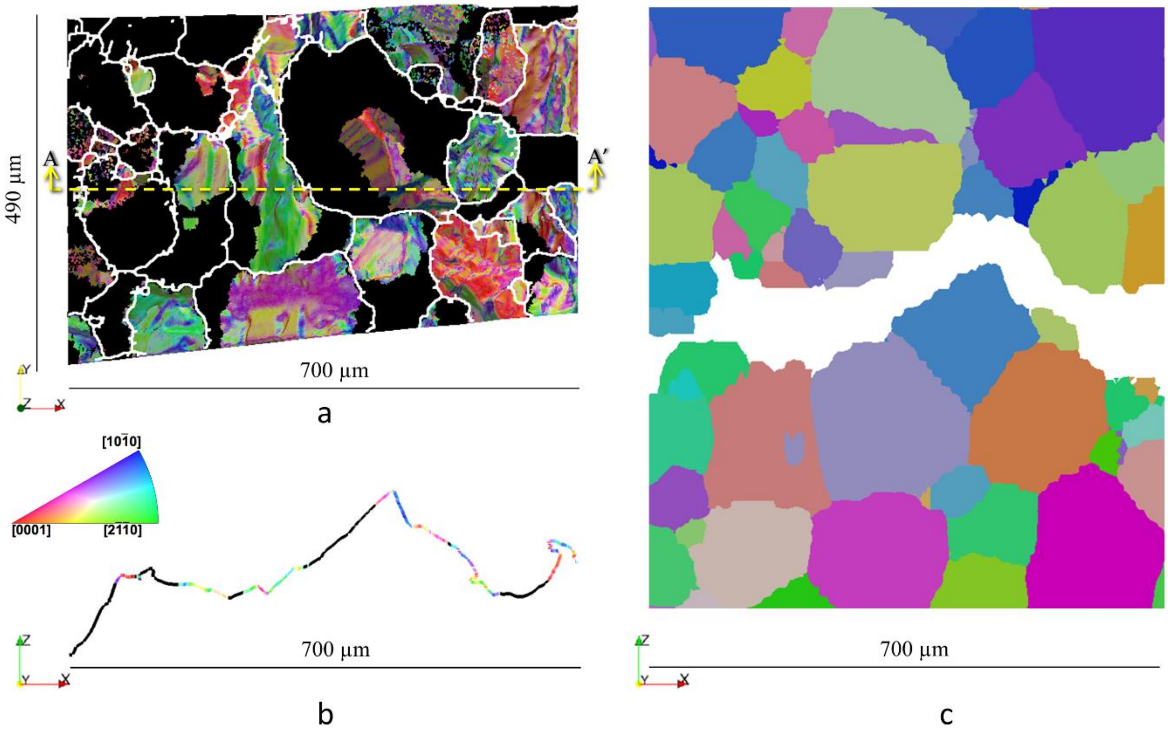

Figure 6.12 – a) Aerial view of crack-surface crystallography map from Figure 6.10 indicating section A-A’. b) Crack trace along A-A’ with IPF coloring plotted with respect to local crack-surface normal. c.) Cross section of post-mortem HEDM data shown at the same location as section A-A’ with IPF coloring plotted with respect to the z-axis.

CHAPTER 7

CONCLUSIONS AND FUTURE WORK

7.1. Conclusions

A study of the fatigue behavior of the hot rolled magnesium alloy WE43 in the VHCF regime was conducted at ultrasonic frequencies at room temperature. The fatigue life behavior, crack initiation, and fatigue crack growth in three heat treatments of WE43 was examined and compared. Additionally, the effect of local microstructure on fatigue crack behavior was investigated using *in situ* and thin foil specimens in ultrasonic fatigue. Three-dimensional short fatigue crack growth behavior was characterized using high-energy X-ray techniques. For this study, the following conclusions can be made.

- Heat treatment had a significant effect on fatigue strengths at 10^9 cycles for the T5, underaged, and T6 conditions, with values of 110 MPa, 65 MPa, and 65 MPa, respectively. The dramatic difference in fatigue strength correlated with differences in tensile properties and hardness derived from nanoindentation experiments.

- Damage from cyclic strain accumulation at favorable microstructural regions was identified as the dominant crack initiation mechanism. Crack initiation sites in each of the T5, underaged, and T6 conditions featured large facets oriented for high resolved shear stress.

- Heat treatment had no significant effect on average crack growth rates. Despite local variations in short crack growth rate, average crack growth rates for each of the T5, underaged, and T6 conditions were very similar at stress intensities greater than 1.5 MPa·m$^{1/2}$.

- It appears that fatigue lives in the VHCF regime in WE43 are primarily determined by the number of cycles to initiate a grain size crack. Small fatigue crack growth appears to provide only a minor contribution to fatigue lives in this regime.

- Crack paths in each of the T5, underaged, and T6 conditions were strongly affected by local microstructure, with cracks predominantly propagating in a crystallographic transgranular manner. Crack propagation in foil specimens exhibited much higher levels of crystallographic transgranular growth parallel to the basal system, at the expense of other growth pathways, except intergranular crack propagation, which occurred more frequently in foils than in cylindrical specimens.

- Investigation of crack behavior using in situ and foil specimens confirmed that tilt and twist misorientation angles often correlated with the ease of crack propagation across grain boundaries. However, this was not always the case, and an overview of all grain boundaries showed a high degree of scatter, with no reliable trend linking tilt or twist misorientation to crack retardation or arrest. An accurate quantitative relation between tilt and twist misorientation and levels of crack retardation or arrest has yet to be developed.

- In addition to grain boundary parameters like tilt and twist misorientation, both nominal Schmid factor and crystallographic plane orientation were shown to frequently have a significant effect on crack path selection and crack growth rate, but again an overview of all boundaries showed significant scatter and no clear correlation.

- The accuracy of twist misorientation measurement, and therefore any evaluation of a geometric model involving twist misorientation, is strongly dependent on accurate measurement of the 3D orientation of the grain boundary. In some cases, relatively small levels of error in grain boundary orientation can produce large errors in twist misorientation angle, the magnitude of which depends on the crystallographic orientation of the two grains under consideration. Foil specimens partially simplify this issue, as a higher proportion of grains comprising the specimen volume intersect the specimen free surface, allowing for determination of three-dimensional grain boundary orientation.

- Although the models of fatigue crack-grain boundary interaction evaluated in this study consider the effect of many microstructural, crack, and grain boundary parameters such as nominal Schmid factor, crack length, tilt misorientation, and twist misorientation, they fail to consider the effect of neighboring grains beyond those interacting with the surface-observed crack. These neighboring grains can have a strong effect not only on fatigue behavior observed on the surface, but also on the local stress state controlling fatigue behavior, which may not be adequately captured by the nominal Schmid factor. It is important to note that we are interested in the small crack behavior near a single initiating feature as a component of fatigue behavior that is not yet well understood, rather than volume averaged crack growth behavior. Accurate modeling of short crack growth requires both comprehensive three-dimensional characterization of microstructure and fatigue behavior, and a model formulation that considers this complex three-dimensional problem.

- Micro-beach marks provide an opportunity for the characterization of local subsurface fatigue crack growth rates on the micro-scale on individual fracture facets as long as the facet orientation is known.

- The combined use of X-ray tomography and near-field HEDM allows for the characterization of fracture surface crystallography over an entire three-dimensional crack surface at high resolution and provides a significant improvement over fractography based techniques coupled with EBSD which are generally limited to the interrogation of individual facets.

7.2. Recommendations for Future Work

Based on the findings discussed in this dissertation, the following recommendations are made for future work in this area.

1) While an investigation of fatigue crack growth and fatigue life behavior in three conditions of WE43 exhibited no major effect of precipitation on fatigue behavior, many variables were being considered in the study, including grain size and residual work hardening. A study investigating only the effects of variation in precipitate development on fatigue behavior in the binary Mg-Y and Mg-Nd alloys should provide more insight into the role of these specific alloying elements and possible benefits to fatigue properties through precipitation strengthening.

2) Large grains with high nominal Schmid factors were identified as favorable fatigue crack initiation sites, but other critical microstructural parameters such as combinations of hard and soft grains and regions of micro-texture, etc. that may lead to a higher likelihood of crack initiation remain to be identified and studied in more detail. Further interrogation

and analysis of microstructural sites leading to nascent and fatal crack formation should be performed to identify key microstructural characteristics leading to cyclic damage accumulation and crack initiation, beyond those explored in this dissertation.

3) Accurate modeling of grain boundary effects on fatigue crack growth is hampered by a lack of understanding of three-dimensional microstructure. The three-dimensional characterization of fatigue fracture surfaces and microstructure detailed in Chapter 6 should be used in conjunction with crystal plasticity finite element analysis of actual 3D microstructures to more accurately characterize the local driving forces for crack propagation in each grain.

4) Although interrogation of three-dimensional fatigue behavior using high-energy X-ray techniques is extremely time intensive, additional datasets beyond those detailed in this dissertation should be collected to provide further insight into the highly complex three-dimensional nature of fatigue crack propagation. These additional datasets could then be used to further improve predictive models of fatigue crack growth and crack-grain boundary interaction.

5) Micro-beach marks provide a useful tool for the investigation of local subsurface crack growth behavior. Despite this, the mechanisms governing the formation of micro-beach marks are not yet understood, and their formation on fracture facets is not predictable. A study should be conducted to identify the mechanisms responsible for micro-beach mark formation, and to develop of method for reliably inducing micro-beach mark formation on the fracture surface.

6) While three-dimensional characterizations of grain shape and crystallography provide a wealth of information on three-dimensional fatigue behavior, these characterizations could be further improved with the incorporation of three-dimensional characterizations of fatigue crack growth rate on a larger scale, beyond single facet characterizations using micro-beach marks. These larger scale characterizations of fatigue crack growth rate should be incorporated into future high-energy X-ray studies by using either macroscopic marker-banding techniques or micro-beach marks, if micro-beach mark formation can be extended beyond individual facets and made more reliable.

7) The UFSEM system is an extremely useful and adaptable tool for the experimental interrogation of fatigue behavior, as is evident in its capabilities to investigate fatigue behavior at high resolution in both laboratory air and vacuum. The following upgrades to the UFSEM system are recommended to extend this flexibility to additional fatigue studies:

    a) Mean-stress capabilities to interrogate the effect of different load ratios on fatigue behavior, including the interrogation of fatigue in thin foil specimens. This would permit high resolution characterization of fatigue crack propagation behavior in relation to different microstructural features such as grain boundaries.

    b) A means to monitor the temperature of the specimen in situ, which would reduce uncertainty, as well as various improvements for automation that would result in user time savings and increased knowledge grained for each experiment.

APPENDICES

Appendix A

Ultrasonic Fatigue Specimen Drawings

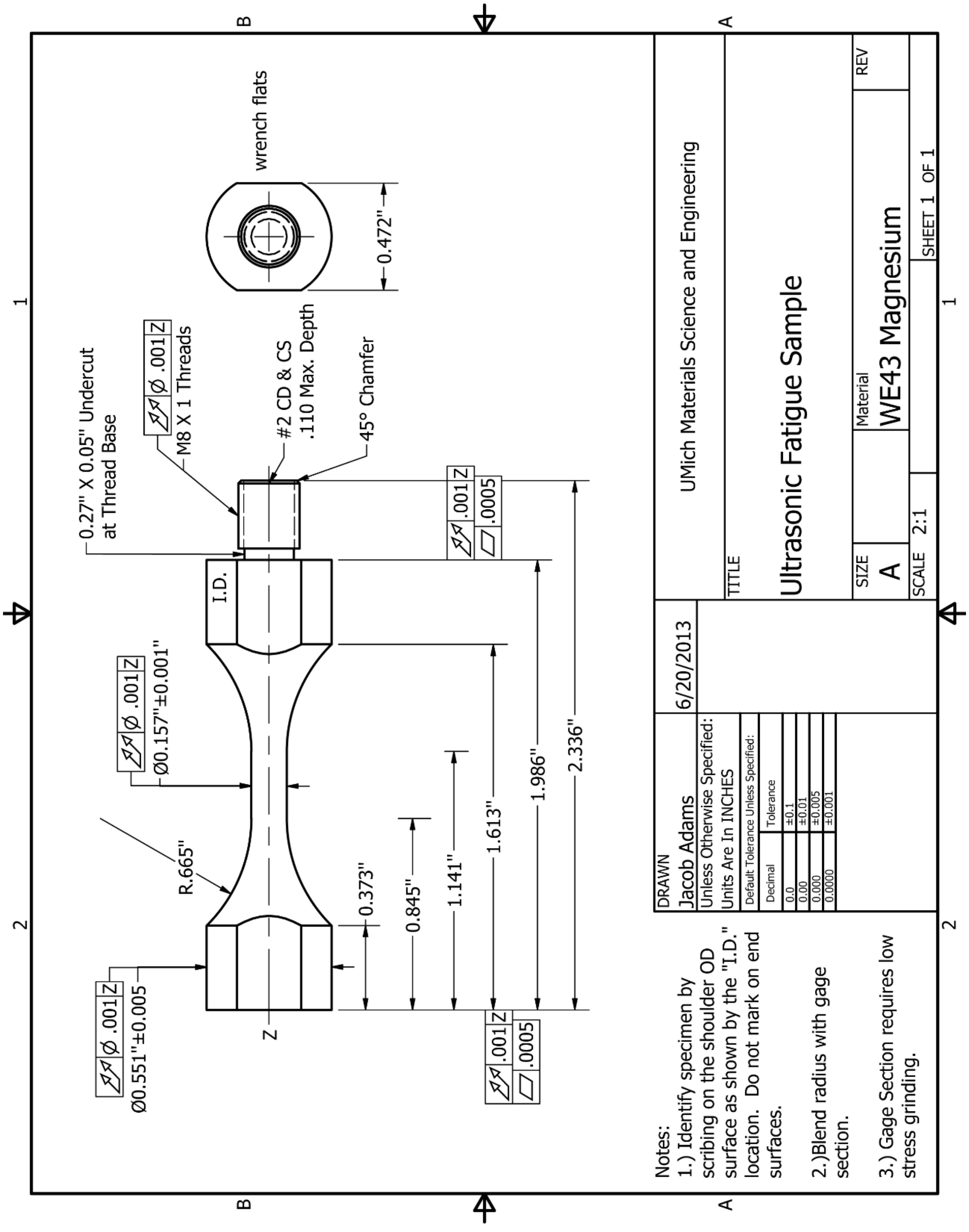

Figure A. 1 - WE43 Fatigue Life Specimen

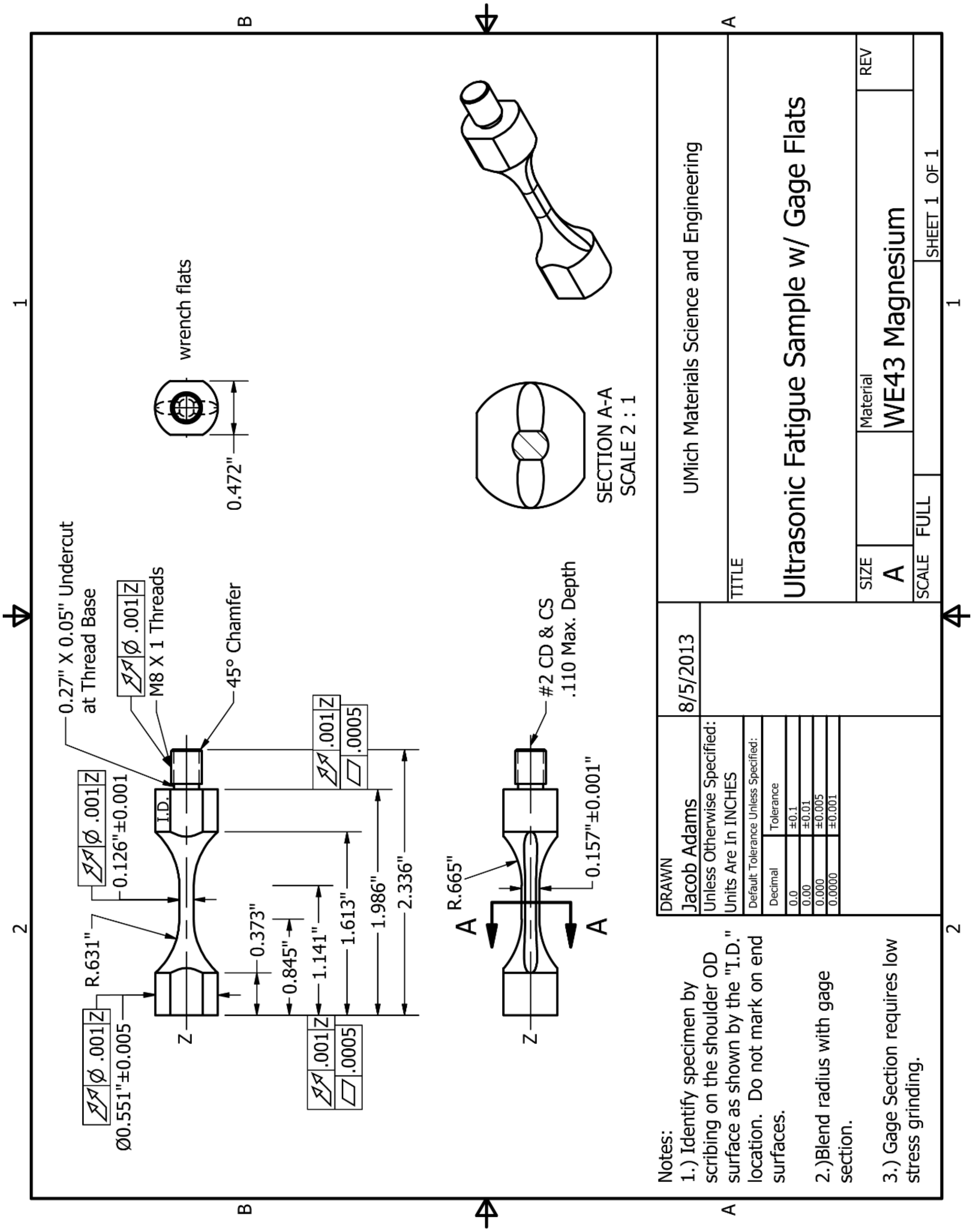

Figure A. 2 - WE43 Short Crack Growth Specimen

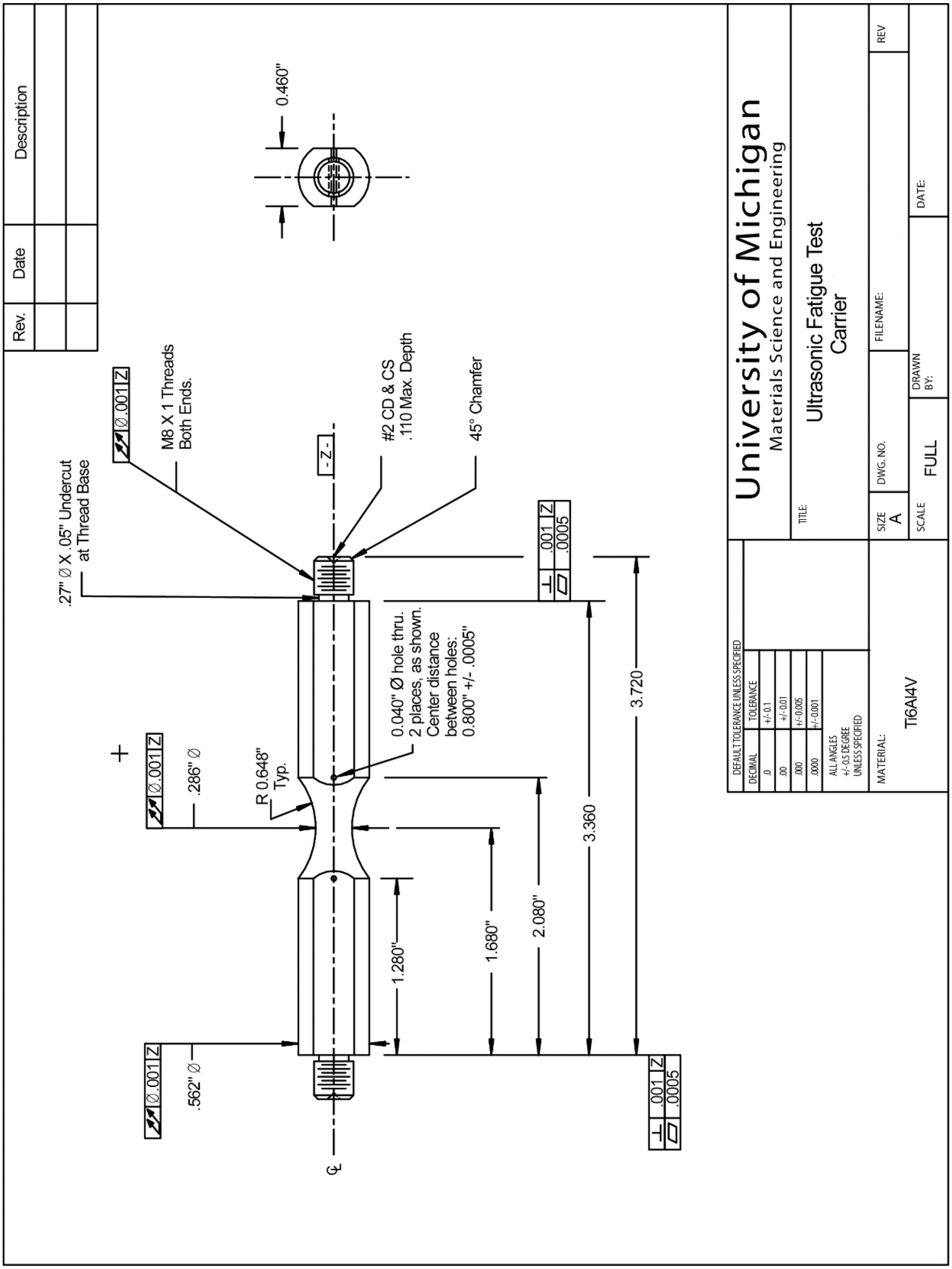

Figure A. 3 - Ultrasonic Fatigue Carrier Specimen

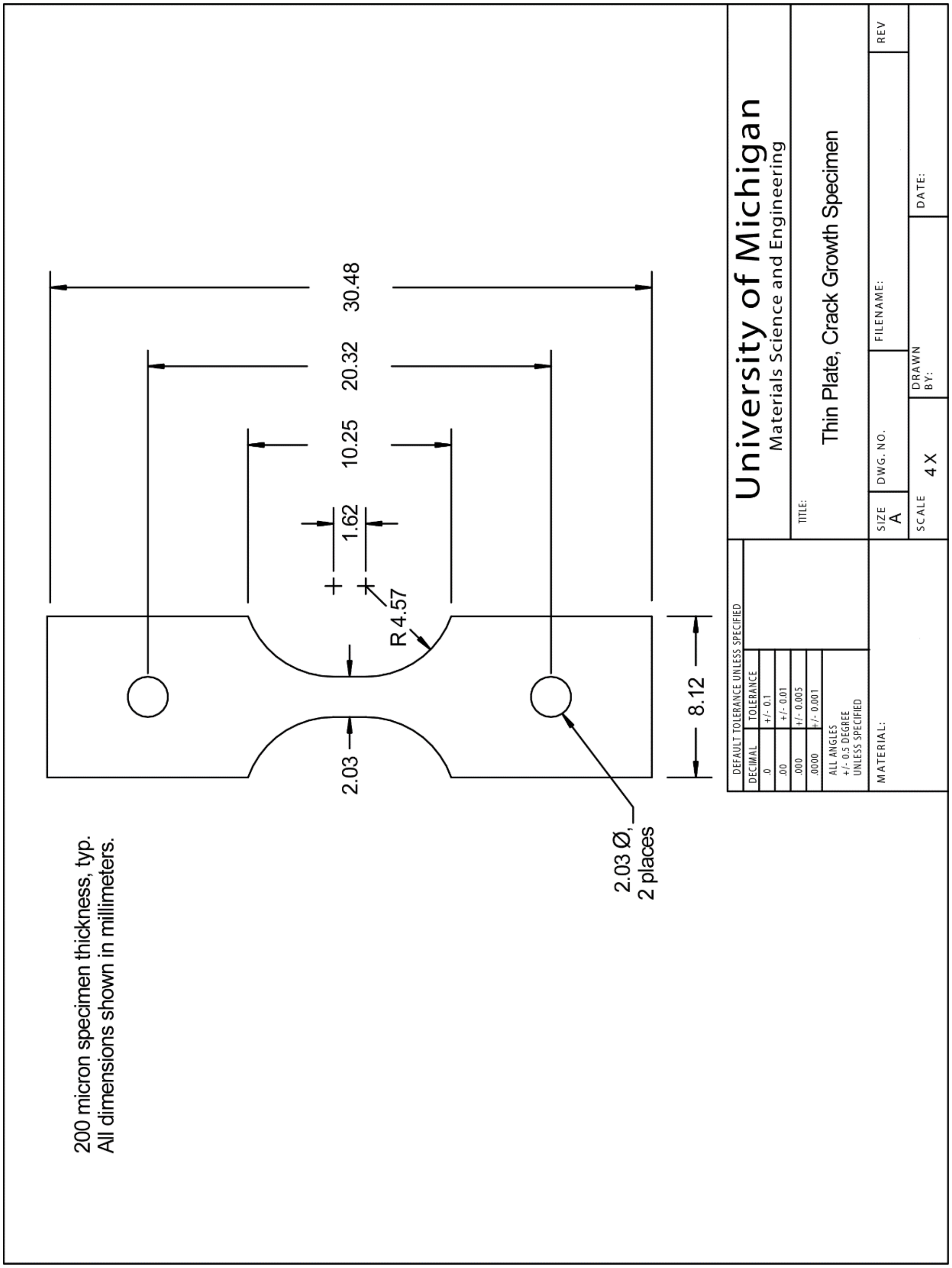

Figure A. 4 - Ultrasonic Fatigue Foil Specimen

Appendix B

Ultrasonic Fatigue Testing Principles

Ultrasonic fatigue has been used since the 1950s [164] to accelerate fatigue testing by increasing the testing frequency. Higher testing frequencies have been used, but as the specimen length is inversely related to frequency, a testing frequency of 20 kHz is the practical limit for investigation of structural materials. This section discusses the principles of operation of ultrasonic fatigue equipment.

The velocity of a wave propagating along a smooth cylindrical bar of constant diameter is given as

$$k = \sqrt{\frac{E}{\rho}} \tag{B.1}$$

where E is the Elastic modulus and ρ is the density of the material. The equation for the displacement, u, due to the first mode of vibration is then given as a function of position, x, and time, t,

$$u(x,t) = A_o \cos(kx)\sin(\omega t) \tag{B.2}$$

The amplitude at any point x along the bar is given by

$$A(x) = A_o \cos(kx) \tag{B.3}$$

where A_o is the amplitude at the end of the bar and

$$k = \sqrt{\frac{\pi}{l}}\ , \ \ \omega = \frac{\pi c}{l} \tag{B.4}$$

The strain, ε, at each point along the bar is given by

$$\varepsilon(x,t) = -kA_o \sin(kx)\sin(\omega t) \tag{B.5}$$

Using Equations B.1 and B.4,

$$l = \frac{1}{2f}\sqrt{\frac{E_d}{\rho}} \tag{B.6}$$

where $f = \frac{\omega}{2\pi}$, l is the wavelength of the acoustic pulse, and E_d is the dynamic elastic modulus. The load train components used in ultrasonic fatigue are designed with consideration of this resonance length in order to ensure that the amplitude of the acoustic does not become attenuated.

Appendix C

Determination of 3-dimensional Grain Boundary Orientation

The determination of grain boundary orientation is critical for the accurate characterization of grain boundary misorientation parameters. While the two-dimensional trace of the grain boundary can be measured on the specimen free surface using non-destructive methods, determination of the three-dimensional orientation of a grain boundary frequently requires destructive characterization techniques such as serial sectioning or FIB tomography.

Quantitative characterization of the three-dimensional morphology of a fracture surface provides an opportunity to characterize the complete orientation of grain boundaries that intersect both the specimen free surface and the fracture surface in a non-destructive manner. Fractographs of specimen fracture surfaces gathered using scanning electron microscopy were characterized using tilt photogrammetry through the software package MeX from Alicona (Figure C. 1). Traces of grain boundaries on the fracture surface could then be measured in three dimensions. Together with grain boundary traces measured on the specimen free surface, traces measured on the fracture surface could then be used to determine the orientation of a plane representing grain boundary and containing both trace vectors, by using the cross product:

$$\bar{n} = \overline{V_S} \times \overline{V_F} \qquad \text{[C.7]}$$

where V_S and V_F are the vectors describing the grain boundary traces measured on the free and fracture surfaces, respectively, and n is the normal vector to the grain boundary plane (Figure C. 2).

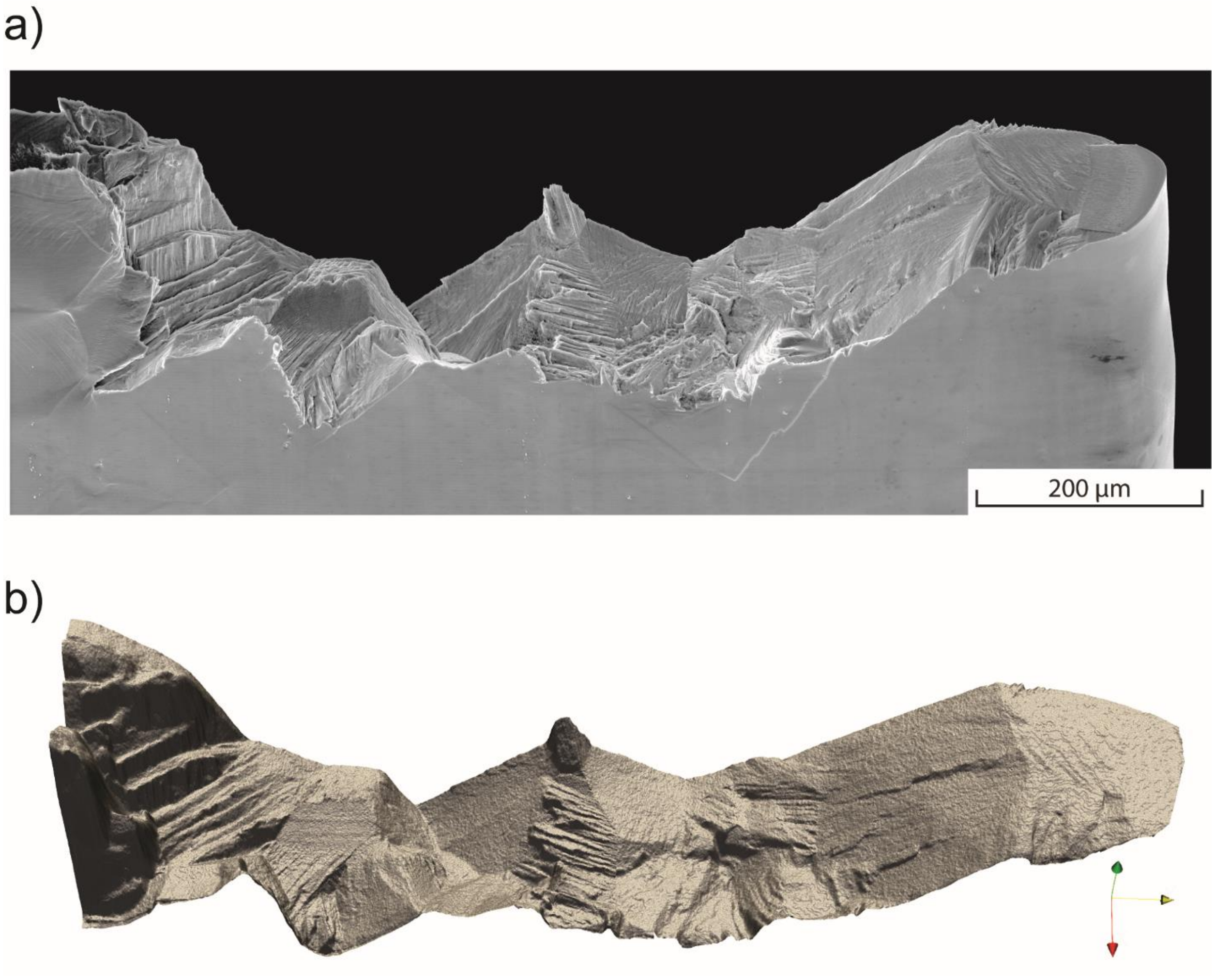

Figure C. 1 - Fracture surface from a WE43 magnesium foil specimen investigated using ultrasonic fatigue. a) Electron microscopy is used to characterize the fracture surface and to produce a b) 3-dimensional surface mesh of surface morphology using tilt photogrammetry in Alicona MeX.

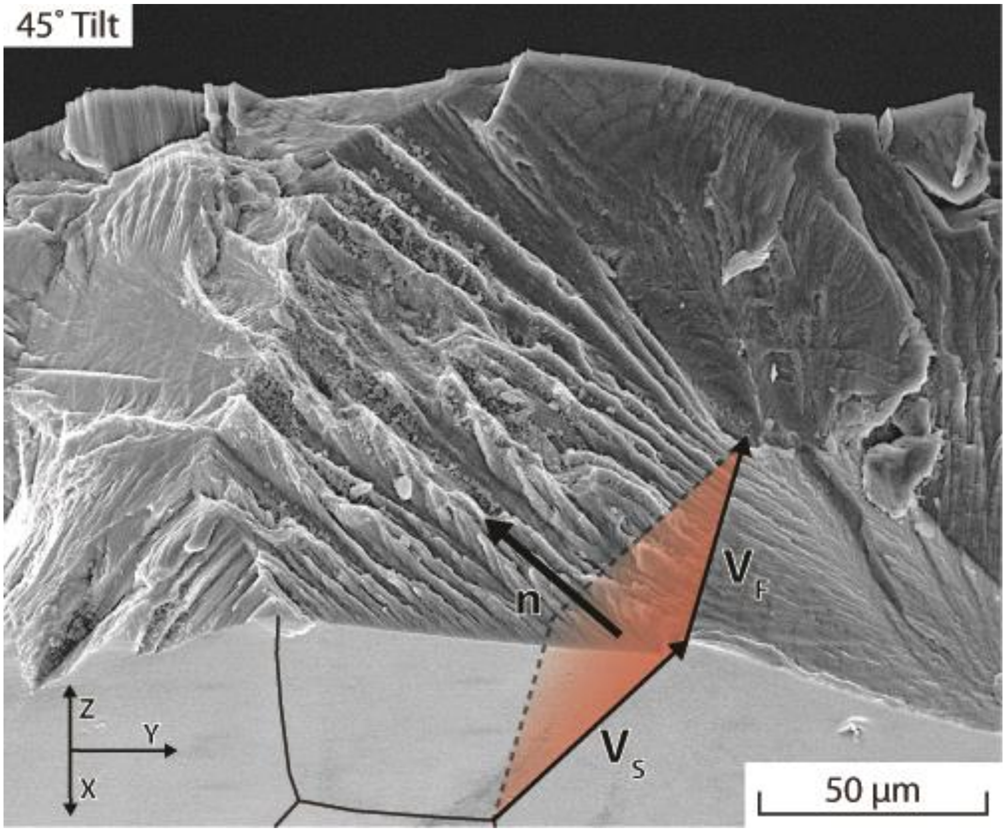

Figure C. 2 - Determination of grain boundary orientation in three dimensions using grain boundary traces measured from the free surface (V_S) and the fracture surface mesh (V_F).

REFERENCES

[1] Cole GS. Issues that Influence Magnesium’s Use in the Automotive Industry. Mater Sci Forum 2003;419–422:43–50. doi:10.4028/www.scientific.net/MSF.419-422.43.

[2] Nascimento L, Yi S, Bohlen J, Fuskova L, Letzig D, Kainer KU. High cycle fatigue behaviour of magnesium alloys. Procedia Eng 2010;2:743–50. doi:10.1016/j.proeng.2010.03.080.

[3] Zhu X, Jones JW, Allison JE. Effect of frequency, environment, and temperature on fatigue behavior of E319 cast aluminum alloy: Stress-controlled fatigue life response. Metall Mater Trans A 2008;39A:2681–8. doi:10.1007/s11661-008-9631-1.

[4] Miao J, Pollock TM, Wayne Jones J. Crystallographic fatigue crack initiation in nickel-based superalloy René 88DT at elevated temperature. Acta Mater 2009;57:5964–74. doi:10.1016/j.actamat.2009.08.022.

[5] Stanzl-Tschegg S, Mughrabi H, Schoenbauer B. Life time and cyclic slip of copper in the VHCF regime. Int J Fatigue 2007;29:2050–9. doi:10.1016/j.ijfatigue.2007.03.010.

[6] Bathias C, Paris PC. Gigacycle Fatigue in Mechanical Practice. New York: Marcel Dekker; 2005.

[7] Stanzl-Tschegg S. Very high cycle fatigue measuring techniques. Int J Fatigue 2014;60:2–17. doi:10.1016/j.ijfatigue.2012.11.016.

[8] Mayer H. Recent developments in ultrasonic fatigue. Fatigue Fract Eng Mater Struct 2016;39:3–29. doi:10.1111/ffe.12365.

[9] Liu L, Husseini NS, Torbet CJ, Kumah DP, Clarke R, Pollock TM, et al. In Situ Imaging of High Cycle Fatigue Crack Growth in Single Crystal Nickel-Base Superalloys by Synchrotron X-Radiation. J Eng Mater Technol 2008;130:21008. doi:10.1115/1.2840966.

[10] Geathers J, Torbet CJ, Jones JW, Daly S. Investigating environmental effects on small fatigue crack growth in Ti–6242S using combined ultrasonic fatigue and scanning electron microscopy. Int J Fatigue 2015;70:154–62. doi:10.1016/j.ijfatigue.2014.09.007.

[11] Adams JF, Allison JE, Jones JW. The effects of heat treatment on very high cycle fatigue behavior in hot-rolled WE43 magnesium. Int J Fatigue 2016;93:372–86. doi:10.1016/j.ijfatigue.2016.05.033.

[12] Spear AD, Li SF, Lind JF, Suter RM, Ingraffea AR. Three-dimensional characterization of microstructurally small fatigue-crack evolution using quantitative fractography combined with post-mortem X-ray tomography and high-energy X-ray diffraction microscopy. Acta Mater 2014;76:413–24. doi:10.1016/j.actamat.2014.05.021.

[13] King A, Ludwig W, Herbig M, Buffière JY, Khan AA, Stevens N, et al. Three-dimensional in situ observations of short fatigue crack growth in magnesium. Acta Mater 2011;59:6761–71. doi:10.1016/j.actamat.2011.07.034.

[14] Withers PJ, Preuss M. Fatigue and Damage in Structural Materials Studied by X-Ray Tomography. Annu Rev Mater Res 2012;42:81–103. doi:10.1146/annurev-matsci-070511-155111.

[15] Avedesian MM, Baker H, editors. Magnesium and Magnesium Alloys. ASM International; 1999.

[16] Nie J-F. Precipitation and Hardening in Magnesium Alloys. Metall Mater Trans A 2012;43:3891–939. doi:10.1007/s11661-012-1217-2.

[17] Sitzmann E, Marquis EA. Chemistry and morphology of β′ precipitates in an aged Mg-Nd-Y-Zr alloy. Philos Mag Lett 2015;95:7–13. doi:10.1080/09500839.2014.995737.

[18] Natarajan AR, Solomon ELS, Puchala B, Marquis EA, Van der Ven A. On the early stages of precipitation in dilute Mg-Nd alloys. Acta Mater 2015;108:367–79. doi:10.1016/j.actamat.2016.01.055.

[19] Natarajan AR, Van der Ven A. A unified description of ordering in HCP Mg-RE alloys. Acta Mater 2017;124:620–32. doi:10.1016/j.actamat.2016.10.057.

[20] Nie JF. Effects of precipitate shape and orientation on dispersion strengthening in magnesium alloys. Scr Mater 2003;48:1009–15. doi:10.1016/S1359-6462(02)00497-9.

[21] Moreno IP, Nandy TK, Jones JW, Allison JE, Pollock TM. Microstructural characterization of a die-cast magnesium-rare earth alloy. Scr Mater 2001;45:1423–9. doi:10.1016/S1359-6462(01)01179-4.

[22] Angelini V, Ceschini L, Morri A, Apelian D. Influence of heat treatment on microstructure and mechanical properties of rare earth rich magnesium alloy. Int J Met Cast 2016;11:382–95. doi:10.1007/s40962-016-0070-2.

[23] Yu K, Li W, Wang R, Wang B, Li C. Effect of T5 and T6 Tempers on a Hot-Rolled WE43 Magnesium Alloy. Mater Trans 2008;49:1818–21. doi:10.2320/matertrans.MRA2008602.

[24] Marrow TJ, Buffiere JY, Withers PJ, Johnson G, Engelberg D. High resolution X-ray tomography of short fatigue crack nucleation in austempered ductile cast iron. Int J Fatigue 2004;26:717–25. doi:10.1016/j.ijfatigue.2003.11.001.

[25] Mises R v. Mechanics of Plastic Deformation in Crystals. Zeitschrift Für Angew Math Und Mech 1928;8:161–85.

[26] Wang QY, Bathias C, Kawagoishi N, Chen Q. Effect of inclusion on subsurface crack initiation and gigacycle fatigue strength. Int Jounal Fatigue 2002;24:1269–74.

[27] Ando S, Nakamura K, Takashima K, Tonda H. {11-22} <-1-123> slip in magnesium single crystal. Japan Inst Light Met 1992;42:765–71.

[28] Hutchinson WB, Barnett MR. Effective values of critical resolved shear stress for slip in polycrystalline magnesium and other hcp metals. Scr Mater 2010;63:737–40. doi:10.1016/j.scriptamat.2010.05.047.

[29] Wagoner RH, Lou XY, Li M, Agnew SR. Forming behavior of magnesium sheet. J Mater Process Technol 2006;177:483–5. doi:10.1016/j.jmatprotec.2006.04.121.

[30] Agnew SR, Duygulu Ö. Plastic anisotropy and the role of non-basal slip in magnesium alloy AZ31B. Int J Plast 2005;21:1161–93. doi:10.1016/j.ijplas.2004.05.018.

[31] Blicharski M, Nourbakhsh S, Nutting J. Structure and properties of plastically deformed α-Ti. Met Sci 1979;13:516–22. doi:10.1179/030634579790438318.

[32] Hantzsche K, Bohlen J, Wendt J, Kainer KU, Yi SB, Letzig D. Effect of rare earth additions on microstructure and texture development of magnesium alloy sheets. Scr Mater 2010;63:725–30. doi:10.1016/j.scriptamat.2009.12.033.

[33] Kocks UF, Tomé CN, Wenk HR. Texture and Anisotropy: Preferred Orientations in Polycrystals and their Effect on Materials Properties. Cambridge University Press; 1998.

[34] Farzadfar SA, Sanjari M, Jung IH, Essadiqi E, Yue S. Role of yttrium in the microstructure and texture evolution of Mg. Mater Sci Eng A 2011;528:6742–53. doi:10.1016/j.msea.2011.05.064.

[35] Mackenzie LWF, Pekguleryuz M. The influences of alloying additions and processing parameters on the rolling microstructures and textures of magnesium alloys. Mater Sci Eng A 2008;480:189–97. doi:10.1016/j.msea.2007.07.003.

[36] Jäger A, Lukáč P, Gärtnerová V, Haloda J, Dopita M. Influence of annealing on the microstructure of commercial Mg alloy AZ31 after mechanical forming. Mater Sci Eng A 2006;432:20–5. doi:10.1016/j.msea.2006.06.070.

[37] Stanford N, Atwell D, Beer a., Davies C, Barnett MR. Effect of microalloying with rare-earth elements on the texture of extruded magnesium-based alloys. Scr Mater 2008;59:772–5. doi:10.1016/j.scriptamat.2008.06.008.

[38] Ball EA, Prangnell PB. Tensile-compressive yield asymmetries in high strength wrought magnesium alloys. Scr Metall Mater 1994;31:111–6. doi:10.1016/0956-716X(94)90159-7.

[39] Mackenzie LWF, Davis B, Humphreys FJ, Lorimer GW. The deformation, recrystallisation and texture of three magnesium alloy extrusions. Mater Sci Technol 2007;23:1173–80. doi:10.1179/174328407X226509.

[40] Bettles CJ, Gibson MA. Current wrought magnesium alloys: Strengths and Weaknesses. J Mater 2005;57:46–9. doi:10.1007/s11837-005-0095-0.

[41] Agnew SR. Wrought magnesium: A 21st Century Outlook. J Mater 2004;56:20–1. doi:10.1007/s11837-004-0120-8.

[42] Suresh S. Fatigue of Materials. 2nd ed. Cambridge University Press; 2004.

[43] Potzies C, Kainer KU. Fatigue of magnesium alloys. Adv Eng Mater 2004;6:281–9. doi:10.1002/adem.200400021.

[44] Sakai T. Review and Prospects for Current Studies on Very High Cycle Fatigue of Metallic Materials for Machine Structural Use. J Solid Mech Mater Eng 2009;3:425–39. doi:10.1299/jmmp.3.425.

[45] Unigovski Y, Eliezer A, Abramov E, Snir Y, Gutman EM. Corrosion fatigue of extruded magnesium alloys. Mater Sci Eng A 2003;360:132–9. doi:10.1016/S0921-5093(03)00409-X.

[46] Nový F, Janeček M, Škorik V, Muller J, Wagner L. Very high cycle fatigue behaviour of as-extruded AZ31, AZ80, and ZK60 magnesium alloys. Int J Mater Res 2009;100:288–91. doi:10.3139/146.110043.

[47] Yang F, Lv F, Yang XM, Li SX, Zhang ZF, Wang QD. Enhanced very high cycle fatigue performance of extruded Mg-12Gd-3Y-0.5Zr magnesium alloy. Mater Sci Eng A 2011;528:2231–8. doi:10.1016/j.msea.2010.12.092.

[48] Mughrabi H. On the life-controlling microstructural fatigue mechanisms in ductile metals and alloys in the gigacycle regime. Fatigue Fract Eng Mater Struct 1999;22:633–41. doi:10.1046/j.1460-2695.1999.00186.x.

[49] Wang QY, Zhang HY, Sriraman SR, Liu SL. Super Long Life Fatigue of AE42 and AM60 Magnesium Alloys. Key Eng Mater 2006;306–308:181–6. doi:10.4028/www.scientific.net/KEM.306-308.181.

[50] Yang F, Yin SM, Li SX, Zhang ZF. Crack initiation mechanism of extruded AZ31 magnesium alloy in the very high cycle fatigue regime. Mater Sci Eng A 2008;491:131–6. doi:10.1016/j.msea.2008.02.003.

[51] Mayer H, Stich A, Zettl B, Haldenwanger HG. High cycle fatigue of magnesium alloys. In: Kainer KU, editor. Magnes. Proc. 6th Int. Conf. Magnes. Alloy. Their Appl., vol. 2, Wiley-VCH Verlag GmbH; 2004, p. 743–50.

[52] Gu XN, Zhou WR, Zheng YF, Cheng Y, Wei SC, Zhong SP, et al. Corrosion fatigue behaviors of two biomedical Mg alloys – AZ91D and WE43 – In simulated body fluid. Acta Biomater 2010;6:4605–13. doi:10.1016/j.actbio.2010.07.026.

[53] Chan KS. Roles of microstructure in fatigue crack initiation. Int J Fatigue 2010;32:1428–47. doi:10.1016/j.ijfatigue.2009.10.005.

[54] Lukáš P, Kunz L. Specific features of high-cycle and ultra-high-cycle fatigue. Fatigue Fract Eng Mater Struct 2002;25:747–53. doi:10.1046/j.1460-2695.2002.00562.x.

[55] Renner F, Zenner H. Fatigue strength of die-cast magnesium components. Fatigue Fract Eng Mater Struct 2002;25:1157–68. doi:10.1046/j.1460-2695.2002.00607.x.

[56] Mayer H, Papakyriacou M, Zettl B, Stanzl-Tschegg S. Influence of porosity on the fatigue limit of die cast magnesium and aluminium alloys. Int J Fatigue 2003;25:245–56. doi:10.1016/S0142-1123(02)00054-3.

[57] Sajuri Z Bin, Miyashita Y, Hosokai Y, Mutoh Y. Effects of Mn content and texture on fatigue properties of as-cast and extruded AZ61 magnesium alloys. Int J Mech Sci 2006;48:198–209. doi:10.1016/j.ijmecsci.2005.09.003.

[58] YANG Y, LI X. Influence of neodymium on high cycle fatigue behavior of die cast AZ91D magnesium alloy. J Rare Earths 2010;28:456–60. doi:10.1016/S1002-0721(09)60133-2.

[59] Ishihara S, Namito T, Yoshifuji S, Goshima T. On fatigue lives of diecast and extruded Mg alloys. Int J Fatigue 2012;35:56–62. doi:10.1016/j.ijfatigue.2010.11.023.

[60] Caton MJ, Jones JW, Boileau JM, Allison JE. The effect of solidification rate on the growth of small fatigue cracks in a cast 319-type aluminum alloy. Metall Mater Trans A 1999;30:3055–68. doi:10.1007/s11661-999-0216-4.

[61] Tokaji K, Kamakura M, Ishiizumi Y, Hasegawa N. Fatigue behaviour and fracture mechanism of a rolled AZ31 magnesium alloy. Int J Fatigue 2004;26:1217–24. doi:10.1016/j.ijfatigue.2004.03.015.

[62] Bernard JD, Jordon JB, Lugo M, Hughes JM, Rayborn DC, Horstemeyer MF. Observations and modeling of the small fatigue crack behavior of an extruded AZ61 magnesium alloy. Int J Fatigue 2013;52:20–9. doi:10.1016/j.ijfatigue.2013.02.015.

[63] Uematsu Y, Kakiuchi T, Tamada K, Kamiya Y. EBSD analysis of fatigue crack initiation behavior in coarse-grained AZ31 magnesium alloy. Int J Fatigue 2016;84:1–8. doi:10.1016/j.ijfatigue.2015.11.010.

[64] Shih T-S, Liu W-S, Chen Y-J. Fatigue of as-extruded AZ61A magnesium alloy. Mater Sci Eng A 2002;325:152–62. doi:10.1016/S0921-5093(01)01411-3.

[65] Uematsu Y, Tokaji K, Matsumoto M. Effect of aging treatment on fatigue behaviour in extruded AZ61 and AZ80 magnesium alloys. Mater Sci Eng A 2009;517:138–45. doi:10.1016/j.msea.2009.03.066.

[66] Zhang B, Poirier DR, Chen W. Microstructural effects on high-cycle fatigue-crack initiation in A356.2 casting alloy. Metall Mater Trans A 1999;30A:2659–66. doi:10.1007/s11661-999-0306-3.

[67] Uematsu Y, Tokaji K, Kamakura M, Uchida K, Shibata H, Bekku N. Effect of extrusion conditions on grain refinement and fatigue behaviour in magnesium alloys. Mater Sci Eng A 2006;434:131–40. doi:10.1016/j.msea.2006.06.117.

[68] Bernard JD, Jordon JB, Horstemeyer MF, Kadiri HE, Baird J, Lamb D, et al. Structure-property relations of cyclic damage in a wrought magnesium alloy. Scr Mater 2010;63:751–6. doi:10.1016/j.scriptamat.2010.05.048.

[69] Atrens A, Hoffelner W, Duerig TW, Allison JE. Subsurface Crack Initiation in High Cycle Fatigue in Ti6Al4V and in a Typical Martensitic Stainless Steel. Scr Metall 1983;17:601–6.

[70] Ravi Chandran KS, Jha SK. Duality of the S-N fatigue curve caused by competing failure modes in a titanium alloy and the role of Poisson defect statistics. Acta Mater 2005;53:1867–81. doi:10.1016/j.actamat.2004.12.032.

[71] Szczepanski CJ, Jha SK, Larsen JM, Jones JW. Microstructural Influences on Very-High-Cycle Fatigue-Crack Initiation in Ti-6246. Metall Mater Trans A 2008;39:2841–51. doi:10.1007/s11661-008-9633-z.

[72] Huang Z, Wagner D, Bathias C, Paris PC. Subsurface crack initiation and propagation mechanisms in gigacycle fatigue. Acta Mater 2010;58:6046–54. doi:10.1016/j.actamat.2010.07.022.

[73] Stanzl-Tschegg SE, Schönbauer B. Mechanisms of strain localization, crack initiation and fracture of polycrystalline copper in the VHCF regime. Int J Fatigue 2010;32:886–93. doi:10.1016/j.ijfatigue.2009.03.016.

[74] Moore AR, Torbet CJ, Shyam A, Jones JW, Walukas DM, Decker RF, et al. FATIGUE BEHAVIOR OF THIXOMOLDED ® MAGNESIUM AZ91D USING ULTRASONIC TECHNIQUES. Magnes Technol 2004.

[75] Berger C, Pyttel B, Trossmann T. Very high cycle fatigue tests with smooth and notched specimens and screws made of light metal alloys. Int J Fatigue 2006;28:1640–6. doi:10.1016/j.ijfatigue.2005.05.015.

[76] Li T, Wang QY, Dou QF, Wang C, Sriraman MR. Investigations on Fatigue Properties of Die Cast Magnesium Alloy AZ91HP at Very High Cycles. Key Eng Mater 2007;353–358:235–8. doi:10.4028/www.scientific.net/KEM.353-358.235.

[77] Xue Y, Horstemeyer MF, McDowell DL, Kadiri HE, Fan J. Microstructure-based multistage fatigue modeling of a cast AE44 magnesium alloy. Int J Fatigue 2007;29:666–76. doi:10.1016/j.ijfatigue.2006.07.005.

[78] He C, Liu Y, Dong J, Wang Q, Wagner D, Bathias C. Fatigue crack initiation behaviors throughout friction stir welded joints in AA7075-T6 in ultrasonic fatigue. Int J Fatigue 2015;81:171–8. doi:10.1016/j.ijfatigue.2015.07.012.

[79] Sakai T, Kikuchi S, Nakamura Y, Ninomiya N. A Study on Very High Cycle Fatigue Properties of Low Flammability Magnesium Alloy in Rotating Bending and Axial Loading. Appl Mech Mater 2015;782:27–41. doi:10.4028/www.scientific.net/AMM.782.27.

[80] Karr U, Stich A, Mayer H. Very high cycle fatigue of wrought magnesium alloy AZ61. Procedia Struct Integr 2016;2:1047–54. doi:10.1016/j.prostr.2016.06.134.

[81] Shiozawa K, Kashiwagi T, Murai T, Takahashi T. Fatigue behaviour and fractography of extruded AZ80 magnesium alloys in very high cycle regime. Procedia Eng 2010;2:183–91. doi:10.1016/j.proeng.2010.03.020.

[82] Xu DK, Liu L, Xu YB, Han EH. The crack initiation mechanism of the forged Mg–Zn–Y–Zr alloy in the super-long fatigue life regime. Scr Mater 2007;56:1–4. doi:10.1016/j.scriptamat.2006.09.006.

[83] Paris PC, Gomez MP, Anderson WE. A rational analytic theory of fatigue. Trend Eng 1961;13:9–14. doi:10.11648/j.ijmea.s.2015030201.11.

[84] Paris P, Erdogan F. A Critical Analysis of Crack Propagation Laws. Trans Am Soc Met 1963:528–34.

[85] Zapffe CA, Worden CO. Fractographic registrations of fatigue. Trans Am Soc Met 1951;43:958–69.

[86] Forsyth PJE, Ryder DA. Fatigue fracture. Aircr Eng 1960;32:96–9.

[87] Laird C, Smith GC. Crack propagation in high stress fatigue. Philos Mag 1962;7:847–57. doi:10.1080/14786436208212674.

[88] ASTM Special Technical Publication N0. 415 - Fatigue Crack Propagation. 69th Annu. Meet. Am. Soc. Test. Mater., 1967.

[89] Wanhill RJH. Formation of brittle fatigue striations. Corrosion 1975;31:66–71. doi:10.5006/0010-9312-31.2.66.

[90] Laird C. ASTM STP 415 - The Influence of Metallurgical Structure on the Mechanisms of Fatigue Crack Propagation. Am Soc Test Mater 1967:131. doi:10.1520/STP47230S.

[91] Mcevily AJ, Matsunaga H. On Fatigue Striations. Sci Iran Trans B Mech Eng 2010;17:75–82.

[92] Broek D, Van der Vet WJ. Systematic electron fractography of fatigue in aluminium alloys - NLR-TR 68002. 1967.

[93] Riemelmoser FO, Pippan R, Stüwe HP. An argument for a cycle-by-cycle propagation of fatigue cracks atsmall stress intensity ranges. Acta Mater 1998;46:1793–9. doi:10.1016/S1359-6454(97)00366-2.

[94] Nix KJ, Flower HM. The use of electron optical techniques in the study of fatigue in high strength aluminium alloy 7010. Mater. Exp. Des. fatigue Proc. fatigue ’81, 1981, p. 117–26.

[95] Lankford J, Davidson DL. Fatigue crack mecromechanisms in ingot and powder metallurgy 7xxx aluminium alloys in air and vacuum. Acta Metall 1983;31:1273–84.

[96] Roven HJ, Nes E. Cyclic deformation of ferritic steel-II. Stage II crack propagation. Acta Metall Mater 1991;39:1735–54. doi:10.1016/0956-7151(91)90142-N.

[97] Darvish M, Johansson S. BEACH MARK FORMATION CAUSED BY CHANGES IN ENVIRONMENTAL HUMIDITY DURING FATIGUE. Fatigue Fract Eng Mater Struct 1995;18:319–27. doi:10.1111/j.1460-2695.1995.tb00878.x.

[98] Darvish M, Johansson S. Fatigue crack growth studies under combination of single overload and cyclic condensation environment. Eng Fract Mech 1995;52. doi:10.1016/0013-7944(94)00217-6.

[99] Branco R, Antunes F V., Costa JD, Yang FP, Kuang ZB. Determination of the Paris law constants in round bars from beach marks on fracture surfaces. Eng Fract Mech 2012;96:96–106. doi:10.1016/j.engfracmech.2012.07.009.

[100] Liu XL, Chen X, Tao CH. Fatigue Propagation Life Evaluating for Materials or Components Suffered Load Spectrum by Quantitative Fractography. Adv Mater Res 2014;887–888:1053–9. doi:10.4028/www.scientific.net/AMR.887-888.1053.

[101] Furuya Y. Visualization of internal small fatigue crack growth. Mater Lett 2013;112:139–41. doi:10.1016/j.matlet.2013.09.015.

[102] Pearson S. Initiation of fatigue cracks in commercial aluminium alloys and the subsequent propagation of very short cracks. Eng Fract Mech 1975;7:235–47. doi:10.1016/0013-7944(75)90004-1.

[103] Tanaka K, Nakai Y, Yamashita M. Fatigue growth threshold of small cracks. Int J Fract 1981;17:519–33. doi:10.1007/BF00033345.

[104] Lankford J. The Growth of Small Fatigue Cracks in 7075-T6 Aluminum. Fatigue Eng Mater Struct 1982;5:233–48. doi:10.1111/j.1460-2695.1982.tb01251.x.

[105] Suresh S, Ritchie RO. Propagation of short fatigue cracks. Int Met Rev 1984;29:445–75. doi:10.1179/imtr.1984.29.1.445.

[106] Ritchie RO, Lankford J. Small fatigue cracks: A statement of the problem and potential solutions. Mater Sci Eng 1986;84:11–6. doi:10.1016/0025-5416(86)90217-X.

[107] Elber W. Fatigue Crack Closure Under Cyclic Tension. Eng Fract Mech 1970;2:37–45. doi:10.1016/0013-7944(70)90028-7.

[108] Gall K, Biallas G, Maier HJ, Horstemeyer MF, McDowell DL. Environmentally influenced microstructurally small fatigue crack growth in cast magnesium. Mater Sci Eng A 2005;396:143–54. doi:10.1016/j.msea.2005.01.014.

[109] Haitham EK, Horstemeyer MF, Jordon JB, Xue Y. Fatigue Crack Growth Mechanisms in High-Pressure Die-Cast Magnesium Alloys. Metall Mater Trans A 2008;39:190–205. doi:10.1007/s11661-007-9328-x.

[110] Nan ZY, Ishihara S, McEvily AJ, Shibata H, Komano K. On the sharp bend of the S–N curve and the crack propagation behavior of extruded magnesium alloy. Scr Mater 2007;56:649–52. doi:10.1016/j.scriptamat.2007.01.009.

[111] Newman JC. The merging of fatigue and fracture mechanics concepts: a historical perspective. Prog Aerosp Sci 1998;34:347–90. doi:10.1016/S0376-0421(98)00006-2.

[112] McDowell DL, Dunne FPE. Microstructure-sensitive computational modeling of fatigue crack formation. Int J Fatigue 2010;32:1521–42. doi:10.1016/j.ijfatigue.2010.01.003.

[113] Morris WL. The Noncontinuum Crack Tip Deformation Behaviour of Surface Microcracks. Metall Trans A 1980;11A:1117–23.

[114] Nicoletto G, Konečná R, Pirondi A. Fatigue crack paths in coarse-grained magnesium. Fatigue Fract Eng Mater Struct 2005;28:237–44. doi:10.1111/j.1460-2695.2004.00832.x.

[115] Bieler TR, Eisenlohr P, Zhang C, Phukan HJ, Crimp MA. Grain boundaries and interfaces in slip transfer. Curr Opin Solid State Mater Sci 2014;18:212–26. doi:10.1016/j.cossms.2014.05.003.

[116] King A, Ludwig W, Herbig M, Buffière J-Y, Khan AA, Stevens N, et al. Three-dimensional in situ observations of short fatigue crack growth in magnesium. Acta Mater 2011;59:6761–71. doi:10.1016/j.actamat.2011.07.034.

[117] Zhai T, Wilkinson AJ, Martin JW. Crystallographic mechanism for fatigue crack propagation through grain boundaries. Acta Mater 2000;48:4917–27. doi:10.1016/S1359-6454(00)00214-7.

[118] Bilby B. A., Cottrell A. H., Swinden K. H. The Spread of Plastic Yield from a Notch. Proc R Soc A Math Phys Eng Sci 1963;272:304–14.

[119] Zhang YH, Edwards L. The Effect of Grain Boundaries on the Development of Plastic Deformation Ahead of Small Fatigue Cracks. Scr Metall Mater 1992;26:1901–6. doi:10.1016/0956-716X(92)90056-K.

[120] Edwards L, Zhang YH. Investigation of small fatigue cracks—I. Plastic deformation associated with small fatigue cracks. Acta Metall Mater 1994;42:1413–21. doi:10.1016/0956-7151(94)90160-0.

[121] Tanaka K, Akiniwa Y, Nakai Y, Wei RP. Modelling of small fatigue crack growth interacting with grain boundary. Eng Fract Mech 1986;24:803–19. doi:10.1016/0013-7944(86)90266-3.

[122] Rios ERDL, Xin XJ, Navarro a. Modelling Microstructurally Sensitive Fatigue Short Crack Growth. Proc R Soc A Math Phys Eng Sci 1994;447:111–34. doi:10.1098/rspa.1994.0131.

[123] Krupp U. Fatigue Crack Propagation in Metals and Alloys: Microstructural Aspects and Modelling Concepts. Wiley-VCH Verlag GmbH; 2007.

[124] Bayerschen E, McBride AT, Reddy BD, Böhlke T. Review on slip transmission criteria in experiments and crystal plasticity models. J Mater Sci 2016;51:2243–58. doi:10.1007/s10853-015-9553-4.

[125] Schaef W, Marx M, Vehoff H, Heckl A, Randelzhofer P. A 3-D view on the mechanisms of short fatigue cracks interacting with grain boundaries. Acta Mater 2011;59:1849–61. doi:10.1016/j.actamat.2010.11.051.

[126] Marx M, Schaef W, Vehoff H. Interaction of short cracks with the local microstructure. Procedia Eng 2010;2:163–71. doi:10.1016/j.proeng.2010.03.018.

[127] Zhai T, Jiang XP, Li JX, Garratt MD, Bray GH. The grain boundary geometry for optimum resistance to growth of short fatigue cracks in high strength Al-alloys. Int J Fatigue 2005;27:1202–9. doi:10.1016/j.ijfatigue.2005.06.021.

[128] Luster J, Morris MA. Compatibility of deformation in two-phase Ti-Al alloys: Dependence on microstructure and orientation relationships. Metall Mater Trans A 1995;26:1745–56. doi:10.1007/BF02670762.

[129] Pilchak AL, Williams REA, Williams JC. Crystallography of fatigue crack initiation and growth in fully lamellar Ti-6Al-4V. Metall Mater Trans A Phys Metall Mater Sci 2010;41:106–24. doi:10.1007/s11661-009-0064-2.

[130] Panwar S, Adams JF, Allison JE, Jones JW, Sundararaghavan V. A grain boundary interaction model for microstructurally short fatigue cracks 2018:under preparation.

[131] Davies PA, Randle V. Combined application of electron backscatter diffraction and stereo-photogrammetry in fractography studies. J Microsc 2001;204:29–38. doi:10.1046/j.1365-2818.2001.00922.x.

[132] Garrett GG, Knot JF. Crystallographic fatigue crack growth in aluminium alloys. Acta Metall 1975;23:841–8.

[133] Spear AD, Ingraffea AR. Effect of chemical milling on low-cycle fatigue behavior of an Al-Mg-Si alloy. Corros Sci 2013;68:144–53. doi:10.1016/j.corsci.2012.11.006.

[134] Gupta VK, Agnew SR. Fatigue crack surface crystallography near crack initiating particle clusters in precipitation hardened legacy and modern Al-Zn-Mg-Cu alloys. Int J Fatigue 2011;33:1159–74. doi:10.1016/j.ijfatigue.2011.01.018.

[135] Ro YJ, Agnew SR, Gangloff RP. Uncertainty in the determination of fatigue crack facet crystallography. Scr Mater 2005;52:531–6. doi:10.1016/j.scriptamat.2004.10.040.

[136] Ro YJ, Agnew SR, Gangloff RP. Crystallography of fatigue crack propagation in precipitation-hardened Al-Cu-Mg/Li. Metall Mater Trans A Phys Metall Mater Sci 2007;38 A:3042–62. doi:10.1007/s11661-007-9344-x.

[137] Ro YJ, Agnew SR, Gangloff RP. Environmental fatigue-crack surface crystallography for Al-Zn-Cu-Mg-Mn/Zr. Metall Mater Trans A Phys Metall Mater Sci 2008;39 A:1449–65. doi:10.1007/s11661-008-9522-5.

[138] Slavik DC, Wert JA, Gangloff RP. Determining fracture facet crystallography using electron backscatter patterns and quantitative tilt fractography. J Mater Res 1993;8:2482–91. doi:10.1557/JMR.1993.2482.

[139] Sinha V, Mills MJ, Williams JC. Determination of crystallographic orientation of dwell-fatigue fracture facets in Ti-6242 alloy. J Mater Sci 2007;42:8334–41. doi:10.1007/s10853-006-0252-z.

[140] Themelis G, Chikwembani S, Weertman J. Determination of the orientation of CuBi grain boundary facets using a photogrammetric technique. Mater Charact 1990;24:27–40. doi:10.1016/1044-5803(90)90069-V.

[141] Uchic M, Groeber M, Shah M, Callahan P, Shiveley A, Scott M, et al. An Automated Multi-Modal Serial Sectioning System for Characterization of Grain-Scale Microstructures in Engineering Materials. Proc 1st Int Conf 3D Mater Sci 2012:195–202. doi:10.1007/978-3-319-48762-5_30.

[142] Barter SA, Molent L, Wanhill RJH. Marker loads for quantitative fractography of fatigue cracks in aerospace alloys. Bridg Gap between Theory Oper Pract 25th ICAF Symp 2009:14–54.

[143] Burns JT, Larsen JM, Gangloff RP. Effect of initiation feature on microstructure-scale fatigue crack propagation in Al-Zn-Mg-Cu. Int J Fatigue 2012;42:104–21. doi:10.1016/j.ijfatigue.2011.08.001.

[144] Stock SR. Recent advances in X-ray microtomography applied to materials. Int Mater Rev 2008;53:129–81. doi:10.1179/174328008X277803.

[145] Ludwig W, King A, Reischig P, Herbig M, Lauridsen EM, Schmidt S, et al. New opportunities for 3D materials science of polycrystalline materials at the micrometre lengthscale by combined use of X-ray diffraction and X-ray imaging. Mater Sci Eng A 2009;524:69–76. doi:10.1016/j.msea.2009.04.009.

[146] Buffiére JY, Limodin N, Réthoré J, Ludwig W, Hild F, Gravouil A, et al. 3D Characterisation of Fatigue Cracks Using X-ray Tomography: From Synchrotron to Laboratory Sources. Suppl. Proc. Vol. 2 Mater. Charact. Comput. Model. Energy, 2010.

[147] Maire E, Withers PJ. Quantitative X-ray tomography. Int Mater Rev 2014;59:1–43. doi:10.1179/1743280413Y.0000000023.

[148] Ludwig W, Buffière JY, Savelli S, Cloetens P. Study of the interaction of a short fatigue crack with grain boundaries in a cast Al alloy using X-ray microtomography. Acta Mater 2003;51:585–98. doi:10.1016/S1359-6454(02)00320-8.

[149] Toda H, Sinclair I, Buffiére JY, Maire E, Connolley T, Joyce M, et al. Assessment of the fatigue crack closure phenomenon in damage-tolerant aluminium alloy by in-situ high-resolution synchrotron X-ray microtomography. Philos Mag 2003;83:2429–48. doi:10.1080/1478643031000115754.

[150] Khor KH, Buffière JY, Ludwig W, Toda H, Ubhi HS, Gregson PJ, et al. In situ high resolution synchrotron x-ray tomography of fatigue crack closure micromechanisms. J Phys Condens Matter 2004;16. doi:10.1088/0953-8984/16/33/012.

[151] Ferrié E, Buffière JY, Ludwig W. 3D characterisation of the nucleation of a short fatigue crack at a pore in a cast Al alloy using high resolution synchrotron microtomography. Int J Fatigue 2005;27:1215–20. doi:10.1016/j.ijfatigue.2005.07.015.

[152] Buffiere JY, Ferrie E, Proudhon H, Ludwig W. Three-dimensional visualisation of fatigue cracks in metals using high resolution synchrotron X-ray micro-tomography. Mater Sci Technol 2006;22:1019–24. doi:10.1179/174328406X114135.

[153] Proudhon H, Buffière JY, Fouvry S. Three-dimensional study of a fretting crack using synchrotron X-ray micro-tomography. Eng Fract Mech 2007;74:782–93. doi:10.1016/j.engfracmech.2006.06.019.

[154] Sinclair R, Preuss M, Maire E, Buffiere JY, Bowen P, Withers PJ. The effect of fibre fractures in the bridging zone of fatigue cracked Ti-6Al-4V/SiC fibre composites. Acta Mater 2004;52:1423–38. doi:10.1016/j.actamat.2003.11.024.

[155] Birosca S, Buffiere JY, Karadge M, Preuss M. 3-D observations of short fatigue crack interaction with lamellar and duplex microstructures in a two-phase titanium alloy. Acta Mater 2011;59:1510–22. doi:10.1016/j.actamat.2010.11.015.

[156] Proudhon H, Moffat A, Sinclair I, Buffiere JY. Three-dimensional characterisation and modelling of small fatigue corner cracks in high strength Al-alloys. Comptes Rendus Phys 2012;13:316–27. doi:10.1016/j.crhy.2011.12.005.

[157] Li SF, Suter RM. Adaptive reconstruction method for three-dimensional orientation imaging. J Appl Crystallogr 2013;46:512–24. doi:10.1107/S0021889813005268.

[158] Renversade L, Quey R, Ludwig W, Menasche D, Maddali S, Suter RM, et al. Comparison between diffraction contrast tomography and high-energy diffraction microscopy on a slightly deformed aluminium alloy. Int Union Crystallogr J 2016;3:32–42. doi:10.1107/S2052252515019995.

[159] Herbig M, King A, Reischig P, Proudhon H, Lauridsen EM, Marrow J, et al. 3-D growth of a short fatigue crack within a polycrystalline microstructure studied using combined diffraction and phase-contrast X-ray tomography. Acta Mater 2011;59:590–601. doi:10.1016/j.actamat.2010.09.063.

[160] Grinberg NM, Serdyuk VA, Zmeevets SG. Effect of Structural State Upon Fatigue Fracture in MA12 Magnesium Alloy in Air and in Vacuo. Probl Prochnosti 1979:1026–31.

[161] Tokaji K, Nakajima M, Uematsu Y. Fatigue crack propagation and fracture mechanisms of wrought magnesium alloys in different environments. Int J Fatigue 2009;31:1137–43. doi:10.1016/j.ijfatigue.2008.12.012.

[162] Uematsu Y, Kakiuchi T, Nakajima M, Nakamura Y, Miyazaki S, Makino H. Fatigue crack propagation of AZ61 magnesium alloy under controlled humidity and visualization of hydrogen diffusion along the crack wake. Int J Fatigue 2014;59:234–43. doi:10.1016/j.ijfatigue.2013.08.014.

[163] Rozali S, Mutoh Y, Nagata K. Effect of frequency on fatigue crack growth behavior of magnesium alloy AZ61 under immersed 3.5 mass% NaCl environment. Mater Sci Eng A 2011;528:2509–16. doi:10.1016/j.msea.2010.12.048.

[164] Willertz LE. Ultrasonic fatigue. Int Met Rev 1980;25:65–78. doi:10.1179/imtr.1980.25.1.65.

[165] Mason WP. Piezoelectric Crystals and Their Application to Ultrasonics. New York: D. Van Nostrand Company, Inc; 1950.

[166] Furuya Y. Specimen size effects on gigacycle fatigue properties of high-strength steel under ultrasonic fatigue testing. Scr Mater 2008;58:1014–7. doi:10.1016/j.scriptamat.2008.01.039.

[167] Stanzl-Tschegg S, Schönbauer B. Near-threshold fatigue crack propagation and internal cracks in steel. Procedia Eng 2010;2:1547–55. doi:10.1016/j.proeng.2010.03.167.

[168] Caton MJ, Jones JW, Mayer H, Stanzl-Tschegg S, Allison JE. Demonstration of an endurance limit in cast 319 aluminum. Metall Mater Trans A 2003;34:33–41. doi:10.1007/s11661-003-0206-x.

[169] Szczepanski CJ, Jha SK, Larsen JM, Jones JW. Microstructural influences on very-high-cycle fatigue-crack initiation in Ti-6246. Metall Mater Trans A Phys Metall Mater Sci 2008;39:2841–51. doi:10.1007/s11661-008-9633-z.

[170] Mayer H. Fatigue crack growth and threshold measurements at very high frequencies. Int Mater Rev 1999;44:1–34. doi:10.1179/095066099771048801.

[171] Caton MJ, Jones JW, Allison JE. The influence of heat treatment and solidification time on the behavior of small-fatigue-cracks in a cast aluminum alloy. Mater Sci Eng A 2001;314:81–5. doi:10.1016/S0921-5093(00)01916-X.

[172] Okamoto H. Mg-Y (magnesium-yttrium). J Phase Equilibria Diffus 2010;31:199. doi:10.1007/s11669-010-9661-4.

[173] Nie JF, Muddle BC. Characterisation of strengthening precipitate phases in a Mg–Y–Nd alloy. Acta Mater 2000;48:1691–703. doi:10.1016/S1359-6454(00)00013-6.

[174] Azzeddine H, Bradai D. Texture and Microstructure of WE54 Alloy after Hot Rolling and Annealing. Mater Sci Forum 2011;702–703:453–6. doi:10.4028/www.scientific.net/MSF.702-703.453.

[175] Mayama T, Aizawa K, Tadano Y, Kuroda M. Influence of twinning deformation and lattice rotation on strength differential effect in polycrystalline pure magnesium with rolling texture. Comput Mater Sci 2009;47:448–55. doi:10.1016/j.commatsci.2009.09.009.

[176] Ritchie RO, Suresh S. Some considerations on fatigue crack closure at near-threshold stress intensities due to fracture surface morphology. Metall Trans A 1982;13:937–40. doi:10.1007/BF02642409.

[177] Papakyriacou M, Mayer H, Fuchs U, Stanzl-Tschegg SE, Wei RP. Influence of atmospheric moisture on slow fatigue crack growth at ultrasonic frequency in aluminium and magnesium alloys. Fatigue Fract Eng Mater Struct 2002;25:795–804. doi:10.1046/j.1460-2695.2002.00571.x.

[178] Githens AS. Deformation Mechanisms of Magnesium Alloy WE43 under Monotonic Tensile Loading. University of Michigan, 2015.

[179] ASTM International. ASTM Standard E647 - Standard Test Method for Measurement of Fatigue Crack Growth Rates. Am Soc Test Mater 2014:1–50. doi:10.1520/E0647-13A.2.

[180] Newman JC, Raju IS. NASA Technical Memorandum 85793: Stress-Intensity Factor Equations for Cracks in Three-Dimensional Finite Bodies Subjected to Tension and Bending Loads. 1984.

[181] Avizo Standard 2017.

[182] Bernier J V., Barton NR, Lienert U, Miller MP. Far-field high-energy diffraction microscopy: A tool for intergranular orientation and strain analysis. J Strain Anal Eng Des 2011;46:527–47. doi:10.1177/0309324711405761.

[183] Poulsen FP. Three-Dimensional X-ray Diffraction Microscopy. vol. 209. Springer Tracts in Modern Physics; 2004.

[184] Solomon E, Marquis E. Private Communication 2016.

[185] Ogarevic V V., Stephens RI. Fatigue of Magnesium Alloys. Annu Rev Mater Sci 1990;20:141–77.

[186] McFadyen N, Bell R, Vosikovsky O. Fatigue crack growth of semi-elliptical surface cracks. Int J Fatigue 1990;12:43–50. doi:10.1016/0142-1123(90)90341-B.

[187] Ravichandran KS. A theoretical model for roughness induced crack closure. Int J Fract 1990;44:97–110. doi:10.1007/BF00047062.

[188] Zurek AK, James MR, Morris WL. The effect of grain size on fatigue growth of short cracks. Metall Trans A 1983;14A:1697–705.

[189] Turnbull A, de los Rios ER. The Effect of Grain Size on Fatigue Crack Growth in an Aluminium Magnesium Alloy. Fatigue Fract Eng Mater Struct 1995;18:1355–66. doi:10.1111/j.1460-2695.1995.tb00861.x.

[190] Yue TM, Ha HU, Musson NJ. Grain size effects on the mechanical properties of some squeeze cast light alloys. J Mater Sci 1995;30:2277–83. doi:10.1007/BF01184573.

[191] Horstemeyer MF, Yang N, Gall K, McDowell DL, Fan J, Gullett PM. High cycle fatigue of a die cast AZ91E-T4 magnesium alloy. Acta Mater 2004;52:1327–36. doi:10.1016/j.actamat.2003.11.018.

[192] Liu W-C, Dong J, Zhang P, Jin L, Peng T, Zhai C-Q, et al. Fatigue behavior of hot-extruded Mg–10Gd–3Y magnesium alloy. J Mater Res 2010;25:773–83. doi:10.1557/JMR.2010.0104.

[193] Tsushida M, Shikada K, Kitahara H, Ando S, Tonda H. Relationship between Fatigue Strength and Grain Size in AZ31 Magnesium Alloys. Mater Trans 2008;49:1157–61. doi:10.2320/matertrans.MC2007101.

[194] Li Z, Wang Q, Luo AA, Zhang P, Peng L. Size Effect on Magnesium Alloy Castings. Metall Mater Trans A 2016;47A:2686–704. doi:10.1007/s11661-016-3436-4.

[195] Miao J, Pollock TM, Wayne Jones J. Microstructural extremes and the transition from fatigue crack initiation to small crack growth in a polycrystalline nickel-base superalloy. Acta Mater 2012;60:2840–54. doi:10.1016/j.actamat.2012.01.049.

[196] Stanzl SE, Mayer HR, Tschegg EK. The influence of air humidity on near-threshold fatigue crack growth of 2024-T3 aluminum alloy. Mater Sci Eng A 1991;147:45–54. doi:10.1016/0921-5093(91)90803-U.

[197] Sajuri ZB, Miyashita Y, Mutoh Y. Effects of humidity and temperature on the fatigue behaviour of an extruded AZ61 magnesium alloy. Fatigue Fract Eng Mater Struct 2005;28:373–9. doi:10.1111/j.1460-2695.2005.00775.x.

[198] Stanzl-tschegg S. Fatigue crack growth and thresholds at ultrasonic frequencies. Int Jounal Fatigue 2006;28:1456–64. doi:10.1016/j.ijfatigue.2005.06.058.

[199] Gall K, Biallas G, Maier HJ, Gullett P, Horstemeyer MF, McDowell DL, et al. In-situ observations of high cycle fatigue mechanisms in cast AM60B magnesium in vacuum and water vapor environments. Int J Fatigue 2004;26:59–70. doi:10.1016/S0142-1123(03)00079-3.

[200] Murakami Y, Yokoyama NN, Nagata J. Mechanism of fatigue failure in ultralong life regime. Fatigue Fract Eng Mater Struct 2002;25:735–46. doi:10.1046/j.1460-2695.2002.00576.x.

[201] Shiozawa K, Lu L. Very high-cycle fatigue behaviour of shot-peened high-carbon-chromium bearing steel. Fatigue Fract Eng Mater Struct 2002;25:813–22. doi:10.1046/j.1460-2695.2002.00567.x.

[202] Shamblen CE, Chang DR. Effect of inclusions on LCF life of HIP plus heat treated powder metal René 95. Metall Trans B 1985;16:775–84. doi:10.1007/BF02667513.

[203] Toft A, Madew C, Beardsmore D, Teng H, Jackson M. Displacement Controlled Stress Intensity Factor Solutions for Structural Integrity Assessments of Welding Residual Stress Distributions. ASME Press. Vessel. Pip. Div. Conf., 2008, p. 1–10.

[204] Rasband WS. ImageJ n.d.

[205] Wen W, Zhai T. Quantification of resistance of grain boundaries to short-fatigue crack growth in three dimensions in high-strength al alloys. Metall Mater Trans A 2012;43:2743–52. doi:10.1007/s11661-012-1099-3.

[206] Wilkinson AJ. Modelling the effects of texture on the statistics of stage I fatigue crack growth. Philos Mag A 2001;81:841–55. doi:10.1080/01418610108214323.

[207] Guerra-Rosa L, Moura Branco C, Radon JC. Monotonic and cyclic crack tip plasticity. Int J Fatigue 1984;6:17–24. doi:10.1016/0142-1123(84)90004-5.

[208] Pierson K, Hochhalter JD, Fletcher PT, Spear AD. Data-Driven correlation analysis between observed 3D fatigue-crack path and computed fields from high-fidelity, crystal-plasticity, finite-element simulations. J Mater 2018:submitted.